BỘ GIÁO DỤC VÀ ĐÀO TẠO
VIỆN HÀN LÂM KHOA HỌC VÀ CÔNG NGHỆ VIỆT NAM

HỌC VIỆN KHOA HỌC VÀ CÔNG NGHỆ

Đinh Phú Hùng

DANH MỤC CÔNG TRÌNH CÔNG BỐ

LUẬN ÁN TIẾN SĨ NGÀNH KHOA HỌC MÁY TÍNH

NÂNG CAO HIỆU QUẢ TỔNG HỢP HÌNH ẢNH Y HỌC THEO TIẾP CẬN TỐI ƯU HOÁ

Hà Nội, 2023

DANH MỤC CÁC BÀI BÁO ĐÃ XUẤT BẢN
LIÊN QUAN ĐẾN LUẬN ÁN

[CT1] **P. H. Dinh** and L. G. Nguyen, 2022, A new medical image enhancement algorithm using adaptive parameters, *International Journal of Imaging Systems and Technology*, vol. 32, no. 6, pp. 2198–2218. **(SCIE, Q2)**.

[CT2] **P. H. Dinh**, 2023, Combining Spectral Total Variation with Dynamic Threshold Neural P Systems for Medical Image Fusion, *Biomedical Signal Processing and Control*, vol. 80, pp. 104343. **(SCIE, Q1)**.

[CT3] **P. H. Dinh**, 2022, A novel approach using structure tensor for medical image fusion, *Multidimensional Systems and Signal Processing*, vol. 33, pp. 1001–1021. **(SCIE, Q2)**.

[CT4] **P. H. Dinh**, 2023, A novel approach using the local energy function and its variations for medical image fusion, *The Imaging Science Journal*, pp. 660-676. **(SCIE, Q2)**.

[CT5] **P. H. Dinh** and L. G. Nguyen, 2023, Medical image fusion based on Transfer learning techniques and Coupled Neural P Systems, *Neural Computing and Applications*, **(SCIE, Q1)**.

[CT6] **Đinh Phú Hùng**, Nguyễn Huy Đức, Nguyễn Long Giang, 2022, Tổng hợp hình ảnh y học dựa trên giải thuật tối ưu MPA, *Hội nghị Khoa học công nghệ Quốc gia lần thứ XIV về Nghiên cứu Cơ bản và Ứng dụng Công nghệ thông tin (FAIR2022).*

Received: 19 February 2022 | Revised: 9 May 2022 | Accepted: 31 May 2022

DOI: 10.1002/ima.22778

RESEARCH ARTICLE

WILEY

A new medical image enhancement algorithm using adaptive parameters

Phu-Hung Dinh[1] | **Nguyen Long Giang**[2]

[1]Department of Network and Information Security, Thuyloi University, Hanoi, Vietnam

[2]Institute of Information Technology, Vietnam Academy of Science and Technology, Hanoi, Vietnam

Correspondence
Phu-Hung Dinh, Department of Network and Information Security, Thuyloi University, 175 Tay Son, Dong Da, Hanoi, Vietnam.
Email: hungdp@tlu.edu.vn

Funding information
Thuyloi University Foundation for Science and Technology, Grant/Award Number: TLU.STF.21-03

Abstract

The quality of medical images plays a vital role in many image processing applications such as image segmentation, feature extraction, image classification, image recognition, and image fusion. Some of the common problems with Medical images are noise, blur, or low contrast. According to our observations, current image enhancement algorithms only focus on solving individual problems such as gray level adjustment, noise reduction, or sharpness enhancement. This paper proposes a novel algorithm to solve problems on images simultaneously. First, we propose an image decomposition algorithm. This algorithm allows decomposing the image into three components: structure (I_S), texture (I_T), and noise (I_N). Second, the structural component (I_S) is enhanced by the contrast-limited adaptive histogram equalization method to obtain I_{CLAHE}. We use the structure tensor salient detection operator and the Laplace edge detection operator to add structural and texture features. These operators are applied to the I_{CLAHE} and I_T components to obtain the I_{STS} and I_{LED} components, respectively. The I_T and I_{LED} components are used to generate the enhanced component (called I_{T_E}) by using the Max operator. Third, the Marine predators algorithm is used to find the optimal parameters β_1, β_2, β_3, and β_4 corresponding to I_{CLAHE}, I_{STS}, I_{T_E}, and I_N. Finally, the enhanced image is made up of the sum of the I_{CLAHE}, I_{STS}, I_{T_E}, and I_N images multiplied by the optimal parameters β_1, β_2, β_3, and β_4, respectively. Six state-of-the-art image enhancement approaches, seven medical image fusion algorithms, and six image quality metrics have been utilized to verify the proposed approach's effectiveness. The experimental results show that the proposed method significantly improves the quality of the input medical images as well as significantly improves the efficiency of current medical image synthesis algorithms.

KEYWORDS

CLAHE, image enhancement, LED, MPA, STS

1 | INTRODUCTION

The medical images often encounter some problems, such as blur, noise, and low contrast. These limitations significantly degrade the performance of the methods such as medical image fusion, image segmentation, and pattern recognition. In general, we can divide image enhancement algorithms into two groups: spatial domain-based algorithms and transform domain-based algorithms. Spatial domain-based methods compute

directly on individual pixels or blocks of pixels. Although spatial domain-based methods improve image quality to some extent, they still have some limitations. The first limitation is that the output image can be over-enhanced. The second limitation is that important information can be eliminated. Transform domain-based methods include the following several steps. Firstly, the input image is transformed into the transform domain by the transform method. Secondly, the transform-domain components are enhanced by a predefined method. Finally, the enhanced components are transformed back to the spatial domain.

Three main problems need to be addressed to improve the quality of an image. Those issues are gray level adjustment & contrast enhancement, noise reduction, and image sharpening. For contrast enhancement, Histogram equalization (HE) is one of the most commonly used traditional methods. This method has gained popularity because of its computational simplicity. However, the images obtained after enhancement by the HE method often suffer from noise amplification and artifacts. As a result, the structural details are likely to be eliminated or reduced. Some of the improved algorithms of the HE method can be mentioned as Contrast limited adaptive histogram equalization (CLAHE),[47] Bi-histogram equalization (BHE),[52] Dynamic Histogram Equalization (DHE),[44] and Dynamic quadri-histogram equalization (DQHE).[18] Lidong et al.[28] have combined CLAHE with Discrete wavelet transform (DWT) for image enhancement. Some common noise filters can be mentioned as the mean filter or median filter for image denoising. Other advanced methods can be listed as sparse representation-based approaches[23] and convolutional network-based approaches.[31] Regarding image sharpness enhancement, the traditional method applied is based on edge detection filters such as Sobel, Prewitt, Compass operator, and Laplacian.

Especially in improving the quality of medical images, the methods mentioned above are also used to improve the quality. For example, Joseph et al.[21] have used histogram specifications to enhance the contrast of the Magnetic resonance (MR) images. Ismail et al.[20] have applied the DHE for low contrast MR images to preserve the brightness. Chen et al.[4] have introduced an algorithm called Hierarchical correlation histogram analysis (HCHA) for automatic contrast enhancement. Isa et al.[19] have introduced an algorithm called Average intensity replacement with Adaptive histogram equalization (AIR-AHE) for automatic contrast enhancement of brain MR images. Subramani et al.[48] have introduced adaptive fuzzy histogram equalization for MR brain image enhancement. Yang et al.[60] have combined DWT with HE for enhancing contrast in the brain MR images. Sahnoun et al.[46] have introduced a new MR image enhancement approach based on Singular value decomposition (SVD) and DWT. Histogram-based algorithms have been used for enhancing medical images.[18]

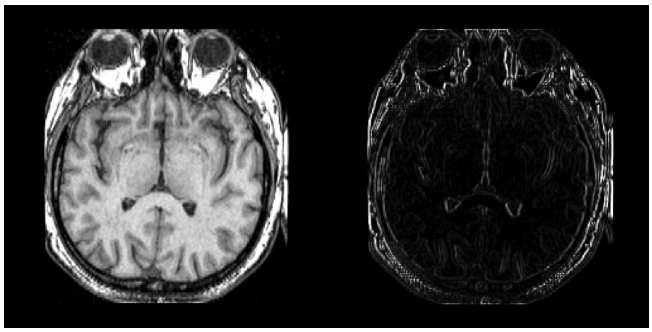

FIGURE 1 The input image and structure tensor saliency

Medical image enhancement is also an important pre-processing step in many applications. For instance, Ullah et al.[54] have proposed a method to enhance the image quality and use it as a pre-processing step before image classification. Veluchamy et al.[55] used the BHE to enhance the image quality before image segmentation. This allows for improving the efficiency of image segmentation. Eichinger et al.[14] have enhanced the input image quality to improve the efficiency of detecting multiple sclerosis lesions from MR images.

In recent years, many new optimization algorithms have been applied to many image processing problems. For example, the Marine predators algorithm (MPA),[12] the Equilibrium optimization algorithm (EOA),[8,10] Grasshopper Optimisation Algorithm (GOA)[11] are applied in the fusion of medical images. Especially in improving image quality, many meta-heuristic-based optimization algorithms have been applied to improve image quality. For example, Kandhway et al.[22] have used Krill herd optimization (KHO) to enhance the contrast of medical images. Maurya et al.[34] proposed the use of Cuckoo Search Optimization (CSO) for improving contrast and brightness. Luque_Chang et al.[30] have introduced Moth Swarm Algorithm (MSA) for image contrast enhancement. Other optimization algorithms have also been used such as Artificial bee colony (ABC),[5] Barnacles Mating Optimizer (BMO),[2] Genetic algorithm (GA),[1] Social spider optimization algorithm (SSOA),[33] and Particle swarm optimization (PSO).[53]

The MPA[15] was a recently proposed meta-heuristic algorithm. So far, this algorithm has been effectively applied in many applications, such as medical image synthesis,[9] multilevel image segmentation,[32] and fault diagnosis of rolling bearing.[6] However, according to our observation, the MPA has not been used to enhance medical imaging in any previous studies. This motivated us to apply MPA in the image enhancement model. The

ALGORITHM 1 MPA algorithm

Initialize the required parameters (the population $(i=\overline{1,n})$, matrix E and Prey.)
Assign parameters: $FADs = 0.2$; $K = 0.5$; r in [0,1].
r1 and r2 are random indexes.
$\vec{U}$ is the binary vector.
$\vec{X}_{min}$ and $\vec{X}_{max}$ are the vectors containing the lower and upper bounds.
while $l < l_{max}$ **do.**
  /* Stage 1: */.
  if $l < \frac{1}{3} l_{max}$ **then.**
    Update prey according to Equation (6).
  end
  /* Stage 2: */.
  else if $\left(l > \frac{1}{3} l_{max}\right)$ and $\left(l < \frac{2}{3} l_{max}\right)$ **then.**
    For the first half of the population.
    Prey is updated according to Equation (8).
    For the second half of the population.
    Prey is updated according to Equation (10).
  end
  /* Stage 3: */.
  else if $l > \frac{2}{3} l_{max}$ **then.**
    Prey is updated according to Equation (12).
  end
  /* Eddy formation and FADs' effect */
  if $(r \le FADs)$ **then**

$$\overrightarrow{Pr_i}\left(p_x,p_y\right) = \overrightarrow{Pr_i}\left(p_x,p_y\right) + CF^*\left(\left(\vec{X}_{min} + \vec{R} \otimes \left(\vec{X}_{max} - \vec{X}_{min}\right)\right) \otimes \vec{U}\right)$$

  end
  else if (r > FADs) **then**

$$\overrightarrow{Pr_i}\left(p_x,p_y\right) = \overrightarrow{Pr_i}\left(p_x,p_y\right) + (FADs^*(1-r) + r) * \left(\overrightarrow{Pr_{r1}}\left(p_x,p_y\right) - \overrightarrow{Pr_{r2}}\left(p_x,p_y\right)\right)$$

  end
  $l = l + 1$.
end

effectiveness of MPA in our proposed model can be seen in detail in the experimental section.

According to our current knowledge, current image enhancement methods only focus on solving individual problems on the image, such as increasing contrast, reducing noise, or increasing sharpness. Therefore, concurrent improvement of image problems is significant for many image processing applications. In this work, we propose a novel algorithm to improve the quality of the brain MR images. Some of our key contributions are listed as follows:

- First, a new image decomposition algorithm is proposed to decompose an input image into three components: structure, texture, and noise.
- Second, a novel image enhancement algorithm is introduced to simultaneously solve image problems such as adjusting contrast, reducing noise, and increasing sharpness.
- Third, the proposed image enhancement algorithm allows for improving the performance of existing image fusion algorithms.

The remaining of this paper is organized as follows: the Structure tensor salient (STS) detection operator and the MPA algorithm are introduced briefly in Section 2. The image decomposition algorithm and image enhancement algorithm are introduced in Section 3. Some evaluation indexes and experimental results are mentioned in Section 4. Finally, the conclusion and future work are given in Section 5.

2 | BACKGROUND

In this section, we introduce two main algorithms, STS detection operator and MPA. We will not mention other basic algorithms like CLAHE, Laplace edge detection (LED) operator, and Anisotropic diffusion filtering (ADF), even though these algorithms are used in our proposed model.

2.1 | Structure tensor salient detection operator

A structure tensor is an essential tool for obtaining image features. Its applications in image processing can be mentioned as follows: medical image fusion,[13] extended focused imaging in microscopy,[45] and corner detection.[56]

ALGORITHM 2 **STN decomposition**

Input: I (A gray image).

Output: I_S, I_T, I_N.

Step 1: The input image I was blurred with a Gaussian filter, obtaining an I_{GF} image.

Step 2: The total variation image reconstruction (TVIR)[3,57] algorithm is applied to the I_{GF} image to obtain a structure component (I_S).

Step 3: The detailed component I_D is determined by Equation (13)

$$I_D = I - I_S \tag{13}$$

Step 4: Texture component (I_T) obtained by applying Anisotropic diffusion filtering (ADF)[43] to I_D component.

Step 5: Noise component (I_N) is determined by Equation (14)

$$I_N = I_D - I_T \tag{14}$$

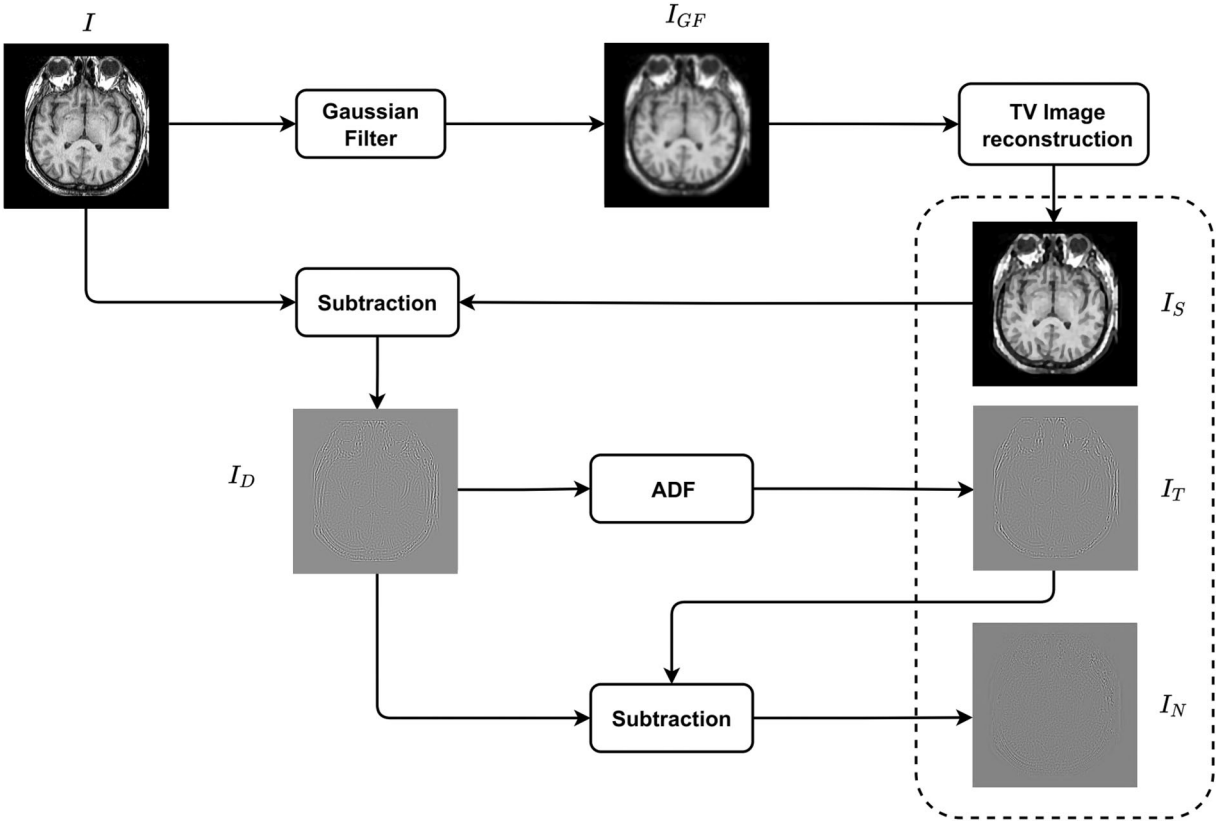

FIGURE 2 The decomposition of an image into three components

Given the image matrix I, the structure tensor is defined as Equation (1).

$$ST = \begin{bmatrix} \sum_w E_i^2 & \sum_w E_i E_j \\ \sum_w E_i E_j & \sum_w E_j^2 \end{bmatrix} \quad (1)$$

where, w is a local window. E_i and E_j as the gradient in the i and j direction, respectively.

In addition, the eigenvalues of the structure tensor provide more information about the local geometry of the input image. Eigenvalues can be calculated as Equations (2) and (3).

$$v_1 = \frac{1}{2}\left(\sum_w E_i^2 + \sum_w E_j^2 + \sqrt{\left(\sum_w E_i^2 - \sum_w E_j^2\right)^2 + 4\left(\sum_w E_i E_j\right)^2}\right) \quad (2)$$

$$v_2 = \frac{1}{2}\left(\sum_w E_i^2 + \sum_w E_j^2 - \sqrt{\left(\sum_w E_i^2 - \sum_w E_j^2\right)^2 + 4\left(\sum_w E_i E_j\right)^2}\right) \quad (3)$$

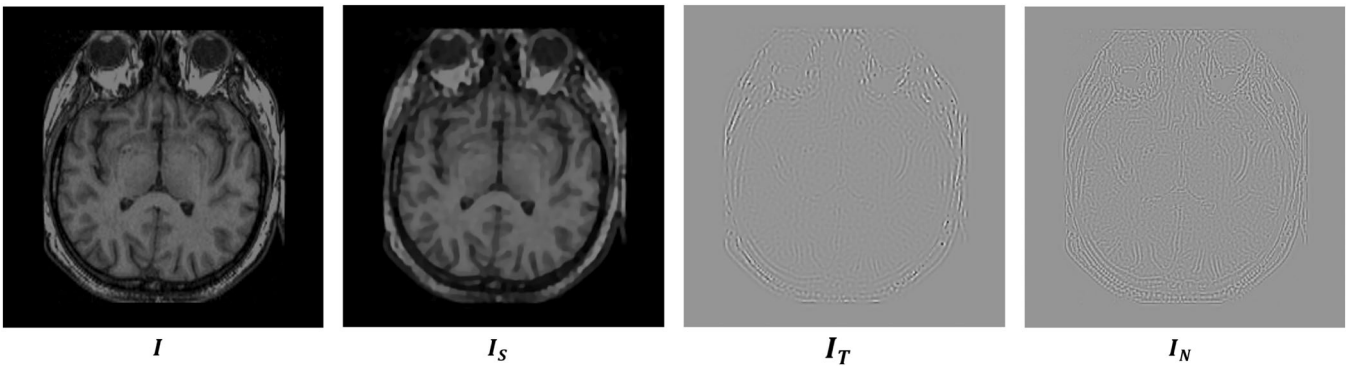

FIGURE 3 The three components I_S, I_T, and I_N of the image

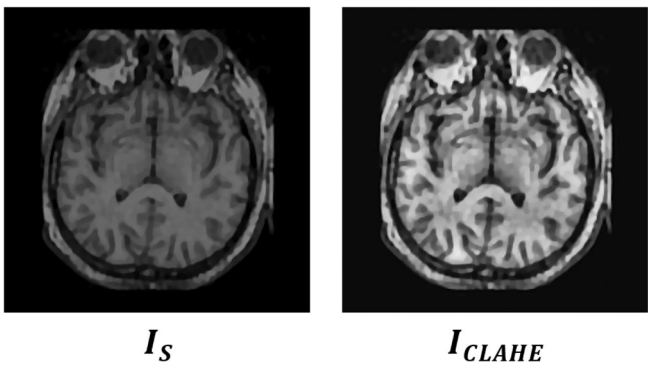

FIGURE 4 The I_S Component and its enhancement by the CLAHE method

The STS detection operator can be defined as Equation (4). Figure 1 illustrates the tensor structure saliency obtained from an input image.

$$STS = \sqrt{(v_1 + v_2)^2 + 0.5(v_1 - v_2)^2} \quad (4)$$

2.2 | Marine predators algorithm

MPA can be summarized through three main stages: (See Algorithm 1 for details).

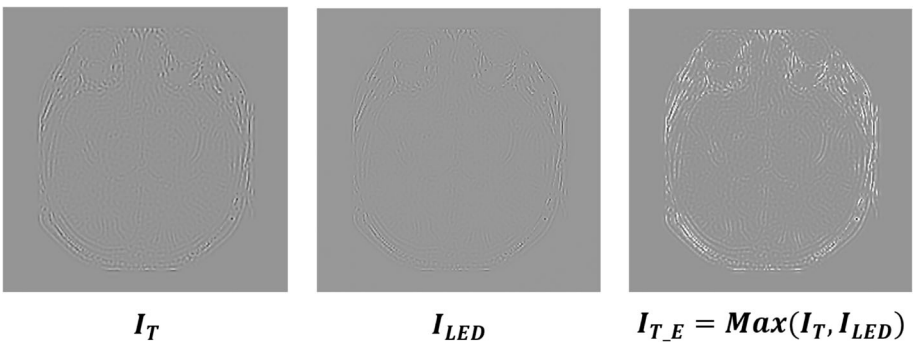

FIGURE 5 Feature enrichment of the I_T component

ALGORITHM 3 The image enhancement algorithm

Input: The gray image I.
Output: The enhanced image (I_E).

Step 1: The image I is decomposed into three components: I_S, I_T, and I_N by applying the STN decomposition method.

Step 2: The CLAHE method is utilized to generate an enhanced image (I_{CLAHE}) from an image (I_S).

Step 3: The STS is utilized to produce an image (I_{STS}) from I_{CLAHE}.

Step 4: The LED operator is implemented to create an edge image (I_{LED}) from I_T.

Step 5: Generate I_{T_E} image enhanced by Equation (15).

$$I_{T\_E} = Max(I_T, I_{LED}) \tag{15}$$

Step 6: An enhanced image (I_{Temp}) is created by utilizing the MPA to find four parameters $\beta_1 \in [0.9, 1.5]$, $\beta_2 \in [0.1, 1.5]$, $\beta_3 \in [0.9, 1.5]$), and $\beta_4 \in [0.1, 1.5]$) as Equation (16).

$$I_{Temp} = \beta_1 \cdot I_{CLAHE} + \beta_2 \cdot I_{STS} + \beta_3 \cdot I_{T\_E} + \beta_4 \cdot I_N \tag{16}$$

Fitness function (O_F) was used as Equation (17)

$$O_F = \frac{V}{M} \cdot \left((E_2 - E_1) + \frac{G_2 - G_1}{PSNR(I_{Temp}, I)} \right) \tag{17}$$

where,

- I and I_E are the input and output images with size ($H \times W$).
- I_{Temp} is the temporary enhancement image in each loop.
- V is the variance of image I_{Temp}.
- M is the mean of image I_{Temp}.
- E_1 and E_2 are the entropy of I and I_{Temp}, respectively.
- G_1 and G_2 are the average gradient of I and I_{Temp}, respectively.
- PSNR is calculated according to Equation (18)

$$PSNR(I_{Temp}, I) = 10^* log_{10} \frac{maxvalue^2}{MSE} \tag{18}$$

- MSE is calculated according to Equation (19).

$$MSE = \frac{1}{H \cdot W} \sum_{i=0}^{H-1} \sum_{j=0}^{W-1} \left(I_{Temp}(p_i, p_j) - I(p_i, p_j) \right)^2 \tag{19}$$

Step 7: With the found optimal parameters $(\beta_1^*, \beta_2^*, \beta_3^*$, and $\beta_4^*)$, the enhanced image (I_E) is determined as Equation (20)

$$I_E = \beta_1^* \cdot I_{CLAHE} + \beta_2^* \cdot I_{STS} + \beta_3^* \cdot I_{T\_E} + \beta_4^* \cdot I_N \tag{20}$$

Stage 1: In the first third of the loop, the prey's moving step size, and its position is determined by Equations (5) and (6).

$$\begin{aligned} \overrightarrow{SS_i}(p_x, p_y) = & \vec{R}_B(p_x, p_y) \\ & \otimes \left(\vec{E}_i(p_x, p_y) - \vec{R}_B(p_x, p_y) \otimes \overrightarrow{Pr_i}(p_x, p_y) \right) \end{aligned} \tag{5}$$

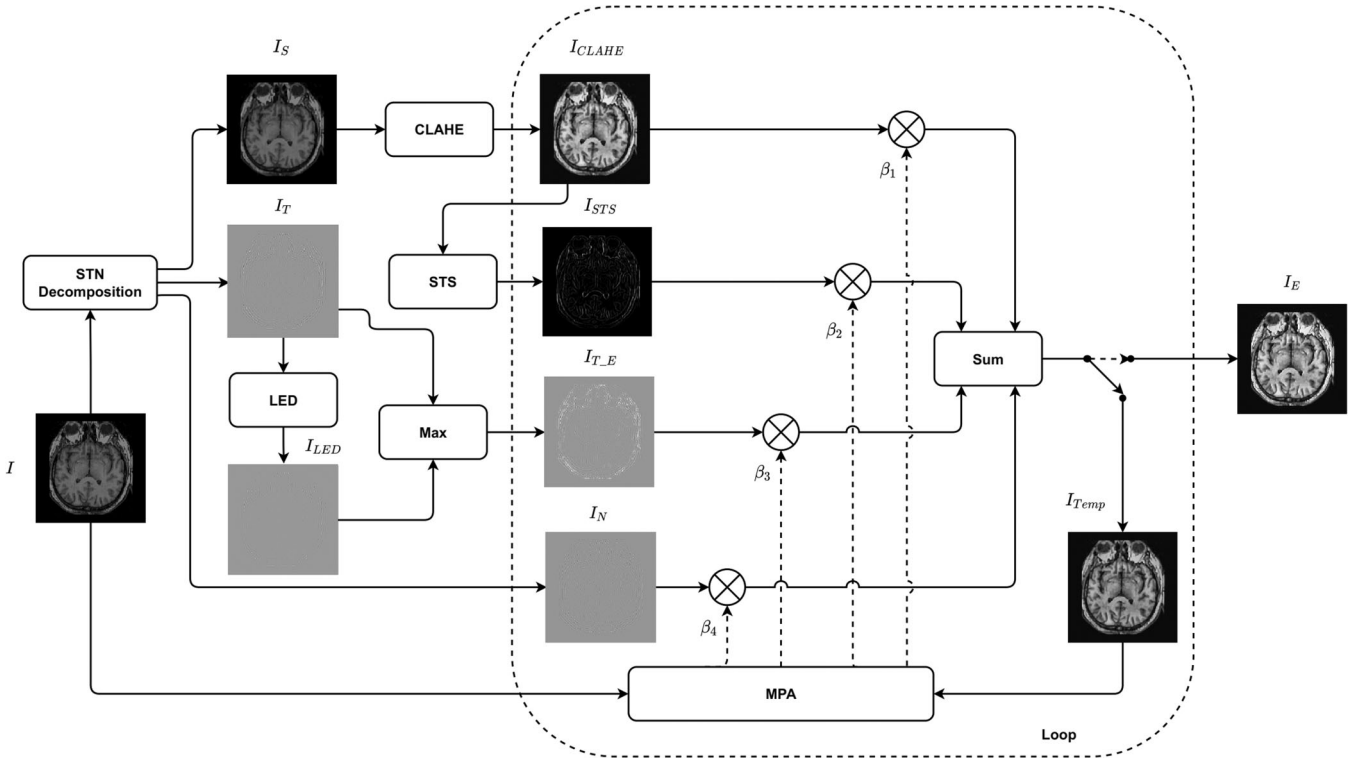

FIGURE 6 The diagram of the image enhancement algorithm

TABLE 1 Evaluation indexes

Num	Metrics	Name
1	MLI	Mean Light Intensity
2	CI	Contrast Index
3	E	Entropy
4	AG	Average Gradient
5	$Q^{AB/F}$[59]	Edge-based similarity measure
6	MI[16]	Mutual Information

$$\overrightarrow{Pr_i}\left(p_x,p_y\right)=\overrightarrow{Pr_i}\left(p_x,p_y\right)+K.\vec{R}\otimes\overrightarrow{SS_i}\left(p_x,p_y\right) \quad (6)$$

where, $\overrightarrow{SS_i}\left(p_x,p_y\right)$ is a vector containing the moving step size of prey. $E(p_x, p_y)$ is a matrix built on the fittest solution. $\vec{R}$ is a vector storing random values that follow a uniform distribution. K is a constant whose value is 0.5. $\otimes$ is the entry-wise multiplication operator. $\vec{R}_B$ is a vector of random numbers generated by the normal distribution.

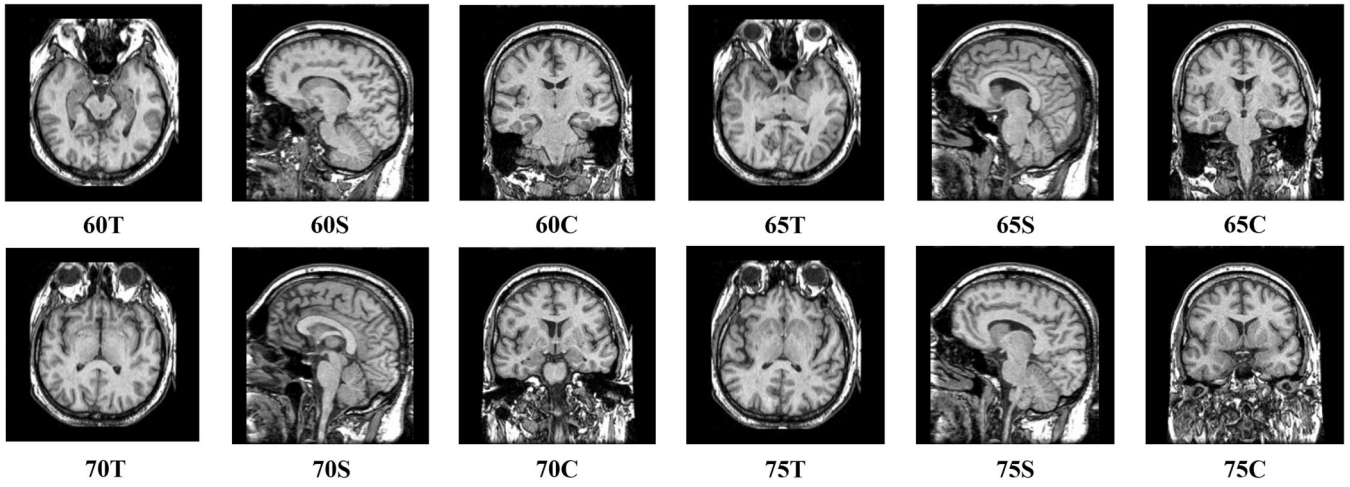

FIGURE 7 Some medical images in dataset D0

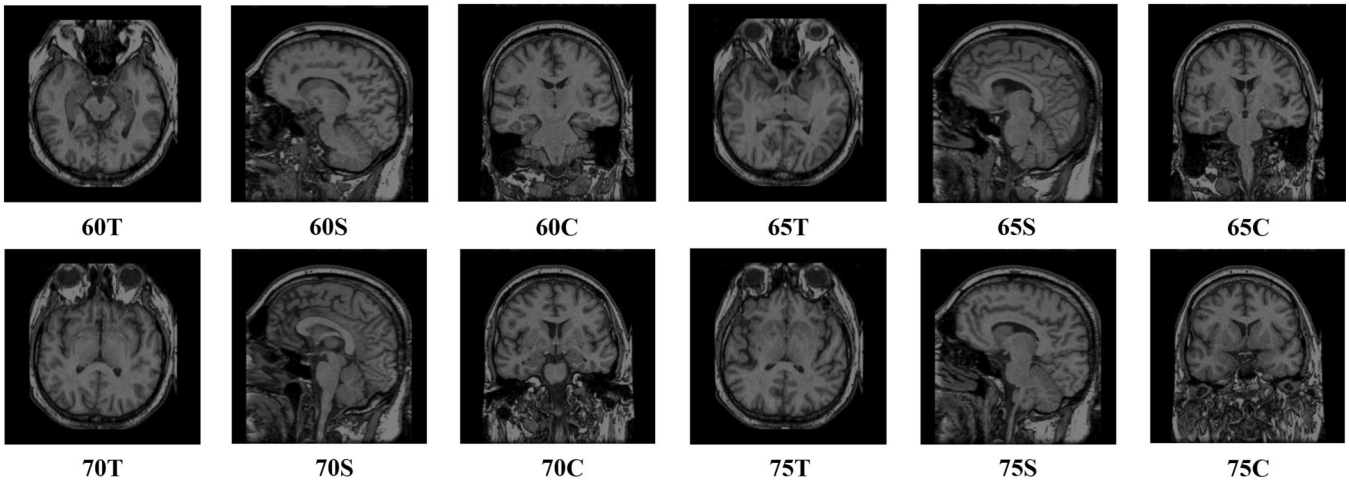

FIGURE 8 Some medical images in dataset D1

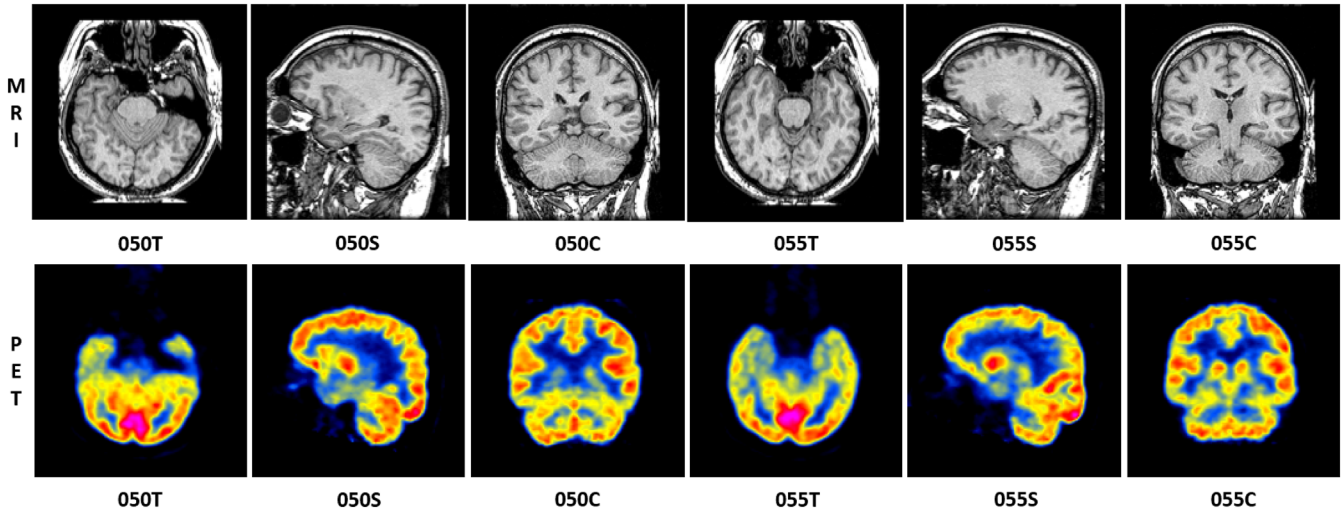

FIGURE 9 Some medical images in dataset D3

TABLE 2 Optimization algorithms

Num	Algorithms	Year
1	DA (Dragonfly algorithm)[36]	2015
2	ALO (Ant Lion Optimizer)[35]	2015
3	GWO (Gray Wolf Optimizer)[39]	2014
4	MVO (Multi-Verse Optimizer)[40]	2015
5	SSA (Salp Swarm Algorithm)[41]	2017
6	SCA (Sine Cosine Algorithm)[37]	2016
7	WOA (Whale Optimization Algorithm)[38]	2016
8	MPA (Equilibrium Optimization Algorithm)[15]	2020

TABLE 3 Some image enhancement algorithms

Num	Algorithms	Year
1	NE (No Enhancement)	
2	FCCE (Fuzzy-Contextual Contrast Enhancement)[42]	2017
3	EFF (Exposure Fusion Framework)[61]	2017
4	EGIF (Effective Guided Image Filtering)[29]	2018
5	RRM (Robust Retinex Model)[26]	2018
6	FFM (Fractional-Order Fusion Model)[7]	2019
7	SDD (Semi-Decoupled Decomposition)[17]	2020

Stage 2: In the next third of the loop, the prey's moving step size, and its position is determined by Equations (7), (8), (9), and (10).

TABLE 4 Some image fusion algorithms

Num	Algorithms	Year
1	PC-LLE-NSCT (Alg_1)[62]	2019
2	NSST-MSMG-PCNN (Alg_2)[50]	2020
3	MLCF-MLMG-PCNN (Alg_3)[51]	2021
4	JBF-LGE (Alg_4)[27]	2021
5	CSE (Contrast and structure extraction) (Alg_5)[49]	2021
6	CNPS-NSST (Coupled neural P systems in NSST domain) (Alg_6)[24]	2021
7	DTNP-NSCT (Dynamic threshold neural P systems in NSCT domain) (Alg_7)[25]	2021

For the first half of the population:

$$\overrightarrow{SS_i}\left(p_x,p_y\right)=\overrightarrow{R_L}\left(p_x,p_y\right)\otimes\left(\overrightarrow{E_i}\left(p_x,p_y\right)-\overrightarrow{R_L}\left(p_x,p_y\right)\otimes\overrightarrow{Pr_i}\left(p_x,p_y\right)\right) \tag{7}$$

$$\overrightarrow{Pr_i}\left(p_x,p_y\right)=\overrightarrow{Pr_i}\left(p_x,p_y\right)+K.\vec{R}\otimes\overrightarrow{SS_i}\left(p_x,p_y\right) \tag{8}$$

For the second half of the population:

$$\overrightarrow{SS_i}\left(p_x,p_y\right)=\overrightarrow{R_B}\left(p_x,p_y\right)\otimes\left(\overrightarrow{R_B}\left(p_x,p_y\right)\otimes E_i\left(p_x,p_y\right)-\overrightarrow{Pr_i}\left(p_x,p_y\right)\right) \tag{9}$$

$$\overrightarrow{Pr_i}\left(p_x,p_y\right))=E_i\left(p_x,p_y\right)+K.CF\otimes\overrightarrow{SS_i}\left(p_x,p_y\right) \tag{10}$$

TABLE 5 Four indexes from 30 independent runs on the Dataset D2

Dataset	Algs	Best	Worst	Mean	SD
070T	DA	0.695111414011694	0.669198154980659	0.684398469783033	0.008373979131028
	ALO	0.695137630079690	0.656038593403487	0.683701166332468	0.009407973825317
	GWO	0.694780037770273	0.675608697888588	0.687173533713143	0.005354121012140
	MVO	0.693267308875936	0.655348033561780	0.676025593833513	0.010520795435026
	SSA	0.678483123202359	0.653558607923842	0.671818266377605	0.004581587792121
	SCA	0.689956110124383	0.658859661620494	0.673400687582457	0.007786678898958
	WOA	0.695113120139038	0.659747686915307	0.678255556752285	0.010421139145008
	MPA	**0.695169878706778**	**0.695111633898089**	**0.695137038602832**	**0.000017766009350**
070S	DA	0.589101486531184	0.583018702993587	0.588064740083802	0.001446070102545
	ALO	0.589112420276191	0.563389625795496	0.582364127929733	0.005720265782300
	GWO	0.588958804026073	0.584818325711638	0.587460077942036	0.001355120097889
	MVO	0.588590741102465	0.566321244833973	0.579122996391213	0.005997075945179
	SSA	0.585215777745244	0.569559632199487	0.577087036234181	0.004683043810424
	SCA	0.588992200587215	0.574367914890738	0.584366463122916	0.003318588234138
	WOA	0.589099753771276	0.565003286693969	0.582047747202921	0.006716686969345
	MPA	**0.589113550337631**	**0.589098343320556**	**0.589105704307832**	**0.000004141752329**
070C	DA	0.714894878610970	0.692390158833342	0.707745935689339	0.006604936255880
	ALO	0.704793485049798	0.714899194606991	0.704793485049798	0.011657462834954
	GWO	0.714531250141631	0.690233293091893	0.708436898012035	0.005373698605653
	MVO	0.709455637936643	0.668503421926879	0.695599664653921	0.010444296849015
	SSA	0.707247111038313	0.677970919290012	0.689563669876958	0.006250311135621
	SCA	0.714631350255784	0.681445409431920	0.699858525905848	0.008487337040112
	WOA	0.714891274324171	0.673659027423800	0.701114842841765	0.012981442337560
	MPA	**0.714910907022665**	**0.714884106742242**	**0.714895951617184**	**0.000005320057142**

Note: The bold values are the best values obtained from our algorithm (maximum compared to other values).

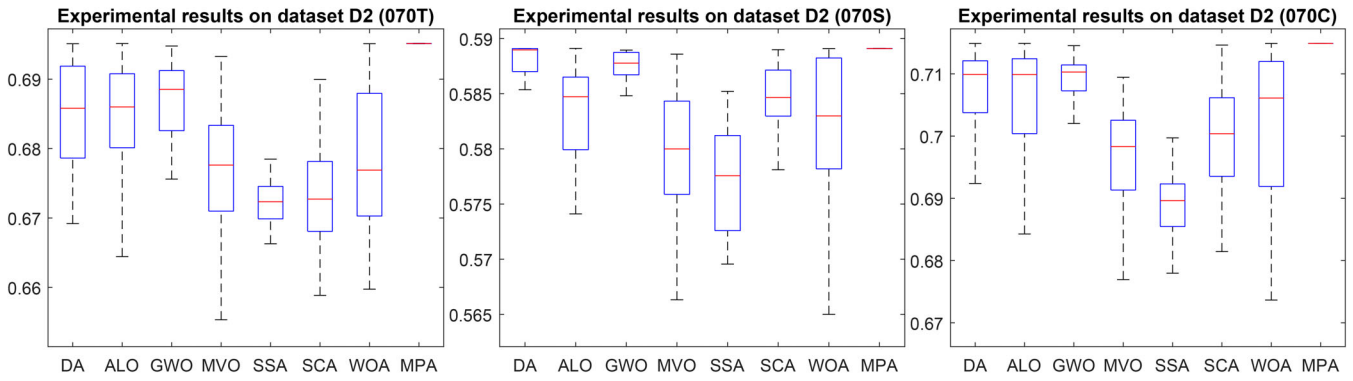

FIGURE 10 Fitness value obtained different algorithms on datatset D2

TABLE 6 P-values from Wilcoxon rank-sum test

Dataset	Algorithms	P-values
070T	MPA versus DA	3.019859359162151e-11
	MPA versus ALO	2.609852787955851e-10
	MPA versus GWO	3.019859359162151e-11
	MPA versus MVO	3.019859359162151e-11
	MPA versus SSA	3.019859359162151e-11
	MPA versus SCA	3.019859359162151e-11
	MPA versus WOA	4.077164846825348e-11
070S	MPA versus DA	3.474196606831804e-10
	MPA versus ALO	5.072313498155892e-10
	MPA versus GWO	3.019859359162151e-11
	MPA versus MVO	3.019859359162151e-11
	MPA versus SSA	3.019859359162151e-11
	MPA versus SCA	3.019859359162151e-11
	MPA versus WOA	4.504322112705322e-11
070C	MPA versus DA	8.101362326146523e-10
	MPA versus ALO	1.596405099603837e-07
	MPA versus GWO	3.019859359162151e-11
	MPA versus MVO	3.019859359162151e-11
	MPA versus SSA	3.019859359162151e-11
	MPA versus SCA	3.019859359162151e-11
	MPA versus WOA	3.689725853981014e-11

where

$$-CF = \left(1 - \frac{l}{l_{max}}\right)^{\frac{2^* l}{l_{max}}}.$$

Stage 3: In the last third of the loop, the prey's moving step size, and its position is determined by Equations (11) and (12).

$$\overrightarrow{SS_i}\left(p_x, p_y\right) = \overrightarrow{R_L}\left(p_x, p_y\right) \otimes \left(\overrightarrow{R_L}\left(p_x, p_y\right) \otimes \overrightarrow{E_i}\left(p_x, p_y\right) - \overrightarrow{Pr_i}\left(p_x, p_y\right)\right) \tag{11}$$

$$\overrightarrow{Pr_i}\left(p_x, p_y\right) = \overrightarrow{E_i}\left(p_x, p_y\right) + K.CF \otimes \overrightarrow{SS_i}\left(p_x, p_y\right) \tag{12}$$

where, $\overrightarrow{R_L}$ is a vector generated by the the *Lévy* distribution.

3 | PROPOSED APPROACH

This section introduces two new algorithms: image decomposition algorithm and image enhancement algorithm.

3.1 | Three-component decomposition method

An image can consist of three main components: structure, texture, and noise. Therefore, splitting this image into such components facilitates effective image enhancement. This section proposes an algorithm (called Structure-Texture-Noise [STN] decomposition) that decomposes an input image into three components: structure, texture, and noise. The detailed steps of the image decomposition algorithm are presented in Algorithm 2 and illustrated in Figure 2.

3.2 | The proposed image enhancement algorithm

The proposed image enhancement algorithm is built based on algorithms such as CLAHE, STS, LED, and MPA. We first apply the STN decomposition algorithm to decompose an input image I into three components:

TABLE 7 Evaluation indexes obtained from different algorithms on D0 and D1

Dataset	Num	Algorithm	MLI	CI	Entropy	AG
D0	1	NE	0.3050	0.3216	4.6314	0.0802
	2	FCCE	0.3250	0.3379	5.5607	0.0853
	3	EFF	0.3606	0.3629	5.5651	0.0927
	4	EGIF	0.3199	0.3761	4.8231	0.1151
	5	RRM	0.3591	0.3594	5.6699	0.1036
	6	FFM	0.3450	0.3401	5.9318	0.0883
	7	SDD	0.3669	0.3666	5.8616	0.0925
	8	Proposed	**0.3975**	**0.4036**	**6.3156**	**0.1474**
D1	1	NE	0.1525	0.1608	4.6314	0.0401
	2	FCCE	0.2536	0.2612	5.6641	0.0734
	3	EFF	0.2821	0.2718	5.4223	0.0655
	4	EGIF	0.1750	0.2215	4.9067	0.0688
	5	RRM	0.2278	0.2290	5.6485	0.0630
	6	FFM	0.2599	0.2451	5.7019	0.0584
	7	SDD	0.2336	0.2379	5.7394	0.0565
	8	Proposed	**0.3835**	**0.3731**	**6.2892**	**0.0846**

Note: The bold values are the best values obtained from our algorithm (maximum compared to other values).

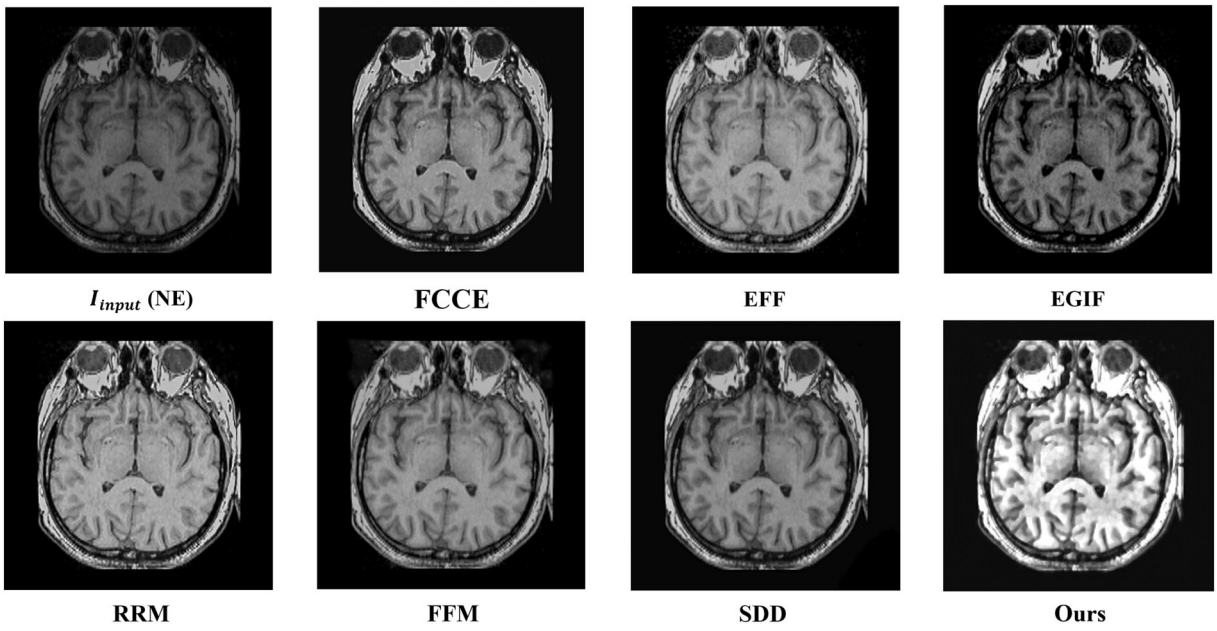

FIGURE 11 An example for images enhanced by eight algorithms on Dataset D1

structure (I_S), texture (I_T), and noise (I_N). Figure 3 illustrates an input image and three components, I_S, I_T, and I_N, obtained after applying the STN decomposition method. The structural component (I_S) is enhanced by the CLAHE method, obtaining I_{CLAHE}. It is an effective method to improve the contrast and brightness of an image. Figure 4 illustrates the I_S component enhanced by the CLAHE method. We use the STS operator to get the feature from the I_{CLAHE} image. This feature (I_{STS}) is then used to add information to the I_{CLAHE}. The texture component (I_T) is also enhanced by using the Laplacian edge detection operator. Figure 5 illustrates how we enhanced the I_T component to create I_{T_E}. Finally, the MPA algorithm is used to find the optimal parameters for the enhanced components (I_{CLAHE}, I_{STS}, I_{T_E}, and I_N). The enhanced image (I_E) is made up of the sum of the I_{CLAHE}, I_{STS}, I_{T_E}, and I_N images multiplied by the optimal parameters β_1, β_2, β_3, and β_4, respectively.

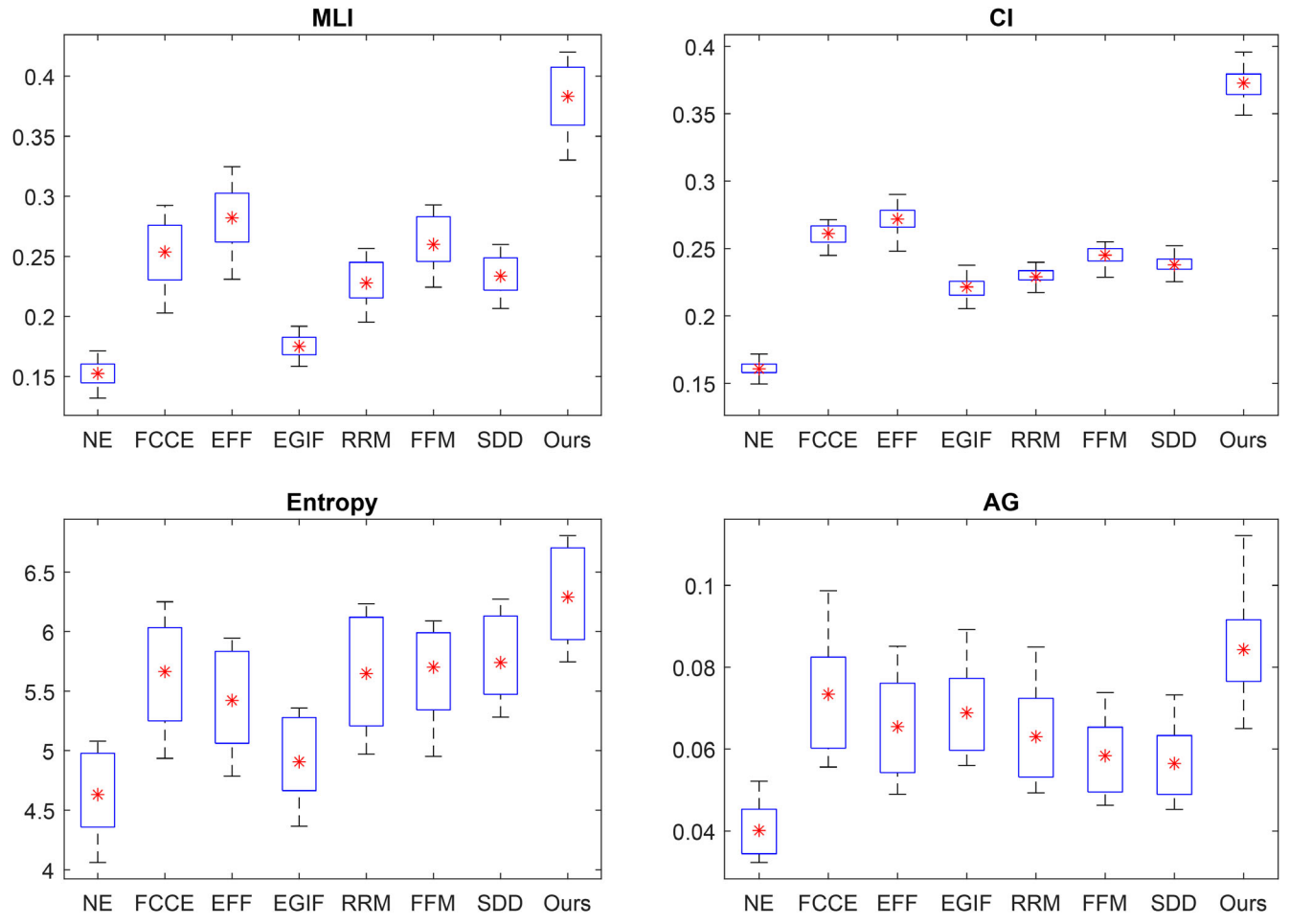

FIGURE 12 Evaluation indexes obtained by different algorithms on dataset D1

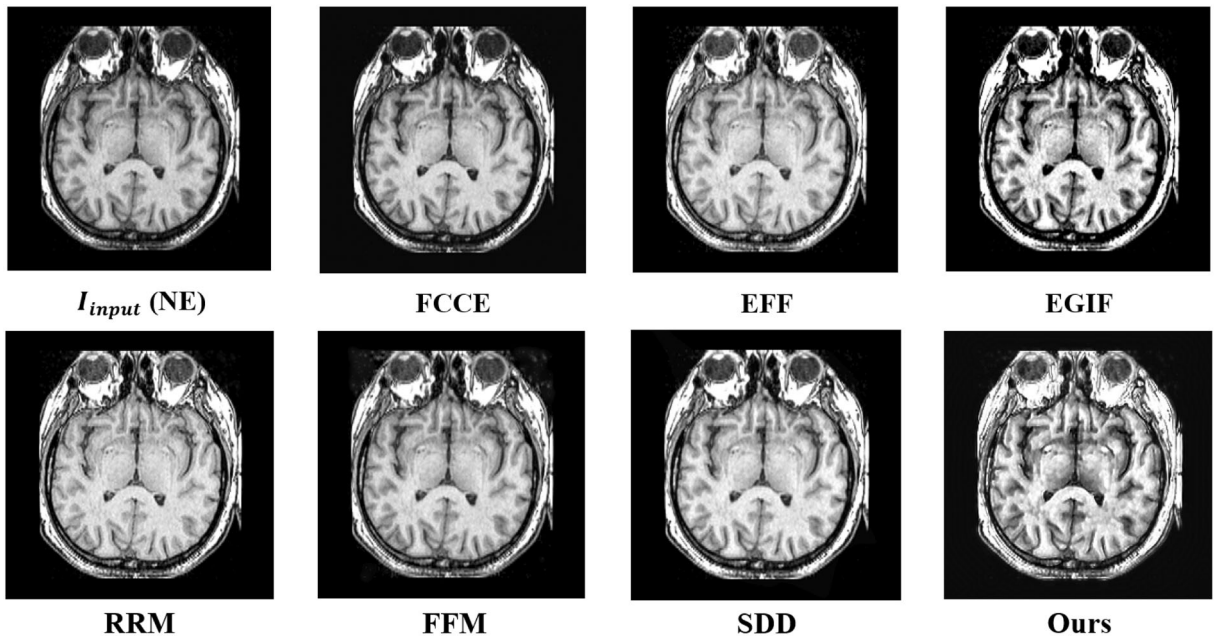

FIGURE 13 An example for images enhanced by different algorithms on Dataset D0

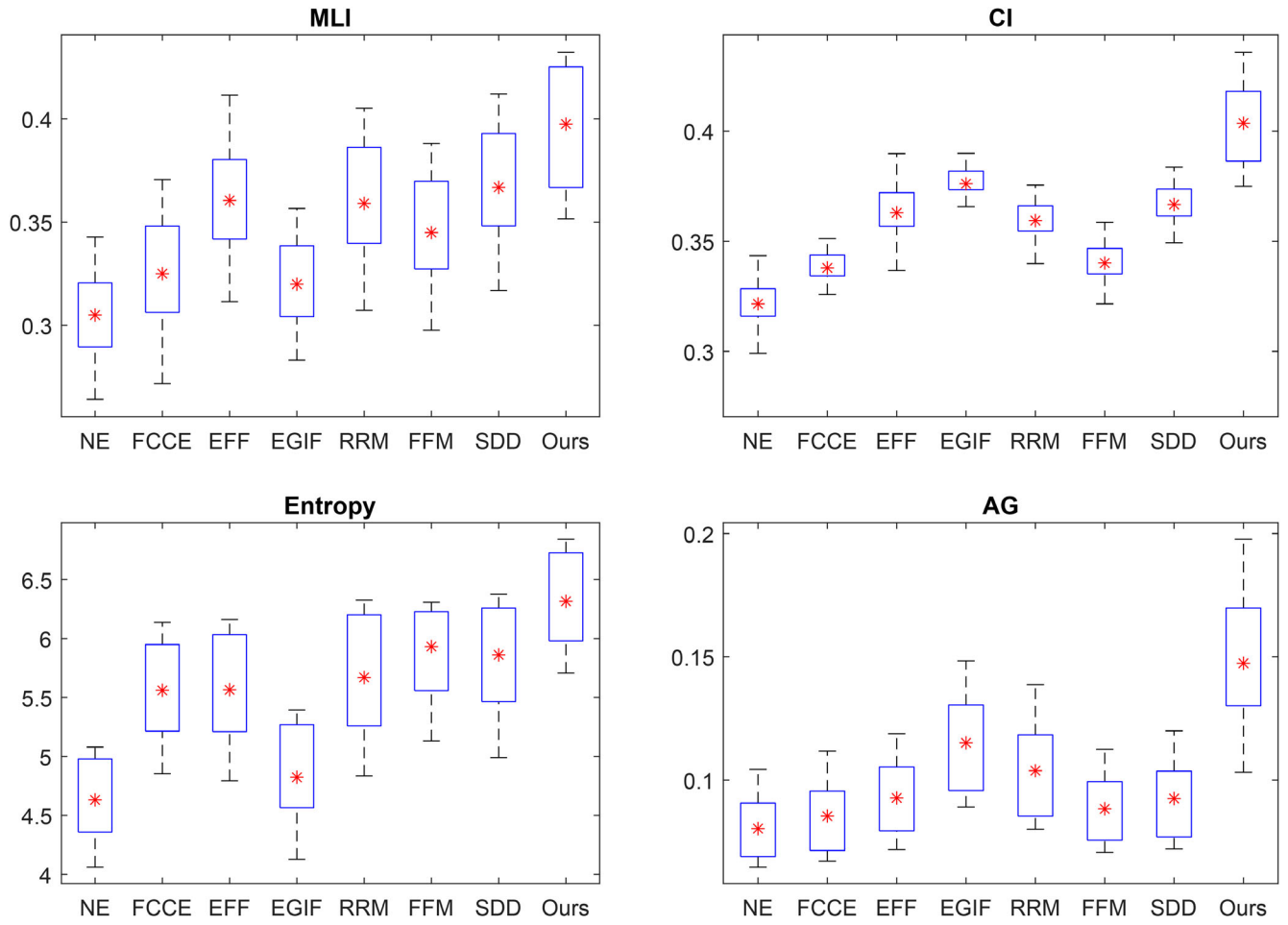

FIGURE 14 Evaluation indexes obtained by different algorithms on dataset D0

TABLE 8 Optimal parameters obtained on the dataset D0 and D1

Dataset	β_1	β_2	β_3	β_4
D0	1.0011	1.1998	1.1999	1.1285
D1	1.2907	0.7967	0.9545	0.9920

Algorithm 3 illustrates the steps of the algorithm in detail, and Figure 6 illustrates the diagram of the algorithm.

4 | EXPERIMENTAL RESULTS

This section introduces the evaluation indexes, experimental setup, and evaluation.

4.1 | Evaluation indexes

We selected six commonly used indicators for the experimental part, and they are described in Table 1. Four evaluation indexes from 1 to 4 are used to evaluate the

TABLE 9 Average running time on the dataset (D1)

Algorithms	Average running time (s)
FCCE	0.047856
EFF	0.298958
EGIF	0.031338
RRM	2.807581
FFM	0.797329
SDD	0.448706
Proposed approach (50 loops)	24.747323

effectiveness of the image enhancement algorithm. Six evaluation indexes are used to test the effectiveness of the image synthesis methods in the case of the input image enhanced by our proposed algorithm.

4.2 | Experimental Setup

One hundred eighty magnetic resonance imaging (MRI) and positron emission tomography (PET) images

TABLE 10 Evaluation indexes obtained by different algorithms in the two cases before and after using our image enhancement algorithm on dataset D3

Datasets	Algorithms	Types	MLI	CI	E	AG	Qabf	MI
Set-T	Alg1	Before	0.2795	0.3249	5.5404	0.0724	0.6942	3.0354
		After	**0.3318**	**0.3529**	**6.3630**	**0.0925**	**0.7222**	**3.5302**
	Alg2	Before	0.3148	0.3937	5.6302	0.0759	0.6199	2.4631
		After	**0.3462**	**0.4035**	**6.2270**	**0.0952**	**0.6255**	**2.7315**
	Alg3	Before	0.3231	0.3873	5.1023	0.0674	0.5942	2.6319
		After	**0.3571**	**0.3957**	**5.9033**	**0.0877**	**0.6015**	**3.1434**
	Alg4	Before	0.3074	0.3455	4.8495	0.0684	0.7178	4.3910
		After	**0.3599**	**0.3706**	**5.9439**	**0.0887**	**0.7537**	**5.7807**
	Alg5	Before	0.2756	0.3165	5.2769	0.0655	0.7434	3.6663
		After	**0.3243**	**0.3496**	**6.2598**	**0.0857**	**0.7564**	**3.9412**
	Alg6	Before	0.2888	0.3329	5.3130	0.0735	0.7070	3.2731
		After	**0.3432**	**0.3637**	**6.0178**	**0.0939**	**0.7357**	**4.0908**
	Alg7	Before	0.2991	0.3388	5.3990	0.0706	0.7120	3.3447
		After	**0.3515**	**0.3653**	**6.0600**	**0.0910**	**0.7512**	**4.1313**
Set-S	Alg1	Before	0.3219	0.3124	6.3709	0.0831	0.7059	3.3813
		After	**0.3990**	**0.3453**	**6.9472**	**0.1118**	**0.7465**	**3.9006**
	Alg2	Before	0.3392	0.3905	6.2654	0.0867	0.6678	2.5171
		After	**0.3808**	**0.3992**	**6.6739**	**0.1148**	**0.6216**	**2.7008**
	Alg3	Before	0.3477	0.3806	5.9830	0.0778	0.6108	2.7661
		After	**0.3930**	**0.3849**	**6.6219**	**0.1067**	**0.6013**	**3.1306**
	Alg4	Before	0.3512	0.3307	5.6692	0.0794	0.7381	5.0347
		After	**0.4280**	**0.3606**	**6.7940**	**0.1088**	**0.7818**	**6.3580**
	Alg5	Before	0.3107	0.3001	6.2098	0.0751	0.7507	3.8228
		After	**0.3864**	**0.3407**	**6.8762**	**0.1041**	**0.7782**	**3.9165**
	Alg6	Before	0.3297	0.3164	6.2581	0.0842	0.7157	3.6292
		After	**0.4103**	**0.3552**	**6.8673**	**0.1136**	**0.7611**	**4.3368**
	Alg7	Before	0.3413	0.3235	6.2772	0.0815	0.7211	3.7479
		After	**0.4185**	**0.3554**	**6.8787**	**0.1107**	**0.7742**	**4.4097**
Set-C	Alg1	Before	0.2886	0.3171	5.8940	0.0982	0.7203	3.1741
		After	**0.3611**	**0.3566**	**6.6787**	**0.1242**	**0.7417**	**3.6318**
	Alg2	Before	0.3033	0.3826	5.8035	0.1018	0.6299	2.4732
		After	**0.3484**	**0.3947**	**6.4161**	**0.1274**	**0.6505**	**2.7522**
	Alg3	Before	0.3123	0.3747	5.3588	0.0953	0.6230	2.6773
		After	**0.3608**	**0.3856**	**6.2380**	**0.1222**	**0.6432**	**3.1838**
	Alg4	Before	0.3186	0.3381	5.1012	0.0955	0.7562	4.6741
		After	**0.3917**	**0.3743**	**6.2949**	**0.1230**	**0.7886**	**6.0716**
	Alg5	Before	0.2878	0.3102	5.5751	0.0910	0.7655	3.6959
		After	**0.3541**	**0.3533**	**6.4829**	**0.1176**	**0.7813**	**3.8505**
	Alg6	Before	0.3013	0.3269	5.7136	0.1000	0.7309	3.3756
		After	**0.3758**	**0.3686**	**6.3904**	**0.1270**	**0.7594**	**4.1467**
	Alg7	Before	0.3101	0.3312	5.7388	0.0973	0.7405	3.5328
		After	**0.3833**	**0.3691**	**6.3973**	**0.1242**	**0.7781**	**4.3110**

Note: The bold values are the best values obtained from our algorithm (maximum compared to other values).

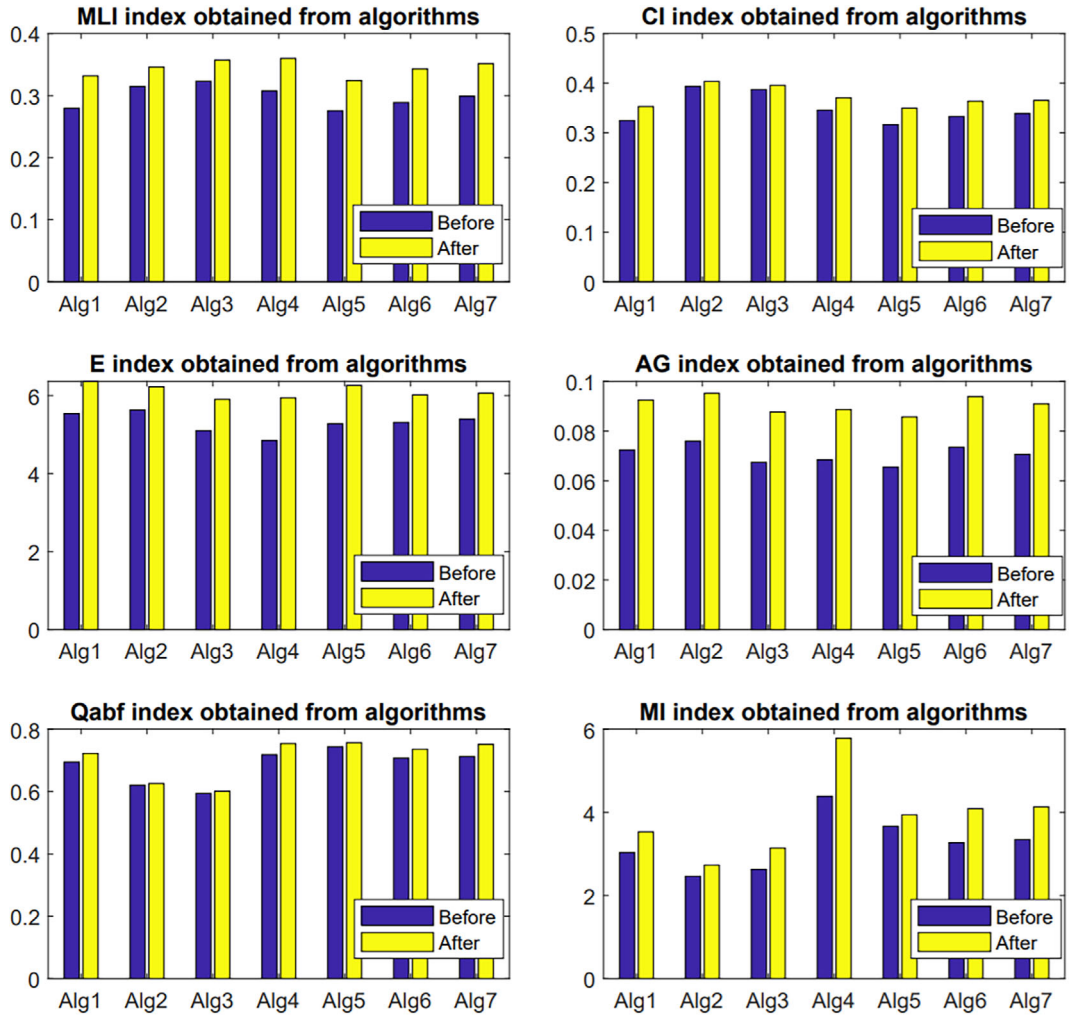

FIGURE 15 Evaluation indexes obtained by different algorithms in two cases before and after using our enhancement method on dataset D3 (Set-T)

of size 256 × 256 pixels were utilized for the experiment. These images were collected from the 50th to 79th slices according to the Transaxial (T), Sagittal (S), and Coronal (C) axis from source (http://www.med.harvard.edu/AANLIB/), respectively. We divided 180 medical images for the experimental part as follows:

- Dataset (D0) includes 90 MRI images (30 images (T), 30 images (S), and 30 images (C)) used to evaluate the image enhancement algorithm. Some MRI images in D0 are illustrated in Figure 7.
- Dataset (D1) is generated from the dataset D0 by reducing contrast and intensity. Some MRI images in D1 are illustrated in Figure 8.
- Dataset (D2) includes two images (70 T, 70C) used to test the effectiveness of the MPA algorithm in our image enhancement algorithm. These images are the 70th brain slices according to the T and C axis.
- Dataset (D3) includes 180 images utilized to evaluate our proposed method for improving the performance of current medical image fusion algorithms. These images include Set-T (60 MRI and PET images), Set-S (60 MRI and PET images), and Set-C (60 MRI and PET images)) according to the T, S, and C axis, respectively. Several pairs of images in the dataset (D3) are illustrated in Figure 9.

Computer configuration and software we used for testing:

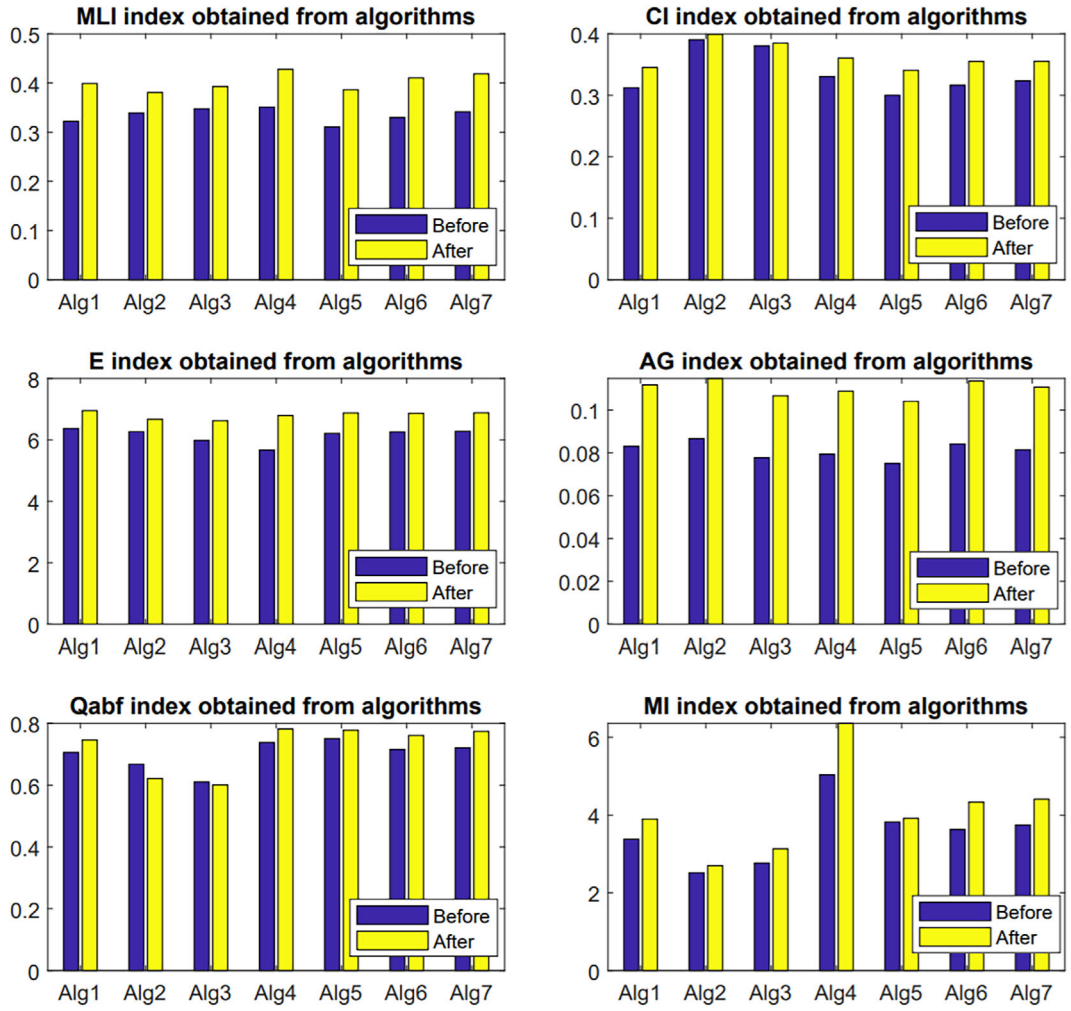

FIGURE 16 Evaluation indexes obtained by different algorithms in two cases before and after using our enhancement method on dataset D3 (Set-S)

- Intel Core i9 10900K, 3.7GHz processor, and 64GB RAM.
- Matlab R2020b.

We design some experiments to evaluate the effectiveness of our algorithms as follows:

Experiment #1. To prove the effectiveness of the MPA algorithm in the proposed model, we have used seven other meta-heuristic-based optimization algorithms for comparison. These optimization algorithms include DA, ALO, GWO, MVO, SSA, SCA, and WOA (see details in Table 2). Each algorithm is used to run 30 times on the Dataset D2 (070 T, 070S, 070C). Four indexes, Best, Worst, Mean, and Standard deviation (SD), are used to evaluate the performance of optimal algorithms. Moreover, the Wilcoxon rank-sum test[58] is utilized to test the experimental results.

Experiment #2. To test the effectiveness of the proposed image enhancement method. We use some other image enhancement algorithms for comparison. These algorithms are described in Table 3. Four image quality metrics (MLI, CI, E, and AG) are used in this experiment (See details in Table 1). Both datasets D0 and D1 are used in this experiment.

Experiment #3. To test the effectiveness of the image enhancement method for

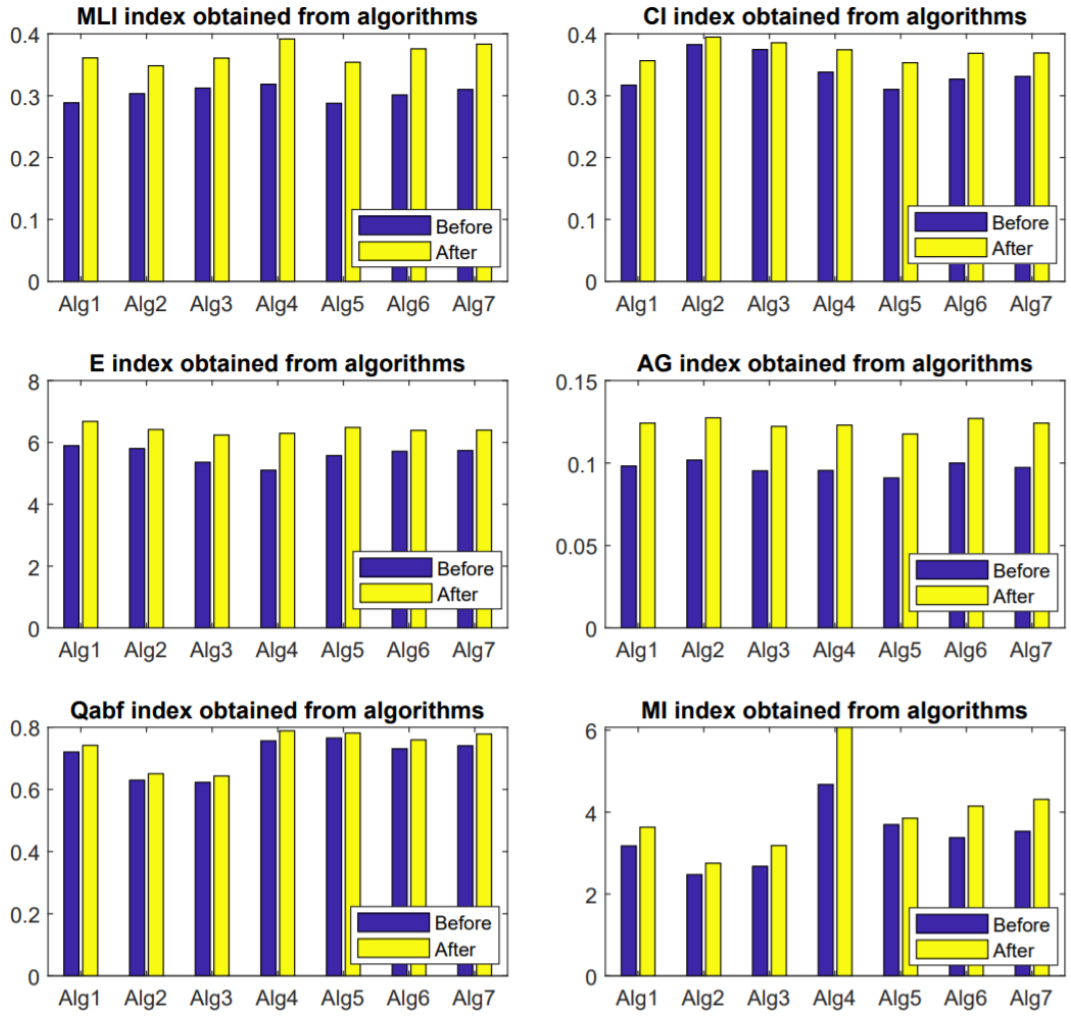

FIGURE 17 Evaluation indexes obtained by different algorithms in two cases before and after using our enhancement method on dataset D3 (Set-C)

improving the performance of image synthesis algorithms. We select a number of recently proposed synthesis algorithms. These algorithms are described in Table 4. The evaluation indexes (MLI, CI, E, AG, $Q^{AB/F}$, and MI) used in this experiment are described in detail in Table 1.

Some necessary parameters are set as follows:

- $n = 50$ (The number of population).
- $l_{max} = 50$.
- K = 0.5.
- FADs = 0.2;
- r is a random parameter in [0,1].

4.3 | Evaluation

The results of the first experiment are illustrated in Table 5. The results of the 30 different runs are also shown in Figure 10. It is clear that the mean and standard deviation of the fitness function are the lowest when using the MPA algorithm. These experimental results explain why we choose the MPA algorithm. Moreover, from Table 6, the results obtained from the Wilcoxon rank-sum test are statistically significant since the p-values are less than 0.05.

The results of the second experiment are illustrated in Table 7 and Figures 11, 12, 13, and 14. Optimal parameters (β_1, β_2, β_3, and β_4) obtained from the proposed image enhancement algorithm are shown in

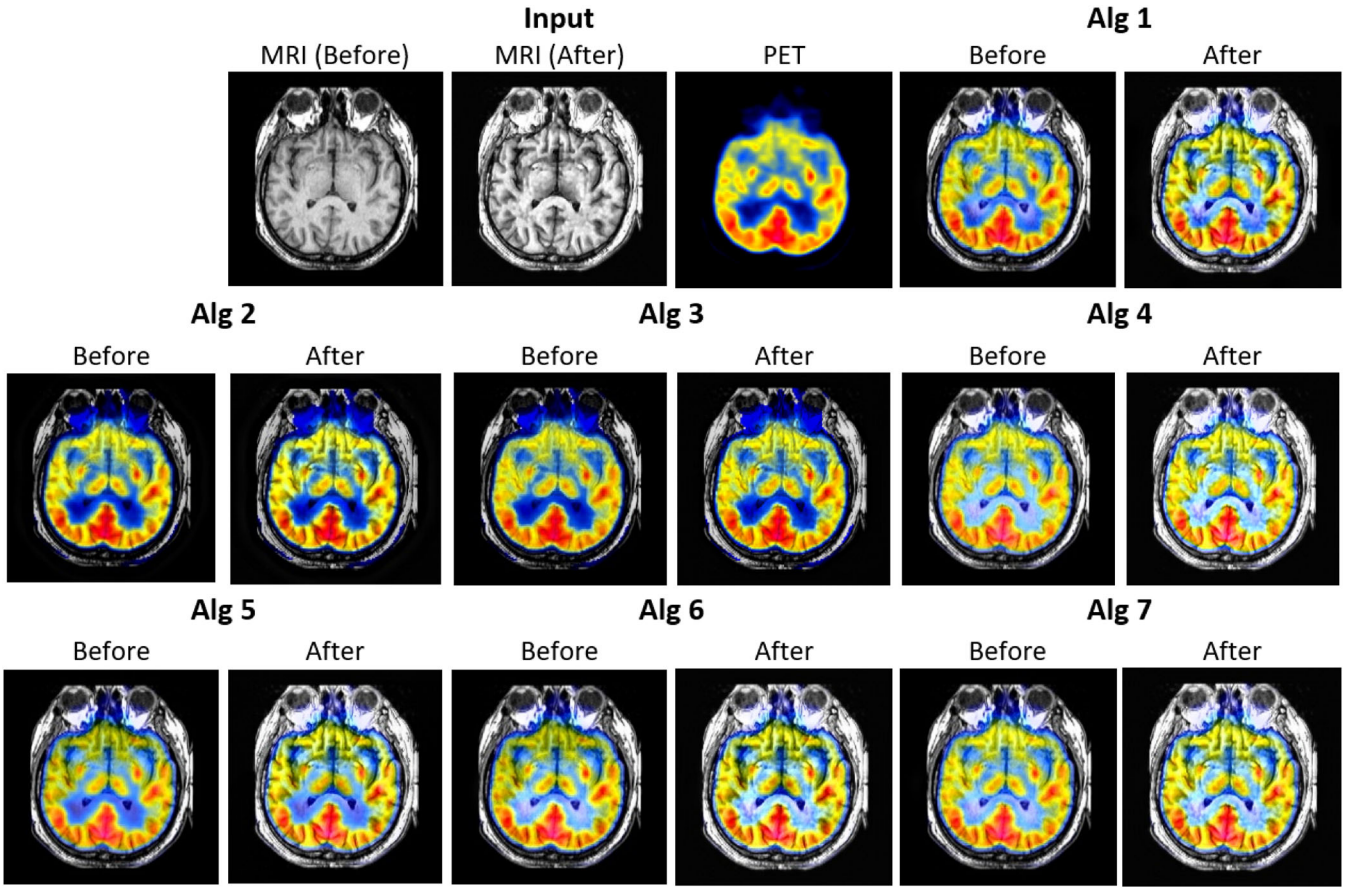

FIGURE 18 The fusion images obtained by different algorithms in the two cases before and after using our image enhancement algorithm

Table 8. It is easy to see that MLI, CI, Entropy, and AG indexes obtained from the proposed image enhancement algorithm are the highest in both data sets D0 and D1. For low-quality images in dataset (D1), it is easy to see that our method has improved the image quality significantly. The optimal parameter β_1 is 1.209, which allows the I_{CLAHE} component to improve the luminous intensity significantly. The optimal parameters β_2, β_3, and β_4, are all lower than 1, allowing a small amount of structural and texture features to be added to the image. For images in dataset (D1), images with light intensity are not weak. The optimal parameter β_1 is 1.0011, which shows that the I_{CLAHE} component has ensured enough light intensity for the image without adding more. The optimal parameters β_2, β_3, and β_4, are all larger than 1, which shows that components I_{STS}, I_{T_E}, and I_N only need to add a large amount of information to the image. Therefore, the adaptive parameters allow adjusting the required amount of information of the four components I_{CLAHE}, I_{STS}, I_{T_E}, and I_N to produce a high-quality enhanced image. These results show that our algorithm is effective in improving image quality.

Because our image enhancement method is based on the MPA optimization algorithm, it consumes a large amount of running time. From Table 9, it is easy to see that the time consuming is the largest compared to the running time of other algorithms. With population $n = 50$ and 50 loops, our method takes about 25 s to complete. This is the drawback of our algorithm.

The results of the third experiment are illustrated in Table 10 and Figures 15, 16, and 17. Output images obtained by image fusion algorithms are shown in Figure 18. The quality of the composite images obtained from the algorithms is improved when applying our image enhancement method. All six evaluation indexes increased significantly. The most significant change to mention is the details of the image. By intuitive, it is easy to see that the output composite image is of high sharpness when using our enhancement method. For example, the AG index of the Alg1 method increased from 0.0724 to 0.0925 on the dataset (Set-T). Experimental results have shown that our image enhancement method is significantly effective in improving the performance of image synthesis algorithms.

5 | CONCLUSION AND FUTURE WORK

In this paper, a novel image enhancement method is proposed to solve simultaneously problems on images. Six evaluation metrics and many algorithms have been used for comparison. One hundred eighty brain images have been utilized in the experimental section. The experimental results show that our approach is effective in improving the quality of medical images. In addition, this method also helps to improve the performance of image fusion algorithms. However, the limitation of our algorithm is the running time.

In the future, we intend to improve our algorithm in the following aspects. Firstly, search for better image enhancement algorithms to replace the CLAHE and ADF algorithms. Secondly, apply the latest optimization algorithms based on meta-heuristic to replace the MPA algorithm.

ACKNOWLEDGMENTS

This research is funded by Thuyloi University Foundation for Science and Technology under grant number TLU.STF.21-03.

CONFLICT OF INTEREST

The authors declare no conflicts of interest.

DATA AVAILABILITY STATEMENT

Research data are not shared.

ORCID

Phu-Hung Dinh https://orcid.org/0000-0002-8050-4086
Nguyen Long Giang https://orcid.org/0000-0001-6184-1469

REFERENCES

1. Acharya UK, Kumar S. Genetic algorithm based adaptive histogram equalization (GAAHE) technique for medical image enhancement. *Optik*. 2021;230:166273. doi:10.1016/j.ijleo.2021.166273
2. Ahmed S, Ghosh KK, Bera SK, Schwenker F, Sarkar R. Gray level image contrast enhancement using barnacles mating optimizer. *IEEE Access*. 2020;8:169196-169214. doi:10.1109/access.2020.3024095
3. Chan SH, Khoshabeh R, Gibson KB, Gill PE, Nguyen TQ. An augmented lagrangian method for total variation video restoration. *IEEE Trans Image Process*. 2011;20(11):3097-3111. doi:10.1109/tip.2011.2158229
4. Chen CM, Chen CC, Wu MC, et al. Automatic contrast enhancement of brain MR images using hierarchical correlation histogram analysis. *J Med Biol Eng*. 2015;35(6):724-734. doi:10.1007/s40846-015-0096-6
5. Chen J, Yu W, Tian J, Chen L, Zhou Z. Image contrast enhancement using an artificial bee colony algorithm. *Swarm Evolut Comput*. 2018;38:287-294. doi:10.1016/j.swevo.2017.09.002
6. Chen X, Qi X, Wang Z, Cui C, Wu B, Yang Y. Fault diagnosis of rolling bearing using marine predators algorithm-based support vector machine and topology learning and out-of-sample embedding. *Measurement*. 2021;176:109116. doi:10.1016/j.measurement.2021.109116
7. Dai Q, Pu YF, Rahman Z, Aamir M. Fractional-order fusion model for low-light image enhancement. *Symmetry*. 2019;11(4):574. doi:10.3390/sym11040574
8. Dinh PH. Combining gabor energy with equilibrium optimizer algorithm for multi-modality medical image fusion. *Biomed Signal Process Control*. 2021;68:102696. doi:10.1016/j.bspc.2021.102696
9. Dinh PH. An improved medical image synthesis approach based on marine predators algorithm and maximum gabor energy. *Neural Comput & Applic*. 2021;34:4367-4385. doi:10.1007/s00521-021-06577-4
10. Dinh PH. Multi-modal medical image fusion based on equilibrium optimizer algorithm and local energy functions. *Appl Intell*. 2021;51:8416-8431. doi:10.1007/s10489-021-02282-w
11. Dinh PH. A novel approach based on grasshopper optimization algorithm for medical image fusion. *Expert Syst Appl*. 2021;171:114576. doi:10.1016/j.eswa.2021.114576
12. Dinh PH. A novel approach based on three-scale image decomposition and marine predators algorithm for multi-modal medical image fusion. *Biomed Signal Process Control*. 2021;67:102536. doi:10.1016/j.bspc.2021.102536
13. Dinh PH. A novel approach using structure tensor for medical image fusion. *Multidim Syst Sign Process*. 2022. doi:10.1007/s11045-022-00829-9
14. Eichinger P, Schön S, Pongratz V, et al. Accuracy of unenhanced MRI in the detection of new brain lesions in multiple sclerosis. *Radiology*. 2019;291(2):429-435. doi:10.1148/radiol.2019181568
15. Faramarzi A, Heidarinejad M, Mirjalili S, Gandomi AH. Marine predators algorithm: a nature-inspired metaheuristic. *Expert Syst Appl*. 2020;152:113377. doi:10.1016/j.eswa.2020.113377
16. Guihong Q, Zhang D, Yan P. Information measure for performance of image fusion. *Electron Lett*. 2002;38:313-315.
17. Hao S, Han X, Guo Y, Xu X, Wang M. Low-light image enhancement with semi-decoupled decomposition. *IEEE Trans Multimedia*. 2020;22(12):3025-3038. doi:10.1109/tmm.2020.2969790
18. Huang Z, Wang Z, Zhang J, Li Q, Shi Y. Image enhancement with the preservation of brightness and structures by employing contrast limited dynamic quadri-histogram equalization. *Optik*. 2021;226:165877. doi:10.1016/j.ijleo.2020.165877
19. Isa IS, Sulaiman SN, Mustapha M, Karim NKA. Automatic contrast enhancement of brain MR images using average intensity replacement based on adaptive histogram equalization (AIR-AHE). *Biocyber Biomed Eng*. 2017;37(1):24-34. doi:10.1016/j.bbe.2016.12.003
20. Ismail WZW, Sim KS. Contrast enhancement dynamic histogram equalization for medical image processing application. *Int J Imaging Syst Technol*. 2011;21(3):280-289. doi:10.1002/ima.20295
21. Joseph J, Sivaraman J, Periyasamy R, Simi V. An objective method to identify optimum clip-limit and histogram

specification of contrast limited adaptive histogram equalization for MR images. *Biocyber Biomed Eng*. 2017;37(3):489-497. doi:10.1016/j.bbe.2016.11.006
22. Kandhway P, Bhandari AK, Singh A. A novel reformed histogram equalization based medical image contrast enhancement using krill herd optimization. *Biomed Signal Process Control*. 2020;56:101677. doi:10.1016/j.bspc.2019.101677
23. Lei L, Xi F, Chen S, Liu Z. A sparse representation denoising algorithm for finger-vein image based on dictionary learning. *Multimed Tools Appl*. 2021;80(10):15135-15159. doi:10.1007/s11042-021-10516-9
24. Li B, Peng H, Luo X, et al. Medical image fusion method based on coupled neural p systems in nonsubsampled shearlet transform domain. *Int J Neural Syst*. 2020;31(01):2050050. doi:10.1142/s0129065720500501
25. Li B, Peng H, Wang J. A novel fusion method based on dynamic threshold neural p systems and nonsubsampled contourlet transform for multi-modality medical images. *Signal Process*. 2021;178:107793. doi:10.1016/j.sigpro.2020.107793
26. Li M, Liu J, Yang W, Sun X, Guo Z. Structure-revealing low-light image enhancement via robust retinex model. *IEEE Trans Image Process*. 2018;27(6):2828-2841. doi:10.1109/tip.2018.2810539
27. Li X, Zhou F, Tan H, Zhang W, Zhao C. Multimodal medical image fusion based on joint bilateral filter and local gradient energy. *Inf Sci*. 2021;569:302-325. doi:10.1016/j.ins.2021.04.052
28. Lidong H, Wei Z, Jun W, Zebin S. Combination of contrast limited adaptive histogram equalisation and discrete wavelet transform for image enhancement. *IET Image Process*. 2015;9(10):908-915. doi:10.1049/iet-ipr.2015.0150
29. Lu Z, Long B, Li K, Lu F. Effective guided image filtering for contrast enhancement. *IEEE Signal Proc Lett*. 2018;25(10):1585-1589. doi:10.1109/lsp.2018.2867896
30. Luque-Chang A, Cuevas E, Pérez-Cisneros M, Fausto F, Valdivia-González A, Sarkar R. Moth swarm algorithm for image contrast enhancement. *Knowl-Based Syst*. 2021;212:106607. doi:10.1016/j.knosys.2020.106607
31. Lyu Z, Zhang C, Han M. DSTnet: a new discrete shearlet transform-based CNN model for image denoising. *Multimedia Systems*. 2021;27:1165-1177. doi:10.1007/s00530-021-00753-1
32. Mahajan S, Mittal N, Pandit AK. Image segmentation using multilevel thresholding based on type II fuzzy entropy and marine predators algorithm. *Multimed Tools Appl*. 2021;80(13):19335-19359. doi:10.1007/s11042-021-10641-5
33. Maurya L, Mahapatra PK, Kumar A. A social spider optimized image fusion approach for contrast enhancement and brightness preservation. *Appl Soft Comput*. 2017;52:575-592. doi:10.1016/j.asoc.2016.10.012
34. Maurya L, Lohchab V, Mahapatra PK, Abonyi J. Contrast and brightness balance in image enhancement using cuckoo search-optimized image fusion. *J King Saud Univ Comput Inf Sci*. 2021. doi:10.1016/j.jksuci.2021.07.008
35. Mirjalili S. The ant lion optimizer. *Adv Eng Softw*. 2015;83:80-98. doi:10.1016/j.advengsoft.2015.01.010
36. Mirjalili S. Dragonfly algorithm: a new meta-heuristic optimization technique for solving single-objective, discrete, and multi-objective problems. *Neural Comput & Applic*. 2015;27(4):1053-1073. doi:10.1007/s00521-015-1920-1
37. Mirjalili S. SCA: a sine cosine algorithm for solving optimization problems. *Knowl-Based Syst*. 2016;96:120-133. doi:10.1016/j.knosys.2015.12.022
38. Mirjalili S, Lewis A. The whale optimization algorithm. *Adv Eng Softw*. 2016;95:51-67. doi:10.1016/j.advengsoft.2016.01.008
39. Mirjalili S, Mirjalili SM, Lewis A. Grey wolf optimizer. *Adv Eng Softw*. 2014;69:46-61. doi:10.1016/j.advengsoft.2013.12.007
40. Mirjalili S, Mirjalili SM, Hatamlou A. Multi-verse optimizer: a nature-inspired algorithm for global optimization. *Neural Comput & Applic*. 2015;27(2):495-513. doi:10.1007/s00521-015-1870-7
41. Mirjalili S, Gandomi AH, Mirjalili SZ, Saremi S, Faris H, Mirjalili SM. Salp swarm algorithm: a bio-inspired optimizer for engineering design problems. *Adv Eng Softw*. 2017;114:163-191. doi:10.1016/j.advengsoft.2017.07.002
42. Parihar AS, Verma OP, Khanna C. Fuzzy-contextual contrast enhancement. *IEEE Trans Image Process*. 2017;26(4):1810-1819. doi:10.1109/tip.2017.2665975
43. Perona P, Malik J. Scale-space and edge detection using anisotropic diffusion. *IEEE Trans Pattern Anal Mach Intell*. 1990;12(7):629-639. doi:10.1109/34.56205
44. Rao BS. Dynamic histogram equalization for contrast enhancement for digital images. *Appl Soft Comput*. 2020;89:106114. doi:10.1016/j.asoc.2020.106114
45. Ren Z, Guan P, Lam EY, Zhao J. Extended focused imaging in microscopy using structure tensor and guided filtering. *Opt Lasers Eng*. 2021;140:106549. doi:10.1016/j.optlaseng.2021.106549
46. Sahnoun M, Kallel F, Dammak M, et al. A modified DWT-SVD algorithm for t1-w brain MR images contrast enhancement. *IRBM*. 2019;40(4):235-243. doi:10.1016/j.irbm.2019.04.007
47. Sonali SS, Singh AK, Ghrera S, Elhoseny M. An approach for de-noising and contrast enhancement of retinal fundus image using CLAHE. *Opt Laser Technol*. 2019;110:87-98. doi:10.1016/j.optlastec.2018.06.061
48. Subramani B, Veluchamy M. MRI brain image enhancement using brightness preserving adaptive fuzzy histogram equalization. *Int J Imaging Syst Technol*. 2018;28(3):217-222. doi:10.1002/ima.22272
49. Sufyan A, Imran M, Shah SA, Shahwani H, Wadood AA. A novel multimodality anatomical image fusion method based on contrast and structure extraction. *Int J Imaging Syst Technol*. 2021;32(1):324-342. doi:10.1002/ima.22649
50. Tan W, Zhang J, Xiang P, Zhou H, Thitøn W. Infrared and visible image fusion via NSST and PCNN in multiscale morphological gradient domain. In: Schelkens P, Kozacki T, eds. *Optics, Photonics and Digital Technologies for Imaging Applications VI*. SPIE; 2020. doi:10.1117/12.2551830
51. Tan W, Thitøn W, Xiang P, Zhou H. Multi-modal brain image fusion based on multi-level edge-preserving filtering. *Biomed Signal Process Control*. 2021;64:102280. doi:10.1016/j.bspc.2020.102280
52. Tang JR, Isa NAM. Bi-histogram equalization using modified histogram bins. *Appl Soft Comput*. 2017;55:31-43. doi:10.1016/j.asoc.2017.01.053
53. Tirumani VHL, Tenneti M, K CS, Kotamraju SK. Image resolution and contrast enhancement with optimal brightness compensation using wavelet transforms and particle swarm optimization. *IET Image Process*. 2021;15:2833-2840. doi:10.1049/ipr2.12268

54. Ullah Z, Farooq MU, Lee SH, An D. A hybrid image enhancement based brain MRI images classification technique. *Med Hypotheses*. 2020;143:109922. doi:10.1016/j.mehy.2020.109922
55. Veluchamy M, Mayathevar K, Subramani B. Brightness preserving optimized weighted bi-histogram equalization algorithm and its application to MR brain image segmentation. *Int J Imaging Syst Technol*. 2019;29(3):339-352. doi:10.1002/ima.22330
56. Wang M, Zhang W, Sun C, Sowmya A. Corner detection based on shearlet transform and multi-directional structure tensor. *Pattern Recogn*. 2020;103:107299. doi:10.1016/j.patcog.2020.107299
57. Wang Y, Yang J, Yin W, Zhang Y. A new alternating minimization algorithm for total variation image reconstruction. *SIAM J Imag Sci*. 2008;1(3):248-272. doi:10.1137/080724265
58. Wilcoxon F. Individual comparisons by ranking methods. *Biometrics*. 1945;1(6):80. doi:10.2307/3001968
59. Xydeas C, Petrovic V. Objective image fusion performance measure. *Electron Lett*. 2000;36:308. doi:10.1049/el:20000267
60. Yang Y, Su Z, Sun L. Medical image enhancement algorithm based on wavelet transform. *Electron Lett*. 2010;46(2):120. doi:10.1049/el.2010.2063
61. Ying Z, Li G, Ren Y, Wang R, Wang W. A new image contrast enhancement algorithm using exposure fusion framework. *Computer Analysis of Images and Patterns*. Springer International Publishing; 2017:36-46. doi:10.1007/978-3-319-64698-5_4
62. Zhu Z, Zheng M, Qi G, Wang D, Xiang Y. A phase congruency and local laplacian energy based multi-modality medical image fusion method in NSCT domain. *IEEE Access*. 2019;7:20811-20824. doi:10.1109/access.2019.2898111

How to cite this article: Dinh P-H, Giang NL. A new medical image enhancement algorithm using adaptive parameters. *Int J Imaging Syst Technol*. 2022;1-21. doi:10.1002/ima.22778

Biomedical Signal Processing and Control 80 (2023) 104343

Contents lists available at ScienceDirect

Biomedical Signal Processing and Control

journal homepage: www.elsevier.com/locate/bspc

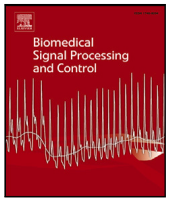

Combining spectral total variation with dynamic threshold neural P systems for medical image fusion

Phu-Hung Dinh *

Department of Network and Information Security, Thuyloi University, 175 Tay Son, Dong Da, Hanoi, Vietnam

ARTICLE INFO

Keywords:
Dynamic threshold neural P systems (DTNPS)
Spectral total variation (STV)
Chameleon Swarm Algorithm (CSA)

ABSTRACT

Synthesis of medical images is one of the indispensable tasks today because of its applications in clinical diagnosis. Composite images often suffer from problems such as poor contrast, loss of detail, and low light intensity. The reason for the above problem is that the input image is of poor quality, and the fusion rules are not really effective. In this paper, we propose a new image synthesis model to simultaneously solve the problems mentioned above. Firstly, the input image is enhanced because the input image's quality significantly affects the fusion image's quality. Next, the Spectral total variation (STV) method is utilized to decompose input images into a base layer and a series of detail layers. An adaptive rule based on the Chameleon Swarm Algorithm (CSA) algorithm is proposed for the synthesis of the base layers. This rule ensures that the synthesized image has good quality in terms of brightness and contrast. To ensure that the details are preserved in the synthesized image, we propose an effective fusion rule for detail layers based on the Dynamic threshold neural P systems (DTNPS). Finally, the base and detail layers that have been composited are summed together to create the composite image. Six evaluation indexes, seven state-of-the-art image synthesis algorithms, and 132 medical images were used to evaluate. The results show that our image synthesis model is more efficient than the current latest image synthesis methods.

1. Introduction

Medical image synthesis is a process of extracting features from multi-modal medical images and fusing those features to form a single image. This image fusion task eases the burden on the clinical diagnostician, and so it has recently received a great deal of research interest. Currently, with the variety of imaging acquisition devices, we can obtain different types of medical images. For example, soft tissues can be clearly visualized in magnetic resonance imaging (MRI), while dense tissues can be clearly shown in Computed tomography (CT) images. Information regarding tissue metabolism is stored in Positron emission tomography (PET) images, whereas how blood flows to tissues and organs is shown in single-photon emission CT (SPECT) images. It is worth noting that both CT and MRI images are high resolution, while PET and SPECT images have low resolution. Some common types of medical imaging synthesis include MRI and PET, MRI and SPECT, and CT and MRI.

Up to now, many medical synthesis algorithms have been proposed. Based on our experience, these algorithms can be divided into the following main groups: deep learning-based approaches, sparse representation-based approaches, transform-based approaches, and meta-heuristic optimization-based approaches. Along with the development of deep learning methods, many approaches based on this technique have been proposed to solve the problem of medical image fusion. For instance, Ding et al. [1] have proposed using Siamese networks combined with the Dual-channel spiking cortical model to synthesize medical images. Wang et al. [2] have introduced a new perceptual high-frequency convolutional neural network (PHF-CNN) in the non-subsampled contourlet transform (NSCT) domain. Li et al. [3] have proposed a new multiscale double-branch residual attention (MS-DRA) network for medical image synthesis. Zhao et al. [4] have proposed combining deep convolutional generative adversarial network (DCGAN) with dense block models. Some other approaches based on deep learning can be found in the studies [5,6].

In recent years, sparse representation (SR) has shown to be an effective tool to solve many problems of image processing, such as noise reduction [7], multi-focus image fusion [8], and especially medical image fusion. Shibu et al. [9] have proposed a new medical image synthesis approach based on the combination of SR and CNN. Yousif et al. [10] have introduced a new approach to medical image fusion using a Siamese CNN and RS. Wang et al. [11] proposed to combine

* Corresponding author.
E-mail address: hungdp@tlu.edu.vn.

https://doi.org/10.1016/j.bspc.2022.104343
Received 16 June 2022; Received in revised form 7 September 2022; Accepted 23 October 2022
Available online 8 November 2022

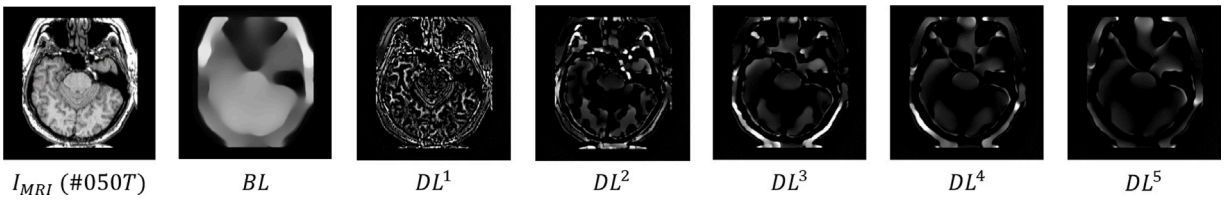

Fig. 1. A base layer and a series of detail layers obtained from STV method.

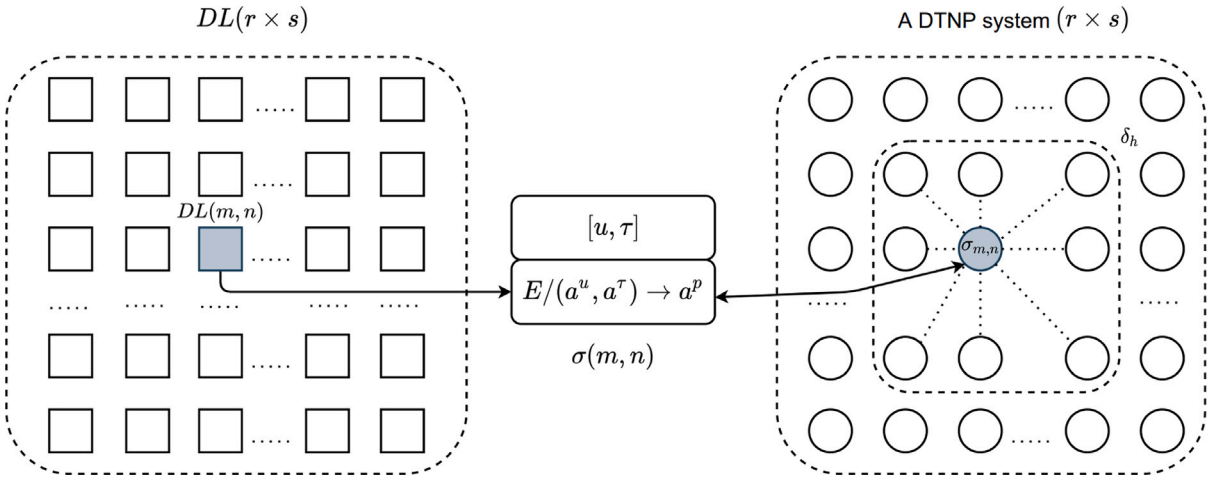

Fig. 2. Illustration for a DTNP system (r × s).

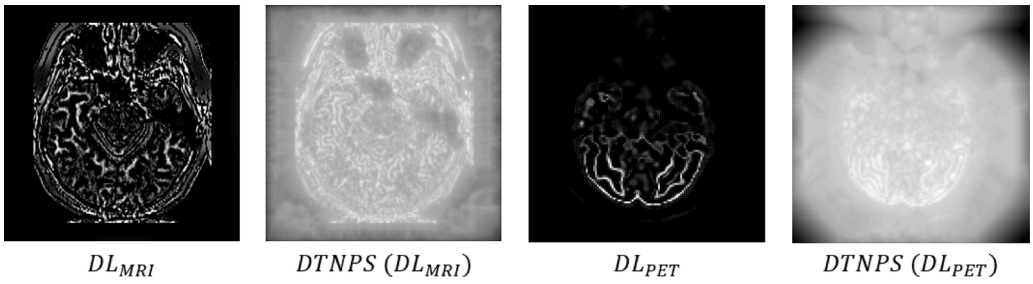

Fig. 3. Illustration for DTNP systems with input and output obtained.

Fig. 4. Synthesize detail layers by applying the FR_DTNPS method.

Convolutional sparse representation (CSR) with Non-subsampled shearlet transform (NSST). Li et al. [12] have proposed a new algorithm based on SR that can not only synthesize medical images but also can denoise them. Wang et al. [13] have proposed to combine adaptive SR with a Laplacian pyramid (LP) method. Hu et al. [14] used SR and combined it with a guidance filter to synthesize medical images.

Transform-based approaches are the popular approaches today. The methods of this group usually go through three main steps. The first step is to decompose the input images from the spatial domain into components on the transform domain. The second step is to synthesize the components on the transform domain. The final step is to transform the synthesized components into the spatial domain. Some popular transformation methods that have been applied to the problem of medical image synthesis can be mentioned, such as LP transform [13,15], discrete stationary wavelet transform (DSWT) [16,17], NSCT [2,18], and NSST [11,19,20]. Commonly used methods to synthesize components on the transform domain can be listed as Min–Max selection [21], averaging rules [22,23], local energy function maximization [24,25], and sum-modified-Laplacian (SML) [26].

Meta-heuristic optimization-based approaches have been proposed in the last few years to improve the efficiency of image synthesis. These approaches have the advantage of ensuring a good quality

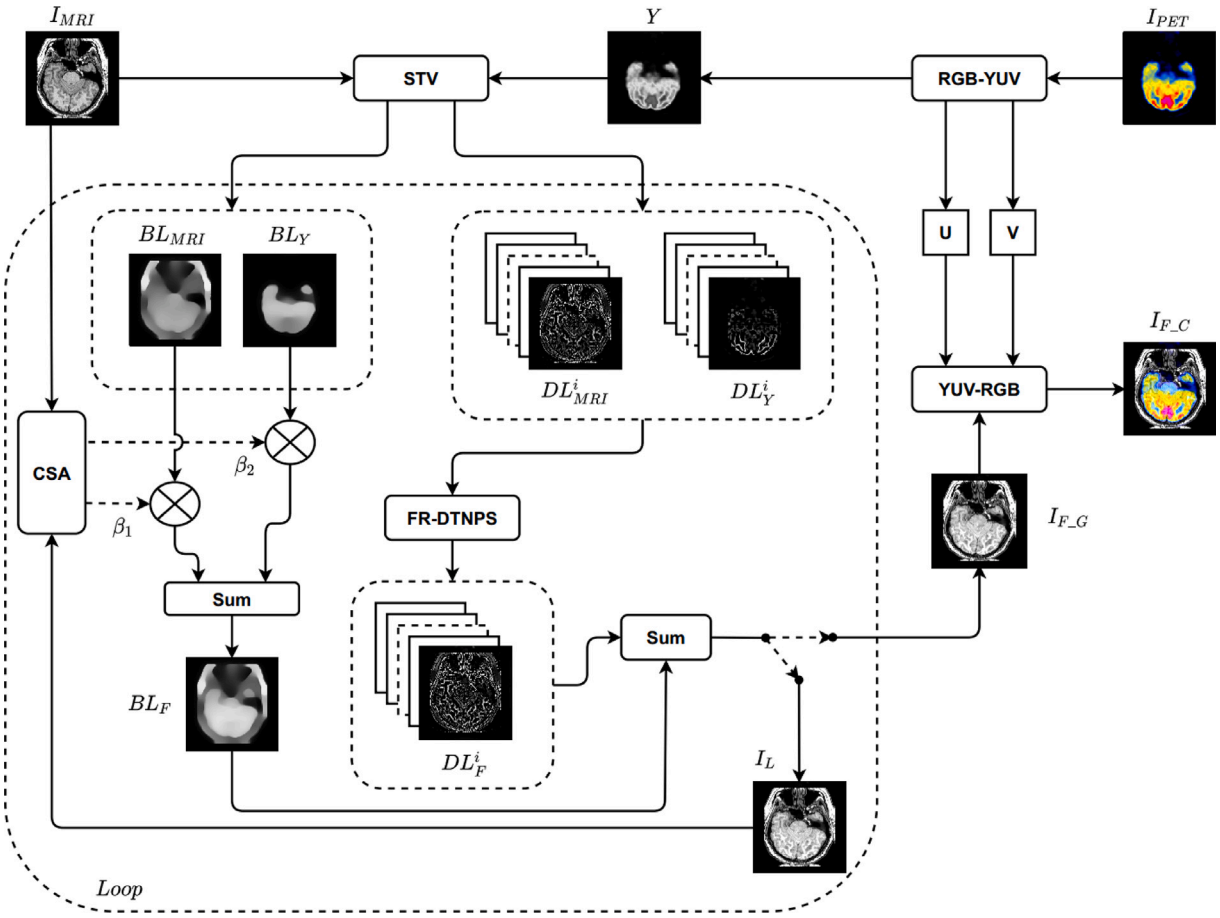

Fig. 5. Our medical image fusion model.

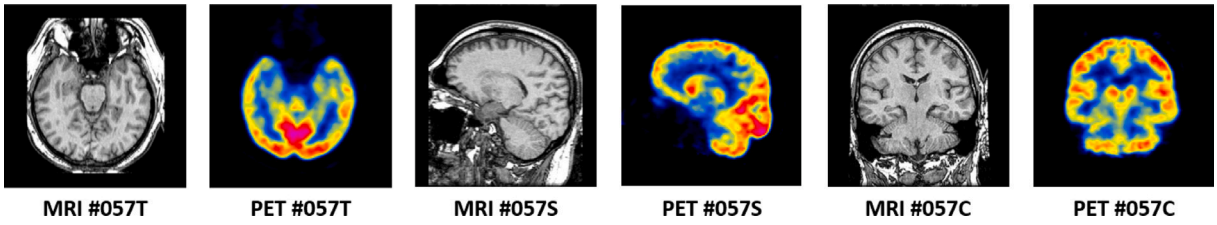

Fig. 6. Three pairs of MRI-PET images in experimental data.

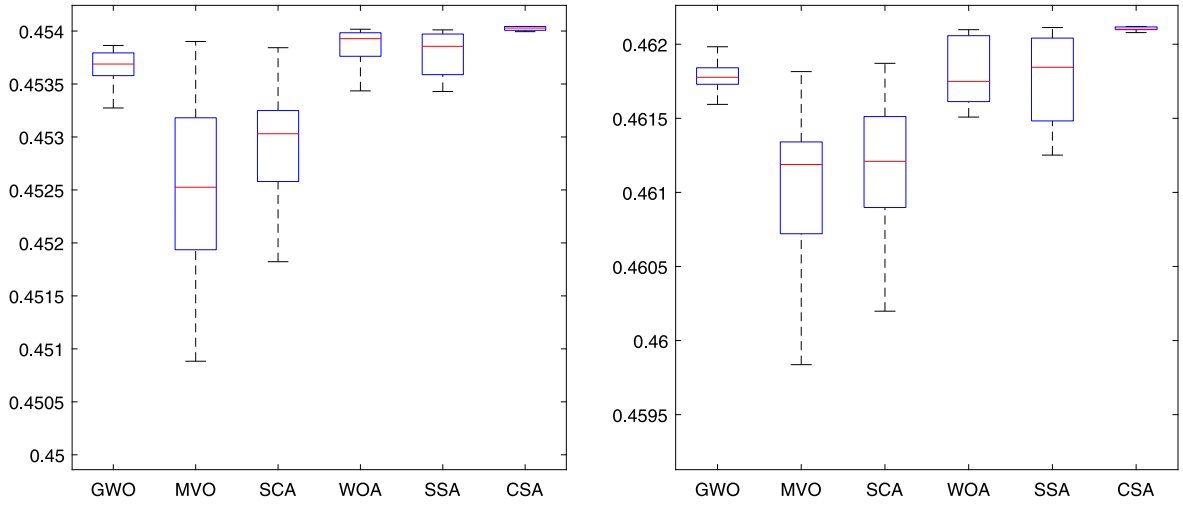

Fig. 7. The value of fitness function obtained by different algorithms.

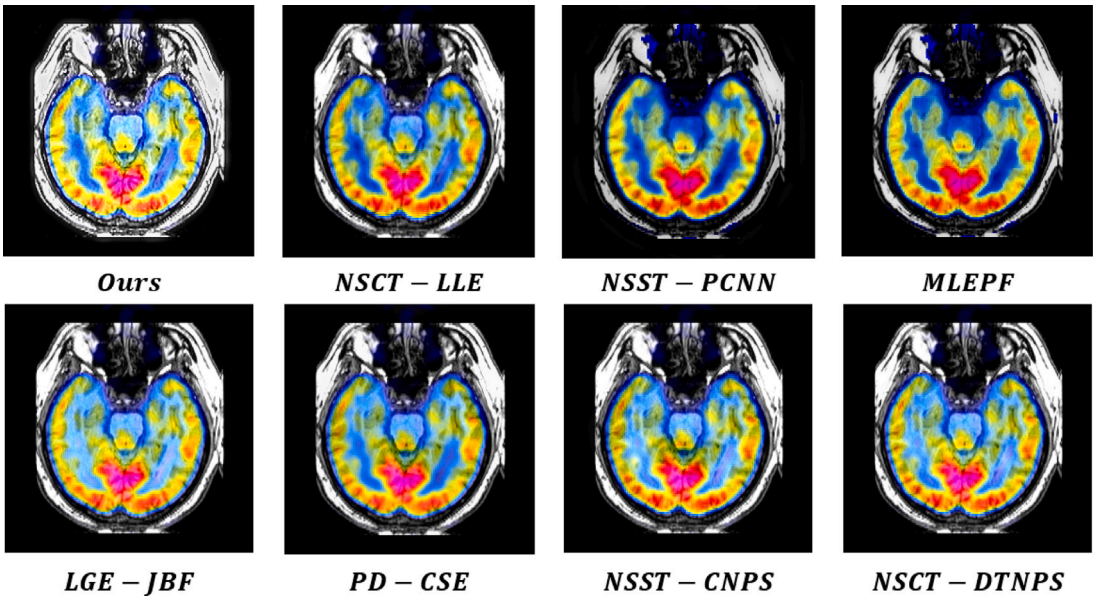

Fig. 8. The output images created by eight image fusion algorithms on data set H1.

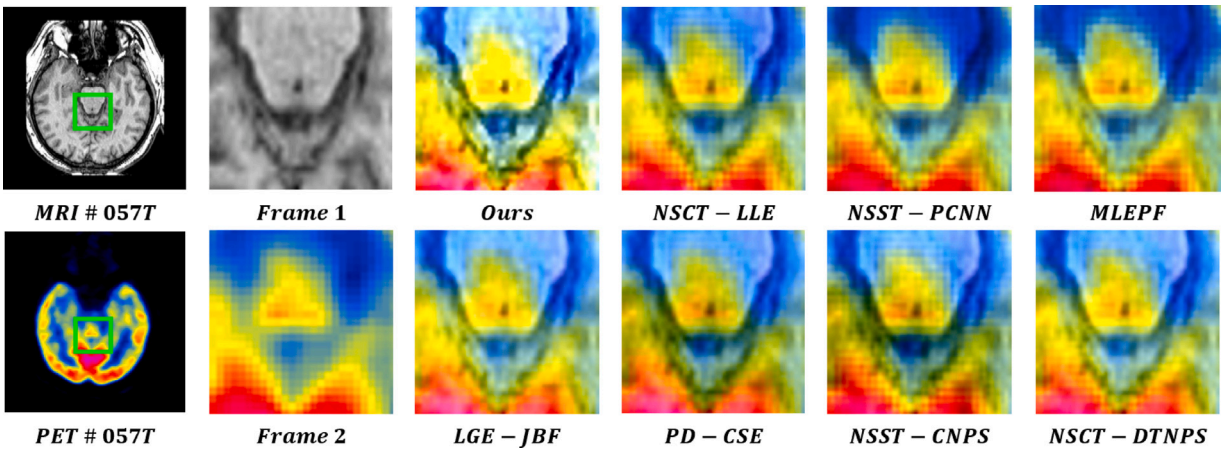

Fig. 9. An image area is cropped from Fig. 8.

output image and preserving information. For example, Dinh [24] has proposed a novel medical image fusion based on the Grasshopper optimization algorithm (GOA). Gao et al. [20] have utilized Particle swarm optimization (PSO) algorithm to fuse medical images in the NSST domain. Dinh [27] has introduced a medical image fusion model using the Marine predators algorithm (MPA) and Structure tensor (TS). Jose et al. [28] have proposed using the Adolescent identity search (AIS) algorithm in the NSST domain for medical image synthesis. Dinh [29] has used the Equilibrium optimization algorithm (EOA) and combine it with the compass operator Prewitt. A number of other optimization-based medical image fusion approaches can be found in studies [30–32].

Currently, two main problems significantly affect the efficiency of image synthesis algorithms. The first problem concerns the quality of the input images. When the input image suffers from problems such as noise, low contrast, and low light intensity, the performance of the compositing algorithms degrades significantly. The second problem concerns the inefficiencies of some existing fusion rules. For example, the averaging rule for the low-frequency component leads to a decrease in the luminance of the composite image. Several studies using this fusion rule can be mentioned as [33,34]. In this paper, we propose a novel image synthesis model to address the above problems. Our image fusion model is based on the STV method, the CSA algorithm, and the DTNP systems. STV method is used to decompose input images into base layers and a series of detail layers. To solve the problem of low-quality input images, we apply the image enhancement method proposed by Dinh et al. [35] to pre-process the input image. This image enhancement method allows the simultaneous improvement of noise, low contrast, and low light problems. To solve the limitation of the average fusion rule, we propose an adaptive fusion rule based on the CSA algorithm for the base layers. DTNP systems are used to create a compositing rule for detail layers, ensuring the composite image's sharpness and preserving information.

The main contributions of our work are as follows:

- Firstly, we propose an efficient fusion rule based on the CSA algorithm for the base layers. This rule allows the output image to have good quality in terms of brightness and contrast.
- Secondly, a fusion rule using DTNP systems is introduced to fuse a series of detail layers. This proposed rule ensures that the fused image retains the details of the input image.
- Thirdly, an image synthesis model has been proposed based on the above two rules. Experiments have shown that our model solves the problems of poor contrast, low light intensity, and loss of detail in the synthesized image.

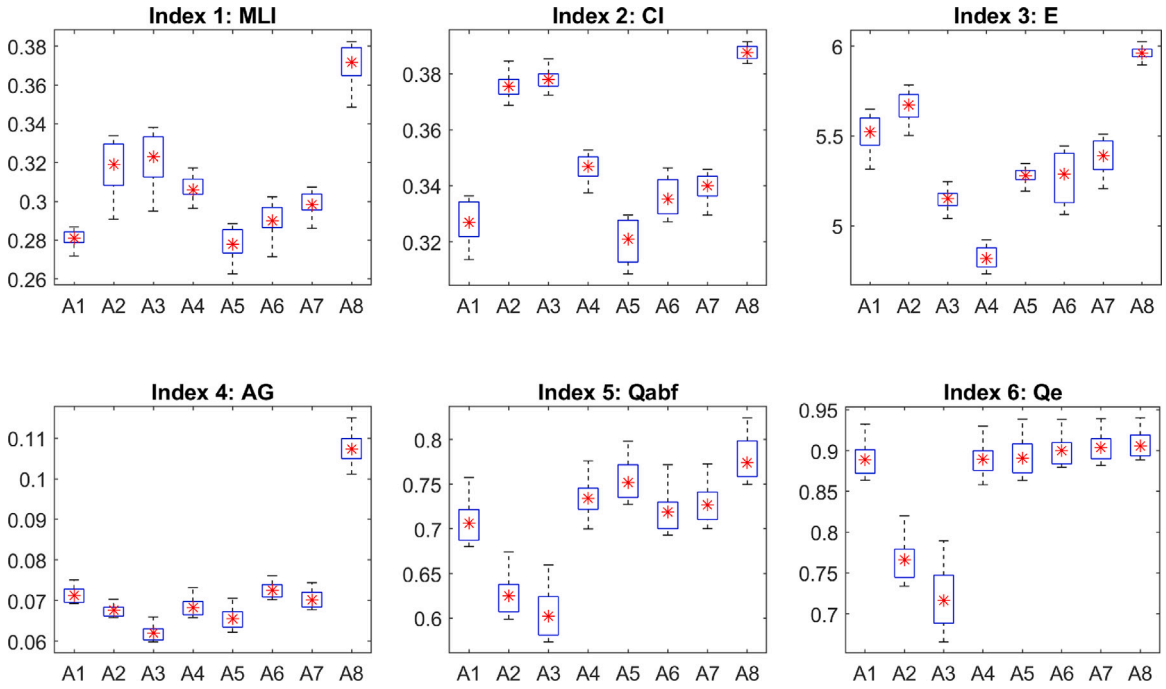

Fig. 10. Six metrics obtained from image synthesis algorithms on data set H1 are illustrated by boxplots.

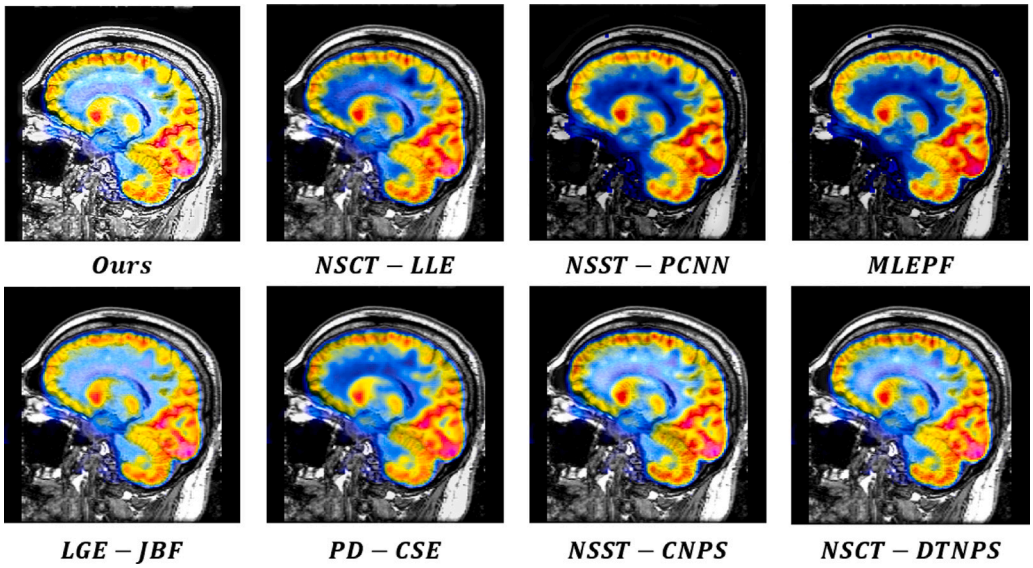

Fig. 11. The output images created by eight image fusion algorithms on data set H2.

The rest of this paper is organized as follows: In Section 2, the Spectral total variation (STV) method, DTNP systems, and the Chameleon swarm algorithm (CSA) are introduced briefly. Section 3 introduces our approach. In Section 4, the experimental results and evaluation are presented. Finally, the conclusion and future work are presented in Section 5.

2. Background

2.1. Spectral Total Variation

The Spectral Total Variation (STV) method was first introduced by Gilboa [36] in 2014. Currently, several applications of the STV can be mentioned, such as image segmentation [37], medical image fusion [38], and image fusion [39].

Assume that $g(x)$ is an input image. The STV transform is defined by Eq. (1).

$$\psi(t;X) = h_{tt}(t;X).t \tag{1}$$

where

- t is the time scale ($t \geq 0$).
- $h_{tt}(t;X)$ is the 2nd derivative with respect to t. It is determined by the following optimization problem (Eq. (2)):

$$h^{l+1} = argmin\frac{1}{2dt}\|g-h\|^2 + E(h) \tag{2}$$

where

- dt is a small time step.
- $l = \overline{1,L}$, L is the maximum number of scales.

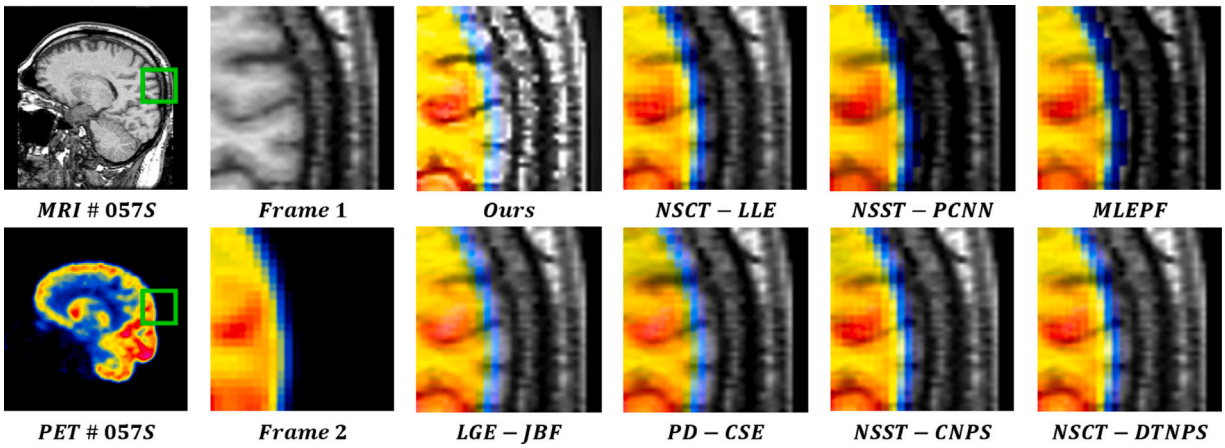

Fig. 12. An image area is cropped from Fig. 11.

- $E(h)$ is regularizing function, and it is calculated according to Eq. (3).

$$E(h) = \int_{\Phi} \|\nabla h(X)\| \, dX \tag{3}$$

where

- Φ is the image domain.
- ∇h is the distributional gradient of h.

The residual layer is calculated according to Eq. (4)

$$\overline{g}(x; L) = (L+1)h(x; L) - Lh(x; L+1) \tag{4}$$

The reconstitution formula is calculated according to Eq. (5)

$$W(x) = \sum_{l=1}^{L} \psi(x; l) + \overline{g}(x; L) \tag{5}$$

Fig. 1 illustrates the components obtained by the STV method.

2.2. Dynamic threshold neural P systems

DTNP systems are introduced by Peng et al. [40] in 2019. This model has also been used in the image processing problems, such as image segmentation [41], medical image fusion [18,42], and multi-focus image fusion [43].

Given an input image I of size $r \times s$ and suppose that $DL(r \times s)$ is a detail layer obtained from the image I by applying the STV method. A DTNP system is represented as a matrix of neurons with dimensions $r \times s$, as shown in Fig. 2. The values of the detail layer $(DL(m,n), m = \overline{1,r}, n = \overline{1,s})$ are the external input of the neuron σ_{mn}. Each neuron is locally connected to its h-neighbor neurons $(\delta_h(\sigma_{mn}))$, which is defined as Eq. (6).

$$\delta_h(\sigma_{mn}) = \{\sigma_{kl}, \quad \text{with} \quad |k-m| \le h, |l-n| \le h\} \tag{6}$$

Each neuron σ_{mn} has two inputs. The first input is the spikes received from its neighboring neurons. The second input is an external input $DL(m,n)$. Each neuron σ_{mn} consists of components: a data unit (u_{mn}), a threshold unit (τ_{mn}), and a spiking rule $(E/(a^u, a^\tau) \to a^p)$. For the spiking rule, the firing condition E is defined as Eq. (7).

$$E \equiv (u_{mn}(t) \ge \tau_{mn}(t)) \wedge (u_{mn}(t) \ge u) \wedge (\tau_{mn}(t) \ge \tau) \tag{7}$$

where $u_{mn}(t)$ and $\tau_{mn}(t)$ are the value of spikes and threshold in neuron σ_{mn} at time t, respectively. Based on the spiking mechanism, $u_{mn}(t+1)$ and $\tau_{mn}(t+1)$ are calculated as Eqs. (8) and (9).

$$u_{mn}(t+1) = \begin{cases} u_{mn}(t) - u + DL(m,n) + \sum_{\sigma_{kl} \in \delta_h} w_{kl} p_{kl}(t) & \text{if } \sigma_{mn} \text{ fires} \\ u_{mn}(t) + DL(m,n) + \sum_{\sigma_{kl} \in \delta_h} w_{kl} p_{kl}(t) & \text{otherwise} \end{cases} \tag{8}$$

$$\tau_{mn}(t+1) = \begin{cases} \tau_{mn}(t) - \tau + p & \text{if } \sigma_{mn} \text{ fires} \\ \tau_{mn}(t) & \text{otherwise} \end{cases} \tag{9}$$

Fig. 3 illustrates the components obtained by applying DTNP systems.

2.3. Chameleon swarm algorithm

The CSA was introduced by Braik [44] in 2022. Algorithm 2 describes some basic steps of the CSA algorithm.

3. Proposed approach

A fusion rule based on DTNP systems (called FR_DTNPS) for the detail layer and our image fusion approach are introduced in this section.

3.1. A fusion rule using DTNP systems (FR - DTNPS)

Algorithm 3 describes how DTNP Systems are applied to build fusion rules for detail layers. The fusion of a series of detail layers is illustrated in Fig. 4.

3.2. Our image fusion approach

Our approach is described in detail in Algorithm 4. Fig. 5 details the schematic diagram of our algorithm.

4. Experimental results and evaluation

4.1. Evaluation indicators

We use six common metrics, and they are described in Table 1.

4.2. Experimental setup

We use three data sets, H1, H2, and H3, with a total of 132 images (256 × 256). Each data set consists of 22 pairs of images (MRI and PET) taken from the source: http://www.med.harvard.edu/AANLIB/. We create one more data set, H4 consisting of 2 pairs of images, 057T (Mri-Pet) and 057S (Mri-Pet). Details of the H1, H2, H3, and H4 data sets are described in Table 2. Several MRI and PET images in the dataset are shown in Fig. 6.

We designed many different experiments to evaluate the effectiveness of the proposed model.

Algorithm 1: DTNP Systems

Input: $DL_{mn}(r \times s)$
Output: $P_{mn}(r \times s)$
Assign parameters: T; τ_0; p; h; $W = w_{mn}(h \times h)$;
/* Initialization: */
$U = u_{mn}(r \times s) = (0)(r \times s)$
$T = \tau_{mn}(r \times s) = (\tau_0)(r \times s)$
$P = p_{mn}(r \times s) = (0)(r \times s)$
/* DTNP systems work as follows: */
for $t = 1 : T$ **do**
  for $m = 1 : r$ **do**
    for $n = 1 : s$ **do**
      u_{mn} is updated according to Eq. (8)
      τ_{mn} is updated according to Eq. (9)
      if $u_{mn} \geq \tau_{mn}$ **then**
        $P_{mn} = P_{mn} + p$
      end
    end
  end
end

Algorithm 2: CSA algorithm

/* Initialization: */
r_1, r_2, r_3, and r^i are randomly selected in [0,1]
l_b and u_b are the lower and upper bounds.
d is the number of dimensions.
Initialize random positions for n chameleons.
Initialize the velocity of dropping chameleons' tongues.
while $t < t_{max}$ **do**
  Define the parameters μ, ω, and a.
  for $i = 1 : n$ **do**
    for $j = 1 : d$ **do**
      if $r_i \geq P_p$ **then**
        $y_{t+1}(i,j) = y_t(i,j) + p_1(P_t(i,j) - G_t(j))r_1 + p_2(G_t(j) - y_t(i,j))r_2$
      end
      else
        $y_{t+1}(i,j) = y_t(i,j) + \mu\left(\left(u_b(j) - l_b(j)\right)r_3 + l_b(j)\right) sgn(rand - 0.5)$
      end
    end
  end
  for $i = 1 : n$ **do**
    $y_{t+1}(i) = yr_t(i) + \overline{y}_t(i)$
  end
  for $i = 1 : n$ **do**
    for $j = 1 : d$ **do**
      $v_{t+1}(i,j) = \omega v_t(i,j) + c_1\left(G_t(j) - y_t(i,j)\right)r_1 + c_2\left(P_t(i,j) - y_t(i,j)\right)r_2$
      $y_{t+1}(i,j) = y_t(i,j) + \left(\left(v_t(i,j)\right)^2 - \left(v_{t-1}(i,j)\right)^2\right)/(2a)$
    end
  end
  Chameleons' positions are adjusted according to u_b and l_b.
  Evaluate the new positions of the chameleons.
  The chameleons' positions are updated.
  $t = t + 1$
end

- **The 1st experiment:** To explain the choice of the CSA, we have utilized five other optimization algorithms to compare. They are described in Table 3. Each algorithm is performed 30 different times on the data set H4. Two evaluation indexes, Mean (M) and Standard Deviation (SD), are used to assess the performance of optimization algorithms. In addition, we also use a non-parametric test (Wilcoxon [47]).
- **The 2nd experiment:** We utilize some of the latest image synthesis algorithms to compare with the proposed model (See details in Table 4). The our approach is denoted as A8.

The necessary parameters are described in Table 5. In the CSA algorithm, the two parameters, $n = 50$ and $t_{max} = 50$, are chosen so because the error of the fitness function between iterations 50 and 49 is less than 10^{-8}.

Algorithm 3: A fusion rule based on DTNP Systems

Input: Detail Layers (DL^i_{MRI}, DL^i_Y), $i = \overline{1,10}$
Output: The fused detail layers (DL^i_F)

Step 1: From DL^i_{MRI} and DL^i_Y, compute the DTNP systems ($P^i_{MRI}(x,y)$, $P^i_Y(x,y)$) according to Eqs. (10) and (11).

$$P^i_{MRI}(x,y) = DTNPS(DL^i_{MRI}) \tag{10}$$

$$P^i_Y(x,y) = DTNPS(DL^i_Y) \tag{11}$$

Step 2: The fused detail layers ($DL^i_F(x,y)$) are calculated according to Eq. (12).

$$DL^i_F(x,y) = \begin{cases} DL^i_{MRI}(x,y) & \text{if } |P^i_{MRI}(x,y)| \geq |P^i_Y(x,y)| \\ DL^i_Y(x,y) & \text{if } |P^i_{MRI}(x,y)| < |P^i_Y(x,y)| \end{cases} \tag{12}$$

Algorithm 4: Our image fusion approach

Input: I_{MRI}, I_{PET}
Output: I_F

MRI images are enhanced by an algorithm proposed by Dinh et al. [35]. The steps of our algorithm are as follows:

Step 1: I_{PET} is converted into three channels (Y, U, and V) by using YUV color model.

Step 2: I_{MRI} and Y images are decomposed into the base layers (BL_{MRI}, BL_Y) and the detail layers (DL^i_{MRI}, DL^i_Y) ($i = \overline{1,10}$) by STV method.

Step 3: DL^i_{MRI} and DL^i_Y ($i = \overline{1,10}$) components are synthesized according to Eq. (13)

$$DL^i_F = FR\_DTNPS(DL^i_{MRI}, DL^i_Y) \tag{13}$$

Step 4: The BL_{MRI} and BL_Y components are fused by using the CSA to find adaptive parameters ($\beta_1 \in [0,1]$ and $\beta_2 \in [0,1]$). Fitness function (F) is described as Eq. (14).

$$F = \frac{V}{A}(Ep_2 - Ep_1) \tag{14}$$

Where

- Ep_1 and Ep_2 are entropy values obtained from image I_L and I_{MRI}, respectively.
- I_L is the composite image obtained in each loop of the CSA.
- A and V are the mean and variance values of image I_L, respectively.

The fused components (BL_F) is calculated according to Eq. (15)

$$BL_F = \beta_1 * BL_{MRI} + \beta_2 * BL_Y \tag{15}$$

Step 5: Gray composite image (I_{F_G}) is calculated according to Eq. (16).

$$I_{F\_G} = BL_F + \sum_{i=1}^{10} DL^i_F \tag{16}$$

Step 6: Color composite image (I_{F_C}) is obtained by converting three channels (I_{F_G}, U, and V) to the RGB model.

4.3. Evaluation

Firstly, the two average optimization parameters (β_1 and β_2) obtained on 3 data sets, H1, H2, and H3, are shown in Table 6. The values of β_1 are quite large (greater than 0.97), while the values of β_2 are pretty small. This result shows that the base layer of the MRI image (BL_{MRI}) is a more informative contributor than the base layer of the PET image (BL_{PET}). As a result, base layer fusion using adaptive parameters effectively determines which base layers contribute significant amounts of information to the composite image.

Secondly, the M and SD indexes of the fitness function obtained after 30 different runs of the optimization algorithms are illustrated in Table 7 and Fig. 7. The mean obtained from the CSA algorithm is the largest, and the standard deviation is the smallest. This result shows that the CSA algorithm is the best among the compared optimization algorithms. Therefore, we have used the CSA algorithm in the proposed

Table 1
Six evaluation indexes.

Num	Indexes	Name
1	ALI	Average Light Intensity
2	CI	Contrast Index
3	E	Entropy
4	AG	Average Gradient
5	$Q^{AB/F}$	Edge-based similarity measure [45]
6	Qe	Piella metrics [46]

Table 2
Data set.

Data sets	Number of images	Description
H1	22 pairs (MRI - PET)	Slices 50 to 71 according to the Transaxial axis
H2	22 pairs (MRI - PET)	Slices 50 to 71 according to the Sagittal axis
H3	22 pairs (MRI - PET)	Slices 50 to 71 according to the Coronal axis
H4	2 pairs (MRI - PET)	Slices 57 according to the Transaxial and Sagittal axis

Table 3
Optimization algorithms.

Num	Algorithms	Years
1	GWO (Grey Wolf Optimizer) [48]	2014
2	MVO (Multi-Verse Optimizer) [49]	2015
3	SCA (Sine Cosine Algorithm) [50]	2016
4	WOA (Whale Optimization Algorithm) [51]	2016
5	SSA (Salp swarm algorithm) [52]	2017

Table 4
Seven image fusion approaches.

Algorithms	Years	Link
NSCT-LLE (A1) [53]	2019	https://github.com/zhiqinzhu123/Source-code-of-medical-image-fusion-in-NSCT-domain
NSST-PCNN (A2) [54]	2020	https://github.com/WeiTan1992/NSST-MSMG-PCNN
MLEPF (A3) [55]	2021	https://github.com/WeiTan1992/MLCF-MLMG-PCNN
LGE-JBF (A4) [21]	2021	https://github.com/lxs6/INS_medical-image-fusion
PD-CSE (A5) [56]	2021	https://github.com/ImranNust/MedicalImageFusion_IMA
NSST-CNPS (A6) [57]	2021	https://github.com/MorvanLi/CNP-MIF
NSCT-DTNP (A7) [58]	2021	https://github.com/MorvanLi/DTNP-MIF

Table 5
Some parameters in our algorithms.

Num	Algorithms	Parameters
1	CSA	Number of chameleons: $n = 50$ Maximum number of loops: $t_{max} = 50$
2	DTNP systems	Initial threshold: $\tau_0 = 1$ Iteration number: $T = 110$ Generated spikes: $p = 1$ Neighborhood radius: $h = 3$
3	STV	Number of bands: $N = 10$ $dt = \frac{1}{N} = 0.1$

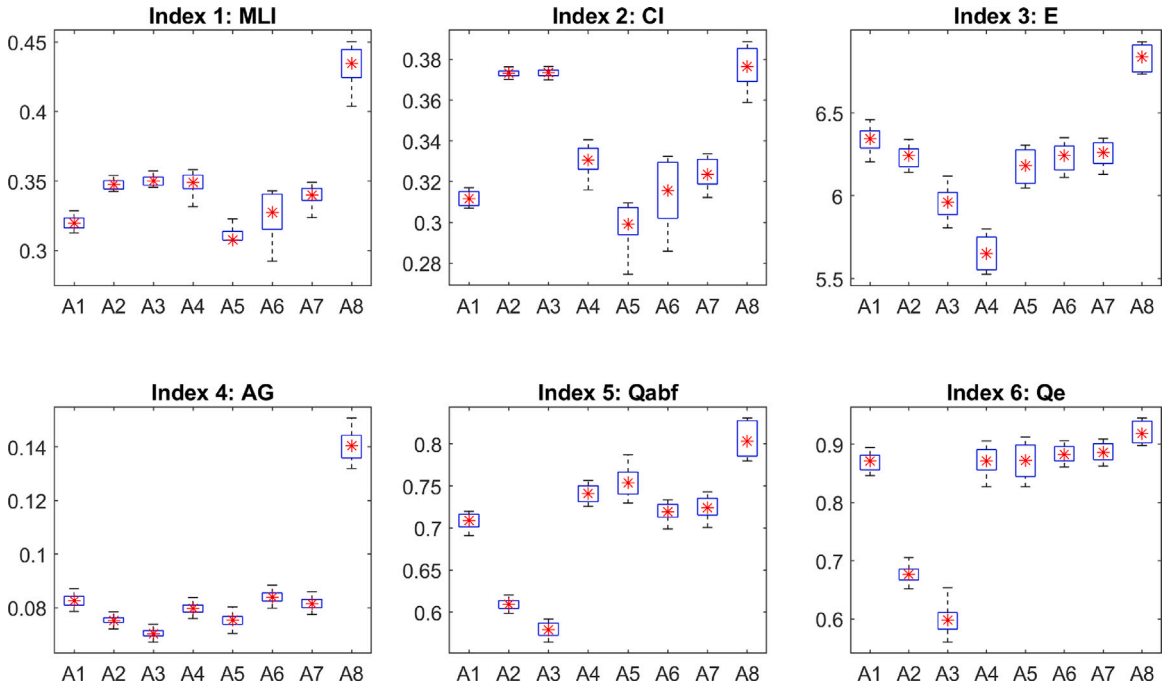

Fig. 13. Six metrics obtained from image synthesis algorithms on data set H2 are illustrated by boxplots.

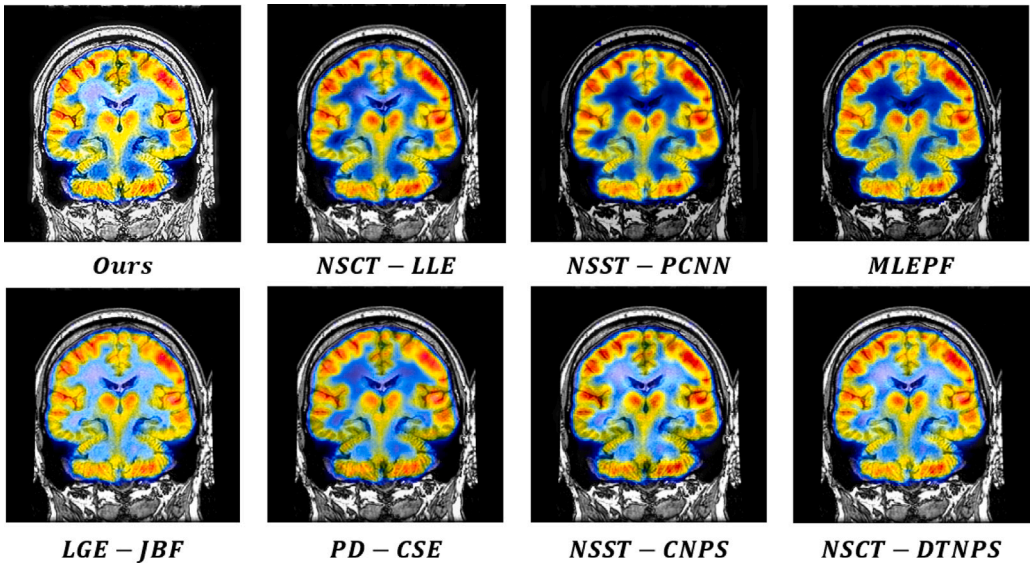

Fig. 14. The output images created by eight image fusion algorithms on data set H3.

Table 6
The two average optimization parameters (β_1 and β_2) obtained on 3 data sets, H1, H2, and H3.

Data set	β_1	β_2
H1	0.97031	0.00472
H2	0.97125	0.01215
H3	0.97122	0.00176

model. Furthermore, from Table 8, the p-values are less than 0.05, and the results are therefore statistically significant.

Thirdly, six indicators for evaluating the quality of composite images are illustrated in Table 9. The fused images obtained from three data sets (H1, H2, and H3) are illustrated in Figs. 8, 11, and 14. Visually, it is easy to see that the images synthesized by our method are of the best quality. Quantitatively, all the evaluation indexes obtained from our model are the best compared to the evaluation indexes obtained from the remaining image fusion algorithms. The four evaluation indexes ALI, MI, E, and AG show that the composite image obtained by our image fusion algorithm has brightness, contrast, amount of information, and sharpness better than the composite images obtained from the remaining image synthesis algorithms. The best results of $Q^{AB/F}$ and Qe show that our image fusion approach is to preserve the details from the input image well. We crop an image area from Figs. 8, 11, and 14 and represent them in Figs. 9, 12, and 15. From

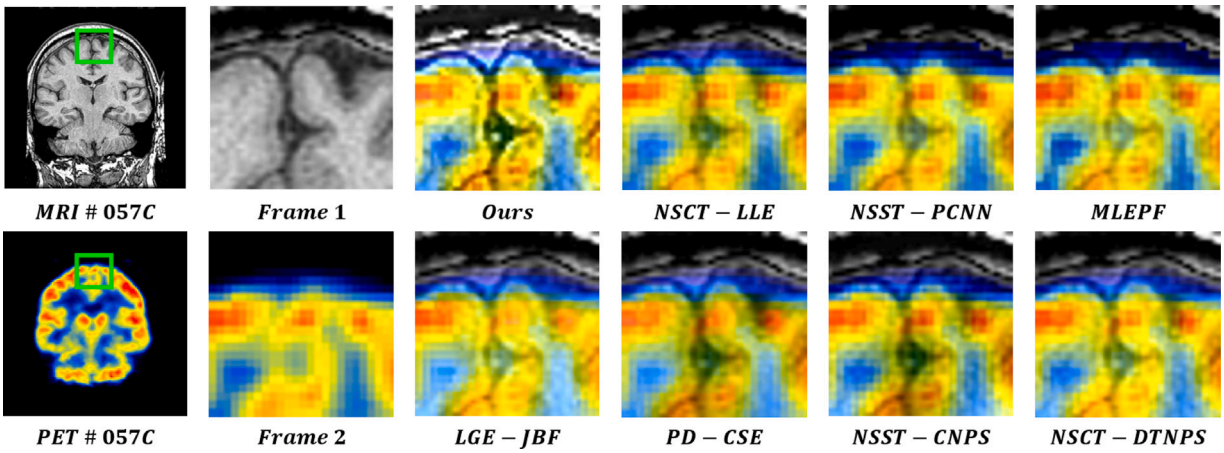

Fig. 15. An image area is cropped from Fig. 14.

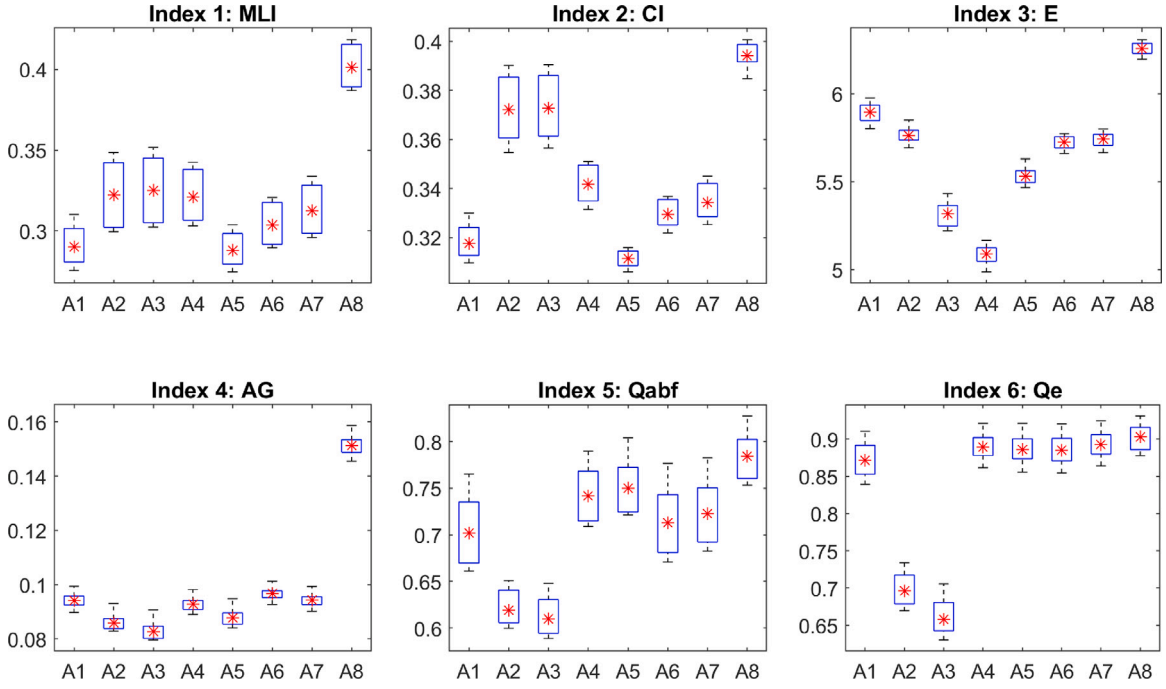

Fig. 16. Six metrics obtained from image synthesis algorithms on data set H3 are illustrated by boxplots.

small frames in Figs. 9, 12, and 15, it is easy to see that the proposed method produces better quality images than the other methods.

Figs. 10, 13, and 16, illustrate the six indicators obtained from different image synthesis algorithms for 66 pairs of MRI-PET images. The data distribution of the evaluation indexes depends on two main factors, the input image and the image synthesis algorithm itself. Visually, it is easy to see that the average value of the evaluation indicators (represented by a red asterisk) obtained from our proposed algorithm is the highest. This result shows that our image fusion model produces better composite images than those generated from the other image fusion methods.

The running times of the image fusion algorithms are shown in Table 10. Our synthesis algorithm takes about 14.32 s on average to complete the synthesis of images. This running time is quite large when compared to some other synthesis algorithms. Therefore, this is the drawback of our algorithm.

5. Conclusion and future work

In this paper, a novel approach is introduced to synthesize medical images. This approach is based on the STV, CSA algorithm, and the fusion rule using DTNP systems (FR_DTNPS). The STV is used to transform images into a base layer and a series of detail layers. The CSA algorithm is used to fuse the base layers with the aim of ensuring that the synthesized image is of good quality. The FR_DTNPS rule ensures that important information from the input image is preserved in the synthesis process. One hundred thirty-two medical images, six evaluation indexes, and seven latest image fusion algorithms were

Table 7
The M and SD indexes of fitness function from thirty runs.

Data set	Algorithms	M	SD
H4(075T)	**CSA**	**0.454024658208212**	**0.000016716373537**
	GWO	0.453634987107202	0.000243690754013
	MVO	0.452482287901068	0.000884435972570
	SCA	0.452867424832344	0.000643487050870
	WOA	0.453810401132191	0.000306227589404
	SSA	0.453729288167299	0.000382543711500
H4(057S)	**CSA**	**0.462063946951917**	**0.000120805667359**
	GWO	0.461745284780825	0.000159829329243
	MVO	0.461005140006423	0.000593977765063
	SCA	0.461127471137806	0.000542499019299
	WOA	0.461830088573223	0.000216816382370
	SSA	0.461715778894835	0.000409265662282

Table 8
P-values from Wilcoxon test.

Data set	Algs	P-values
H4(057T)	CSA vs. GWO	3.019859359162151e−11
	CSA vs. MVO	3.019859359162151e−11
	CSA vs. SCA	3.019859359162151e−11
	CSA vs. WOA	2.921545213841673e−09
	CSA vs. SSA	1.956779959806124e−10
H4(057S)	CSA vs. GWO	5.461746656616969e−09
	CSA vs. MVO	5.494052450965197e−11
	CSA vs. SCA	1.093669563109906e−10
	CSA vs. WOA	1.697952601710239e−08
	CSA vs. SSA	4.310612299972266e−08

Table 9
Six evaluation indexes of the fused image obtained by eight image synthesis approaches.

Data set	Algs	ALI	CI	E	AG	$Q^{AB/F}$	Qe
H1	*A*1	0.2811	0.3269	5.5239	0.0713	0.7062	0.8888
	*A*2	0.3190	0.3756	5.6738	0.0676	0.6248	0.7663
	*A*3	0.3230	0.3779	5.1512	0.0620	0.6025	0.7163
	*A*4	0.3059	0.3469	4.8193	0.0683	0.7343	0.8898
	*A*5	0.2777	0.3209	5.2796	0.0655	0.7521	0.8907
	*A*6	0.2899	0.3352	5.2885	0.0725	0.7189	0.8999
	*A*7	0.2982	0.3400	5.3902	0.0702	0.7266	0.9038
	*A*8	**0.3718**	**0.3876**	**5.9612**	**0.1074**	**0.7743**	**0.9055**
H2	*A*1	0.3199	0.3117	6.3466	0.0827	0.7091	0.8710
	*A*2	0.3475	0.3733	6.2441	0.0753	0.6091	0.6769
	*A*3	0.3502	0.3735	5.9626	0.0703	0.5792	0.5978
	*A*4	0.3491	0.3305	5.6511	0.0797	0.7412	0.8713
	*A*5	0.3077	0.2992	6.1828	0.0755	0.7535	0.8719
	*A*6	0.3273	0.3155	6.2426	0.0840	0.7190	0.8829
	*A*7	0.3397	0.3236	6.2633	0.0815	0.7238	0.8863
	*A*8	**0.4346**	**0.3765**	**6.8396**	**0.1404**	**0.8035**	**0.9183**
H3	*A*1	0.2901	0.3177	5.8960	0.0941	0.7018	0.8715
	*A*2	0.3221	0.3721	5.7625	0.0859	0.6192	0.6962
	*A*3	0.3250	0.3728	5.3172	0.0827	0.6097	0.6578
	*A*4	0.3210	0.3416	5.0898	0.0927	0.7416	0.8891
	*A*5	0.2877	0.3115	5.5320	0.0878	0.7501	0.8861
	*A*6	0.3036	0.3294	5.7258	0.0967	0.7130	0.8850
	*A*7	0.3123	0.3343	5.7416	0.0943	0.7229	0.8928
	*A*8	**0.4012**	**0.3942**	**6.2567**	**0.1514**	**0.7844**	**0.9028**

utilized to assess. The results show that our image synthesis model is more efficient than the current latest image synthesis methods.

In the future, we plan to improve the efficiency of medical image fusion in the following two ways. Firstly, apply the latest image enhancement methods to improve input image quality. This method has been proven to be effective in improving the performance of medical image synthesis algorithms, according to Dinh et al. [35]. Secondly, apply new meta-heuristic optimization algorithms to improve the quality of the fusion rule as well as the running time.

Table 10
Average running time (ART) of image fusion algorithms on the data set (H1&H2&H3).

Approaches	ART (s)
A1	3.145370
A2	7.443567
A3	7.999702
A4	0.428422
A5	0.265967
A6	3.621259
A7	17.888611
Ours (50 loops)	14.317758

CRediT authorship contribution statement

Phu-Hung Dinh: Conceptualization, Methodology, Software, Data curation, Writing – orginal draft, Visualization, Investigation, Supervision, Validation, Writing – review & editing.

Declaration of competing interest

The authors declare that they have no known competing financial interests or personal relationships that could have appeared to influence the work reported in this paper.

Data availability

Data will be made available on request.

References

[1] Z. Ding, D. Zhou, H. Li, R. Hou, Y. Liu, Siamese networks and multi-scale local extrema scheme for multimodal brain medical image fusion, Biomed. Signal Process. Control 68 (2021) 102697, http://dx.doi.org/10.1016/j.bspc.2021.102697.

[2] Z. Wang, X. Li, H. Duan, Y. Su, X. Zhang, X. Guan, Medical image fusion based on convolutional neural networks and non-subsampled contourlet transform, Expert Syst. Appl. 171 (2021) 114574, http://dx.doi.org/10.1016/j.eswa.2021.114574.

[3] W. Li, X. Peng, J. Fu, G. Wang, Y. Huang, F. Chao, A multiscale double-branch residual attention network for anatomical–functional medical image fusion, Comput. Biol. Med. 141 (2022) 105005, http://dx.doi.org/10.1016/j.compbiomed.2021.105005.

[4] C. Zhao, T. Wang, B. Lei, Medical image fusion method based on dense block and deep convolutional generative adversarial network, Neural Comput. Appl. 33 (12) (2020) 6595–6610, http://dx.doi.org/10.1007/s00521-020-05421-5.

[5] K. Guo, X. Hu, X. Li, MMFGAN: A novel multimodal brain medical image fusion based on the improvement of generative adversarial network, Multimedia Tools Appl. 81 (4) (2021) 5889–5927, http://dx.doi.org/10.1007/s11042-021-11822-y.

[6] M. Rajesh, R. Sitharthan, Image fusion and enhancement based on energy of the pixel using Deep Convolutional Neural Network, Multimedia Tools Appl. 81 (1) (2021) 873–885, http://dx.doi.org/10.1007/s11042-021-11501-y.

[7] M. Shi, F. Zhang, S. Wang, C. Zhang, X. Li, Detail preserving image denoising with patch-based structure similarity via sparse representation and SVD, Comput. Vis. Image Underst. 206 (2021) 103173, http://dx.doi.org/10.1016/j.cviu.2021.103173.

[8] D. Tang, Q. Xiong, H. Yin, Z. Zhu, Y. Li, A novel sparse representation based fusion approach for multi-focus images, Expert Syst. Appl. 197 (2022) 116737, http://dx.doi.org/10.1016/j.eswa.2022.116737.

[9] D.S. Shibu, S.S. Priyadharsini, Multi scale decomposition based medical image fusion using convolutional neural network and sparse representation, Biomed. Signal Process. Control 69 (2021) 102789, http://dx.doi.org/10.1016/j.bspc.2021.102789.

[10] A.S. Yousif, Z. Omar, U.U. Sheikh, An improved approach for medical image fusion using sparse representation and siamese convolutional neural network, Biomed. Signal Process. Control 72 (2022) 103357, http://dx.doi.org/10.1016/j.bspc.2021.103357.

[11] L. Wang, J. Dou, P. Qin, S. Lin, Y. Gao, R. Wang, J. Zhang, Multimodal medical image fusion based on nonsubsampled shearlet transform and convolutional sparse representation, Multimedia Tools Appl. 80 (30) (2021) 36401–36421, http://dx.doi.org/10.1007/s11042-021-11379-w.

[12] X. Li, F. Zhou, H. Tan, Joint image fusion and denoising via three-layer decomposition and sparse representation, Knowl.-Based Syst. 224 (2021) 107087, http://dx.doi.org/10.1016/j.knosys.2021.107087.

[13] Z. Wang, Z. Cui, Y. Zhu, Multi-modal medical image fusion by Laplacian pyramid and adaptive sparse representation, Comput. Biol. Med. 123 (2020) 103823, http://dx.doi.org/10.1016/j.compbiomed.2020.103823.
[14] Q. Hu, S. Hu, F. Zhang, Multi-modality image fusion combining sparse representation with guidance filtering, Soft Comput. (2021) http://dx.doi.org/10.1007/s00500-020-05448-9.
[15] J. Fu, W. Li, J. Du, B. Xiao, Multimodal medical image fusion via laplacian pyramid and convolutional neural network reconstruction with local gradient energy strategy, Comput. Biol. Med. 126 (2020) 104048, http://dx.doi.org/10.1016/j.compbiomed.2020.104048.
[16] Z. Chao, X. Duan, S. Jia, X. Guo, H. Liu, F. Jia, Medical image fusion via discrete stationary wavelet transform and an enhanced radial basis function neural network, Appl. Soft Comput. 118 (2022) 108542, http://dx.doi.org/10.1016/j.asoc.2022.108542.
[17] P.-H. Dinh, Combining Gabor energy with equilibrium optimizer algorithm for multi-modality medical image fusion, Biomed. Signal Process. Control 68 (2021) 102696, http://dx.doi.org/10.1016/j.bspc.2021.102696.
[18] B. Li, H. Peng, J. Wang, A novel fusion method based on dynamic threshold neural P systems and nonsubsampled contourlet transform for multi-modality medical images, Signal Process. 178 (2021) 107793, http://dx.doi.org/10.1016/j.sigpro.2020.107793.
[19] R.R. Nair, T. Singh, An optimal registration on shearlet domain with novel weighted energy fusion for multi-modal medical images, Optik 225 (2021) 165742, http://dx.doi.org/10.1016/j.ijleo.2020.165742.
[20] Y. Gao, S. Ma, J. Liu, Y. Liu, X. Zhang, Fusion of medical images based on salient features extraction by PSO optimized fuzzy logic in NSST domain, Biomed. Signal Process. Control 69 (2021) 102852, http://dx.doi.org/10.1016/j.bspc.2021.102852.
[21] X. Li, F. Zhou, H. Tan, W. Zhang, C. Zhao, Multimodal medical image fusion based on joint bilateral filter and local gradient energy, Inform. Sci. 569 (2021) 302–325, http://dx.doi.org/10.1016/j.ins.2021.04.052.
[22] J. Du, M. Fang, Y. Yu, G. Lu, An adaptive two-scale biomedical image fusion method with statistical comparisons, Comput. Methods Programs Biomed. 196 (2020) 105603, http://dx.doi.org/10.1016/j.cmpb.2020.105603.
[23] C. Pei, K. Fan, W. Wang, Two-scale multimodal medical image fusion based on guided filtering and sparse representation, IEEE Access 8 (2020) 140216–140233, http://dx.doi.org/10.1109/access.2020.3013027.
[24] P.-H. Dinh, A novel approach based on grasshopper optimization algorithm for medical image fusion, Expert Syst. Appl. 171 (2021) 114576, http://dx.doi.org/10.1016/j.eswa.2021.114576.
[25] P.-H. Dinh, An improved medical image synthesis approach based on marine predators algorithm and maximum gabor energy, Neural Comput. Appl. 34 (6) (2021) 4367–4385, http://dx.doi.org/10.1007/s00521-021-06577-4.
[26] H. Ullah, B. Ullah, L. Wu, F.Y. Abdalla, G. Ren, Y. Zhao, Multi-modality medical images fusion based on local-features fuzzy sets and novel sum-modified-Laplacian in non-subsampled shearlet transform domain, Biomed. Signal Process. Control 57 (2020) 101724, http://dx.doi.org/10.1016/j.bspc.2019.101724.
[27] P.-H. Dinh, A novel approach using structure tensor for medical image fusion, Multidimens. Syst. Signal Process. 33 (3) (2022) 1001–1021, http://dx.doi.org/10.1007/s11045-022-00829-9.
[28] J. Jose, N. Gautam, M. Tiwari, T. Tiwari, A. Suresh, V. Sundararaj, R. MR, An image quality enhancement scheme employing adolescent identity search algorithm in the NSST domain for multimodal medical image fusion, Biomed. Signal Process. Control 66 (2021) 102480, http://dx.doi.org/10.1016/j.bspc.2021.102480.
[29] P.-H. Dinh, Multi-modal medical image fusion based on equilibrium optimizer algorithm and local energy functions, Appl. Intell. 51 (11) (2021) 8416–8431, http://dx.doi.org/10.1007/s10489-021-02282-w.
[30] J. Bhardwaj, A. Nayak, Discrete wavelet transform and bird swarm optimized Bayesian multimodal medical image fusion, HELIX 10 (1) (2020) 07–12, http://dx.doi.org/10.29042/2020-10-1-07-12.
[31] C.S. Asha, S. Lal, V.P. Gurupur, P.U.P. Saxena, Multi-modal medical image fusion with adaptive weighted combination of NSST bands using chaotic Grey Wolf optimization, IEEE Access 7 (2019) 40782–40796, http://dx.doi.org/10.1109/access.2019.2908076.
[32] P.-H. Dinh, A novel approach based on three-scale image decomposition and Marine predators algorithm for multi-modal medical image fusion, Biomed. Signal Process. Control 67 (2021) 102536, http://dx.doi.org/10.1016/j.bspc.2021.102536.
[33] Y. Liu, X. Chen, R.K. Ward, Z.J. Wang, Image fusion with convolutional sparse representation, IEEE Signal Process. Lett. 23 (12) (2016) 1882–1886, http://dx.doi.org/10.1109/lsp.2016.2618776.
[34] Y. Liu, X. Chen, R.K. Ward, Z.J. Wang, Medical image fusion via convolutional sparsity based morphological component analysis, IEEE Signal Process. Lett. 26 (2019) 485–489, http://dx.doi.org/10.1109/lsp.2019.2895749.
[35] P.-H. Dinh, N.L. Giang, A new medical image enhancement algorithm using adaptive parameters, Int. J. Imaging Syst. Technol. 32 (6) (2022) 2198–2218, http://dx.doi.org/10.1002/ima.22778.
[36] G. Gilboa, A total variation spectral framework for scale and texture analysis, SIAM J. Imaging Sci. 7 (4) (2014) 1937–1961, http://dx.doi.org/10.1137/130930704.
[37] J. Zhang, J. Qi, Z. Zheng, L. Sun, A robust image segmentation framework based on total variation spectral transform, Pattern Recognit. Lett. 153 (2022) 159–167, http://dx.doi.org/10.1016/j.patrec.2021.12.001.
[38] G. Wang, W. Li, X. Gao, B. Xiao, J. Du, Multimodal medical image fusion based on multichannel coupled neural P systems and max-cloud models in spectral total variation domain, Neurocomputing 480 (2022) 61–75, http://dx.doi.org/10.1016/j.neucom.2022.01.059.
[39] T.-J. Zhang, L.-J. Deng, Z.-C. Wu, C.-C. Zheng, An iterative approach for image fusion with dynamic gradient sparsity and anisotropic spectral–spatial total variation, Signal Image Video Process. (2022) http://dx.doi.org/10.1007/s11760-021-02105-y.
[40] H. Peng, J. Wang, M.J. Pérez-Jiménez, A. Riscos-Núñez, Dynamic threshold neural P systems, Knowl.-Based Syst. 163 (2019) 875–884, http://dx.doi.org/10.1016/j.knosys.2018.10.016.
[41] Y. Cai, S. Mi, J. Yan, H. Peng, X. Luo, Q. Yang, J. Wang, An unsupervised segmentation method based on dynamic threshold neural P systems for color images, Inform. Sci. 587 (2022) 473–484, http://dx.doi.org/10.1016/j.ins.2021.12.058.
[42] S. Mi, L. Zhang, H. Peng, J. Wang, Medical image fusion based on DTNP systems and Laplacian pyramid, J. Membr. Comput. 3 (4) (2021) 284–295, http://dx.doi.org/10.1007/s41965-021-00087-x.
[43] B. Li, H. Peng, J. Wang, X. Huang, Multi-focus image fusion based on dynamic threshold neural P systems and surfacelet transform, Knowl.-Based Syst. 196 (2020) 105794, http://dx.doi.org/10.1016/j.knosys.2020.105794.
[44] M.S. Braik, Chameleon Swarm Algorithm: A bio-inspired optimizer for solving engineering design problems, Expert Syst. Appl. 174 (2021) 114685, http://dx.doi.org/10.1016/j.eswa.2021.114685.
[45] C. Xydeas, V. Petrovic, Objective image fusion performance measure, Electron. Lett. 36 (2000) 308, http://dx.doi.org/10.1049/el:20000267.
[46] G. Piella, H. Heijmans, A new quality metric for image fusion, in: Proceedings 2003 International Conference on Image Processing (Cat. No.03CH37429), IEEE, http://dx.doi.org/10.1109/icip.2003.1247209.
[47] F. Wilcoxon, Individual comparisons by ranking methods, Biom. Bull. 1 (6) (1945) 80, http://dx.doi.org/10.2307/3001968.
[48] S. Mirjalili, S.M. Mirjalili, A. Lewis, Grey wolf optimizer, Adv. Eng. Softw. 69 (2014) 46–61, http://dx.doi.org/10.1016/j.advengsoft.2013.12.007.
[49] S. Mirjalili, S.M. Mirjalili, A. Hatamlou, Multi-verse optimizer: a nature-inspired algorithm for global optimization, Neural Comput. Appl. 27 (2) (2015) 495–513, http://dx.doi.org/10.1007/s00521-015-1870-7.
[50] S. Mirjalili, SCA: A Sine cosine algorithm for solving optimization problems, Knowl.-Based Syst. 96 (2016) 120–133, http://dx.doi.org/10.1016/j.knosys.2015.12.022.
[51] S. Mirjalili, A. Lewis, The whale optimization algorithm, Adv. Eng. Softw. 95 (2016) 51–67, http://dx.doi.org/10.1016/j.advengsoft.2016.01.008.
[52] S. Mirjalili, A.H. Gandomi, S.Z. Mirjalili, S. Saremi, H. Faris, S.M. Mirjalili, Salp Swarm Algorithm: A bio-inspired optimizer for engineering design problems, Adv. Eng. Softw. 114 (2017) 163–191, http://dx.doi.org/10.1016/j.advengsoft.2017.07.002.
[53] Z. Zhu, M. Zheng, G. Qi, D. Wang, Y. Xiang, A phase congruency and local Laplacian energy based multi-modality medical image fusion method in NSCT domain, IEEE Access 7 (2019) 20811–20824, http://dx.doi.org/10.1109/access.2019.2898111.
[54] W. Tan, P. Tiwari, H.M. Pandey, C. Moreira, A.K. Jaiswal, Multimodal medical image fusion algorithm in the era of big data, Neural Comput. Appl. (2020) 1–21, http://dx.doi.org/10.1007/s00521-020-05173-2.
[55] W. Tan, W. Thitøn, P. Xiang, H. Zhou, Multi-modal brain image fusion based on multi-level edge-preserving filtering, Biomed. Signal Process. Control 64 (2021) 102280, http://dx.doi.org/10.1016/j.bspc.2020.102280.
[56] A. Sufyan, M. Imran, S.A. Shah, H. Shahwani, A.A. Wadood, A novel multimodality anatomical image fusion method based on contrast and structure extraction, Int. J. Imaging Syst. Technol. 32 (1) (2021) 324–342, http://dx.doi.org/10.1002/ima.22649.
[57] B. Li, H. Peng, X. Luo, J. Wang, X. Song, M.J. Pérez-Jiménez, A. Riscos-Núñez, Medical image fusion method based on coupled neural P systems in nonsubsampled shearlet transform domain, Int. J. Neural Syst. 31 (01) (2020) 2050050, http://dx.doi.org/10.1142/s0129065720500501.
[58] B. Li, H. Peng, J. Wang, A novel fusion method based on dynamic threshold neural P systems and nonsubsampled contourlet transform for multi-modality medical images, Signal Process. 178 (2021) 107793, http://dx.doi.org/10.1016/j.sigpro.2020.107793.

Multidimensional Systems and Signal Processing
https://doi.org/10.1007/s11045-022-00829-9

A novel approach using structure tensor for medical image fusion

Phu-Hung Dinh[1]

Received: 8 February 2021 / Revised: 18 January 2022 / Accepted: 11 April 2022

Abstract
Medical image fusion has been shown to be effective in supporting clinicians make better clinical diagnoses. Although many algorithms have been proposed for synthesis, they still have certain limitations. Some limitations can be seen as the synthesized image is reduced in contrast or details are not preserved. In this paper, we propose an image fusion algorithm to solve the problems mentioned above. Firstly, an image decomposition method is proposed to decompose the image into two components. This method is based on the Gaussian filter and the Weighted mean curvature filter. Secondly, a fusion method for high-frequency components is based on local energy function using Structure tensor saliency. Finally, we create an adaptive fusion rule using the Marine Predators Algorithm optimization method to fuse low-frequency components. Five latest algorithms and five evaluation indexes have been used to test the proposed algorithm's effectiveness. The obtained experimental results show that the composite image is significantly improved in quality as well as well preserved the information from the input image.

Keywords Marine predators algorithm (MPA) · Two-component decomposition (TCD) · Maximum local energy (MLE) · Structure tensor saliency (STS)

1 Introduction

In recent years, medical image processing applications are becoming more and more popular. In particular, medical image fusion has received much attention from researchers because of its practical applications. With the variety of medical imaging devices, it is possible to obtain medical images containing different types of information (Wang et al. 2021c). For example, magnetic resonance imaging (MRI) provides information about soft tissues and organs with high contrast. In contrast, positron emission tomography (PET) provides information about tissues and organs' metabolic or biochemical functions. Therefore, creating

✉ Phu-Hung Dinh
hungdp@tlu.edu.vn

[1] Thuyloi University, 175 Tay Son Dong Da, Hanoi, Vietnam

an image containing information from multi-modal images will help doctors make better diagnoses.

Until now, image fusion methods are usually performed on the transform domain. Specifically, the images are transformed by a defined image decomposition method. Then, the components on the transform domain are fused according to a predefined rule. Finally, the synthesized components are transformed to the spatial domain (Zhang et al. 2020). The methods of image transformation are also very diverse. Several image transformation methods can be mentioned such as Wavelet transform methods, Pyramid methods, and Multi-scale geometric analysis (MGA) methods. Image decomposition methods based on aforementioned transform have been used in many image fusion studies. For example, Dinh (2021a) has utilized Stationary wavelet transform (SWT) to decompose input images. Laplacian Pyramid has used to transform input images in some studies (Du et al. 2016; Wang et al. 2020b; Fu et al. 2020). Some of the image transforms using phase information have been used such as Non-subsampling contour transform (NSCT) (Zhu et al. 2019; Wang and Shen 2020; Wang et al. 2021d), non-subsampled shearlet transform (NSST) (Liu et al. 2018; Ding et al. 2020; Nair and Singh 2021b, a; Wang et al. 2021b; Gao et al. 2021). In addition, Sparse representation (SR) has also been shown to be effective in decomposing input images in image synthesis algorithms. Some studies can be mentioned as Maqsood and Javed (2020), Shibu and Priyadharsini (2021), Yousif et al. (2022), Li et al. (2021a), Hu et al. (2021) and Barba-J et al. (2022).

Deep learning is a powerful tool for solving image processing problems. It has also been applied to solve the problem of image synthesis in some recent studies. For example, Ding et al. (2021) have utilized Siamese networks and combined them with the local extrema scheme. Another study using this network was also proposed by Yousif et al. (2022). Wang et al. (2021d) have proposed to use convolutional neural networks (CNN) for fusing high frequency sub-bands in NSST domain. Some other studies using deep learning networks can be mentioned as Li et al. (2021b), Zhao et al. (2020) and Guo et al. (2021).

To improve the efficiency of image fusion, many researchers have recently proposed optimization-based approaches. For instance, Dinh (2021c) has used the equilibrium optimizer algorithm (EOA) to build an efficient synthesis rule for low-frequency components. Gao et al. (2021) have proposed to use Particle swarm optimization (PSO) for fusing low frequency sub-bands in the NSST domain. Some other studies also use PSO such as Shehanaz et al. (2021), Tannaz et al. (2019) and Gao et al. (2021). Jose et al. (2021) have utilized adolescent identity search algorithm (AISA) to fuse high frequency sub-bands in the NSST domain. Some other optimization algorithms have also been used such as grasshopper optimization algorithm (GOA) (Dinh 2021d), shark smell optimization (MSSO) (Xu et al. 2020), and gray wolf optimization (GWO) (Daniel et al. 2017). In addition, some potential algorithms can be found in the researches (Tao et al. 2020; Fang et al. 2021; Wei et al. 2021; Stojanovic et al. 2020; Pršić et al. 2016).

Faramarzi et al. (2020) introduced a new metaheuristic-based optimization algorithm called MPA in 2020. Currently, This algorithm has been used effectively in some image processing problems such as medical image fusion Dinh (2021e) and image segmentation Abdel-Basset et al. (2020). Therefore, the application of MPA in image synthesis will bring promising results.

According to our observations, the average rule is used to fuse low-frequency components in some studies (Liu et al. 2016, 2019; Maqsood and Javed 2020) because it allows the algorithm to execute quickly. However, its disadvantage results in low-quality composite images. Therefore, our study will focus on solving this problem by proposing an adaptive fusion rule. Furthermore, to preserve the details from the input image, we propose an efficient

synthesis rule for HFCs based on structure tensor. This rule is compared with some popular synthesis rules today such as Maximum local energy (MLE) (Polinati and Dhuli 2020), Parameter-adaptive pulse coupled neural network (PA-PCNN) (Yin et al. 2019), and Sum modified Laplacian (SML) (Li et al. 2018).

In this work, we propose three new algorithms to improve the efficiency of image compositing. Some of the key contributions are highlighted as follows:

- Firstly, the two-component image composition (TSD) method is proposed to decompose images into two components. This method is built by the Gaussian filter (GF) and the Weighted mean curvature filter (WMCF).
- Secondly, an efficient rule is introduced to fuse the HFCs. This rule is based on maximum local energy using structure tensor saliency.
- Thirdly, an adaptive synthesis rule is proposed for the fusion of LFCs.

The rest of the paper is arranged as follows: Some background knowledge, such as Weighted mean curvature filter (WMCF), the two-component image decomposition, YCbCr color space, Structure tensor, Local Energy using Structure Tensor Saliency, and the MPA algorithm, is introduced briefly in Sect. 2. Section 3 presents the fusion rule based on Maximum local energy using the structure tensor saliency (MLE_STS) as well as the proposed approach. Section 4, Dataset, evaluation indexes, and experiment results are mentioned. Finally, the conclusion and future work are given in Sect. 5.

2 Background

Some background knowledge, such as Weighted mean curvature filter (WMCF), the TSD method, YCbCr color space, Structure Tensor, Local Energy using Structure Tensor Saliency, and MPA algorithm, are introduced in this section.

2.1 Weighted mean curvature filter (WMCF)

Gong and Goksel (2019) proposed the WMCF in 2019, and it has been effectively used in image fusion (Tan et al. 2021). The WMCF is calculated according to Eq. (1). Figure 1 illustrates an input image and an output image after using the WMC filter.

$$F(P) = \Delta P - \frac{P_y^2 P_{yy} + 2P_x P_y P_{xy} + P_x^2 P_{xx}}{P_x^2 + P_y^2} \tag{1}$$

where

- P is an input image.
- Δ is the isotropic Laplace operator.
- P_x and P_y are the partial derivatives in the x and y directions.
- P_x^2, P_y^2, P_{xy} are corresponding second-order partial derivatives.

Step 1: Calculate the distances d_i according to the Eq. (2).

$$d_i = m_i * P, i = \overline{1,8} \tag{2}$$

where the m_i matrices are shown in Fig. 2.

Step 2: The WMCF is calculated according to Eq. (3)

$$F(P) = d_m \tag{3}$$

where $m = \arg\min_i(|d_i|; i = \overline{1,8})$

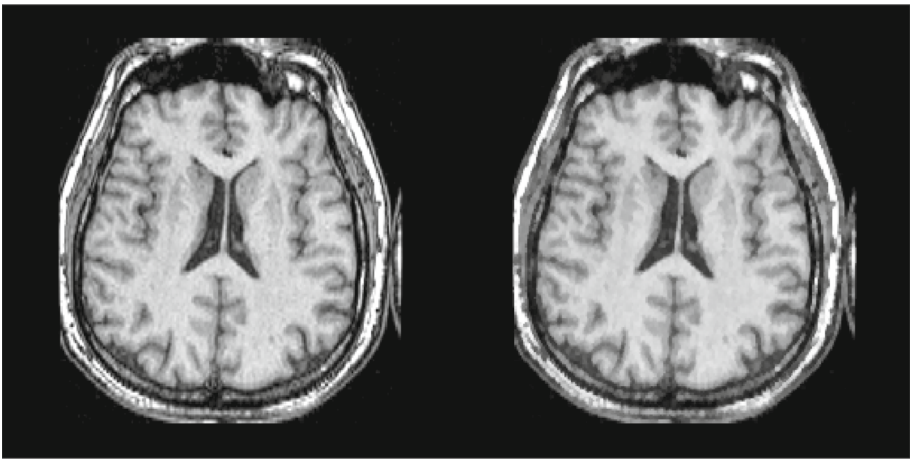

Fig. 1 The WMCF (input and output image)

$$m_1 = \begin{bmatrix} 1/6 & 1/6 & 0 \\ 1/3 & -1 & 0 \\ 1/6 & 1/6 & 0 \end{bmatrix} \quad m_2 = \begin{bmatrix} 1/6 & 1/3 & 1/6 \\ 1/6 & -1 & 1/6 \\ 0 & 0 & 0 \end{bmatrix} \quad m_3 = \begin{bmatrix} 0 & 1/6 & 1/6 \\ 0 & -1 & 1/3 \\ 0 & 1/6 & 1/6 \end{bmatrix} \quad m_4 = \begin{bmatrix} 0 & 0 & 0 \\ 1/6 & -1 & 1/6 \\ 1/6 & 1/3 & 1/6 \end{bmatrix}$$

$$m_5 = \begin{bmatrix} 1/6 & 1/3 & 1/12 \\ 1/3 & -1 & 0 \\ 1/12 & 0 & 0 \end{bmatrix} \quad m_6 = \begin{bmatrix} 1/12 & 1/3 & 1/6 \\ 0 & -1 & 1/3 \\ 0 & 0 & 1/12 \end{bmatrix} \quad m_7 = \begin{bmatrix} 0 & 0 & 1/12 \\ 0 & -1 & 1/3 \\ 1/12 & 1/3 & 1/6 \end{bmatrix} \quad m_8 = \begin{bmatrix} 1/12 & 0 & 0 \\ 1/3 & -1 & 0 \\ 1/6 & 1/3 & 1/12 \end{bmatrix}$$

Fig. 2 Masks of the MWCF

2.2 Two-component decomposition method

Image decomposition is an indispensable step in the image fusion process. Up to now, there have been many different approaches to image decomposition. For example, Maqsood and Javed (2020) have proposed a new medical image fusion method using Two-scale image decomposition. Some other studies can be mentioned as Du et al. (2020) and Wang et al. (2021a). Based on gaussian filter and WMC filter, we propose an image decomposition method as Al (1) (Figs. 1, 2). Figure 3 illustrates the decomposition of an input image into two components:

Algorithm 1: The two-component decomposition method

Input: An image (I_{in})
Output: Two components C_1 and C_2
Step 1: Apply the Gaussian filter for image I_{in} to obtain component (C_1).
Step 2: Apply the WMC filter for (C_1) to obtain an image (I_{wmc}).
Step 3: Component C_2 is determined as Eq. (4).

$$C_2 = I_{in} - I_{wmc} \tag{4}$$

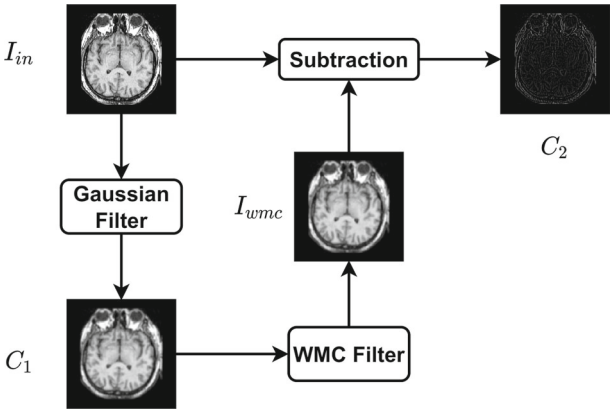

Fig. 3 Illustration for the two-component decomposition

2.3 YCbCr color space

The YCbCr model is commonly used in image processing applications. In particular, this color model has been used in medical image synthesis (Dinh 2021b)

The RGB-YCbCr transformation is represented by Eq. (5)

$$\begin{bmatrix} Yy \\ Cb \\ Cr \end{bmatrix} = \begin{bmatrix} 0.257 & 0.504 & 0.098 \\ -0.148 & -0.291 & 0.439 \\ 0.439 & -0.368 & -0.071 \end{bmatrix} \begin{bmatrix} Rr \\ Gg \\ Bb \end{bmatrix} + \begin{bmatrix} 16 \\ 128 \\ 128 \end{bmatrix} \tag{5}$$

YCbCr is converted to RGB as Eq. (6)

$$\begin{bmatrix} Rr \\ Gg \\ Bb \end{bmatrix} = \begin{bmatrix} 1.164 & 0.000 & 1.596 \\ 1.164 & -0.392 & -0.813 \\ 1.164 & 2.017 & 0.000 \end{bmatrix} \begin{bmatrix} Yy - 16 \\ Cb - 128 \\ Cr - 128 \end{bmatrix} \tag{6}$$

2.4 Structure tensor

The structure tensor is computed by the difference between the pixel values in the image. It is also an essential tool for obtaining image features. In recent times, the tensor structure has been utilized in many image processing applications, such as image fusion (Li et al. 2021c), extended focused imaging in microscopy (Ren et al. 2021), and corner detection (Wang et al. 2020a).

Given the image matrix I, we denote G_i and G_j as the gradient in the i direction, and j direction, respectively. The structure tensor is defined as Eq. (7).

$$ST = \begin{bmatrix} \sum_w G_i^2 & \sum_w G_i G_j \\ \sum_w G_i G_j & \sum_w G_j^2 \end{bmatrix} \tag{7}$$

where, w is a local window.

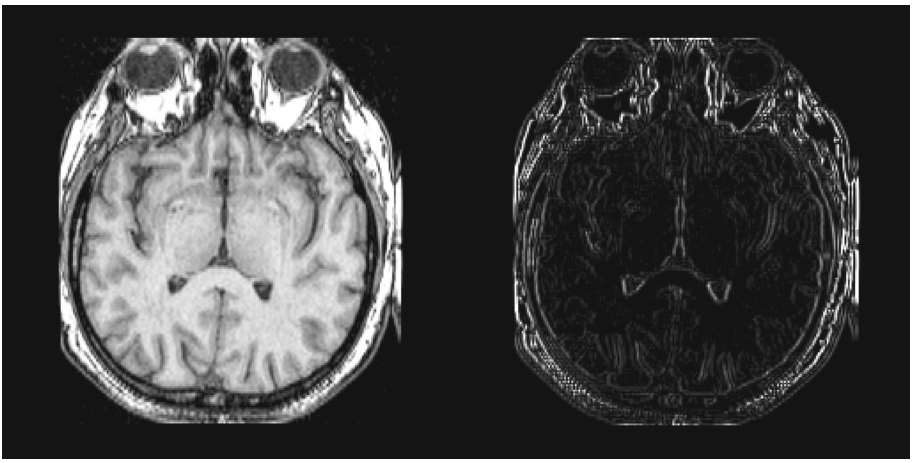

Fig. 4 Illustration for the image structure saliency S

In addition, the eigenvalues of the structure tensor provide more information about the local geometry of the input image. Eigenvalues can be calculated as Eqs. (8) and (9).

$$e_1 = \frac{1}{2}\left(\sum_w G_i^2 + \sum_w G_j^2 + \sqrt{\left(\sum_w G_i^2 - \sum_w G_j^2\right)^2 + 4\left(\sum_w G_i G_j\right)^2}\right) \tag{8}$$

$$e_2 = \frac{1}{2}\left(\sum_w G_i^2 + \sum_w G_j^2 - \sqrt{\left(\sum_w G_i^2 - \sum_w G_j^2\right)^2 + 4\left(\sum_w G_i G_j\right)^2}\right) \tag{9}$$

The structure tensor salient detection operator can be defined as the Eq. (10) (Fig. 4)

$$S = \sqrt{(e_1 + e_2)^2 + 0.5\,(e_1 - e_2)^2} \tag{10}$$

Figure 4 illustrates an input image and the corresponding STS component.

2.5 Local energy using structure tensor saliency

Sharp images provide higher local energy than blurry images. Therefore, some recent studies have used the local energy (LE) function for image fusion. For example, Polinati and Dhuli (2020) have proposed a new image fusion method using maximum local energy. Another study used LE as Dinh (2021d).

Given the image matrix I, let W be a unit window of size $m \times n$. The local energy $LE(i, j)$ function is defined according to the Eq. (11).

$$LE(i, j) = \sum_{p_1=0}^{m-1} \sum_{p_2=0}^{m-1} W(p_1, p_2) * I^2(i + p_1, j + p_2) \tag{11}$$

The local energy using structure tensor saliency is defined according to the Eq. (12).

$$LE\_STS(i,j) = \sum_{p_1=0}^{m-1}\sum_{p_2=0}^{m-1} S(p_1,p_2) * I^2(i+p_1, j+p_2) \tag{12}$$

where S is the structure tensor saliency detection operator as the Eq. (10).

2.6 MPA algorithm

Faramarzi et al. (2020) introduced MPA in 2020. See details in Algorithm (2). The three main stages of the algorithm can be described as follows:

Stage 1: Stepsize (S) and Prey (P) are computed in a third of the loop as Eqs (13) and (14).

$$S(u,v) = B(u,v) \otimes (F(u,v) - B(u,v) \otimes P(u,v)) \tag{13}$$

$$P(u,v) = P(u,v) + H.R \otimes S(u,v) \tag{14}$$

where

- R in [0,1].
- H = 0.5.
- $\otimes$ is denoted for entry-wise multiplications.
- $\overrightarrow{B}$ is randomly selected from Brownian motion.
- $F(u,v)$ contains the fitness solution.

Stage 2: Stepsize (S) and Prey (P) are calculated in the next third of the loop as Eqs (15), (16), (17), and (18).

For the first half of the population:

$$S(u,v) = R_L(u,v) \otimes (F(u,v) - R_L(u,v) \otimes P(u,v)) \tag{15}$$

$$P(u,v) = P(u,v) + H.R \otimes S(u,v) \tag{16}$$

For the second half of the population:

$$S(u,v) = B(u,v) \otimes (B(u,v) \otimes F(u,v) - P(u,v)) \tag{17}$$

$$P(u,v) = F(u,v) + H.AP \otimes S(u,v); \tag{18}$$

where

- $AP = (1 - \frac{l}{l_{max}})^{\frac{2*l}{l_{max}}}$.

Stage 3: Stepsize (S) and Prey (P) are computed in the last third of the loop as Eqs. (19) and (20).

$$S(u,v) = R_L(u,v) \otimes (R_L(u,v) \otimes F(u,v) - P(u,v)) \tag{19}$$

$$P(u,v) = F(u,v) + H.AP \otimes S(u,v) \tag{20}$$

- $\overrightarrow{R_L}$ is generated from the *Lévy* distribution.

Algorithm 2: MPA algorithm

Initialize the population ($i = \overline{1, n}$), matrix F and Prey (P).
Assign parameters: $H = 0.5$; $FADs = 0.2$; r in [0,1];
while $l < l_{max}$ **do**
  /* Stage 1: */
  if $l < \frac{1}{3} l_{max}$ **then**
    Update prey according to Eq. (14);
  end
  /* Stage 2: */
  else if $(l > \frac{1}{3} l_{max})$ *and* $(l < \frac{2}{3} l_{max})$ **then**
    For the first half of the population.
    Update prey according to Eq. (16);
    For the second half of the population.
    Update prey according to Eq. (18);
  end
  /* Stage 3: */
  else if $l > \frac{2}{3} l_{max}$ **then**
    Update prey according to Eq. (20);
  end
  /* Eddy formation and FADs' effect */
  if $(r \leq FADs)$ **then**
    $P(u, v) = P(u, v) + AP * ((X_{min} + R \otimes (X_{max} - X_{min})) \otimes U)$
  end
  else if $(r > FADs)$ **then**
    $S(u, v) = (FADs * (1 - r) + r) * (P_{r1}(u, v) - P_{r2}(u, v))$;
    $P(u, v) = P(u, v) + S(u, v)$;
  end
  $l = l + 1$
end

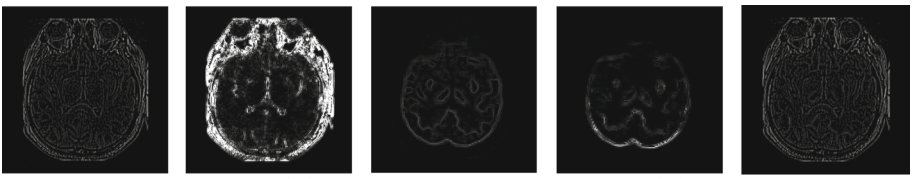

Fig. 5 Illustration for the MLE_MSTS method

3 Proposed approach

In this section, we introduce two algorithms. The first algorithm is a fusion rule based on maximum local energy using structure tensor saliency (MLE_STS). The second algorithm is designed to fuse LFCs.

3.1 MLE_STS

In subsection, MLE_STS is presented in detail as algorithm (3)

Figure 5 illustrates the use of the MLE_STS method.

Algorithm 3: MLE_STS

Input: Components (C_1, C_2)
Output: C_3

Step 1: From components (C_1, C_2), compute the Local energy functions using the structure tensor saliency (LE_STS^1, LE_STS^2) according to Sect. 2.5 as the Eqs. (21) and (22).

$$LE\_STS^1(i,j) = \sum_{p_1=0}^{m-1}\sum_{p_2=0}^{m-1} S_1(p_1,p_2) * C_1^2(i+p_1, j+p_2) \tag{21}$$

$$LE\_STS^2(i,j) = \sum_{p_1=0}^{m-1}\sum_{p_2=0}^{m-1} S_2(p_1,p_2) * C_2^2(i+p_1, j+p_2) \tag{22}$$

where S_1 and S_2 are the structure tensor saliency of C_1 and C_2, respectively.

Step 2: The proposed fusion rule can be calculated as the Eq. (23).

$$C_3(i,j) = \begin{cases} C_1(i,j) & \text{if } |LE\_STS^1(i,j)| \geq |LE\_STS^2(i,j)| \\ C_2(i,j) & \text{if } |LE\_STS^1(i,j)| < |LE\_STS^2(i,j)| \end{cases} \tag{23}$$

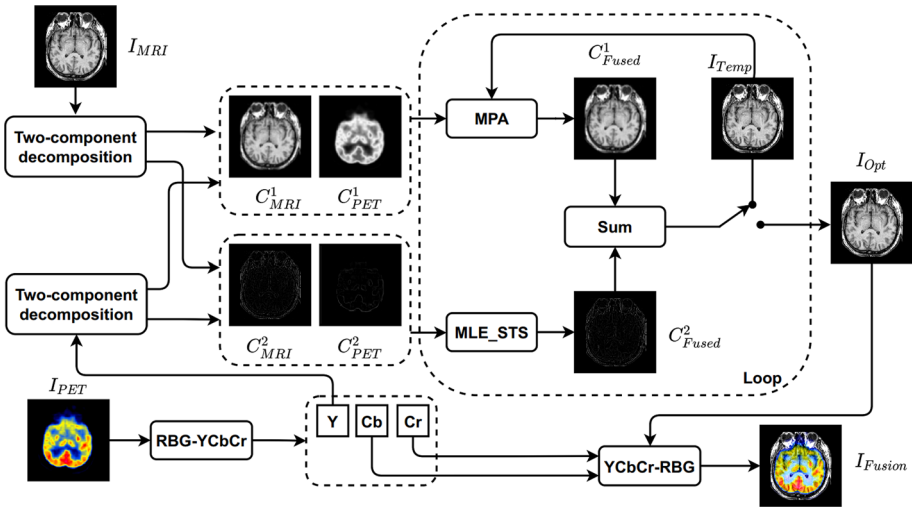

Fig. 6 The diagram of our approach

3.2 The proposed approach using MLE_STS and MPA

We describe some of the main steps in our algorithm as follows. Firstly, color image I_{PET} is transformed to YCbCr color space. Secondly, the TCD method is used to decompose images I_{MRI} and Y into low and high frequency components. Then, the MLE_STS method is utilized for HFCs, and the MPA algorithm is used to fuse LFCs. Finally, the fused components are summed to obtain a gray composite image (I_{opt}). Use the 3 channels I_{opt}, Cb, and Cr to convert to RGB. See details of the proposed algorithm in Fig. 6.

Algorithm 4: The proposed approach

Input: $I_{MRI}, I_{PET}(S \times T)$.
Output: I_{Fusion}
Step 1: Convert image I_{PET} to YCbCr model into Y, Cb, and Cr.
Step 2: The TCD method is used to decompose I_{MRI} and Y into the components (C^1_{MRI}, C^2_{MRI}) and (C^1_{PET}, C^2_{PET}), respectively.
Step 3: C^2_{MRI} and C^2_{PET} are synthesized by the MLE_STS method (See algorithm 3).

$$C^2_{Fused} = MLE\_STS(C^2_{MRI}, C^2_{PET}) \tag{24}$$

Step 4: C^1_{MRI} and C^1_{PET} are synthesized by the MPA with optimal parameters ($\psi_1 \in [0.5, 1]$, $\psi_2 \in [0, 0.5]$, and $\psi_3 \in [0.9, 1]$) as Eq. (25).

$$C^1_{Fused} = \psi_1 * C^1_{MRI} + \psi_2 * C^1_{PET} \tag{25}$$

A fitness function F_O is calculated according to Eq. (26).

$$F_O = \frac{\mu_{Temp}}{\sigma^2_{Temp}} * (E_{Temp} - E_{MRI}) * (E_{Temp} - E_{PET}) * MSE \tag{26}$$

Where $MSE(I_{MRI}, I_{Temp})$, $MSE(Y, I_{Temp})$, and MSE are calculated as Eqs. (27), (28), and (29), respectively.

$$MSE(I_{MRI}, I_{Temp}) = \frac{1}{S * T} \sum_{x=1}^{S} \sum_{y=1}^{T} (I_{Temp}(x, y) - I_{MRI}(x, y))^2 \tag{27}$$

$$MSE(Y, I_{Temp}) = \frac{1}{S * T} \sum_{x=1}^{S} \sum_{y=1}^{T} (I_{Temp}(x, y) - Y(x, y))^2 \tag{28}$$

$$MSE = \psi_3 * MSE(I_{MRI}, I_{Temp}) + (1 - \psi_3) * MSE(Y, I_{Temp}) \tag{29}$$

μ_{Temp} and σ^2_{Temp} are mean and variance of the temporary fused image I_{Temp} ($I_{Temp} = C^1_{Fused} + C^2_{Fused}$) in each iteration of the MPA algorithm. E_{MRI}, E_{PET}, and E_{Temp} are the Entropy of I_{MRI}, Y, and I_{Temp}, respectively.

Step 5: if $C^1_{Fused}(i, j) > 1$ then update $C^1_{Fused}(i, j) > 1$ as Eq. (30)

$$C^1_{Fused}(i, j) = Max(C^1_{MRI}(i, j), C^1_{PET}(i, j)) \tag{30}$$

Step 6: I_{Opt} is obtained at the end of the loop of MPA algorithm.
Step 7: The YCbCr-RGB transformation is utilized to convert I_{Opt}, Cb, and Cr to RGB model to obtain I_{Fusion}.

4 Experiments and results

4.1 Evaluation indexes

We choose some of the following evaluation indexes:

– Average luminous intensity (ALI).

– Sharpness.
– $Q^{AB/F}$ (Xydeas and Petrovic 2000) (Edge-based similarity measure).
– Visual Information Fidelity for Fusion (VIFF) (Han et al. 2013).
– Feature Mutual Information (FMI) (Haghighat et al. 2011).

4.2 Experimental setup

Experimental data (Ds) consists of 3 Groups (75 pairs of MRI and PET images, 256 × 256), namely Ds1, Ds2, and Ds3. Each group has 25 pairs of MRI-PET images collected according to the T, S, and C coordinate axes from 60th to 84th slices, respectively (see Fig. 7 for details). The source images have the address as follows: http://www.med.harvard.edu/AANLIB/. We carry out some experiments as follows:

Experiment #1: To explain why the MPA is selected in our model, we used other optimization algorithms for comparison. They are Ant Lion Optimizer (ALO) (Mirjalili 2015), Multi-Verse Optimizer (MVO) (Mirjalili et al. 2015), Salp swarm algorithm (SSA) (Mirjalili et al. 2017), Sine cosine algorithm (SCA) (Mirjalili 2016), and Grey wolf optimizer (GWO) (Mirjalili and Lewis 2016). Each optimization algorithm is run with 35 different times on the data set X (X1, X2, and X3 using the 82th brain slice). Two evaluation indexes (Average and Standard deviation) are used to evaluate. Additionally, to determine the significance of the results, we have use the Wilcoxon rank-sum test (Wilcoxon 1945)

Experiment #2: To test the effectiveness of the MLE_STS method, some fusion rules are used to compare.

– Max selection rule (MSR).
– MLE (Polinati and Dhuli 2020).
– PA-PCNN (Yin et al. 2019).
– Sum-modified Laplacian (SML) (Li et al. 2019).

In addition, some evaluation indexes in this experiment are selected as follows:

– $Q^{AB/F}$ (Xydeas and Petrovic 2000).
– VIFF (Han et al. 2013).
– FMI (Haghighat et al. 2011).

Experiment #3: To test the efficiency of our model, we use some of the latest algorithms used to compare.

– Convolutional sparse representation (CSR) (A1) (Liu et al. 2016).
– Phase Congruency and Local Laplacian Energy in NSCT domain (PC-LLE-NSCT) (A2) (Zhu et al. 2019).
– Multi-scale morphological gradient with Parameter-Adaptive PCNN in NSST domain (NSST-PAPCNN) (A3) (Yin et al. 2019).
– Multi-level curvature filtering and Multi-level morphological gradient with PCNN (MLCF-MLMG-PCNN) (A4) (Tan et al. 2021).
– Multi-scale morphological gradient with PCNN in NSST domain (NSST-MSMG-PCNN) (A5) (Tan et al. 2020).

In addition, five indexes were utilized to evaluate in this experiment.

– ALI.
– Sharpness.
– $Q^{AB/F}$ (Xydeas and Petrovic 2000).

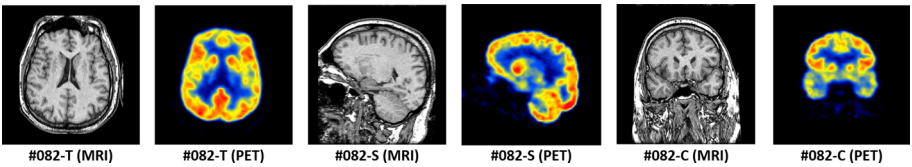

Fig. 7 Three pairs of RMI and PET images in the dataset

Table 1 Optimal parameters on the dataset (Ds1, Ds2, and Ds3)

Dataset	ψ_1	ψ_2	ψ_3
Ds1	0.9921	0.0113	0.999
Ds2	0.9928	0.0148	0.999
Ds3	0.9939	0.0174	0.999

– VIFF (Han et al. 2013).
– FMI (Haghighat et al. 2011).

The proposed algorithm is implemented with the following parameters in MPA algorithm:

– n = 100.
– H = 0.5; FADs = 0.2; r in [0,1]
– $l_{max} = 100$.

4.3 Experimental results and evaluation

In this subsection, the results of the experiments are described and evaluated.

Firstly, the three optimal parameters (ψ_1, ψ_2, and ψ_3) of our model are shown in Table 1. Seventy-five images in dataset Ds were used for this experiment.

Secondly, the two indexes the average and SD from the MPA algorithm are shown in from Table 2, and they are the lowest. This result explains why MPA was chosen. Moreover, the P values from the Wilcoxon rank-sum test are less than 0.05 in Table 3, so the results are statistically significant.

Thirdly, from Table 4, it is easy to see that the indexes $Q^{AB/F}$, VIFF, and FMI obtained from the MLE_STS method are the highest in the proposed approach. This experiment shows that the MLE_STS method is effective in fusing HFCs.

Fourthly, from the Figs. (8, 9, 10) and Table 5, it is clear that the evaluation indexes obtained from the proposed model are better than those obtained from other methods. For example, from Table 5 (Dr1), the ALI of our algorithm was highest, at 0.3324, whereas the figures for other algorithms (CSR (Liu et al. 2016), PC-LLE-NSCT (Zhu et al. 2019), NSST-PA-PCNN (Yin et al. 2019), MLCF-MLMG-PCNN (Tan et al. 2021), and NSST-MSMG-PCNN (Tan et al. 2020)) were lower, at 0.1497, 0.2781, 0.3026, 0.3305, and 0.329, respectively (See Figs. 11, 12, 13 for details).

Finally, to observe the preservation of detailed information contained in the fused images. We cut out a small frame from Figs. 8, 9, and 10 and illustrated them in Figs. 14, 15, and 16, respectively. From Table 5 (Dr3), the $Q^{AB/F}$ index of our algorithm is highest, at 0.8074. Whereas, the figures for methods CSR (Liu et al. 2016), PC-LLE-NSCT (Zhu et al. 2019), NSST-PA-PCNN (Yin et al. 2019), MLCF-MLMG-PCNN (Tan et al. 2021), and NSST-MSMG-PCNN (Tan et al. 2020) were lower, at 0.7094, 0.7546, 0.7502, 0.6745, and 0.6969, respectively. The rest of the evaluation indexes of our model also give better results.

Table 2 Average and SD from 35 different runs

Dataset	Algorithms	Average	SD
X1	**MPA**	**0.001045069482186**	**7.8865e−10**
	ALO	0.001045065146217	1.1160e−08
	MVO	0.001043353669553	6.1600e−07
	SSA	0.001044907125398	3.4989e−07
	SCA	0.001043262980341	1.6351e−06
	GWO	0.001044841186553	1.8571e−07
X2	**MPA**	**0.002999522924040**	**7.0180e−11**
	ALO	0.002999521985754	9.6789e−10
	MVO	0.002992648090986	5.7196e−06
	SSA	0.002916124816694	6.8436e−05
	SCA	0.002994891903872	5.3113e−06
	GWO	0.002998561333884	5.2606e−07
X3	**MPA**	**0.001285451119160**	**4.9965e−11**
	ALO	0.001285450425079	7.5165e−10
	MVO	0.001280786748468	2.4750e−06
	SSA	0.001252934970035	3.4697e−05
	SCA	0.001281482798699	3.7760e−06
	GWO	0.001284208487318	7.1169e−07

Bold values indicate two indexes (average and st) obtained from the MPA algorithm are the smallest

Table 3 *P* values from a non-parametric statistical test

Dataset	Algorithms	*P* values
X1	MPA versus ALO	3.3779e−05
	MPA versus MVO	6.5455e−13
	MPA versus SSA	1.5374e−10
	MPA versus SCA	6.4855e−13
	MPA versus GWO	6.5455e−13
X2	MPA versus ALO	6.5455e−13
	MPA versus MVO	6.5455e−13
	MPA versus SSA	6.5455e−13
	MPA versus SCA	6.5455e−13
	MPA versus GWO	6.5455e−13
X3	MPA versus ALO	8.8245e−12
	MPA versus MVO	6.5455e−13
	MPA versus SSA	3.7121e−09
	MPA versus SCA	6.5455e−13
	MPA versus GWO	6.5455e−13

Table 4 Experimental results by some fusion rules

Dataset	Fusion rules	$Q^{AB/F}$	VIFF	FMI
Dr1	Max selection	0.6423	0.5898	0.8576
	MLE	0.7345	0.6376	0.8689
	PA-PCNN	0.7467	0.6479	0.8694
	SML	0.7574	0.6483	0.8768
	MLE-STS	**0.7886**	**0.6959**	**0.8894**
Dr2	Max selection	0.6567	0.5739	0.8595
	MLE	0.7367	0.6378	0.8698
	PA-PCNN	0.7476	0.6489	0.8693
	SML	0.7587	0.6489	0.8785
	MLE-STS	**0.7975**	**0.6884**	**0.8867**
Dr3	Max selection	0.6446	0.5797	0.8285
	MLE	0.7356	0.6367	0.8368
	PA-PCNN	0.7578	0.6359	0.8386
	SML	0.7591	0.6487	0.8495
	MLE-STS	**0.8074**	**0.6692**	**0.8664**

Bold values indicate the evaluation indexes obtained from the proposed algorithm are the largest (best)

Table 5 Experimental results on the datasets (Dr1, Dr2, and Dr3)

Dataset	Methods	ALI	S	$Q^{AB/F}$	VIFF	FMI
Dr1	CSR	0.1497	0.0522	0.6449	0.1898	0.8413
	PC-LLE-NSCT	0.2781	0.0715	0.6742	0.5745	0.8720
	NSST-PAPCNN	0.3026	0.0709	0.6730	0.5869	0.8714
	MLCF-MLMG-PCNN	0.3305	0.0655	0.6028	0.4792	0.8596
	NSST-MSMG-PCNN	0.3229	0.0747	0.6557	0.6121	0.8595
	Proposed method	**0.3324**	**0.0798**	**0.7886**	**0.6959**	**0.8894**
Dr2	CSR	0.1689	0.0619	0.6599	0.1824	0.8276
	PC-LLE-NSCT	0.3233	0.0826	0.0827	0.7053	0.8689
	NSST-PAPCNN	0.3440	0.0818	0.7066	0.5929	0.8686
	MLCF-MLMG-PCNN	0.3485	0.0775	0.6081	0.4819	0.8477
	NSST-MSMG-PCNN	0.3402	0.0865	0.6632	0.6194	0.8528
	Proposed method	**0.3578**	**0.0897**	**0.7975**	**0.6884**	**0.8867**
Dr3	CSR	0.1554	0.0785	0.7094	0.1887	0.8127
	PC-LLE-NSCT	0.2849	0.1004	0.7546	0.5705	0.8547
	NSST-PAPCNN	0.3049	0.0999	0.7502	0.5855	0.8536
	MLCF-MLMG-PCNN	0.2961	0.0982	0.6745	0.4570	0.8369
	NSST-MSMG-PCNN	0.2869	0.1040	0.6969	0.5733	0.8389
	Proposed method	**0.3235**	**0.1058**	**0.8074**	**0.6692**	**0.8664**

Bold values indicate the evaluation indexes obtained from the proposed algorithm are the largest (best)

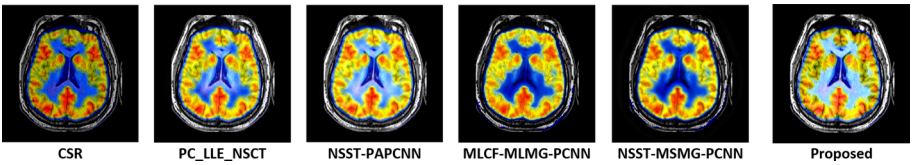

Fig. 8 The fused images from different methods

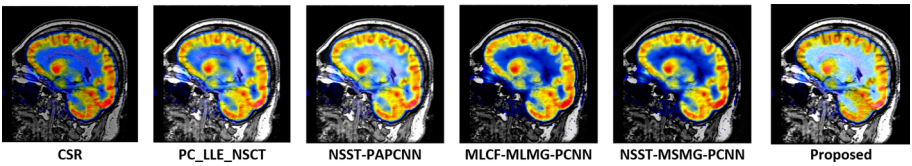

Fig. 9 The fused images from different methods

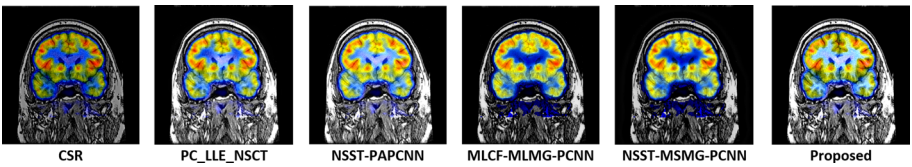

Fig. 10 The fused images different methods

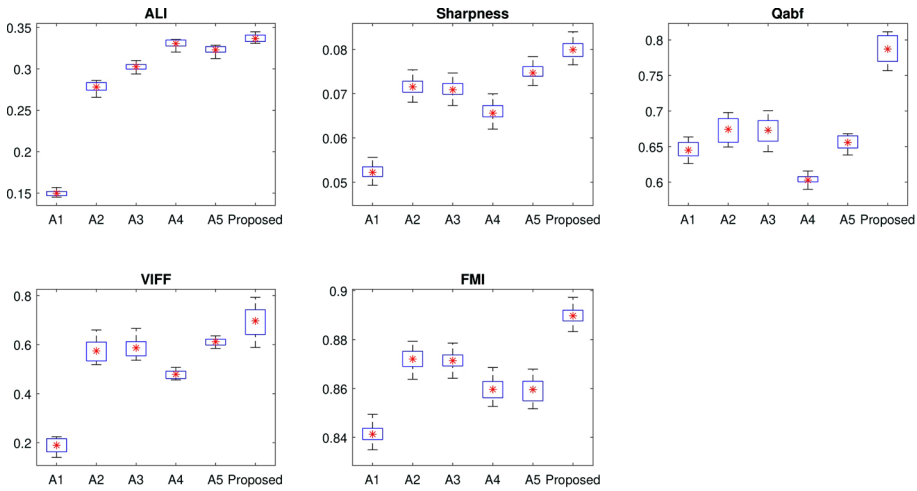

Fig. 11 Evaluation indexes from six algorithms on the dataset ("Dr1")

5 Conclusion

This paper introduces an efficient model for the synthesis of medical images. A method of synthesizing LFCs is based on the MPA optimization algorithm. A synthesis method for HFCs is based on maximum LE function using structure tensor saliency.

The experiments were carried out to test the effectiveness of the proposed model. Five evaluation indexes and five image synthesis algorithms were used for comparison. The exper-

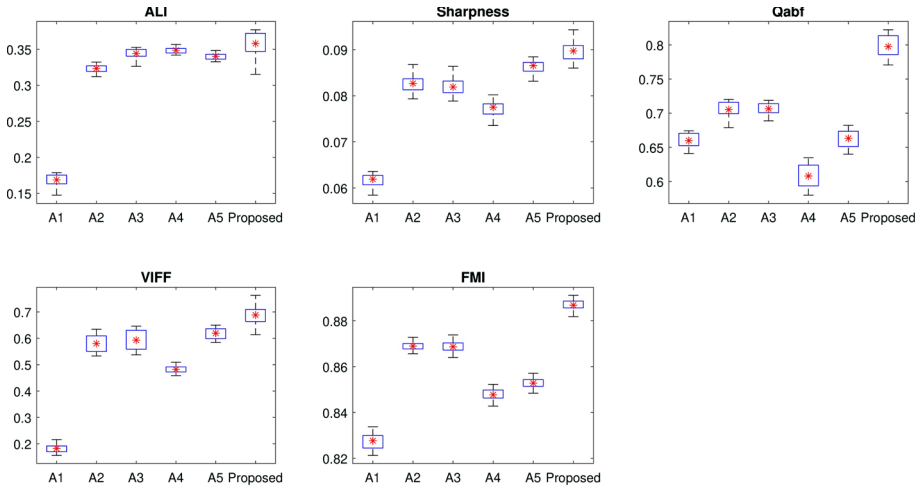

Fig. 12 Evaluation indexes from six algorithms on the dataset ("Dr2")

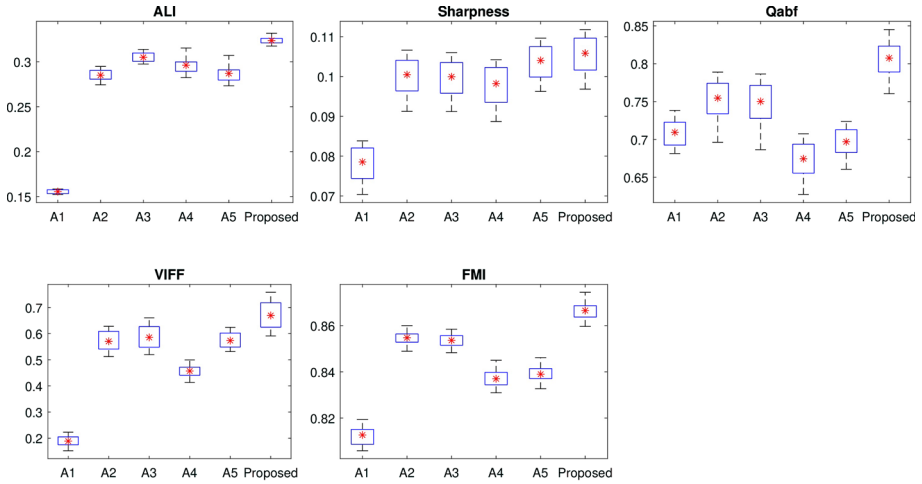

Fig. 13 Evaluation indexes from six algorithms on the dataset ("Dr3")

imental results show that our proposed method is effective in synthesizing medical images. However, the limitation of the proposed algorithm is the running time. When the number of populations and loops is large, the proposed approach can be time-consuming.

In the future, some remaining problems can be focused on solving. Firstly, we intend to propose an algorithm to improve input image quality because the input images are usually low quality, such as low-contrast, blur, and noise. For example, the enhancement of image quality to improve the performance of the synthesis has also been applied in some recent studies such as Maqsood and Javed (2020). Secondly, to ensure that the information in the input image is preserved when decomposing images, we intend to choose recently proposed image decomposition algorithms such as Xing et al. (2020).

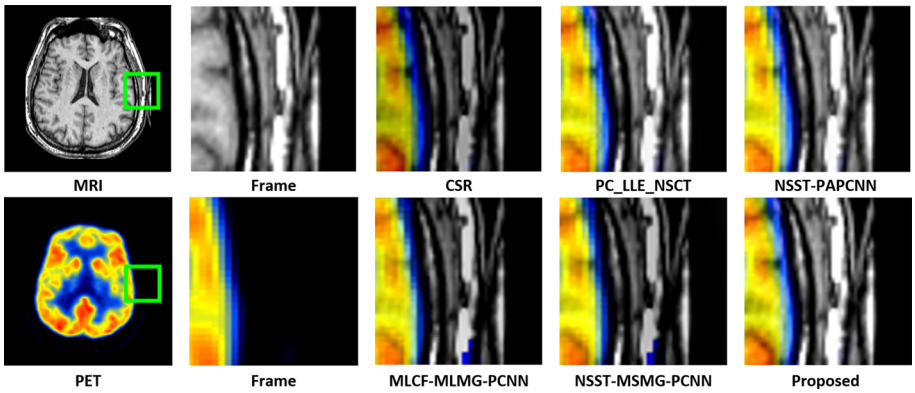

Fig. 14 Frames from the fused images in Fig. 8

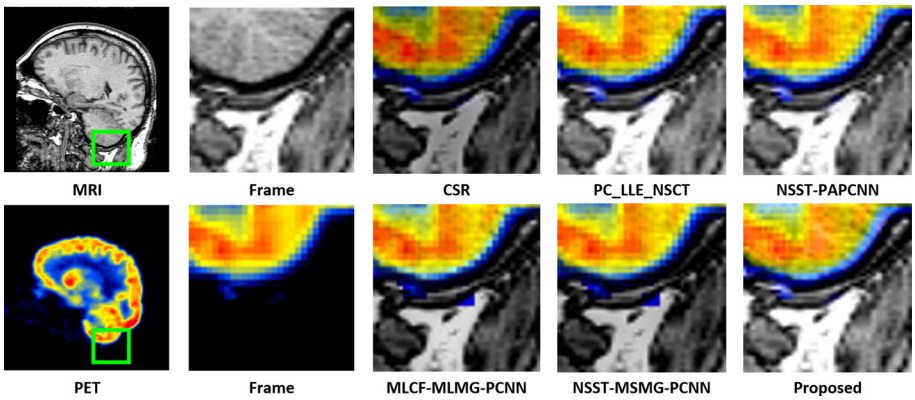

Fig. 15 Frames from the fused images in Fig. 9

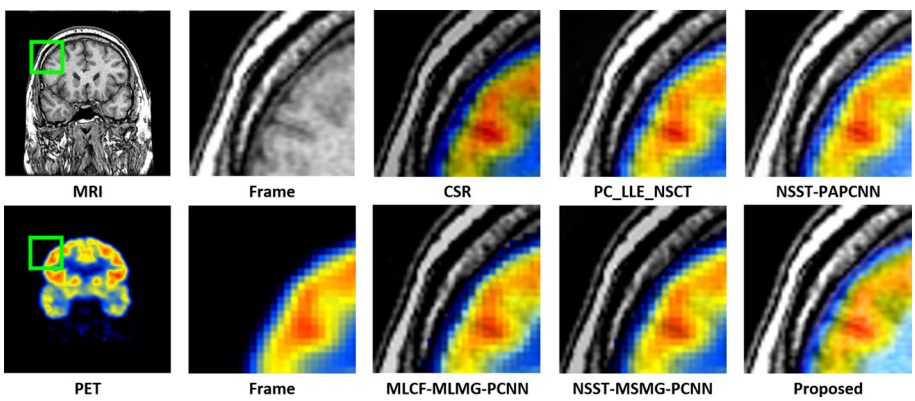

Fig. 16 Frames from the fused images in Fig. 10

Acknowledgements This research is funded by Thuyloi University Foundation for Science and Technology under grant number TLU.STF.21-03.

Declarations

Conflict of interest The authors declare that they have no competing interests.

References

Abdel-Basset, M., Mohamed, R., Elhoseny, M., Chakrabortty, R. K., & Ryan, M. (2020). A hybrid COVID-19 detection model using an improved marine predators algorithm and a ranking-based diversity reduction strategy. *IEEE Access, 8,* 79521–79540. https://doi.org/10.1109/access.2020.2990893.

Barba-J, L., Vargas-Quintero, L., & Calderón-Agudelo, J. A. (2022). Bone SPECT/CT image fusion based on the discrete hermite transform and sparse representation. *Biomedical Signal Processing and Control, 71,* 103096. https://doi.org/10.1016/j.bspc.2021.103096.

Daniel, E., Anitha, J., Kamaleshwaran, K., & Rani, I. (2017). Optimum spectrum mask based medical image fusion using gray wolf optimization. *Biomedical Signal Processing and Control, 34,* 36–43. https://doi.org/10.1016/j.bspc.2017.01.003.

Ding, Z., Zhou, D., Nie, R., Hou, R., & Liu, Y. (2020). Brain medical image fusion based on dual-branch CNNs in NSST domain. *BioMed Research International, 2020,* 1–15. https://doi.org/10.1155/2020/6265708.

Ding, Z., Zhou, D., Li, H., Hou, R., & Liu, Y. (2021). Siamese networks and multi-scale local extrema scheme for multimodal brain medical image fusion. *Biomedical Signal Processing and Control, 68,* 102697. https://doi.org/10.1016/j.bspc.2021.102697.

Dinh, P. H. (2021). Combining Gabor energy with equilibrium optimizer algorithm for multi-modality medical image fusion. *Biomedical Signal Processing and Control, 68,* 102696. https://doi.org/10.1016/j.bspc.2021.102696.

Dinh, P. H. (2021). An improved medical image synthesis approach based on marine predators algorithm and maximum Gabor energy. *Neural Computing and Applications*. https://doi.org/10.1007/s00521-021-06577-4.

Dinh, P. H. (2021). Multi-modal medical image fusion based on equilibrium optimizer algorithm and local energy functions. *Applied Intelligence*. https://doi.org/10.1007/s10489-021-02282-w.

Dinh, P. H. (2021). A novel approach based on grasshopper optimization algorithm for medical image fusion. *Expert Systems with Applications, 171,* 114576. https://doi.org/10.1016/j.eswa.2021.114576.

Dinh, P. H. (2021). A novel approach based on three-scale image decomposition and marine predators algorithm for multi-modal medical image fusion. *Biomedical Signal Processing and Control, 67,* 102536. https://doi.org/10.1016/j.bspc.2021.102536.

Du, J., Li, W., Xiao, B., & Nawaz, Q. (2016). Union Laplacian pyramid with multiple features for medical image fusion. *Neurocomputing, 194,* 326–339. https://doi.org/10.1016/j.neucom.2016.02.047.

Du, J., Li, W., & Tan, H. (2020). Three-layer image representation by an enhanced illumination-based image fusion method. *IEEE Journal of Biomedical and Health Informatics, 24*(4), 1169–1179. https://doi.org/10.1109/jbhi.2019.2930978.

Fang, H., Zhu, G., Stojanovic, V., Nie, R., He, S., Luan, X., & Liu, F. (2021). Adaptive optimization algorithm for nonlinear Markov jump systems with partial unknown dynamics. *International Journal of Robust and Nonlinear Control, 31*(6), 2126–2140. https://doi.org/10.1002/rnc.5350.

Faramarzi, A., Heidarinejad, M., Mirjalili, S., & Gandomi, A. H. (2020). Marine predators algorithm: A nature-inspired metaheuristic. *Expert Systems with Applications, 152,* 113377. https://doi.org/10.1016/j.eswa.2020.113377.

Fu, J., Li, W., Du, J., & Xiao, B. (2020). Multimodal medical image fusion via Laplacian pyramid and convolutional neural network reconstruction with local gradient energy strategy. *Computers in Biology and Medicine, 126,* 104048. https://doi.org/10.1016/j.compbiomed.2020.104048.

Gao, Y., Ma, S., Liu, J., Liu, Y., & Zhang, X. (2021). Fusion of medical images based on salient features extraction by PSO optimized fuzzy logic in NSST domain. *Biomedical Signal Processing and Control, 69,* 102852. https://doi.org/10.1016/j.bspc.2021.102852.

Gong, Y., & Goksel, O. (2019). Weighted mean curvature. *Signal Processing, 164,* 329–339. https://doi.org/10.1016/j.sigpro.2019.06.020.

Guo, K., Hu, X., & Li, X. (2021). MMFGAN: A novel multimodal brain medical image fusion based on the improvement of generative adversarial network. *Multimedia Tools and Applications*. https://doi.org/10.1007/s11042-021-11822-y.

Haghighat, M. B. A., Aghagolzadeh, A., & Seyedarabi, H. (2011). A non-reference image fusion metric based on mutual information of image features. *Computers & Electrical Engineering, 37,* 744–756. https://doi.org/10.1016/j.compeleceng.2011.07.012.

Han, Y., Cai, Y., Cao, Y., & Xu, X. (2013). A new image fusion performance metric based on visual information fidelity. *Information Fusion, 14,* 127–135. https://doi.org/10.1016/j.inffus.2011.08.002.

Hu, Q., Hu, S., & Zhang, F. (2021). Multi-modality image fusion combining sparse representation with guidance filtering. *Soft Computing, 25*(6), 4393–4407. https://doi.org/10.1007/s00500-020-05448-9.

Jose, J., Gautam, N., Tiwari, M., Tiwari, T., Suresh, A., Sundararaj, V., & Rejeesh, M. R. (2021). An image quality enhancement scheme employing adolescent identity search algorithm in the NSST domain for multimodal medical image fusion. *Biomedical Signal Processing and Control, 66,* 102480. https://doi.org/10.1016/j.bspc.2021.102480.

Li, Q., Wang, W., Chen, G., & Zhao, D. (2021). Medical image fusion using segment graph filter and sparse representation. *Computers in Biology and Medicine, 131,* 104239. https://doi.org/10.1016/j.compbiomed.2021.104239.

Li, W., Peng, X., Fu, J., Wang, G., Huang, Y., & Chao, F. (2021). A multiscale double-branch residual attention network for anatomical-functional medical image fusion. *Computers in Biology and Medicine, 141,* 105005. https://doi.org/10.1016/j.compbiomed.2021.105005.

Li, X., Zhang, X., & Ding, M. (2019). A sum-modified-Laplacian and sparse representation based multimodal medical image fusion in Laplacian pyramid domain. *Medical & Biological Engineering & Computing, 57*(10), 2265–2275. https://doi.org/10.1007/s11517-019-02023-9.

Li, X., Zhou, F., Tan, H., Zhang, W., & Zhao, C. (2021). Multimodal medical image fusion based on joint bilateral filter and local gradient energy. *Information Sciences, 569,* 302–325. https://doi.org/10.1016/j.ins.2021.04.052.

Li, Y., Sun, Y., Huang, X., Qi, G., Zheng, M., & Zhu, Z. (2018). An image fusion method based on sparse representation and sum modified-Laplacian in NSCT domain. *Entropy, 20*(7), 522. https://doi.org/10.3390/e20070522.

Liu, X., Mei, W., & Du, H. (2018). Multi-modality medical image fusion based on image decomposition framework and nonsubsampled Shearlet transform. *Biomedical Signal Processing and Control, 40,* 343–350. https://doi.org/10.1016/j.bspc.2017.10.001.

Liu, Y., Chen, X., Ward, R. K., & Wang, Z. J. (2016). Image fusion with convolutional sparse representation. *IEEE Signal Processing Letters, 23*(12), 1882–1886. https://doi.org/10.1109/lsp.2016.2618776.

Liu, Y., Chen, X., Ward, R. K., & Wang, Z. J. (2019). Medical image fusion via convolutional sparsity based morphological component analysis. *IEEE Signal Processing Letters, 26,* 485–489. https://doi.org/10.1109/lsp.2019.2895749.

Maqsood, S., & Javed, U. (2020). Multi-modal medical image fusion based on two-scale image decomposition and sparse representation. *Biomedical Signal Processing and Control, 57,* 101810. https://doi.org/10.1016/j.bspc.2019.101810.

Mirjalili, S. (2015). The ant lion optimizer. *Advances in Engineering Software, 83,* 80–98. https://doi.org/10.1016/j.advengsoft.2015.01.010.

Mirjalili, S. (2016). SCA: A sine cosine algorithm for solving optimization problems. *Knowledge-Based Systems, 96,* 120–133. https://doi.org/10.1016/j.knosys.2015.12.022.

Mirjalili, S., & Lewis, A. (2016). The whale optimization algorithm. *Advances in Engineering Software, 95,* 51–67. https://doi.org/10.1016/j.advengsoft.2016.01.008.

Mirjalili, S., Mirjalili, S. M., & Hatamlou, A. (2015). Multi-verse optimizer: A nature-inspired algorithm for global optimization. *Neural Computing and Applications, 27*(2), 495–513. https://doi.org/10.1007/s00521-015-1870-7.

Mirjalili, S., Gandomi, A. H., Mirjalili, S. Z., Saremi, S., Faris, H., & Mirjalili, S. M. (2017). Salp swarm algorithm: A bio-inspired optimizer for engineering design problems. *Advances in Engineering Software, 114,* 163–191. https://doi.org/10.1016/j.advengsoft.2017.07.002.

Nair, R. R., & Singh, T. (2021). MAMIF: Multimodal adaptive medical image fusion based on b-spline registration and non-subsampled shearlet transform. *Multimedia Tools and Applications, 80*(12), 19079–19105. https://doi.org/10.1007/s11042-020-10439-x.

Nair, R. R., & Singh, T. (2021). An optimal registration on shearlet domain with novel weighted energy fusion for multi-modal medical images. *Optik, 225,* 165742. https://doi.org/10.1016/j.ijleo.2020.165742.

Polinati, S., & Dhuli, R. (2020). Multimodal medical image fusion using empirical wavelet decomposition and local energy maxima. *Optik, 205,* 163947. https://doi.org/10.1016/j.ijleo.2019.163947.

Pršić, D., Nedić, N., & Stojanović, V. (2016). A nature inspired optimal control of pneumatic-driven parallel robot platform. *Proceedings of the Institution of Mechanical Engineers, Part C: Journal of Mechanical Engineering Science, 231*(1), 59–71. https://doi.org/10.1177/0954406216662367.

Ren, Z., Guan, P., Lam, E. Y., & Zhao, J. (2021). Extended focused imaging in microscopy using structure tensor and guided filtering. *Optics and Lasers in Engineering, 140,* 106549. https://doi.org/10.1016/j.optlaseng.2021.106549.

Shehanaz, S., Daniel, E., Guntur, S. R., & Satrasupalli, S. (2021). Optimum weighted multimodal medical image fusion using particle swarm optimization. *Optik, 231,* 166413. https://doi.org/10.1016/j.ijleo.2021.166413.

Shibu, D. S., & Priyadharsini, S. S. (2021). Multi scale decomposition based medical image fusion using convolutional neural network and sparse representation. *Biomedical Signal Processing and Control, 69,* 102789. https://doi.org/10.1016/j.bspc.2021.102789.

Stojanovic, V., He, S., & Zhang, B. (2020). State and parameter joint estimation of linear stochastic systems in presence of faults and non-Gaussian noises. *International Journal of Robust and Nonlinear Control, 30*(16), 6683–6700. https://doi.org/10.1002/rnc.5131.

Tan, W., Tiwari, P., Pandey, H. M., Moreira, C., & Jaiswal, A. K. (2020). Multimodal medical image fusion algorithm in the era of big data. *Neural Computing and Applications*. https://doi.org/10.1007/s00521-020-05173-2.

Tan, W., Thitøn, W., Xiang, P., & Zhou, H. (2021). Multi-modal brain image fusion based on multi-level edge-preserving filtering. *Biomedical Signal Processing and Control, 64,* 102280. https://doi.org/10.1016/j.bspc.2020.102280.

Tannaz, A., Mousa, S., Sabalan, D., & Masoud, P. (2019). Fusion of multimodal medical images using non-subsampled shearlet transform and particle swarm optimization. *Multidimensional Systems and Signal Processing, 31*(1), 269–287. https://doi.org/10.1007/s11045-019-00662-7.

Tao, H., Li, J., Chen, Y., Stojanovic, V., & Yang, H. (2020). Robust point-to-point iterative learning control with trial-varying initial conditions. *IET Control Theory & Applications, 14*(19), 3344–3350. https://doi.org/10.1049/iet-cta.2020.0557.

Wang, G., Li, W., & Huang, Y. (2021). Medical image fusion based on hybrid three-layer decomposition model and nuclear norm. *Computers in Biology and Medicine, 129,* 104179. https://doi.org/10.1016/j.compbiomed.2020.104179.

Wang, L., Dou, J., Qin, P., Lin, S., Gao, Y., Wang, R., & Zhang, J. (2021). Multimodal medical image fusion based on nonsubsampled shearlet transform and convolutional sparse representation. *Multimedia Tools and Applications, 80*(30), 36401–36421. https://doi.org/10.1007/s11042-021-11379-w.

Wang, M., Zhang, W., Sun, C., & Sowmya, A. (2020). Corner detection based on shearlet transform and multi-directional structure tensor. *Pattern Recognition, 103,* 107299. https://doi.org/10.1016/j.patcog.2020.107299.

Wang, S., & Shen, Y. (2020). Multi-modal image fusion based on saliency guided in NSCT domain. *IET Image Processing*. https://doi.org/10.1049/iet-ipr.2019.1319.

Wang, S., Celebi, M. E., Zhang, Y. D., Yu, X., Lu, S., Yao, X., et al. (2021). Advances in data preprocessing for biomedical data fusion: An overview of the methods, challenges, and prospects. *Information Fusion, 76,* 376–421. https://doi.org/10.1016/j.inffus.2021.07.001.

Wang, Z., Cui, Z., & Zhu, Y. (2020). Multi-modal medical image fusion by Laplacian pyramid and adaptive sparse representation. *Computers in Biology and Medicine, 123,* 103823. https://doi.org/10.1016/j.compbiomed.2020.103823.

Wang, Z., Li, X., Duan, H., Su, Y., Zhang, X., & Guan, X. (2021). Medical image fusion based on convolutional neural networks and non-subsampled contourlet transform. *Expert Systems with Applications, 171,* 114574. https://doi.org/10.1016/j.eswa.2021.114574.

Wei, T., Li, X., & Stojanovic, V. (2021). Input-to-state stability of impulsive reaction–diffusion neural networks with infinite distributed delays. *Nonlinear Dynamics, 103*(2), 1733–1755. https://doi.org/10.1007/s11071-021-06208-6.

Wilcoxon, F. (1945). Individual comparisons by ranking methods. *Biometrics Bulletin, 1*(6), 80. https://doi.org/10.2307/3001968.

Xing, C., Wang, M., Dong, C., Duan, C., & Wang, Z. (2020). Using Taylor expansion and convolutional sparse representation for image fusion. *Neurocomputing, 402,* 437–455. https://doi.org/10.1016/j.neucom.2020.04.002.

Xu, L., Si, Y., Jiang, S., Sun, Y., & Ebrahimian, H. (2020). Medical image fusion using a modified shark smell optimization algorithm and hybrid wavelet-homomorphic filter. *Biomedical Signal Processing and Control, 59,* 101885. https://doi.org/10.1016/j.bspc.2020.101885.

Xydeas, C., & Petrovic, V. (2000). Objective image fusion performance measure. *Electronics Letters, 36,* 308. https://doi.org/10.1049/el:20000267.

Yin, M., Liu, X., Liu, Y., & Chen, X. (2019). Medical image fusion with parameter-adaptive pulse coupled neural network in nonsubsampled shearlet transform domain. *IEEE Transactions on Instrumentation and Measurement, 68,* 49–64. https://doi.org/10.1109/tim.2018.2838778.

Yousif, A. S., Omar, Z., & Sheikh, U. U. (2022). An improved approach for medical image fusion using sparse representation and Siamese convolutional neural network. *Biomedical Signal Processing and Control, 72,* 103357. https://doi.org/10.1016/j.bspc.2021.103357.

Zhang, Y. D., Dong, Z., Wang, S. H., Yu, X., Yao, X., Zhou, Q., et al. (2020). Advances in multimodal data fusion in neuroimaging: Overview, challenges, and novel orientation. *Information Fusion, 64,* 149–187. https://doi.org/10.1016/j.inffus.2020.07.006.

Zhao, C., Wang, T., & Lei, B. (2020). Medical image fusion method based on dense block and deep convolutional generative adversarial network. *Neural Computing and Applications, 33*(12), 6595–6610. https://doi.org/10.1007/s00521-020-05421-5.

Zhu, Z., Zheng, M., Qi, G., Wang, D., & Xiang, Y. (2019). A phase congruency and local Laplacian energy based multi-modality medical image fusion method in NSCT domain. *IEEE Access, 7,* 20811–20824. https://doi.org/10.1109/access.2019.2898111.

THE IMAGING SCIENCE JOURNAL
https://doi.org/10.1080/13682199.2023.2190947

A novel approach using the local energy function and its variations for medical image fusion

Phu-Hung Dinh

Faculty of Computer Science and Engineering, Thuyloi University, Hanoi, Vietnam

ABSTRACT

Medical image fusion plays a pivotal role in facilitating clinical diagnosis. However, the quality of input medical images may be marred by noise, low contrast, and lack of sharpness, presenting numerous challenges for medical image synthesis algorithms. Additionally, several fusion rules may degrade the brightness and contrast of the fused image. To this end, this paper presents a novel image synthesis approach to tackle the aforementioned issues. First, the input images undergo pre-processing to enhance their quality. Subsequently, we introduce the three-layer image decomposition (TLID) technique, which decomposes an image into three distinct layers: the base layer (L_B), the small-scale structure layer (L_{SS}), and the large-scale structure layer (L_{LS}). Next, we synthesize the base layers utilizing adaptive rules based on the Marine predators algorithm (MPA), ensuring that the output image is not degraded. Finally, we propose an efficient synthesis method for L_{SS} and L_{LS} layers, based on combining the local energy function with its variations. This fusion technique preserves the intricate details present in the original image. We evaluated our approach on 156 medical images using six evaluation metrics and compared it with seven state-of-the-art image synthesis techniques. Our results demonstrate that our method successfully generates high-quality output images and preserves detailed information throughout the image synthesis process.

ARTICLE HISTORY
Received 17 February 2022
Accepted 2 March 2023

KEYWORDS
Marine predators algorithm (MPA); three-layer image decomposition (TLID); rolling guidance filter (RGF); weighted mean curvature filter (WMCF)

1. Introduction

Medical imaging is an essential component of clinical applications today. With the advent of advanced image acquisition devices, a variety of multimodal medical images can now be obtained. Human organ structures are highly complex, and lesions cannot be adequately described using a single type of multimodal medical imaging. Computed Tomography (CT), magnetic resonance imaging (MRI), positron emission tomography (PET), and single photon emission computed tomography (SPECT) are among the commonly used types of multimodal medical imaging in image fusion. SPECT imaging is particularly useful for diagnosing vascular conditions and detecting tumors, as it offers insights into metabolic activity. In contrast, MRI is renowned for its ability to capture high-resolution images of soft tissues. To provide clinicians with comprehensive diagnostic information, it is crucial to synthesize the necessary information from multimodal medical images.

Traditional approaches to image fusion involve a sequence of three fundamental steps: image decomposition, synthesis of the decomposed components, and transforming the resulting fused image back to the original domain. Presently, various image decomposition methods exist. The first group of such methods comprises multi-scale decomposition (MSD)-based techniques, such as Discrete wavelet transform (DWT), Stationary wavelet transform (SWT), and Laplacian pyramid (LP). For example, Wang et al. [1] utilized the DWT method to decompose input images before fusing them, while Dinh [2] applied the SWT method to obtain high and low-frequency components of input images. Fu et al. [3] employed the LP method to decompose input images. However, MSD-based methods have limited capacity to capture directional information, thus resulting in suboptimal image representation. The second group of methods is multi-scale geometric analysis (MGA)-based approaches, which overcome the limitations of MSD-based methods. These methods include curvelet transform, contourlet transform (CT), non-subsampled contourlet transform (NSCT), shearlet transform (ST), and non-subsampled shearlet transform (NSST). They provide complete information about both phase and direction. For example, Wang et al. [4] employed NSCT to decompose input images, while Gao et al. [5] utilized NSST to transform input images. Several other image synthesis studies based on MGA methods exist, including [6], [7], and [8]. However, these methods have high computational complexity. The third group of image transformation methods

CONTACT Phu-Hung Dinh hungdp@tlu.edu.vn Faculty of Computer Science and Engineering, Thuyloi University, 175 Tay Son, Dong Da, Hanoi, Vietnam

comprises base-detail decomposition (BDD) based techniques, which exhibit benefits over MSD-based methods in terms of both computational efficiency and fusion performance. BDD-based methods enable the decomposition of an input image into base and detail layers by employing filters. For instance, Dinh [9] proposed a novel image fusion approach based on two-scale image decomposition. Li et al. [10] applied three-layer decomposition to fuse medical images. The fourth group of image transformation methods consists of Sparse representation (SR)-based methods, which have proven to be highly effective in various image synthesis studies. Wang et al. [11] presented a new multi-focus image fusion approach based on multi-scale SR. Jie et al. [12] integrated the SR with adaptive energy-choosing schemes to fuse Tri-modal medical images. Total-variational decomposition (TVD) has also been leveraged in several studies for image synthesis. Liu et al. [13] proposed a novel image synthesis method based on the Robust spiking cortical model and TVD. Additionally, Liu et al. [14] utilized spectral total variation and local structural patch measurement to construct an image composite model.

Traditional methods of image fusion have limitations that still persist. One limitation is that these methods are bound to use the same image decomposition method to acquire features and ensure their combinability in the subsequent phase. This results in the disregard of source image differences, which ultimately leads to poor expressiveness of the extracted features. Additionally, traditional methods acquire few and insufficiently diverse features from image decomposition, which still poses limitations on their synthesis performance. Deep learning has proven to be a powerful tool for addressing image processing problems, including image enhancement [15], image denoising [16], and image fusion. In particular, deep learning-based approaches have been instrumental in overcoming the limitations of traditional image fusion methods. Firstly, these approaches can conduct differentiated feature extraction by utilizing diverse network branches. Secondly, the feature fusion strategy can be effectively learned by designing appropriate loss functions. As a result, deep learning-based methods have significantly contributed to image fusion. For instance, Hou et al. [17] proposed a novel method for synthesizing CT and MRI images by combining convolutional neural networks with a dual-channel spiking cortical model. Ding et al. [18] presented an image synthesis method based on Dual-Branch CNNs in the NSST domain. Additionally, Ding et al. [19] employed Siamese networks in conjunction with the multi-scale local extrema scheme. Wang et al. [1] combined Convolutional neural networks (CNN) with Discrete wavelet transform (DWT) to fuse Multi-focus images. Kaur et al. [20] proposed a medical image fusion based on deep belief networks (DBN). Other studies have also employed deep learning techniques to synthesize images, including [21–25].

In recent times, meta-heuristic optimization-based image synthesis methods have been proven effective. Optimization algorithms offer adaptive rules for the synthesis process, leading to an enhanced quality of the output composited image. For example, Dinh [26] proposed a new method that uses the Equilibrium optimizer algorithm (EOA) to synthesize medical images. Shilpa et al. [27] improved the JAYA optimization algorithm and applied it to fuse medical images in the NSST domain. Particle swarm optimization (PSO) was applied by Shehanaz et al. [28] to fuse high-frequency components in the DWT domain. Xu et al. [29] modified the shark smell optimization (SSO) algorithm and combined it with the World Cup Optimization (WCO) algorithm to synthesize low-frequency components in the DWT domain. Dinh [30] utilized the Chameleon swarm algorithm to synthesize the base components, ensuring the preservation of composite image quality. Further optimization techniques for producing medical images are discussed in the research papers [9,31–34].

Based on our observations, the low efficiency of image fusion can be attributed to three main factors. Firstly, low-quality input images are a common issue, characterized by low brightness and contrast, noise, and lack of sharpness, which negatively impacts the quality of the composite image. Secondly, the average rule, a widely adopted method in several studies [35–37], has the advantage of simplicity and low computational complexity in synthesizing low-frequency components. However, its disadvantage is that it leads to a degradation in the brightness and contrast of the output composite image. Thirdly, the synthesis rules for high-frequency components have not been designed efficiently to capture full details from the input images, further impacting the quality of the composite image. In light of the aforementioned limitations, we propose the following approaches to overcome them. Firstly, we suggest enhancing the quality of input images using the Brighten low-light image (BLLI) method [38]. Secondly, we propose using the MPA optimization algorithm to generate adaptive rules for low-frequency components, thereby ensuring optimal brightness and contrast in the output image. Thirdly, we introduce a fusion rule based on the local energy function and its variations to generate an efficient fusion rule for detail layers. This is because the local energy function and its variations have proven effective in many image synthesis studies. For instance, Amini et al. [39] combined the local energy function with local variance fusion rules to synthesize MRI and PET images. Several variations of the local energy function have been proposed in

recent years for medical image synthesis. Compass operators, such as Kirsch and Prewitt, have been combined with a local energy function to synthesize medical images [9, 26]. The structure tensor has been applied in several studies on image fusion [40–42]. Recently, Li et al. [43] combined the structure tensor salient detection operator with a local energy function to construct a synthesis rule for detail components.

In this work, we present a novel method to tackle the aforementioned limitations. Our principal contributions are summarized as follows:

- Firstly, The present study proposes a novel three-layer image composition (TLID) method for image decomposition into three layers, namely, the base layer (L_B), small-scale structure layer (L_{SS}), and large-scale structure layer (L_{LS}). This approach utilizes two filters, namely, the Rolling Guidance Filter (RGF) and the Weighted Median curvature filter (WMCF), to construct the TLID method.
- Secondly, we propose an efficient fusion method to merge the L_{SS} and L_{LS} layers, which involves the combination of the local energy function with its variations.
- Thirdly, in order to mitigate the loss of brightness and contrast during the image compositing process, we propose a novel method for fusing the base layers utilizing adaptive parameters.

The paper is structured as follows: Section 2 provides an overview of background methods including Rolling Guidance Filter (RGF), Weighted mean curvature filter (WMCF), Structure Tensor, Local Energy and its variations, and MPA algorithm. Section 3 introduces the TLID method, which combines variations of the local energy function (FR-CVLEF) to form a new fusion rule, as well as our proposed image fusion model. Section 4 contains experimental data and settings, results, and evaluations. Finally, Section 5 concludes the paper and presents future work.

2. Background

2.1. Rolling guidance filter (RGF)

The Rolling Guidance Filter (RGF) [44] is a digital image filtering technique that has gained popularity in recent years due to its ability to effectively denoise images while preserving their sharpness and details. RGF is a non-local means filter that is designed to exploit the global structures and textures of an image, which allows it to effectively remove noise without blurring the image or losing important information. The filter comprises of two primary stages: removing small structures and recovering edges.

Step 1: The small structure is removed by the GF.

The symbols I and I_G refer to the input and output images obtained following filtration via the Gaussian filter, respectively. The computation of I_G is performed in accordance with Equation (1).

$$I_G(u) = \frac{1}{H_u} \sum_{v \in N(u)} \exp\left(- \frac{\|u - v\|^2}{2\sigma_g^2} \right) . I(v) \tag{1}$$

where

- u and v are the position.
- σ_g is the standard deviation of GF.
- $N(u)$ is the set of neighboring pixels whose center is u.
- H_u is calculated according to Equation (2).

$$H_u = \sum_{v \in N(u)} \exp\left(- \frac{\|u - v\|^2}{2\sigma_g^2} \right). \tag{2}$$

Step 2: Edge is recovered by the guided filter.

The symbol E^1 denotes the GF output from the initial step. K^{t+1} represents the outcome achieved at the t-th iteration. Computation of K^{t+1} is executed in accordance with Equation (3).

$$K^{t+1}(u) = \frac{1}{H_u} \sum_{v \in N(u)} \exp\left(- \frac{\|u - v\|^2}{2\sigma_g^2} - \frac{\left\|K(u)^t - K(v)^t\right\|^2}{2\sigma_r^2} \right) . I(v) \tag{3}$$

where

- H_u is calculated according to Equation (4).
- σ_r is the standard deviation of the Guided Filter.

$$H_u = \sum_{v \in N(u)} \exp\left(- \frac{\|u - v\|^2}{2\sigma_g^2} - \frac{\left\|K(u)^t - K(v)^t\right\|^2}{2\sigma_r^2} \right). \tag{4}$$

The output images obtained from the RGF with several loops are illustrated in Figure 1.

2.2. Weighted mean curvature filter (WMCF)

The WMCF is a technique used in image processing and computer vision. It was introduced by Gong et al. [45], and its advantages are scale invariance, sampling invariance, and contrast invariance. Several applications of this filter can be mentioned as multi-spectral and panchromatic image fusion [46], as well as medical image fusion [47]. We denote an input image as R, and define the symbol m_i ($i = \overline{1, 8}$) as the mask matrices of the WMFC filter, as illustrated in Figure 2.

The WMCF can be calculated in two steps:

Step 1: Determine the distance k_i as in Equation (5).

$$k_i = m_i * R, \quad i = \overline{1, 8} \tag{5}$$

Figure 1. RGF output images with some loops.

$$m_1 = \begin{bmatrix} 1/6 & 1/6 & 0 \\ 1/3 & -1 & 0 \\ 1/6 & 1/6 & 0 \end{bmatrix} \quad m_2 = \begin{bmatrix} 1/6 & 1/3 & 1/6 \\ 1/6 & -1 & 1/6 \\ 0 & 0 & 0 \end{bmatrix} \quad m_3 = \begin{bmatrix} 0 & 1/6 & 1/6 \\ 0 & -1 & 1/3 \\ 0 & 1/6 & 1/6 \end{bmatrix} \quad m_4 = \begin{bmatrix} 0 & 0 & 0 \\ 1/6 & -1 & 1/6 \\ 1/6 & 1/3 & 1/6 \end{bmatrix}$$

$$m_5 = \begin{bmatrix} 1/6 & 1/3 & 1/12 \\ 1/3 & -1 & 0 \\ 1/12 & 0 & 0 \end{bmatrix} \quad m_6 = \begin{bmatrix} 1/12 & 1/3 & 1/6 \\ 0 & -1 & 1/3 \\ 0 & 0 & 1/12 \end{bmatrix} \quad m_7 = \begin{bmatrix} 0 & 0 & 1/12 \\ 0 & -1 & 1/3 \\ 1/12 & 1/3 & 1/6 \end{bmatrix} \quad m_8 = \begin{bmatrix} 1/12 & 0 & 0 \\ 1/3 & -1 & 0 \\ 1/6 & 1/3 & 1/12 \end{bmatrix}$$

Figure 2. Masks of the MWCF.

Step 2: This filter is defined as Equation (6).

$$F(R) = k_m \tag{6}$$

where $m = i\arg\min(|k_i|;\ i = \overline{1, 8})$

Figure 3 illustrates the results of using the WMCF.

2.3. Structure tensor (ST)

The computation of the ST is based on the gradient of the gray-scale image, and finds wide-ranging applications such as hyperspectral and panchromatic image fusion [48], image denoising [49], and medical image fusion [43]. Let I be an input image. The ST can be calculated using Equation (7).

$$ST = \begin{bmatrix} \sum_w K_i^2 & \sum_w K_i K_j \\ \sum_w K_i K_j & \sum_w K_j^2 \end{bmatrix} \tag{7}$$

where,

- w is a local window.
- K_i and K_j are the gradients in the i-direction and j-direction, respectively.

Furthermore, the operator for detecting salient features using the structure tensor, referred to as the Structure Tensor Salient Detection Operator (STSDO) [50], is derived from the eigenvalues (t_1 and t_2) as per Equation (8).

$$S = \sqrt{(t_1 + t_2)^2 + 0.5(t_1 - t_2)^2} \tag{8}$$

Where t_1 and t_2 are determined according to Equations (9) and (10).

$$t_1 = \frac{1}{2}\left(\sum_w K_i^2 + \sum_w K_j^2 + \sqrt{\left(\sum_w K_i^2 - \sum_w K_j^2\right)^2 + 4\left(\sum_w K_i K_j\right)^2} \right) \tag{9}$$

$$t_2 = \frac{1}{2}\left(\sum_w K_i^2 + \sum_w K_j^2 - \sqrt{\left(\sum_w K_i^2 - \sum_w K_j^2\right)^2 + 4\left(\sum_w K_i K_j\right)^2} \right) \tag{10}$$

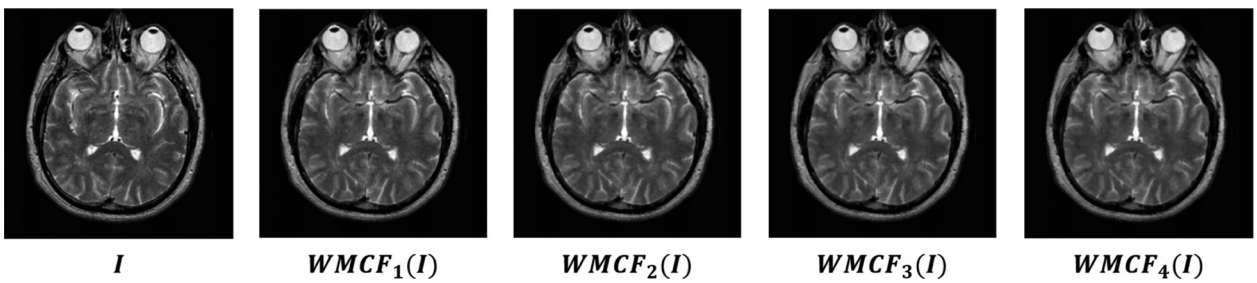

Figure 3. Some images obtained from the WMCF filter.

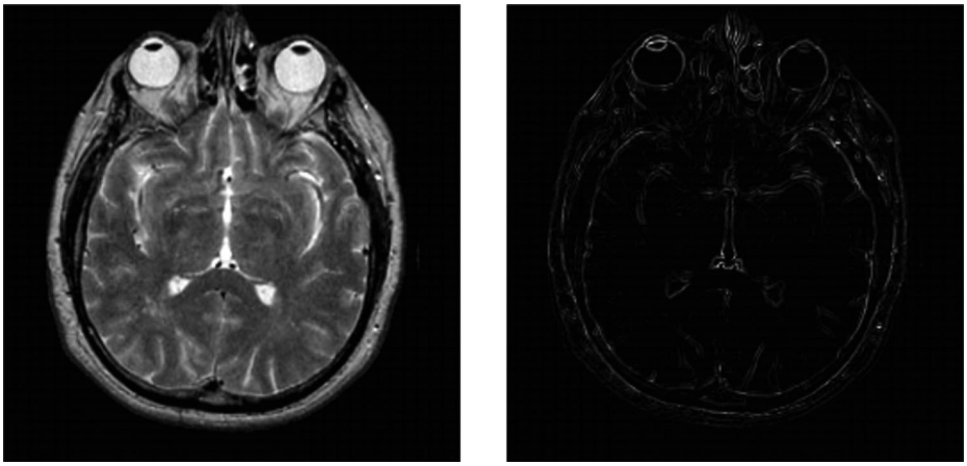

Figure 4. The image obtained by the STSDO.

Figure 4 illustrates the image obtained by applying the STSD operator.

2.4. Local energy function and its variations

2.4.1. Local energy function

The Local Energy Function (LEF) has found numerous applications in studies related to image fusion [39, 51]. The computation of $LEF(i, j)$ is performed using Equation (11).

$$LEF(i,j) = \sum_{u=0}^{k-1}\sum_{v=0}^{k-1} W_{LE}(u,v)I^2(i+u, j+v) \tag{11}$$

- W_{LE} is a unit window of size $k \times k$.
- I is the input image.

2.4.2. Local energy function using the Prewitt compass operator (LEF_PCO)

Dinh [26] proposed the LEF-PCO method for developing the synthesis rule for detail components. We denote an input image as I, and refer to the k-th mask of the Prewitt compass operator as W^k_{PCO}, with further clarification provided in Figure 5. The computation of LEF-PCO is carried out using Equation (12).

$$LEF\_PCO^k(i,j) = \sum_{u=0}^{m-1}\sum_{v=0}^{m-1} W^k_{PCO}(u,v)I^2(i+u, j+v) \tag{12}$$

2.4.3. Local energy function combined with the structure tensor saliency

Dinh [52] introduced the Local Energy Function combined with the Structure Tensor Salient Detection Operator (LEF_STSDO) for generating fusion rules for detailed components.

The LEF_STSDO is defined as Equation (13).

$$LEF\_STSDO = W_{STSDO} \odot LEF \tag{13}$$

where,

- W_{STSDO} is defined as the STSDO in Equation (8).
- $\odot$ represents entry-wise multiplication.
- LEF represents the local energy function and is defined by Equation (11).

$$W^1_{PCO} = \begin{bmatrix} -1 & 0 & 1 \\ -1 & 0 & 1 \\ -1 & 0 & 1 \end{bmatrix} \quad W^2_{PCO} = \begin{bmatrix} 0 & 1 & 1 \\ -1 & 0 & 1 \\ -1 & -1 & 0 \end{bmatrix} \quad W^3_{PCO} = \begin{bmatrix} 1 & 1 & 1 \\ 0 & 0 & 0 \\ -1 & -1 & -1 \end{bmatrix} \quad W^4_{PCO} = \begin{bmatrix} 1 & 1 & 0 \\ 1 & 0 & -1 \\ 0 & -1 & -1 \end{bmatrix}$$

$$W^5_{PCO} = \begin{bmatrix} 1 & 0 & -1 \\ 1 & 0 & -1 \\ 1 & 0 & -1 \end{bmatrix} \quad W^6_{PCO} = \begin{bmatrix} 0 & -1 & -1 \\ 1 & 0 & -1 \\ 1 & 1 & 0 \end{bmatrix} \quad W^7_{PCO} = \begin{bmatrix} -1 & -1 & -1 \\ 0 & 0 & 0 \\ 1 & 1 & 1 \end{bmatrix} \quad W^8_{PCO} = \begin{bmatrix} -1 & -1 & 0 \\ -1 & 0 & 1 \\ 0 & 1 & 1 \end{bmatrix}$$

Figure 5. An illustration of the masks employed by the Prewitt compass operator.

2.5. MPA algorithm

The MPA algorithm was initially proposed by Faramarzi et al. [53]. This algorithm has exhibited superior optimization performance compared to other algorithms such as Genetic algorithm (GA), Gravitational Search Algorithm (GSA) [54], and Salp Swarm Algorithm (SSA) [55]. The MPA algorithm has found numerous applications in various domains such as structural damage detection [56], image segmentation [57], and medical image fusion [52, 58]. The MPA algorithm can be outlined in three main steps as follows:

Step 1: During the first third of the loop, the prey exhibits faster movement than the predator. The calculation of stepsize ($\overrightarrow{X}i$) and prey ($\overrightarrow{Y}i$) is performed using Equations (14) and (15).

$$\overrightarrow{X}_i = \overrightarrow{R}_B \otimes (\overrightarrow{T}_i - \overrightarrow{R}_B \otimes \overrightarrow{Y}_i); i = \overline{1, n} \quad (14)$$

$$\overrightarrow{Y}_i = \overrightarrow{Y}_i + h.\overrightarrow{R} \otimes \overrightarrow{X}_i \quad (15)$$

Where

- $\overrightarrow{R}$ in [0,1].
- $h = 0.5$.
- $\otimes$ is entry-wise multiplication.
- $\overrightarrow{R}_B$ is selected randomly from a Brownian motion distribution.
- $\overrightarrow{T}$ holds the fitness solution.

Step 2: During the subsequent third of the loop, updates to $\overrightarrow{X}i$ and $\overrightarrow{Y}i$ are made using Equations (16), (17), (18), and (19).

For the first half of the population:

$$\overrightarrow{X}_i = \overrightarrow{R}_L \otimes (\overrightarrow{T}_i - \overrightarrow{R}_L \otimes \overrightarrow{Y}_i); \quad i = \overline{1, n/2} \quad (16)$$

$$\overrightarrow{Y}_i = \overrightarrow{Y}_i + h.\overrightarrow{R} \otimes \overrightarrow{X}_i \quad (17)$$

For the second half of the population:

$$\overrightarrow{X}_i = \overrightarrow{R}_B \otimes (\overrightarrow{R}_B \otimes \overrightarrow{T}_i - \overrightarrow{Y}_i); \quad i = \overline{n/2, n} \quad (18)$$

$$\overrightarrow{Y}_i = \overrightarrow{T}_i + h.a \otimes \overrightarrow{X}_i; \quad (19)$$

where

- $a = (1 - \frac{I}{I_{\max}})^{\frac{2*I}{I_{\max}}}$.
- $\overrightarrow{R_L}$ is generated from the *Lévy* distribution.

Step 3: Updates to $\overrightarrow{X}i$ and $\overrightarrow{Y}i$ are made during the final third of the loop using Equations (20) and (21).

$$\overrightarrow{X}_i = R_L \otimes (R_L \otimes \overrightarrow{T}_i - \overrightarrow{Y}_i); \quad i = \overline{1, n} \quad (20)$$

$$\overrightarrow{Y}_i = \overrightarrow{T}_i + h.a \otimes \overrightarrow{X}_i \quad (21)$$

Fish Aggregating Devices (FDAs) effect: $\overrightarrow{Y}_i$ is updated according to Equation (22).

$$\overrightarrow{Y}_i = \begin{cases} \overrightarrow{Y}_i + a((X_{\min} + \overrightarrow{R} \otimes (X_{\max} - X_{\min})) \otimes \overrightarrow{U}) \\ \quad if\ (k \le FADs) \\ \overrightarrow{Y}_i + (FADs*(1-k) + k)(\overrightarrow{Y}_{k1} - \overrightarrow{Y}_{k2}) \\ \quad if\ (k > FADs) \end{cases} \quad (22)$$

where,

- $\overrightarrow{U}$ represents the binary vector array.
- k is a uniform random number in the range of [0,1].
- k_1 and k_2 represent random indexes of the prey matrix.

3. Our approach

This section presents three algorithms. The first algorithm is the TLID method. The second algorithm introduces a new fusion rule that combines variations of the local energy function. The third algorithm proposes our image fusion method.

3.1. Three-layer image decomposition method

Image synthesis begins with image decomposition, which involves separating the source image into layers with complementary information. Typically, image decomposition algorithms create a base layer and one or more detail layers. In previous studies, a two-layer image decomposition method was commonly used, with the base layer obtained using the average [59] or low-pass filters [35]. However, these filters can cause loss of detailed information in the image, resulting in incomplete detail layers. To address these limitations, we propose a three-layer image decomposition method based on RGF and WMC filters. The algorithmic steps of this method are presented in Algorithm 1, and the process is illustrated in Figure 6. An illustrative

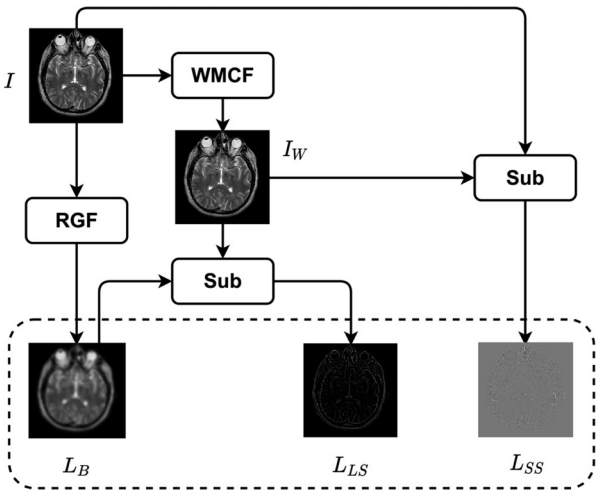

Figure 6. Diagram illustrating in detail how to decompose an input image into three layers.

example of a three-layer image decomposition is illustrated in Figure 7.

Algorithm 1. The three-layer image decomposition

Input: I
Output: Three layers L_B, L_{SS}, and L_{LS}
Step 1: The generation of the base layer (L_B) involves applying the RGF filter to the image I.
Step 2: The WMC filter (WMCF) is employed to filter the image I, resulting in an image denoted as I_W.
Step 3: The layer containing small-scale structures (L_{SS}) is obtained by applying Equation (23).

$$L_{SS} = I - I_W \tag{23}$$

Step 4: According to Equation (24), the large-scale structure layer (L_{LS}) can be obtained.

$$L_{LS} = I_W - L_B \tag{24}$$

3.2. Fusion rules based on combining variations of the local energy function

In this subsection, we introduce a novel fusion rule, named FR-CVLEF, which combines variations of the local energy function to fuse the small-scale and large-scale structure layers. Figure 8 illustrates the use of the FR-CVLEF.

3.3. Our image fusion method

In this subsection, we present our approach, which involves three main steps. Firstly, we enhance the input image (I_{MRI}) using two methods: unsharp masking and the Brighten Low-Light Image (BLLI) method [38]. Next, the image I_{PET} is transformed into the channels Y, U, and V. We then decompose I_{MRI} and Y into base layers, small-scale structure layers (L_{SS}), and large-scale structure layers (L_{LS}) using the TLID method. After that, we fuse the base layers using an adaptive rule and the L_{SS} and L_{LS} layers using the FR-CVLEF to obtain the synthesized layers L_B^F, L_{SS}^F and L_{LS}^F, respectively. We then calculate the composite gray image ($I^F Gray$) by summing the three layers, L_B^F, L_{SS}^F and L_{LS}^F. Finally, we convert I_{Gray}^F, U, and V into a color composite image (I_{Color}^F). Our approach is illustrated in Algorithm 3 and Figure 9.

4. Experimental setup and evaluation

4.1. Experimental data

A total of 156 images, including 78 pairs of MRI and PET images, were utilized in this study. The images were sourced from 'The Whole Brain Atlas' (http://www.med.harvard.edu/AANLIB/) and are described in detail in Table 1. The three pairs of images in the K4 dataset are illustrated in Figure 10.

4.2. Experimental setup

We design some experiments as follows:

Experiment #1 We selected several optimization algorithms for comparison with the MPA algorithm. The algorithms considered are described in Table 2, and the experimental data used in this study is the K4 dataset.

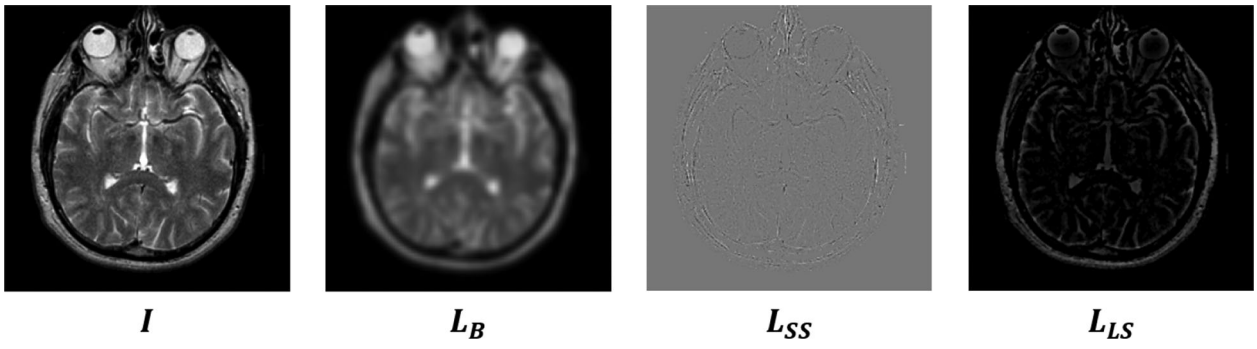

Figure 7. Three resulting images obtained after decomposing an input image I.

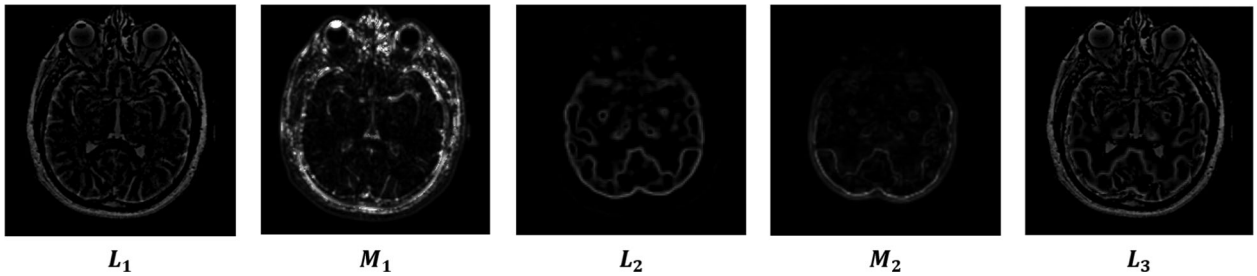

Figure 8. Illustration for the FR-CVLEF method.

Algorithm 2. FR-CVLEF

Input: Two layers (L_1, L_2)
Output: A fused layer L_3

Step 1: Calculate the local energy function for the L_1 and L_2 layers according to Equations (25) and (26).

$$LEF_1(i,j) = \sum_{u=0}^{k-1}\sum_{v=0}^{k-1} W_{LE}(u,v)L_1^2(i+u, j+v) \tag{25}$$

$$LEF_2(i,j) = \sum_{u=0}^{k-1}\sum_{v=0}^{k-1} W_{LE}(u,v)L_2^2(i+u, j+v) \tag{26}$$

Step 2: Calculate the LEF-PCO for the L_1 and L_2 layers according to Equations (27) and (28).

$$LEF\_PCO_1^k(i,j) = \sum_{u=0}^{m-1}\sum_{v=0}^{m-1} W_{PCO}^k(u,v)L_1^2(i+u, j+v) \tag{27}$$

$$LEF\_PCO_2^k(i,j) = \sum_{u=0}^{m-1}\sum_{v=0}^{m-1} W_{PCO}^k(u,v)L_2^2(i+u, j+v) \tag{28}$$

Step 3: Calculate the local energy function combined with the structure tensor salient detection operator for the L_1 and L_2 layers according to Equations (29) and (30).

$$LEF\_STSDO_1 = W_{STSDO}(L_1) \odot LEF(L_1) \tag{29}$$

$$LEF\_STSDO_2 = W_{STSDO}(L_2) \odot LEF(L_2) \tag{30}$$

Step 4: Calculate the maximum value of local energy functions and its variations for L_1 and L_2 layers corresponding to Equations (31) and (32).

$$M_1 = Max(LEF_1, LEF\_PCO_1^k, LEF\_STSDO_1) \tag{31}$$

$$M_2 = Max(LEF_2, LEF\_PCO_2^k, LEF\_STSDO_2) \tag{32}$$

Step 5: The FR-CVLEF is defined as Equation (33).

$$L_3(i,j) = \begin{cases} L_1(i,j) \text{ if } |M_1(i,j)| \geq |M_2(i,j)| \\ L_2(i,j) \text{ if } |M_1(i,j)| < |M_2(i,j)| \end{cases} \tag{33}$$

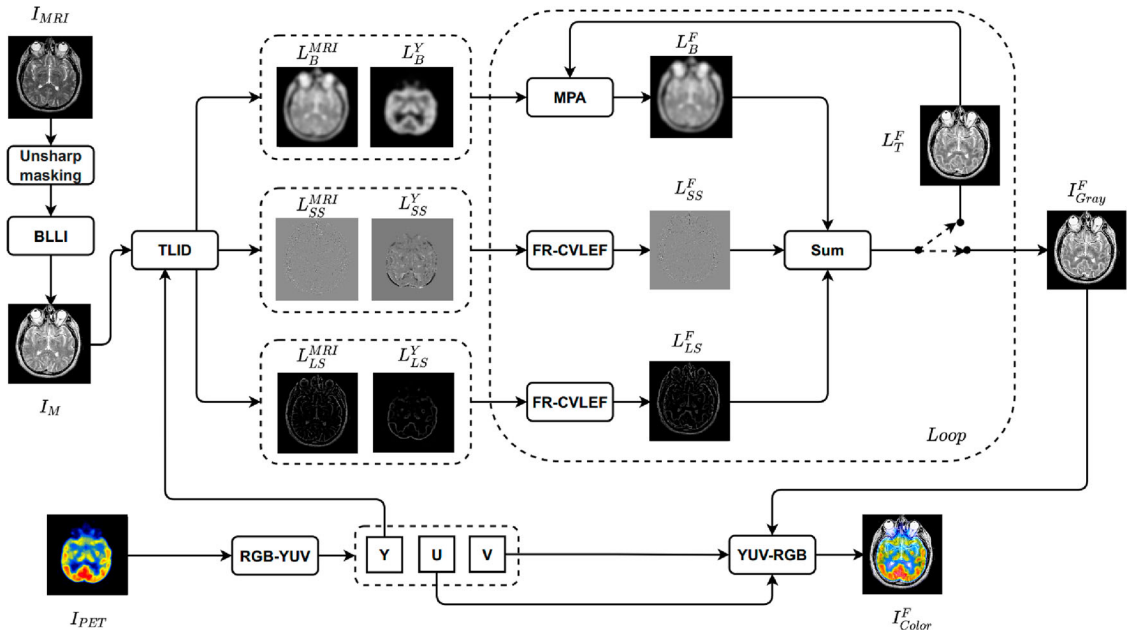

Figure 9. The diagram of our approach.

Experiment #2 Several fusion rules were used for comparison with the proposed rule (FR_CVLEF), as outlined below:

- Max selection rule (R_{Max}).
- Maximum local energy (R_{MLE}) [63].
- PA-PCNN ($R_{PA-PCNN}$) [64].
- Sum-modified laplacian (R_{SML}) [65].

Experiment #3 Our study involves a comparative analysis between our algorithm and seven

Algorithm 3. The proposed approach

Input: I_{MRI}, $I_{PET}(S \times T)$.
Output: I_{Fusion}

Step 1: Enhancing the input image I_{MRI} using the Unsharp masking and the BLLI [38] method, obtaining the I_M image.
Step 2: Convert I_{PET} from RGB to YUV color space, obtaining three components Y, U, and V.
Step 3: Decompose I_M and Y by TLID method, obtained layers, (L_B^{MRI}, L_B^Y), (L_{SS}^{MRI}, L_{SS}^Y), and (L_{LS}^{MRI}, L_{LS}^Y), respectively.
Step 4: (L_{SS}^{MRI}, L_{SS}^Y), and (L_{LS}^{MRI}, L_{LS}^Y) layers are fused by the FR_CVLEF method according to Equations (34) and (35).

$$L_{SS}^F = FR\_CVLEF(L_{SS}^{MRI}, L_{SS}^Y) \tag{34}$$

$$L_{LS}^F = FR\_CVLEF(L_{LS}^{MRI}, L_{LS}^Y) \tag{35}$$

Step 5: L_B^{MRI} and L_B^Y are fused by by adaptive parameters ($\rho_1 \in [0.8, 1]$, $\rho_2 \in [0, 0.2]$, and $\rho_3 \in [0.9, 1]$) according to Equation (36).

$$L_B^F = \rho_1 L_B^{MRI} + \rho_2 L_B^Y \tag{36}$$

Where the MPA algorithm is used to find the extrema of the fitness function according to Equation (37).

$$F = \frac{\mu_T}{R \times \sigma_T^2}(H_T - H_M)(H_T - H_Y). \tag{37}$$

Where $R(I_{MRI}, L_T^F)$, $R(Y, L_T^F)$, and R are determined as Equations (38), (39), and (40), respectively.

$$R(I_M, L_T^F) = \frac{1}{S \times T}\sum_{s=1}^{S}\sum_{t=1}^{T}(L_T^F(s,t) - I_M(s,t))^2 \tag{38}$$

$$R(Y, L_T^F) = \frac{1}{S \times T}\sum_{s=1}^{S}\sum_{t=1}^{T}(L_T^F(s,t) - Y(s,t))^2 \tag{39}$$

$$R = \rho_3 R(I_M, L_T^F) + (1 - \rho_3)R(Y, L_T^F) \tag{40}$$

μ_T and σ_T^2 are mean and variance of L_T^F ($L_T^F = L_B^F + L_{SS}^F + L_{LS}^F$) in each iteration of the MPA algorithm. H_M, H_Y, and H_T are the Entropy of I_M, Y, and L_T^F, respectively.
Step 6: The image L_T^F obtained after loop termination is a fusion gray image (I_{Gray}^F).
Step 7: I_{Gray}^F, U, and V are converted into I_{Color}^F.

Table 1. Dataset.

Groups	Number of images	Description
K1	26 pairs (MRI (T2) – PET)	Slices from 61 to 86 along the Transaxial (T) axis.
K2	26 pairs (MRI (T2) – PET)	Slices from 61 to 86 along the Sagittal (S) axis.
K3	26 pairs (MRI (T2) – PET)	Slices from 61 to 86 along the Coronal (C) axis.
K4	3 pairs (MRI (T2) – PET)	Slice #78 along the T, S, and C axis.

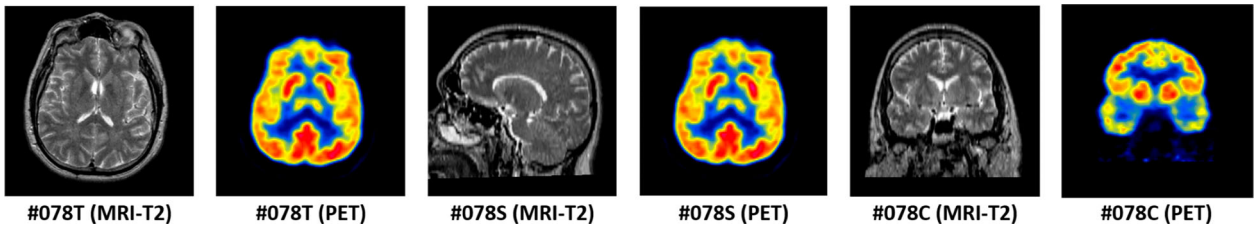

Figure 10. Illustration of several pairs of MRI and PET images.

Table 2. Five optimization algorithms.

Num	Algorithms	Description
1	MVO [60]	Multi-Verse Optimizer
2	WOA [61]	Whale Optimization Algorithm
3	SSA [55]	Salp swarm algorithm
4	SCA [62]	Sine cosine algorithm
5	GWO [61]	Grey wolf optimizer

Table 3. Seven image fusion algorithms.

Num	Algorithms	Years
1	PC-LLE-NSCT (*G*1) [66]	2019
2	TLD-SR (*G*2) [10]	2021
3	JBF-LGE (*G*3) [43]	2021
4	CSE (Contrast and structure extraction) (*G*4) [67]	2021
5	CNPS-NSST (*G*5) [68]	2021
6	DTNP-NSCT (*G*6) [69]	2021
7	ACO (*G*7) [70]	2022

contemporary image fusion algorithms, which are comprehensively described in Table 3.

We compare our algorithm with seven contemporary image fusion algorithms (as detailed in Table 3).

For Experiments #2 and #3, we utilized data sets K1, K2, and K3. We evaluated the performance of the image fusion algorithms using the following five indicators:

- Average light intensity (Q_{ALI}).
- Contrast index (Q_{CI}).

Table 4. Q_M and Q_{SD} from 30 different runs.

Dataset	Algorithms	Q_M	Q_{SD}
K4(#78T)	MPA	0.017876671935888	0.000009033932259
	MVO	0.016518230357696	0.001090932265423
	WOA	0.017277469311324	0.000534054285376
	SSA	0.016899097232778	0.001118836345425
	SCA	0.017217245270695	0.000289792732718
	GWO	0.017669608631168	0.000189772085703
K4(#78S)	MPA	0.029647134938738	0.000026405604409
	MVO	0.028356602594419	0.001161220657539
	WOA	0.028698747803551	0.000690713025417
	SSA	0.027886822958534	0.002416877831579
	SCA	0.029093335806103	0.000290569097601
	GWO	0.029300807571747	0.000241217843724
K4(#78C)	MPA	0.005885862817517	0.000003159852779
	MVO	0.005790921812435	0.000067984350292
	WOA	0.005828160907535	0.000074232890256
	SSA	0.005816524467147	0.000069518552257
	SCA	0.005774386053179	0.000043737425495
	GWO	0.005836384455938	0.000020781565237

- Sharpness (Q_S).
- Edge-based similarity measure ($Q^{AB/F}$) [71].
- Feature mutual information [72] (Q_{FMI}).

The necessary parameters used in our model are set as follows:

- $n = 50$, $l_{\max} = 50$.
- $h = 0.5$; $FADs = 0.2$; $k \in [0, 1]$.

4.3. Results and evaluation

The results of the three experiments described in Section 4.2 are presented here. In the first experiment, we ran each optimization algorithm 30 times independently and evaluated the mean (Q_M) and standard deviation (Q_{SD}) using two metrics. The results are presented in Table 4 and Figure 11. The MPA algorithm outperformed the others, producing the highest Q_M value and the lowest Q_{SD} value. Therefore, it is the preferred choice for the proposed model. We also conducted a Wilcoxon rank-sum test [73] to assess the significance of the results, and the P-values were found to be above 0.05, indicating statistical significance, as shown in Table 5.

Table 5. P-values from Wilcoxon test.

Dataset	Algorithms	P-values
K4(#78T)	MPA vs MVO	3.019859359162151e−11
	MPA vs WOA	3.689725853981014e−11
	MPA vs SSA	6.065757009046759e−11
	MPA vs SCA	3.019859359162151e−11
	MPA vs GWO	3.689725853981014e−11
K4(#78S)	MPA vs MVO	3.019859359162151e−11
	MPA vs WOA	1.464306887715034e−10
	MPA vs SSA	6.695518965500180e−11
	MPA vs SCA	3.019859359162151e−11
	MPA vs GWO	4.077164846825348e−11
K4(#78C)	MPA vs MVO	3.019859359162151e−11
	MPA vs WOA	8.993406027014880e−11
	MPA vs SSA	3.019859359162151e−11
	MPA vs SCA	3.019859359162151e−11
	MPA vs GWO	4.504322112705322e−11

Table 6. Two evaluation metrics ($Q^{AB/F}$ and Q_{FMI}) obtained from different fusion rules.

Dataset	Fusion rules	$Q^{AB/F}$	Q_{FMI}
K1	R_{Max}	0.4829	0.8144
	R_{MLE}	0.7124	0.8720
	$R_{PA-PCNN}$	0.6669	0.8658
	R_{SML}	0.6984	0.8632
	FR-CVLEF	0.7440	0.8737
K2	R_{Max}	0.4868	0.8092
	R_{MLE}	0.7271	0.8749
	$R_{PA-PCNN}$	0.6893	0.8689
	R_{SML}	0.6802	0.8619
	FR-CVLEF	0.7539	0.8782
K3	R_{Max}	0.4957	0.8073
	R_{MLE}	0.7454	0.8728
	$R_{PA-PCNN}$	0.7152	0.8664
	R_{SML}	0.7146	0.8600
	FR-CVLEF	0.7716	0.8743

Table 7. Adaptive parameters obtained in three data sets K1, K2, and K3.

Dataset	ρ_1	ρ_2	ρ_3
K1	0.9927	0.0453	0.999
K2	0.9829	0.0524	0.999
K3	0.9942	0.0575	0.999

In the second experiment, we compared our fusion rules with four other fusion rules for SS and LS layers. We evaluated the five indicators, and the results are presented in Table 6. Our FR_CVLEF rule performed

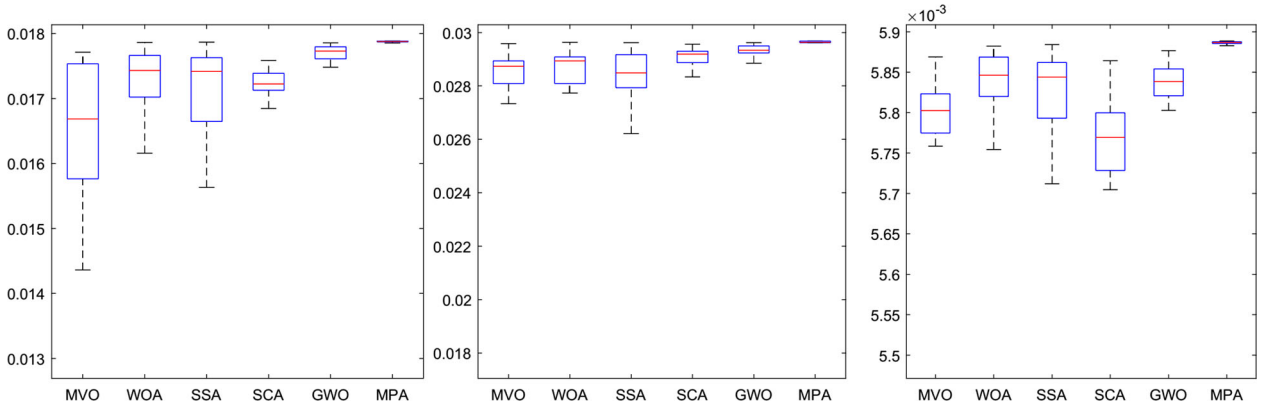

Figure 11. The fitness function values obtained from various optimization algorithms in 30 independent on dataset K4 runs are visually presented in the form of a box plot.

the best as it obtained the highest scores for two evaluation indicators, $Q^{AB/F}$ and Q_{FMI}, compared to the other fusion rules.

For the third experiment, adaptive parameters were obtained and are listed in Table 7. A value of approximately 1 for ρ_3 indicates that the fused image has the highest similarity to the MRI image. Moreover, the ρ_1 value is considerably larger than the ρ_2 value, which suggests that the MRI images provide substantial information to the output image. The output images were generated using seven image fusion algorithms, including our own algorithm, which is depicted in Figures 12, 15, and 18. Visual inspection indicates that the output image produced by our algorithm exhibits high quality in terms of light intensity, contrast, and sharpness. A small area was cropped from the image to observe its details, as shown in Figures 13, 16, and 19. The details in these small areas are well preserved. In terms of quantitative analysis, Table 8 presents the five evaluation indicators obtained from various image fusion algorithms. The proposed method's output image has significantly higher quality than the other image fusion methods due to the adaptive rule used for the base layers. The FR_CVLRF method guarantees the output images retain the input image details.

Table 9 displays the average running times of the image fusion algorithms. The algorithm developed by us takes an average of 4.58 seconds to complete the fusion process. However, this time increases as the number of iterations increases, making it a disadvantage of our algorithm.

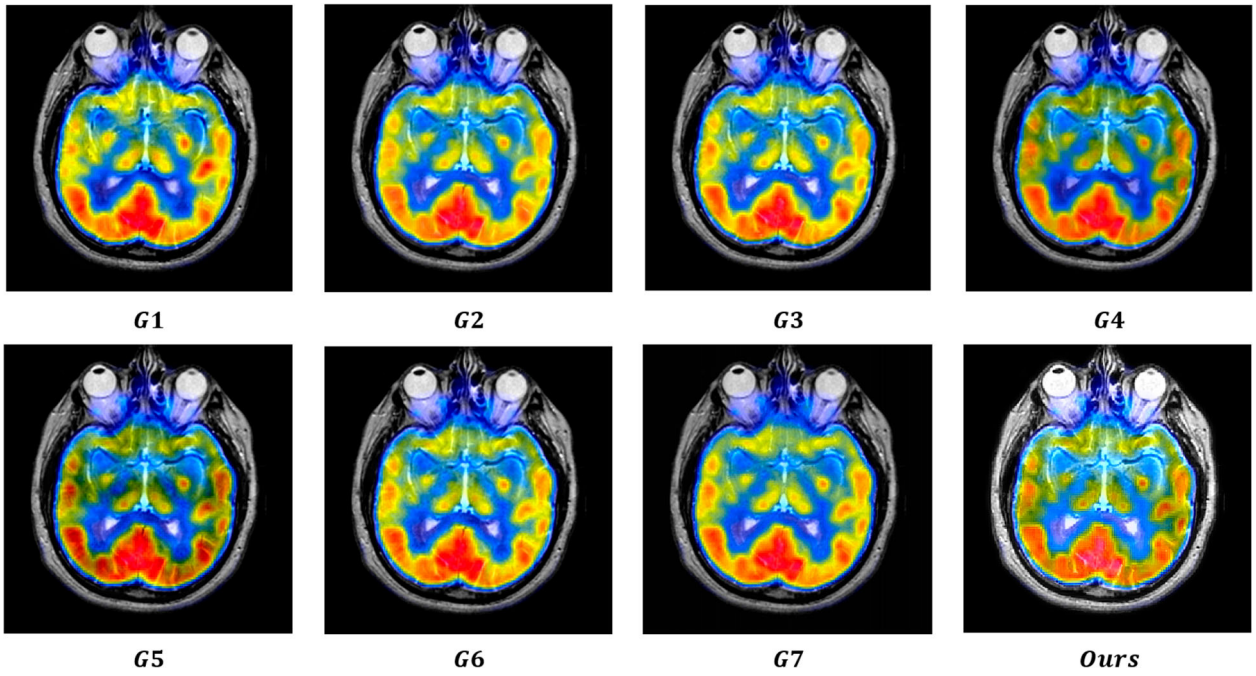

Figure 12. Results obtained from eight image fusion algorithms for MRI-PET image pair #068T in K1.

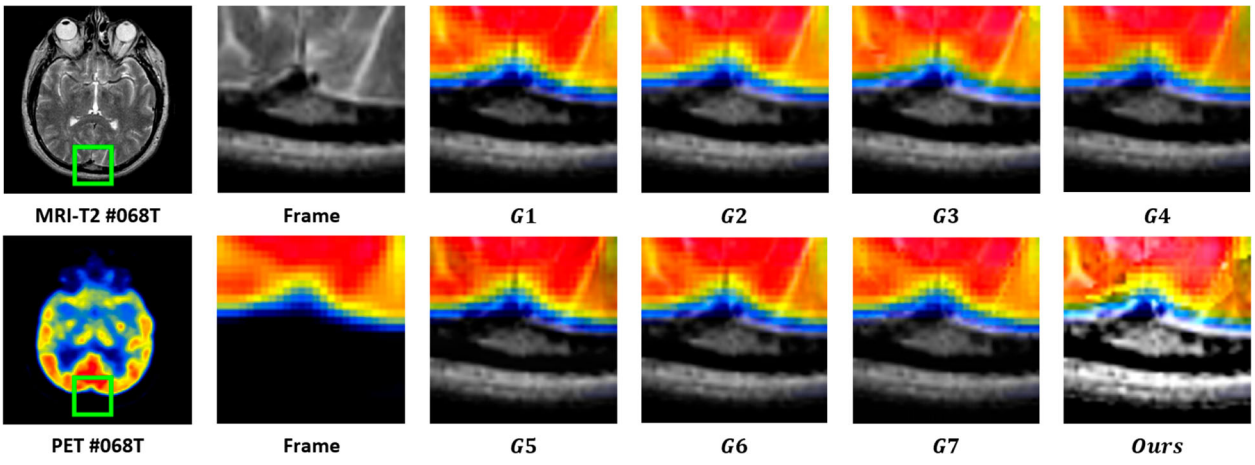

Figure 13. Frames cropped from Figure 12.

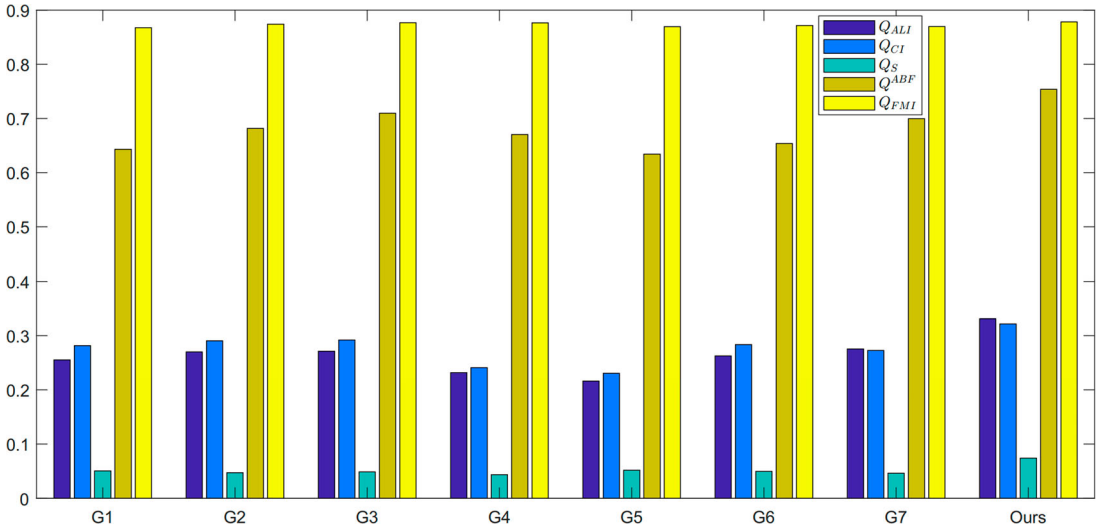

Figure 14. Five evaluation indicators are obtained from eight image synthesis algorithms on K1.

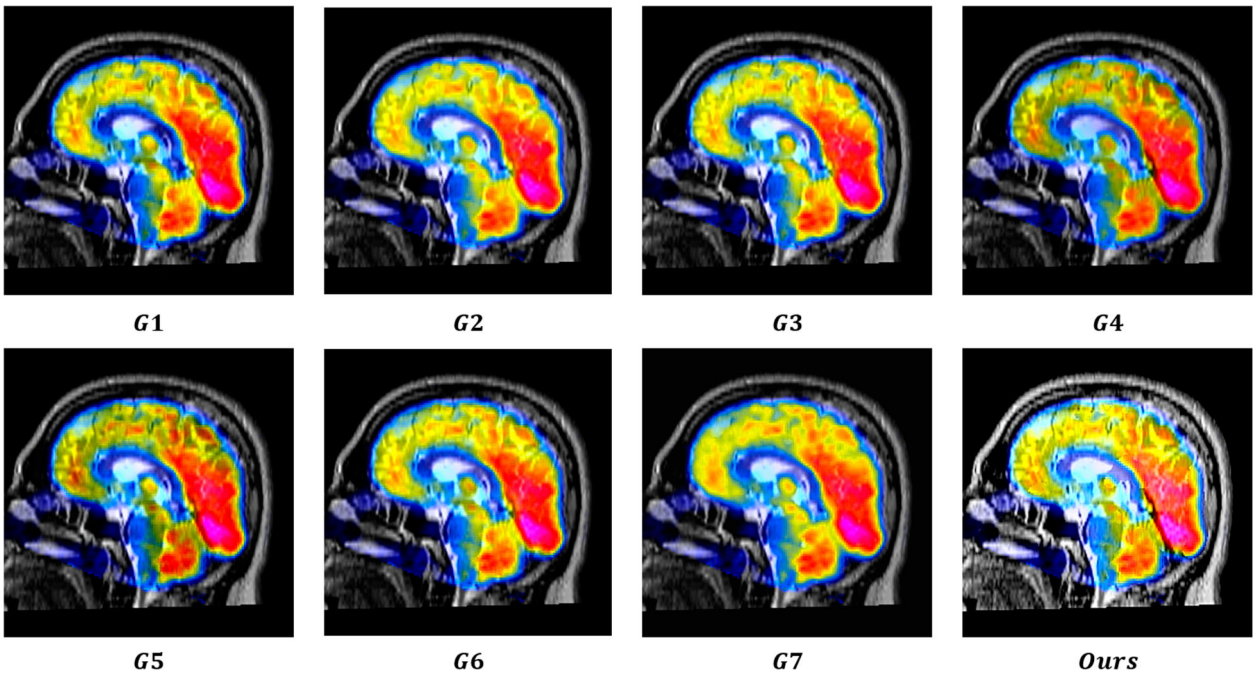

Figure 15. Results obtained from eight image fusion algorithms for MRI-PET image pair #068S in K2.

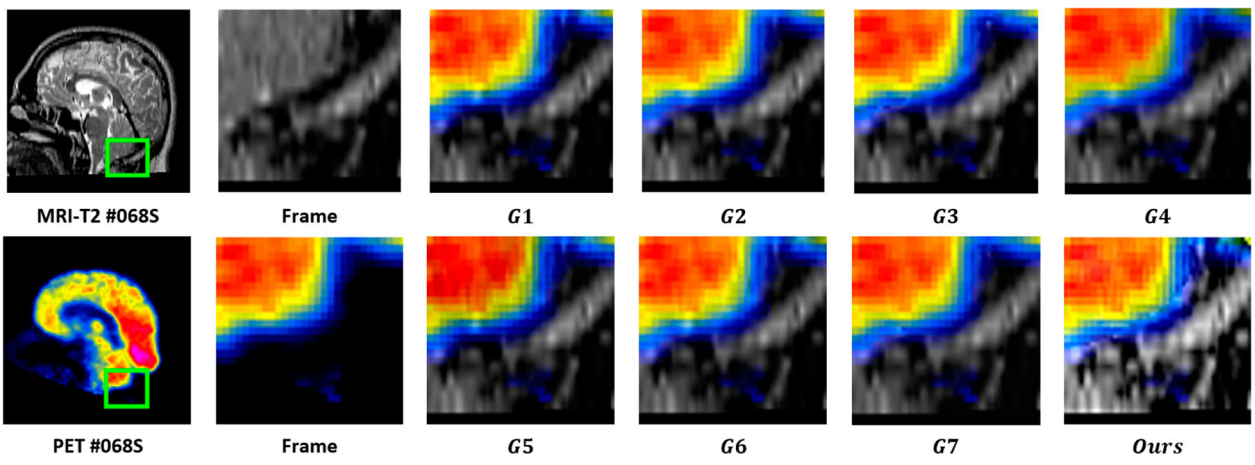

Figure 16. Frames cropped from Figure 15.

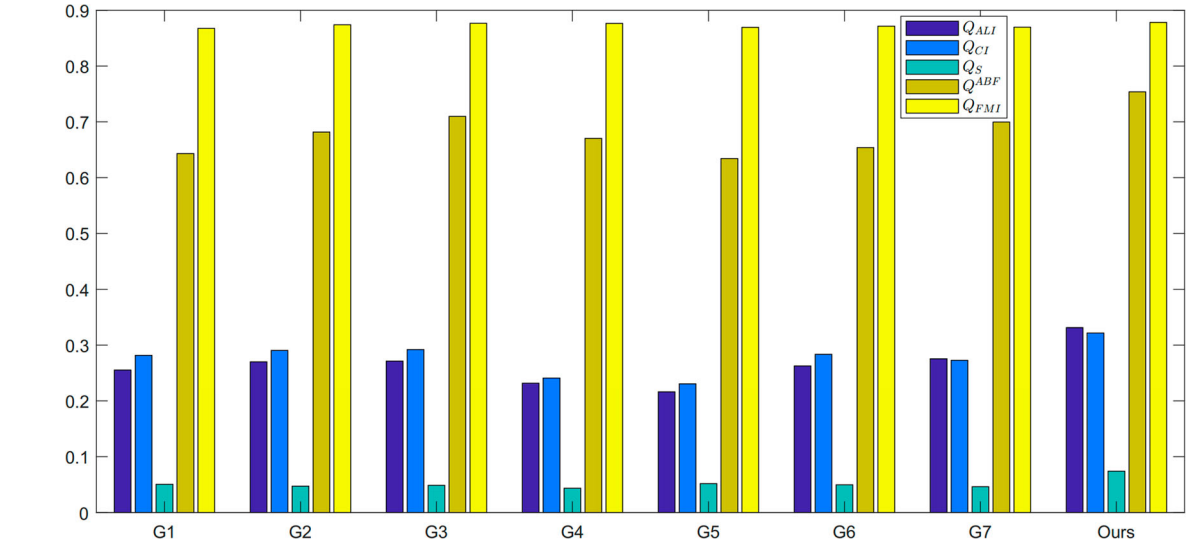

Figure 17. Five evaluation indicators are obtained from eight image synthesis algorithms on K2.

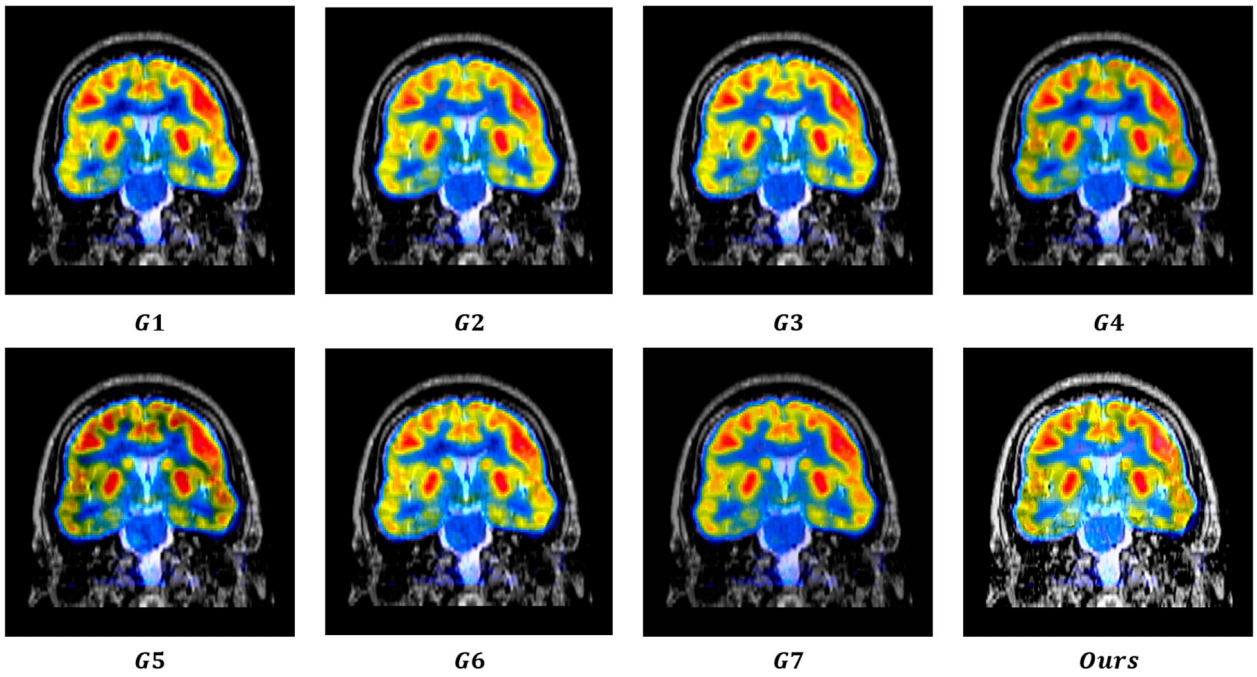

Figure 18. Results obtained from eight image fusion algorithms for MRI-PET image pair #068C in K3.

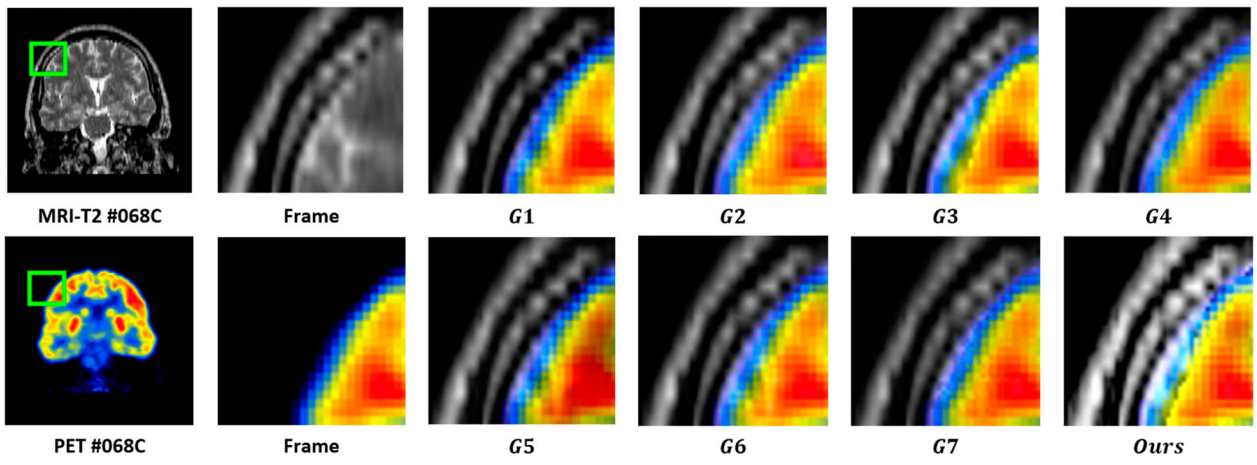

Figure 19. Frames cropped from Figure 18.

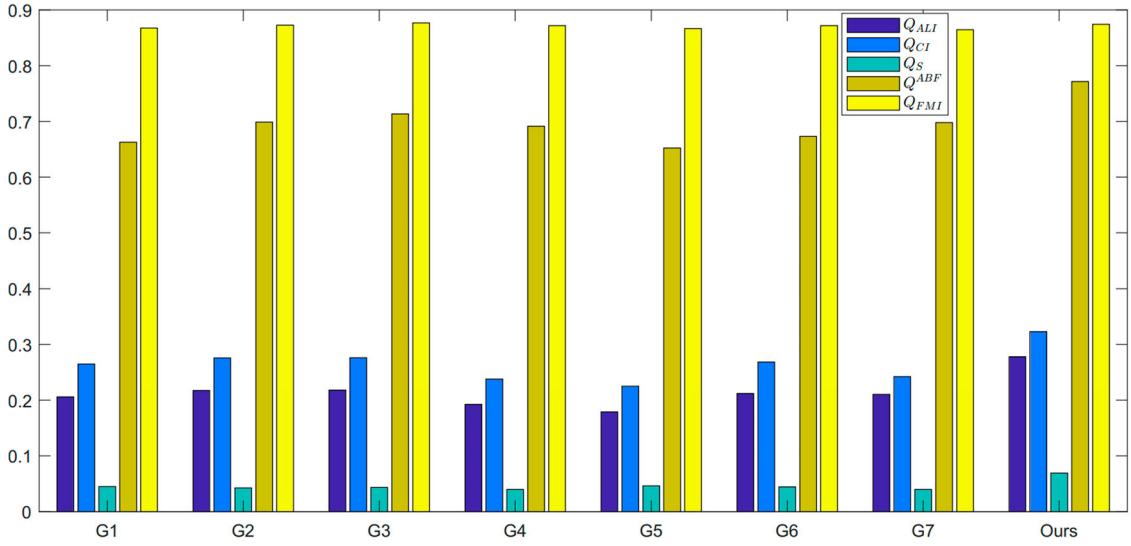

Figure 20. Five evaluation indicators are obtained from eight image synthesis algorithms on K3.

Table 8. The evaluation indicators obtained from image fusion algorithms.

Dataset	Algorithms	Q_{ALI}	Q_{CI}	Q_S	$Q^{AB/F}$	Q_{FMI}
K1	G1	0.2492	0.2910	0.0528	0.6248	0.8569
	G2	0.2634	0.2997	0.0499	0.6786	0.8646
	G3	0.2634	0.2992	0.0511	0.6771	0.8682
	G4	0.2233	0.2479	0.0461	0.6552	0.8681
	G5	0.2060	0.2382	0.0546	0.6192	0.8583
	G6	0.2558	0.2922	0.0522	0.6376	0.8619
	G7	0.2415	0.2596	0.0470	0.6587	0.8562
	Ours	0.3131	0.3356	0.0829	0.7440	0.8737
K2	G1	0.2555	0.2816	0.0506	0.6432	0.8675
	G2	0.2700	0.2905	0.0474	0.6818	0.8740
	G3	0.2713	0.2920	0.0487	0.7099	0.8765
	G4	0.2317	0.2410	0.0435	0.6703	0.8762
	G5	0.2162	0.2305	0.0517	0.6344	0.8694
	G6	0.2626	0.2835	0.0497	0.6537	0.8714
	G7	0.2754	0.2727	0.0463	0.6996	0.8695
	Ours	0.3313	0.3217	0.0740	0.7539	0.8782
K3	G1	0.2060	0.2648	0.0452	0.6628	0.8674
	G2	0.2175	0.2757	0.0428	0.6987	0.8726
	G3	0.2181	0.2761	0.0435	0.7133	0.8766
	G4	0.1925	0.2380	0.0398	0.6914	0.8716
	G5	0.1789	0.2251	0.0463	0.6524	0.8665
	G6	0.2120	0.2684	0.0446	0.6732	0.8716
	G7	0.2103	0.2421	0.0400	0.6980	0.8644
	Ours	0.2778	0.3230	0.0693	0.7716	0.8743

Table 9. Average running time (ART) of image fusion algorithms on the data set (K1&K2&K3).

Approaches	ART (s)
G1	3.02972
G2	14.92673
G3	0.26316
G4	0.10035
G5	3.36244
G6	17.90511
G7	1.05729
Ours (50 loops)	4.57611

5. Conclusion

In this paper, a new approach for fusing medical images is introduced, which combines a local energy function and variations of it with the MPA algorithm. The proposed method starts by introducing a three-layer image decomposition technique, which separates the input images into three distinct layers: the base layer (L_B), the small-scale structure layer (L_{SS}), and the large-scale structure layer (L_{LS}). Next, a fusion rule built on combining the local energy function with its variations is introduced to fuse the L_{SS} and L_{LS} layers. Thirdly, the base layers are synthesized based on the MPA algorithm. The method was tested using 156 MRI-T2 and PET images, along with five evaluation metrics and seven state-of-the-art image fusion algorithms. The proposed adaptive rules for the base layers resulted in an output composite image that had a high level of quality in terms of brightness intensity and contrast. For example, from Table 8, the Q_{ALI} and Q_{CI} indexes obtained from the proposed model are the highest, at 0.3131 and 0.3356 on data set K1. Furthermore, applying the FR_CVLEF method to the small-scale and large-scale

structure layers has also shown significant efficiency in the detailed information of the output image. For instance, from Table 8, the Q_S, $Q_{AB/F}$, and Q_{FMI} indexes obtained from the proposed model are the highest, at 0.0829, 0.7440, and 0.8737 on data set K1, respectively.

In the future, our goal is to enhance the performance of the proposed model in several aspects. First, apply new image enhancement methods [74–76] to replace the BLLI method. This allows for significantly improved performance of image synthesis. Second, select some recent optimization algorithms, such as the Chameleon swarm algorithm (CSA) [77, 78] and White Shark Optimizer (WSO) [79], to replace the MPA algorithm. This can improve the runtime of the proposed model.

Disclosure statement

No potential conflict of interest was reported by the author(s).

Notes on contributor

Phu-Hung Dinh was born in Vietnam. Currently, he is a lecturer at the Faculty of Computer Science and Engineering, Thuyloi University, Hanoi, Vietnam. His research interests include signal processing, image processing, meta-heuristic optimization, and computer vision. Furthermore, he is also a reviewer for many prestigious journals, such as Expert systems with applications, Artificial intelligence review, Computers in biology and medicine, Biomedical signal processing & control, ISA transactions, BMC Bioinformatics, Applied Intelligence, Soft Computing, Imaging science journal, and Journal of Supercomputing.

ORCID

Phu-Hung Dinh http://orcid.org/0000-0002-8050-4086

References

[1] Wang Z, Li X, Duan H, et al. Multifocus image fusion using convolutional neural networks in the discrete wavelet transform domain. Multimed Tools Appl. 2019;78(24):34483–34512. doi:10.1007/s11042-019-08070-6.

[2] Dinh PH. Combining gabor energy with equilibrium optimizer algorithm for multi-modality medical image fusion. Biomed Signal Process Control. 2021;68:102696. doi:10.1016/j.bspc.2021.102696.

[3] Fu J, Li W, Du J, et al. Multimodal medical image fusion via laplacian pyramid and convolutional neural network reconstruction with local gradient energy strategy. Comput Biol Med. 2020;126:104048. doi:10.1016/j.compbiomed.2020.104048.

[4] Wang Z, Li X, Duan H, et al. Medical image fusion based on convolutional neural networks and non-subsampled contourlet transform. Expert Syst Appl. 2021;171:114574. doi:10.1016/j.eswa.2021.114574.

[5] Gao Y, Ma S, Liu J, et al. Fusion of medical images based on salient features extraction by PSO optimized fuzzy logic in NSST domain. Biomed Signal Process Control. 2021;69:102852. doi:10.1016/j.bspc.2021.102852.

[6] Nair RR, Singh T. MAMIF: multimodal adaptive medical image fusion based on b-spline registration and non-subsampled shearlet transform. Multimed Tools Appl. 2021;80(12):19079–19105. doi:10.1007/s11042-020-10439-x.

[7] Wang S, Shen Y. Multi-modal image fusion based on saliency guided in NSCT domain. IET Image Process.. 2020;14:3188–3201. doi:10.1049/iet-ipr.2019.1319..

[8] Nair RR, Singh T. An optimal registration on shearlet domain with novel weighted energy fusion for multimodal medical images. Optik. 2021;225:165742. doi:10.1016/j.ijleo.2020.165742.

[9] Dinh PH. A novel approach based on grasshopper optimization algorithm for medical image fusion. Expert Syst Appl. 2021;171:114576. doi:10.1016/j.eswa.2021.114576.

[10] Li X, Zhou F, Tan H. Joint image fusion and denoising via three-layer decomposition and sparse representation. Knowl Based Syst. 2021;224:107087. doi:10.1016/j.knosys.2021.107087.

[11] Wang Y, Li X, Zhu R, et al. A multi-focus image fusion framework based on multi-scale sparse representation in gradient domain. Signal Processing. 2021;189:108254. doi:10.1016/j.sigpro.2021.108254.

[12] Jie Y, Zhou F, Tan H, et al. Tri-modal medical image fusion based on adaptive energy choosing scheme and sparse representation. Measurement. 2022;204:112038. doi:10.1016/j.measurement.2022.112038.

[13] Liu Y, Zhou D, Nie R, et al. Robust spiking cortical model and total-variational decomposition for multimodal medical image fusion. Biomed Signal Process Control. 2020;61:101996. doi:10.1016/j.bspc.2020.101996.

[14] Liu Y, Hou R, Zhou D, et al. Multimodal medical image fusion based on the spectral total variation and local structural patch measurement. Int J Imaging Syst Technol. 2020;31(1):391–411. doi:10.1002/ima.22460.

[15] Wang J, Li X, Wang Z, et al. Exposure correction using deep learning. J Electron Imaging. 2019;28(3):1. doi:10.1117/1.jei.28.3.033003.

[16] Gai S, Bao Z. New image denoising algorithm via improved deep convolutional neural network with perceptive loss. Expert Syst Appl. 2019;138:112815. doi:10.1016/j.eswa.2019.07.032.

[17] Hou R, Zhou D, Nie R, et al. Brain CT and MRI medical image fusion using convolutional neural networks and a dual-channel spiking cortical model. Med Biol Eng Comput. 2018;57(4):887–900. doi:10.1007/s11517-018-1935-8.

[18] Ding Z, Zhou D, Nie R, et al. Brain medical image fusion based on dual-branch CNNs in NSST domain. Biomed Res Int. 2020;2020:1–15. doi:10.1155/2020/6265708.

[19] Ding Z, Zhou D, Li H, et al. Siamese networks and multi-scale local extrema scheme for multimodal brain medical image fusion. Biomed Signal Process Control. 2021;68:102697. doi:10.1016/j.bspc.2021.102697.

[20] Kaur M, Singh D. Fusion of medical images using deep belief networks. Cluster Comput. 2019;23(2):1439–1453. doi:10.1007/s10586-019-02999-x.

[21] Yousif AS, Omar Z, Sheikh UU. An improved approach for medical image fusion using sparse representation and siamese convolutional neural network. Biomed Signal Process Control. 2022;72:103357. doi:10.1016/j.bspc.2021.103357.

[22] Guo K, Hu X, Li X. MMFGAN: A novel multimodal brain medical image fusion based on the improvement of generative adversarial network. Multimed Tools Appl. 2021;81:5889–5927. doi:10.1007/s11042-021-11822-y.

[23] Li W, Peng X, Fu J, et al. A multiscale double-branch residual attention network for anatomical–functional medical image fusion. Comput Biol Med. 2021;141:105005. doi:10.1016/j.compbiomed.2021.105005.
[24] Wang Z, Li X, Yu S, et al. VSP-fuse: multifocus image fusion model using the knowledge transferred from visual salience priors. IEEE Trans Circuits Syst Video Technol. 2022:1–1. doi:10.1109/tcsvt.2022.3229691.
[25] Wang Z, Li X, Duan H, et al. A self-supervised residual feature learning model for multifocus image fusion. IEEE Trans Image Process. 2022;31:4527–4542. doi:10.1109/tip.2022.3184250.
[26] Dinh PH. Multi-modal medical image fusion based on equilibrium optimizer algorithm and local energy functions. Appl Intell. 2021;51:8416–8431. doi:10.1007/s10489-021-02282-w.
[27] Shilpa S, Rajan MR, Asha C, et al. Enhanced JAYA optimization based medical image fusion in adaptive non subsampled shearlet transform domain. Eng Sci Technol Int J. 2022;35:101245. doi:10.1016/j.jestch.2022.101245..
[28] Shehanaz S, Daniel E, Guntur SR, et al. Optimum weighted multimodal medical image fusion using particle swarm optimization. Optik. 2021;231:166413. doi:10.1016/j.ijleo.2021.166413.
[29] Xu L, Si Y, Jiang S, et al. Medical image fusion using a modified shark smell optimization algorithm and hybrid wavelet-homomorphic filter. Biomed Signal Process Control. 2020;59:101885. doi:10.1016/j.bspc.2020.101885.
[30] Dinh PH. Medical image fusion based on enhanced three-layer image decomposition and chameleon swarm algorithm. Biomed Signal Process Control. 2023;84:104740. doi:10.1016/j.bspc.2023.104740.
[31] Jose J, Gautam N, Tiwari M, et al. An image quality enhancement scheme employing adolescent identity search algorithm in the NSST domain for multimodal medical image fusion. Biomed Signal Process Control. 2021;66:102480. doi:10.1016/j.bspc.2021.102480.
[32] Dinh PH. An improved medical image synthesis approach based on marine predators algorithm and maximum gabor energy. Neural Comput Appl. 2021;34:4367–4385. doi:10.1007/s00521-021-06577-4.
[33] Nguyen TT, Wang HJ, Dao TK, et al. A scheme of color image multithreshold segmentation based on improved moth-flame algorithm. IEEE Access. 2020;8:174142–174159. doi:10.1109/access.2020.3025833.
[34] Nguyen TT, Ngo TG, Dao TK, et al. Microgrid operations planning based on improving the flying sparrow search algorithm. Symmetry. 2022;14(1):168. doi:10.3390/sym14010168.
[35] Liu Y, Chen X, Ward RK, et al. Image fusion with convolutional sparse representation. IEEE Signal Process Lett. 2016;23(12):1882–1886. doi:10.1109/lsp.2016.2618776.
[36] Liu Y, Chen X, Ward RK, et al. Medical image fusion via convolutional sparsity based morphological component analysis. IEEE Signal Process Lett. 2019;26:485–489. doi:10.1109/lsp.2019.2895749.
[37] Maqsood S, Javed U. Multi-modal medical image fusion based on two-scale image decomposition and sparse representation. Biomed Signal Process Control. 2020;57:101810. doi:10.1016/j.bspc.2019.101810.
[38] Dong X, Wang G, Pang Y, et al. Fast efficient algorithm for enhancement of low lighting video. In: 2011 IEEE International Conference on Multimedia and Expo. IEEE; 2011. doi:10.1109/icme.2011.6012107.
[39] Amini N, Fatemizadeh E, Behnam H. MRI-PET image fusion based on NSCT transform using local energy and local variance fusion rules. J Med Eng Technol. 2014;38(4):211–219. doi:10.3109/03091902.2014.904014.
[40] Yin H. Tensor sparse representation for 3-d medical image fusion using weighted average rule. IEEE Trans Biomed Eng. 2018;65(11):2622–2633. doi:10.1109/tbme.2018.2811243.
[41] Zhou J, Xing X, Yan M, et al. A fusion algorithm based on composite decomposition for PET and MRI medical images. Biomed Signal Process Control. 2022;76:103717. doi:10.1016/j.bspc.2022.103717.
[42] Du J, Li W, Tan H. Three-layer medical image fusion with tensor-based features. Inf Sci (Ny). 2020;525:93–108. doi:10.1016/j.ins.2020.03.051.
[43] Li X, Zhou F, Tan H, et al. Multimodal medical image fusion based on joint bilateral filter and local gradient energy. Inf Sci (Ny). 2021;569:302–325. doi:10.1016/j.ins.2021.04.052.
[44] Zhang Q, Shen X, Xu L, et al. Rolling guidance filter. In: Computer Vision–ECCV 2014. Springer International Publishing; 2014. p. 815–830. doi:10.1007/978-3-319-10578-9_53.
[45] Gong Y, Goksel O. Weighted mean curvature. Signal Processing. 2019;164:329–339. doi:10.1016/j.sigpro.2019.06.020.
[46] Pan Y, Liu D, Wang L, et al. A multispectral and panchromatic images fusion method based on weighted mean curvature filter decomposition. Appl Sci. 2022;12(17):8767. doi:10.3390/app12178767.
[47] Tan W, Thitøn W, Xiang P, et al. Multi-modal brain image fusion based on multi-level edge-preserving filtering. Biomed Signal Process Control. 2021;64:102280. doi:10.1016/j.bspc.2020.102280.
[48] Dong W, Xiao S, Liang J, et al. Fusion of hyperspectral and panchromatic images using structure tensor and matting model. Neurocomputing. 2020;399:237–246. doi:10.1016/j.neucom.2020.02.050.
[49] Liu K, Xu W, Wu H, et al. Weighted hybrid order total variation model using structure tensor for image denoising. Multimed Tools Appl. 2022;82:927–943. doi:10.1007/s11042-022-12393-2..
[50] Zhou Z, Li S, Wang B. Multi-scale weighted gradient-based fusion for multi-focus images. Inf Fusion. 2014;20:60–72. doi:10.1016/j.inffus.2013.11.005.
[51] Polinati S, Dhuli R. Multimodal medical image fusion using empirical wavelet decomposition and local energy maxima. Optik. 2020;205:163947. doi:10.1016/j.ijleo.2019.163947.
[52] Dinh PH. A novel approach using structure tensor for medical image fusion. Multidimens Syst Signal Process. 2022;33(3):1001–1021. doi:10.1007/s11045-022-00829-9.
[53] Faramarzi A, Heidarinejad M, Mirjalili S, et al. Marine predators algorithm: A nature-inspired metaheuristic. Expert Syst Appl. 2020;152:113377. doi:10.1016/j.eswa.2020.113377.
[54] Rashedi E, Nezamabadi-pour H, Saryazdi S. GSA: A gravitational search algorithm. Inf Sci (Ny). 2009;179(13):2232–2248. doi:10.1016/j.ins.2009.03.004.
[55] Mirjalili S, Gandomi AH, Mirjalili SZ, et al. Salp swarm algorithm: A bio-inspired optimizer for engineering design problems. Adv Eng Softw. 2017;114:163–191. doi:10.1016/j.advengsoft.2017.07.002.
[56] Ho LV, Nguyen DH, Mousavi M, et al. A hybrid computational intelligence approach for structural damage

detection using marine predator algorithm and feedforward neural networks. Comput Struct. 2021;252:106568. doi:10.1016/j.compstruc.2021.106568.
[57] Houssein EH, Hussain K, Abualigah L, et al. An improved opposition-based marine predators algorithm for global optimization and multilevel thresholding image segmentation. Knowl Based Syst. 2021;229:107348. doi:10.1016/j.knosys.2021.107348.
[58] Dinh PH. A novel approach based on three-scale image decomposition and marine predators algorithm for multi-modal medical image fusion. Biomed Signal Process Control. 2021;67:102536. doi:10.1016/j.bspc.2021.102536.
[59] Li S, Kang X, Hu J. Image fusion with guided filtering. IEEE Trans Image Process. 2013;22(7):2864–2875. doi:10.1109/tip.2013.2244222.
[60] Mirjalili S, Mirjalili SM, Hatamlou A. Multi-verse optimizer: a nature-inspired algorithm for global optimization. Neural Comput Appl. 2015;27(2):495–513. doi:10.1007/s00521-015-1870-7.
[61] Mirjalili S, Lewis A. The whale optimization algorithm. Adv Eng Softw. 2016;95:51–67. doi:10.1016/j.advengsoft.2016.01.008.
[62] Mirjalili S. SCA: a sine cosine algorithm for solving optimization problems. Knowl Based Syst. 2016;96:120–133. doi:10.1016/j.knosys.2015.12.022.
[63] Lu H, Zhang L, Serikawa S. Maximum local energy: an effective approach for multisensor image fusion in beyond wavelet transform domain. Comput Math Appl. 2012;64(5):996–1003. doi:10.1016/j.camwa.2012.03.017.
[64] Yin M, Liu X, Liu Y, et al. Medical image fusion with parameter-adaptive pulse coupled neural network in nonsubsampled shearlet transform domain. IEEE Trans Instrum Meas. 2019;68:49–64. doi:10.1109/tim.2018.2838778.
[65] Li X, Zhang X, Ding M. A sum-modified-laplacian and sparse representation based multimodal medical image fusion in laplacian pyramid domain. Med Biol Eng Comput. 2019;57(10):2265–2275. doi:10.1007/s11517-019-02023-9.
[66] Zhu Z, Zheng M, Qi G, et al. A phase congruency and local laplacian energy based multi-modality medical image fusion method in NSCT domain. IEEE Access. 2019;7:20811–20824. doi:10.1109/access.2019.2898111.
[67] Sufyan A, Imran M, Shah SA, et al. A novel multimodality anatomical image fusion method based on contrast and structure extraction. Int J Imaging Syst Technol. 2021;32(1):324–342. doi:10.1002/ima.22649.
[68] Li B, Peng H, Luo X, et al. Medical image fusion method based on coupled neural *p* systems in nonsubsampled shearlet transform domain. Int J Neural Syst. 2020;31(01):2050050. doi:10.1142/s0129065720500501.
[69] Li B, Peng H, Wang J. A novel fusion method based on dynamic threshold neural p systems and nonsubsampled contourlet transform for multi-modality medical images. Signal Processing. 2021;178:107793. doi:10.1016/j.sigpro.2020.107793.
[70] Zhu R, Li X, Huang S, et al. Multimodal medical image fusion using adaptive co-occurrence filter-based decomposition optimization model. Bioinformatics. 2021;38(3):818–826. doi:10.1093/bioinformatics/btab721.
[71] Xydeas C, Petrovic V. Objective image fusion performance measure. Electron Lett. 2000;36:308. doi:10.1049/el:20000267.
[72] Haghighat MBA, Aghagolzadeh A, Seyedarabi H. A non-reference image fusion metric based on mutual information of image features. Comput Electr Eng. 2011;37:744–756. doi:10.1016/j.compeleceng.2011.07.012.
[73] Wilcoxon F. Individual comparisons by ranking methods. Biometrics Bulletin. 1945;1(6):80. doi:10.2307/3001968.
[74] Su Y, Li Z, Yu H, et al. Multi-band weighted lp norm minimization for image denoising. Inf Sci (Ny). 2020;537:162–183. doi:10.1016/j.ins.2020.05.049.
[75] Dinh PH, Giang NL. A new medical image enhancement algorithm using adaptive parameters. Int J Imaging Syst Technol. 2022;32:2198–2218. doi:10.1002/ima.22778.
[76] Dinh PH. A novel approach based on marine predators algorithm for medical image enhancement. Sens Imaging. 2023;24(1):6. doi:10.1007/s11220-023-00411-y.
[77] Braik MS. Chameleon swarm algorithm: a bio-inspired optimizer for solving engineering design problems. Expert Syst Appl. 2021;174:114685. doi:10.1016/j.eswa.2021.114685.
[78] Dinh PH. Combining spectral total variation with dynamic threshold neural *p* systems for medical image fusion. Biomed Signal Process Control. 2023;80:104343. doi:10.1016/j.bspc.2022.104343.
[79] Braik M, Hammouri A, Atwan J, et al. White shark optimizer: A novel bio-inspired meta-heuristic algorithm for global optimization problems. Knowl Based Syst. 2022;243:108457. doi:10.1016/j.knosys.2022.108457.

LIÊN HIỆP CÁC HỘI KHOA HỌC VÀ KỸ THUẬT VIỆT NAM

FAIR

KỶ YẾU HỘI NGHỊ KHOA HỌC CÔNG NGHỆ QUỐC GIA LẦN THỨ XV

Nghiên cứu cơ bản và Ứng dụng công nghệ thông tin

Proceedings of the 15th National Conference on Fundamental and Applied Information Technology Research (FAIR'2022)

Học viện Kỹ thuật Mật mã, Hà Nội
03-04/11/2022

NHÀ XUẤT BẢN KHOA HỌC TỰ NHIÊN VÀ CÔNG NGHỆ

ĐỊA CHỈ LIÊN HỆ

- **Viện Công nghệ thông tin - Đại học Quốc gia Hà Nội**
  P.612, E3, 144 Xuân Thủy, Cầu Giấy, Hà Nội

LỜI NÓI ĐẦU

Nhằm góp phần thúc đẩy nghiên cứu cơ bản và ứng dụng về Công nghệ thông tin tại Việt Nam, Liên hiệp các Hội Khoa học và Kỹ thuật Việt Nam, Viện Hàn lâm Khoa học và Công nghệ Việt Nam phối hợp cùng Học viện Kỹ thuật Mật mã, Ban Cơ yếu Chính phủ và các cơ quan khoa học, các nhà khoa học từ các viện nghiên cứu, các trường đại học đã tổ chức Hội nghị Khoa học quốc gia lần thứ XV về "Nghiên cứu cơ bản và ứng dụng Công nghệ thông tin" (gọi tắt là FAIR'2022) từ ngày 03-04/11/2022 tại Học viện Kỹ thuật Mật mã, Ban Cơ yếu Chính phủ.

Chủ đề chính của Hội nghị FAIR'2022 là "An toàn và bảo mật thông tin trong cuộc Cách mạng Công nghiệp lần thứ IV". Tuy nhiên, do truyền thống của Hội nghị nên cũng không hạn chế về nội dung trong các hướng nghiên cứu khác thuộc lĩnh vực công nghệ thông tin và truyền thông. Hội nghị FAIR'2022 được sự bảo trợ chuyên môn của 3 cơ sở đào tạo uy tín trong lĩnh vực công nghệ thông tin và truyền thông là Học viện Công nghệ Bưu chính Viễn thông, Trường Đại học Công nghệ Thông tin & Truyền thông - Đại học Thái Nguyên, Viện Công nghệ Thông tin – Đại học Quốc gia Hà Nội.

Hội nghị đã nhận được 128 báo cáo khoa học đăng ký tham dự về tất cả các vấn đề thời sự của Công nghệ thông tin và truyền thông. Ban Chương trình đã tiến hành công việc phản biện và xét duyệt chặt chẽ và chấp nhận 73 bài được trình bày tại Hội nghị, trong số này có 70 bài được lựa chọn đăng trong Kỷ yếu Hội nghị. Các bài báo cáo được trình bày trong 5 tiểu ban song song:

- Cơ sở dữ liệu và hệ thống thông tin.
- Khoa học dữ liệu.
- Trí tuệ nhân tạo và ứng dụng.
- Xử lý ảnh và thị giác máy tính.
- Mật mã và an toàn an ninh mạng.

Thay mặt Ban Tổ chức và Ban Chương trình, chúng tôi xin cảm ơn các tác giả đã gửi bài tham gia Hội nghị, các nhà khoa học đã tham gia phản biện và có ý kiến xác đáng, khách quan về nội dung các bài gửi đăng. Chúng tôi xin đặc biệt cảm ơn Nhà xuất bản Khoa học tự nhiên và Công nghệ của Viện Hàn lâm Khoa học và Công nghệ Việt Nam đã hỗ trợ và giúp đỡ xuất bản cuốn Kỷ yếu này.

Cuối cùng chúng tôi xin bày tỏ lòng biết ơn sâu sắc tới Liên hiệp các Hội Khoa học và Kỹ thuật Việt Nam, Viện Hàn lâm Khoa học và Công nghệ Việt Nam, 3 đơn vị bảo trợ về mặt chuyên môn cho Hội nghị FAIR và Học viện Kỹ thuật Mật mã, Ban Cơ yếu Chính phủ - đơn vị đăng cai Hội nghị FAIR'2022 đã giành nhiều công sức và thời gian tổ chức Hội nghị này. Đồng thời cũng xin được cảm ơn các đơn vị tài trợ đã giúp đỡ nhiều mặt và tài trợ kinh phí góp phần làm cho Hội nghị FAIR'2022 thành công tốt đẹp.

BAN BIÊN TẬP

ĐƠN VỊ TỔ CHỨC **ĐƠN VỊ ĐỒNG HÀNH**

BAN CHỈ ĐẠO

Trưởng ban:
GS.VS. Đặng Vũ Minh — Liên hiệp các Hội KHKT VN
Đồng Trưởng ban:
TSKH. Phan Xuân Dũng — Liên hiệp các Hội KHKT VN

Thành viên:
GS.TS. Đặng Quang Á — Viện Hàn lâm KHCNVN
TS. Nguyễn Hữu Hùng — Học viện KTMM
PGS.TS. Trần Văn Lăng — Viện Hàn lâm KHCNVN
GS.TSKH. Phạm Thế Long — Học viện KTQS
PGS.TS. Vũ Văn San — Học viện CNBCVT
GS.TSKH. Nguyễn Khoa Sơn — Viện Hàn lâm KHCNVN
GS.TS. Vũ Đức Thi — ĐHQG-HN
GS.TS. Nguyễn Thanh Thủy — ĐHQG-HN

BAN TỔ CHỨC

Trưởng ban:
GS.TS. Vũ Đức Thi — ĐHQG-HN
Đồng Trưởng ban:
TS. Nguyễn Hữu Hùng — Học viện KTMM

Phó Trưởng ban
GS.TS. Đặng Quang Á — Viện Hàn lâm KHCNVN

Thành viên:
PGS.TS. Trần Văn Lăng — Viện Hàn lâm KHCNVN
TS. Lê Quang Minh — Viện CNTT, ĐHQG-HN
GS.TS. Từ Minh Phương — Học viện CNBCVT
TS. Nguyễn Văn Tảo — Trường ĐH CNTT&TT
PGS.TS. Trần Xuân Tú — ĐHQG-HN

BAN CHƯƠNG TRÌNH

Trưởng ban:
PGS.TS. Trần Văn Lăng — Viện Hàn lâm KHCNVN

Phó Trưởng ban:
PGS.TS. Lê Mạnh Thạnh — Trường ĐHKH - ĐH Huế
GS.TS. Từ Minh Phương — Học viện CNBCVT
PGS.TS. Trần Đình Khang — Trường ĐHBK Hà Nội
PGS.TS. Bùi Thu Lâm — Học viện KTMM

Trưởng các tiểu ban:
PGS.TS. Trần Đình Khang — Trí tuệ nhân tạo và ứng dụng
GS.TS. Từ Minh Phương — Khoa học dữ liệu
PGS.TS. Lê Mạnh Thạnh — Cơ sở dữ liệu và hệ thống thông tin
PGS.TS. Bùi Thu Lâm — Xử lý ảnh và thị giác máy tính
TS. Lê Quang Minh — Mật mã và an toàn an ninh mạng

Thành viên Ban Chương trình:

PGS.TS. Nguyễn Việt Anh	Viện CNTT
TS. Cao Kim Ánh	Trường ĐH Thăng Long
PGS.TS. Võ Đình Bảy	Trường ĐH KTCN TP.HCM
PGS.TS. Nguyễn Thanh Bình	Trường ĐH CNTT-TT Việt - Hàn
TS. Phan Anh Cang	Trường ĐHSPKT Vĩnh Long
TS. Nguyễn Ngọc Cương	Bộ Công an
PGS.TS. Lê Bá Dũng	Viện CNTT
PGS.TS. Lương Thế Dũng	Học viện KTMM
PGS.TS. Cao Tuấn Dũng	Trường ĐHBK Hà Nội
TS. Hà Mạnh Đào	Trường ĐHCN Hà Nội
TS. Vũ Thị Đào	Học viện KT Mật mã
PGS.TS. Đinh Điền	Trường ĐHKHTN, ĐHQG-TP.HCM
~~TS. Nguyễn Công Điều~~	Trường ĐH Thăng Long
PGS.TS. Trần Cao Đệ	Trường ĐH Cần Thơ
PGS.TS. Đặng Văn Đức	Viện CNTT
PGS.TS. Trần Quang Đức	Trường ĐHBK Hà Nội
TS. Nguyễn Huy Đức	Trường ĐH Thuỷ lợi
PGS.TS. Nguyễn Long Giang	Viện CNTT
PGS.TS. Trần Mạnh Hà	Trường ĐH HUFLIT
TS. Nguyễn Nam Hải	Ban Cơ yếu Chính phủ
TS. Nguyễn Công Hào	Trung tâm CNTT, ĐH Huế
PGS.TS. Nguyễn Mậu Hân	Trường ĐHKH, ĐH Huế
TS. Nguyễn Hữu Hoà	Trường ĐH Cần Thơ
PGS.TS. Huỳnh Xuân Hiệp	Trường ĐH Cần Thơ
TS. Đặng Thị Thu Hiền	Trường ĐH Thủy lợi
TS. Lâm Thành Hiển	Trường ĐH Lạc Hồng
PGS.TS. Huỳnh Trung Hiếu	Trường ĐHCN TP.HCM
PGS.TS. Nguyễn Ngọc Hóa	Trường ĐH Công nghệ
PGS.TS. Trần Văn Hoài	Trường ĐHBK TP.HCM
TS. Nguyễn Thị Minh Huyền	Trường ĐHKHTN, ĐHQG-HN
PGS.TS. Võ Trung Hùng	Trường ĐH SPKT, ĐH-ĐN
PGS.TS. Vũ Chấn Hưng	Viện ĐH Mở Hà Nội
TS. Lê Minh Hưng	Trường ĐH CNTT
PGS.TS. Phạm Nguyên Khang	Trường ĐH Cần Thơ
PGS.TS. Đặng Trần Khánh	Trường ĐH CNTP TP.HCM
TS. Vũ Như Lân	Trường ĐH Thăng Long
PGS.TS. Ngô Thành Long	Học viện KT Quân sự
PGS.TS. Nguyễn Thiện Luận	Trường ĐH Thăng Long
PGS.TS. Vũ Đức Lung	Trường ĐH CNTT
TS. Hoàng Trọng Minh	Học viện CNBCVT
TS. Lê Quang Minh	Viện CNTT, ĐHQG-HN
PGS.TS. Nguyễn Hiếu Minh	Ban Cơ yếu Chính phủ
PGS.TS. Nguyễn Hà Nam	Viện Toán cao cấp
PGS.TS. Nguyễn Thái Nghe	Trường ĐH Cần Thơ
PGS.TS. Đỗ Thanh Nghị	Trường ĐH Cần Thơ
PGS.TS. Phùng Trung Nghĩa	Trường ĐH CNTT&TT, ĐHTN
PGS.TS. Lý Quốc Ngọc	Trường ĐHKHTN, ĐHQG-TP.HCM
PGS.TS. Đỗ Phúc	Trường ĐH CNTT
TS. Lê Hồng Phương	Trường ĐHKHTN, ĐHQG-HN
GS.TS. Từ Minh Phương	HV Công nghệ BCVT
PGS.TS. Hoàng Quang	Trường ĐHKH, ĐH Huế
TS. Nguyễn Hồng Quang	IFI, ĐHQG-HN
PGS.TS. Nguyễn Hữu Quỳnh	Trường ĐH Thuỷ lợi
PGS.TS. Lê Hoàng Sơn	Viện CNTT, ĐHQG-HN
PGS.TS. Nguyễn Thái Sơn	Trường ĐH Trà Vinh
PGS.TS. Ngô Quốc Tạo	Viện CNTT

TS. Nguyễn Văn Tảo	Trường ĐH CNTT&TT, ĐHTN
TS. Trần Minh Tân	Trung tâm Internet Việt Nam
TS. Vũ Đức Thái	Trường ĐH CNTT&TT, ĐHTN
TS. Ngô Đức Thành	Trường ĐH CNTT
TS. Văn Thế Thành	Trường ĐHSP TP.HCM
PGS.TS. Trịnh Đình Thắng	Trường ĐHSP 2 Hà Nội
GS.TS. Vũ Đức Thi	Viện CNTT, ĐHQG-HN
PGS.TS. Quản Thành Thơ	Trường ĐHBK TP.HCM
PGS.TS. Nguyễn Đình Thuân	Trường ĐH CNTT
GS.TS. Nguyễn Thanh Thủy	Trường ĐH Công nghệ
TS. Phạm Thị Thu Thúy	Trường ĐH Nha Trang
TS. Hoàng Lê Uyên Thục	Trường ĐHBK Đà Nẵng
PGS.TS. Đỗ Năng Toàn	Viện CNTT
TS. Nguyễn Anh Tuấn	Trường ĐH HUFLIT
PGS.TS. Nguyễn Thanh Tùng	Trường ĐH Thủy lợi
PGS.TS. Trần Xuân Tú	Viện CNTT, ĐHQG-HN
PGS.TS. Võ Thanh Tú	Trường ĐHKH, ĐH Huế
PGS.TS. Trương Công Tuấn	Trường ĐHKH, ĐH Huế
PGS.TS. Nguyễn Đình Việt	Trường ĐH Công nghệ
TS. Nguyễn Trần Quốc Vinh	Trường ĐHSP, ĐH-ĐN
PGS.TS. Phạm Trần Vũ	Trường ĐHBK TP. HCM
PGS.TS. Vũ Việt Vũ	Viện CNTT, ĐHQG-HN

BAN TỔ CHỨC ĐỊA PHƯƠNG

Trưởng ban:
TS. Nguyễn Hữu Hùng

Phó Trưởng ban:
PGS.TS. Lương Thế Dũng

Thành viên:
TS. Nguyễn Chung Tiến
TS. Hoàng Đức Thọ
TS. Đỗ Quang Trung
TS. Phạm Văn Hưởng
ThS. Đặng Hùng Việt

BAN THƯ KÝ ĐỊA PHƯƠNG

Trưởng ban:
TS. Vũ Thị Đào

Phó Trưởng Ban:
TS. Đào Bá Anh

Thành viên:
ThS. Đào Hồng Nam
ThS. Lê Khắc Vinh
ThS. Lê Đức Thuận
ThS. Trần Thị Hoa
ThS. Hoàng Thanh Nam

BAN KỸ THUẬT VÀ XUẤT BẢN

Trưởng ban:
TS. Lê Quang Minh

Thành viên:
ThS. Phan Thị Quế Anh
CN. Lê Thị Thiên Hương
ThS. Phan Mạnh Thường

DANH SÁCH CÁC NHÀ KHOA HỌC THAM GIA PHẢN BIỆN

GS.TS. Đặng Quang Á	Viện Hàn lâm KHCNVN
PGS.TS. Nguyễn Việt Anh	Viện CNTT
TS. Đào Bá Anh	Học viện KTMM
PGS.TS. Ngô Xuân Bách	Học viện CNBCVT
PGS.TS. Võ Đình Bảy	Trường ĐH KTCN TP.HCM
PGS.TS. Nguyễn Thanh Bình	Trường ĐHBK Đà Nẵng
TS. Nguyễn Đăng Bình	Trường ĐHKH, ĐH Huế
TS. Phan Anh Cang	Trường ĐH Trà Vinh
TS. Trần Tiến Công	Học viện CNBCVT
PGS.TS. Đỗ Xuân Chợ	Học viện CNBCVT
PGS.TS. Phạm Văn Cường	Học viện CNBCVT
PGS.TS. Hoàng Xuân Dậu	Học viện CNBCVT
PGS.TS. Lê Bá Dũng	Viện CNTT
TS. Ngô Quốc Dũng	Học viện CNBCVT
PGS.TS. Nguyễn Đức Dũng	Viện CNTT
TS. Vũ Thị Đào	Học viện KTMM
PGS.TS. Đinh Điền	Trường ĐHKHTN, ĐHQG-TP.HCM
PGS.TS. Trần Cao Đệ	Trường ĐH Cần Thơ
PGS.TS. Đặng Văn Đức	Viện CNTT
TS. Nguyễn Huy Đức	Trường ĐH Thuỷ lợi
PGS.TS. Trần Quang Đức	Trường ĐHBK Hà Nội
PGS.TS. Nguyễn Long Giang	Viện CNTT
TS. Hà Mạnh Đào	Trường ĐH Công nghiệp Hà Nội
PGS.TS. Phạm Văn Hải	Trường ĐHBK Hà Nội
PGS.TS. Hoàng Hữu Hạnh	Học viện CNBCVT
TS. Nguyễn Công Hào	Trung tâm CNTT, ĐH Huế
PGS.TS. Nguyễn Mậu Hân	Trường ĐHKH, ĐH Huế
PGS.TS. Nguyễn Đình Hân	Trường ĐHBK Hà Nội
PGS.TS. Huỳnh Xuân Hiệp	Trường ĐH Cần Thơ
TS. Đặng Thị Thu Hiền	Trường ĐH Thủy lợi
PGS.TS. Huỳnh Trung Hiếu	Trường ĐHCN TP.HCM
PGS.TS. Nguyễn Ngọc Hóa	Trường ĐH Công nghệ
PGS.TS. Trần Văn Hoài	Trường ĐHBK TP.HCM
TS. Phan Ngọc Hoàng	Trường ĐH Bà Rịa - Vũng Tàu
PGS.TS. Nguyễn Mạnh Hùng	Học viện CNBCVT
PGS.TS. Võ Trung Hùng	Đại học Đà Nẵng
TS. Nguyễn Thị Minh Huyền	Trường ĐHKHTN, ĐHQG-HN
TS. Phạm Văn Hưởng	Học viện KTMM
PGS.TS. Trần Đình Khang	Trường ĐHBK Hà Nội
TS. Lâm Đức Khải	Trường ĐH CNTT
PGS.TS. Nguyễn Tấn Khôi	Trường ĐHBK - ĐH Đà Nẵng
PGS.TS. Trần Văn Lăng	Viện Hàn lâm KHCNVN
PGS.TS. Bùi Thu Lâm	Học viện KTMM
PGS.TS. Ngô Thành Long	Học viện KTQS
PGS.TS. Vũ Đức Lung	Trường ĐH CNTT
TS. Trần Thị Lượng	Học viện KTMM
TS. Hoàng Trọng Minh	Học viện CNBCVT
PGS.TS. Nguyễn Hiếu Minh	Ban Cơ yếu Chính phủ
TS. Lê Quang Minh	Viện CNTT, ĐHQG-HN
TS. Nguyễn Bình Minh	Trường ĐHBK Hà Nội
PGS.TS. Nguyễn Hà Nam	Viện Toán cao cấp
TS. Nguyễn Lưu Thùy Ngân	Trường ĐH CNTT
PGS.TS. Nguyễn Thái Nghe	Trường ĐH Cần Thơ
PGS.TS. Đỗ Thanh Nghị	Trường ĐH Cần Thơ
TS. Nguyễn Văn Nghị	Học viện KTMM
PGS.TS. Phùng Trung Nghĩa	Trường ĐH CNTT&TT, ĐHTN

PGS.TS. Lý Quốc Ngọc	Trường ĐHKHTN, ĐHQG-TP.HCM
TS. Nguyễn Chung Tiến	Học viện KTMM
PGS.TS. Võ Viết Minh Nhật	Trường ĐHKH, Đại học Huế
TS. Phan Anh Phong	Trường ĐH Giao thông Vận tải
GS.TS. Đỗ Phúc	Trường ĐH CNTT
TS. Lê Hồng Phương	Trường ĐHKHTN, ĐHQG-HN
GS.TS. Từ Minh Phương	Học viện CNBCVT
PGS.TS. Hoàng Quang	Trường ĐHKH, ĐH Huế
PGS.TS. Nguyễn Hữu Quỳnh	Trường ĐH Thuỷ lợi
PGS.TS. Lê Hoàng Sơn	Viện CNTT, ĐHQG-HN
PGS.TS. Nguyễn Thái Sơn	Trường ĐH Trà Vinh
TS. Nguyễn Văn Tảo	Trường ĐH CNTT&TT, ĐHTN
TS. Trần Minh Tân	Trung tâm Internet Việt Nam
TS. Vũ Đức Thái	Trường ĐH CNTT&TT, ĐHTN
TS. Ngô Đức Thành	Trường ĐH CNTT
TS. Văn Thế Thành	Trường ĐHSP TP.HCM
TS. Phạm Đình Thành	Trường ĐH Tây Bắc
PGS.TS. Lê Mạnh Thạnh	Trường ĐHKH, ĐH Huế
PGS.TS. Trịnh Đình Thắng	Trường ĐHSP 2 Hà Nội
TS. TS. Nguyễn Thắng	Học viện KTMM
PGS.TS. Huỳnh Quyết Thắng	Trường ĐHBK Hà Nội
TS. Hoàng Đức Thọ	Học viện KTMM
TS. Phạm Huy Thông	Viện CNTT, ĐHQG-HN
PGS.TS. Nguyễn Đình Thuân	Trường ĐH CNTT
TS. Hoàng Lê Uyên Thục	Trường ĐHBK - ĐH Đà Nẵng
TS. Phạm Thị Thu Thúy	Trường ĐH Nha Trang
PGS.TS. Đỗ Năng Toàn	Viện CNTT
TS. Phạm Duy Trung	Học viện KTMM
TS. Nguyễn Đào Trường	Học viện KTMM
PGS.TS. Nguyễn Thanh Tùng	Trường ĐH Thủy lợi
PGS.TS. Trần Xuân Tú	Viện CNTT, ĐHQG-HN
PGS.TS. Võ Thanh Tú	Trường ĐHKH, ĐH Huế
TS. Lại Minh Tuấn	Học viện KTMM
TS. Trần Mạnh Tuấn	Trường ĐH Thuỷ lợi
PGS.TS. Trương Công Tuấn	Trường ĐHKH, ĐH Huế
TS. Nguyễn Trần Quốc Vinh	Trường ĐHSP, ĐHĐN
PGS.TS. Vũ Việt Vũ	Viện CNTT, ĐHQG-HN

MỤC LỤC

1. A NOVEL WEB ATTACK DETECTION MODEL BASED ON FEDERATED LEARNING WITH PARAMETERS COMPRESSING METHOD 1

Tran Anh Tu, Luong The Dung, Vu Thi Van, Pham Xuan Sang

2. TRUY VẤN HIỆU QUẢ DỮ LIỆU KÝ TỰ MÃ HÓA TRONG CƠ SỞ DỮ LIỆU THUÊ NGOÀI 8

Hoàng Ngọc Cảnh, Nguyễn Hiếu Minh

3. PROPOSING SECURE AND EFFICIENT MDS MATRICES TO IMPROVE THE DIFFUSION LAYER OF THE AES BLOCK CIPHER 16

Tran Thi Luong

4. ĐỀ XUẤT CHỈ SỐ TRÙNG HỢP NGÔN NGỮ TIẾNG VIỆT NÂNG CAO ĐỘ AN TOÀN CHO HỆ THỐNG MẬT MÃ VIGENÈRE 25

Lê Văn Tuấn, Nguyễn Đào Trường, Đoàn Thị Bích Ngọc

5. A NOVEL IDS SYSTEM BASED ON HEDGE ALGEBRA FOR DETECTING DDOS ATTACKS IN IOT NETWORKS 34

Hoang Trong Minh, Tran Nhat Hoang, Thai Vu Long, Le Vu Quynh Giang, Vu Nhu Lan, Tran Quy Nam

6. TRÍCH CHỌN ĐẶC TRƯNG CHO MẠNG NƠRON TÍCH CHẬP TRONG BÀI TOÁN NHẬN DIỆN TẤN CÔNG MẠNG 43

Nguyễn Năng Hùng Vân, Đỗ Phúc Hảo, Phạm Minh Tuấn

7. VAQR: MỘT TIẾP CẬN HỌC TĂNG CƯỜNG TRONG ĐỊNH TUYẾN FANET 51

Mai Cường Thọ, Nguyễn Thị Hương Lý, Lê Hữu Bình, Võ Thanh Tú

8. LƯỢC ĐỒ CHỮ KÝ SỐ TẬP THỂ ĐẠI DIỆN DỰA TRÊN BÀI TOÁN TÌM CĂN MODULO CỦA SỐ NGUYÊN TỐ LỚN 59

Tuấn Nguyễn Kim, Hoàng Nguyễn Nhật, Duy Hồ Ngọc, Long Phan

9. CHIẾN LƯỢC GIĂNG BẪY THÍCH ỨNG PHỤC VỤ PHÒNG THỦ CHỦ ĐỘNG TRONG MẠNG KHẢ LẬP TRÌNH 67

Văn Đoàn Bảo Khôi, Phạm Nguyễn Thảo Nhi, Phan Thế Duy, Nghi Hoàng Khoa, Phạm Văn Hậu

10. ĐỀ XUẤT GIAO THỨC QUẢN LÝ KHÓA AN TOÀN TRONG MẠNG IOT CÓ PHÂN CẤP 75

Nguyễn Đào Trường, Đoàn Thị Bích Ngọc

11. GIẤU TIN THUẬN NGHỊCH NHIỀU CẤP TRONG ẢNH NHỊ PHÂN 82

Dương Ngọc Vân Khanh, Huỳnh Văn Thanh, Nguyễn Thái Sơn

12. MỘT SỐ TẤN CÔNG LÊN LƯỢC ĐỒ KÝ SỐ ECDSA LIÊN QUAN TỚI GIÁ TRỊ BÍ MẬT K VÀ ĐỀ XUẤT GIẢI PHÁP PHÒNG CHỐNG 90

Nguyễn Văn Nghị, Đỗ Quang Trung

13. PHƯƠNG PHÁP MÃ HÓA CÓ THỂ CHỐI TỪ DỰA TRÊN THUẬT TOÁN ElGamal-SignCryption 95

Dương Phúc Phần, Nguyễn Đức Tâm, Nguyễn Hiếu Minh, Dương Quang Duy, Lê Văn Úy

14. ỨNG DỤNG HỌC MÁY PHÁT HIỆN MÃ ĐỘC TRONG LUỒNG DỮ LIỆU MÃ HÓA 102

Nguyễn Ngọc Hưng, Nguyễn Thị Thuý Quỳnh, Nguyễn Việt Hùng

15. A NEW APPROACH IN DISTRIBUTED LEARNING MODEL APPLYING MALWARE CLASSIFICATION ON ANDROID PLATFORM 111

Le Duc Thuan, Pham Van Huong, Hoang Van Hiep, Nguyen Kim Khanh

16. THUẬT TOÁN HIỆU QUẢ KHAI THÁC TẬP PHỔ BIẾN TUYỆT ĐỐI TRÊN DỮ LIỆU GIAO DỊCH CÓ TRỌNG SỐ CỦA ITEMS 120

Phan Thành Huấn, Lê Hoài Bắc

17. APPLICATION OF THE PROMOTION MODEL BASED CUSTOMER LIFETIME VALUE TO PREVENT CUSTOMERS TRANSFER NETWORK IN VNPT LAM DONG 128

Pham Thi Thu Thuy, Doan Duy Tuyen, Kim Hwa Soo

18. ĐÁNH GIÁ HIỆU QUẢ MỘT SỐ PHƯƠNG PHÁP HỌC SÂU TRONG PHÁT HIỆN BỆNH ĐÁI THÁO ĐƯỜNG QUA ẢNH VÕNG MẠC 139

Lê Tuấn Anh, Nguyễn Tiến Đồng, Lê Hoàng Sơn, Vũ Đức Thi, Nguyễn Long Giang, Nguyễn Như Sơn, Hoàng Thị Minh Châu, Trình Văn Hà, Lê Hoàng Hiệp, Trần Tuấn Hoàn

19. MỘT ĐỀ XUẤT THUẬT TOÁN FUZZY JOIN TRONG XỬ LÝ DỮ LIỆU LỚN 146

Phan Thượng Cang, Trần Thị Tố Quyên

20. MỘT HỆ THỐNG MỚI ĐỂ TRẢ LỜI CÂU HỎI NHIỀU BƯỚC DỰA TRÊN ĐỒ THỊ TRI THỨC LỚN THEO TIẾP CẬN PHÂN TÁN 154

Phan Hồng Trung, Đỗ Phúc

21. VỀ BẢNG QUYẾT ĐỊNH KHÔNG ĐẦY ĐỦ KHÔNG DƯ THỪA 166

Vũ Đức Thi

22. A NETWORK-BASED ANALYSIS OF A WORKFLOW AT HANOI UNIVERSITY OF INDUSTRY 171

Tran Tien Dung, Nguyen Minh Tan

23. KHAI THÁC TOP-K MẪU HỮU ÍCH TRỌNG SỐ PHỔ BIẾN TRÊN CƠ SỞ DỮ LIỆU ĐỊNH LƯỢNG 181

Phan Thị Phương Trang, Lê Hoàng Bình Nguyên, Nguyễn Duy Hàm

24. VỀ SỰ ẢNH HƯỞNG CỦA CÁC THAM SỐ MỜ HÓA TRONG THUẬT TOÁN PHÂN CỤM MỜ 188

Trần Đình Khang, Đỗ Lê Quang, Võ Đức Quang

25. ỨNG DỤNG PHÂN LỚP DỮ LIỆU TRONG DỰ ĐOÁN KHÁCH HÀNG RỜI BỎ DỊCH VỤ TẠI NGÂN HÀNG THƯƠNG MẠI 196

Vũ Văn Hiệu, Trương Hải Nam

26. HỆ THỐNG PHÂN TÍCH VÀ TÌM KIẾM THÔNG TIN CON NGƯỜI TỪ CAMERA GIÁM SÁT 203

Trần Gia Nghĩa, Chế Quang Huy, Trương Văn Cương

27. XÂY DỰNG MÔ HÌNH DỰ BÁO KHÔNG ĐIỀU KIỆN SỬ DỤNG PHƯƠNG PHÁP GIẢM CHIỀU BIẾN DỰA VÀO THỦ THUẬT KERNEL 211

Nguyễn Minh Hải, Đỗ Văn Thành, Nguyễn Đức Dũng

28. GIẢI THUẬT HỌC TĂNG TRƯỞNG GIẢM GRADIENT NGẪU NHIÊN CỤC BỘ TRÊN MÁY TÍNH NHÚNG RASPBERRY PI CHO PHÂN LỚP THÁCH THỨC IMAGENET 218

Đỗ Thanh Nghị, Trần Nguyễn Minh Thư, Bùi Võ Quốc Bảo

29. ỨNG DỤNG ĐỘ ĐO FRÉCHET INCEPTION DISTANCE ĐỂ LỰA CHỌN MẪU SINH RA TỪ GAN CHO TẬP THIỂU SỐ 225

Trần Võ Khánh Ngân, Trần Cao Đệ

30. PHÂN LOẠI BỆNH ALZHEIMER TRÊN ẢNH CHỤP CỘNG HƯỞNG TỪ CỦA NÃO VỚI KỸ THUẬT HỌC SÂU 233

Phan Thượng Cang, Phan Anh Cang, Trương Minh Toàn

31. MỘT PHƯƠNG PHÁP MỚI TRONG VIỆC TĂNG CƯỜNG ẢNH DỰA TRÊN PHÂN CỤM MỜ VÀ TOÁN TỬ TĂNG CƯỜNG ẢNH TỐI 243

Nguyễn Tu Trung, Trần Mạnh Tuấn, Nguyễn Huy Đức, Nguyễn Ngọc Quỳnh Châu

32. EVALUATING THE EFFECTIVENESS OF A MULTI-CRITERIA RECOMMENDER SYSTEM BASED ON THE DEGREE OF INTERACTION BETWEEN CRITERIA, SETS OF CRITERIA 249

Tri Minh Huynh, Vu The Tran, Hiep Xuan Huynh

33. DỰ BÁO CHẤT LƯỢNG CỦA KIỂM THỬ ĐỘT BIẾN BẬC CAO DỰA TRÊN HỌC MÁY 258

Đỗ Văn Nhỏ, Nguyễn Đức Thuận, Nguyễn Thị Ngọc Ánh,

Nguyễn Quang Vũ, Nguyễn Thanh Bình

34. PHÂN VÙNG KHỐI U GAN TRÊN ẢNH CT Ổ BỤNG SỬ DỤNG CHUYỂN ĐỔI HOUNSFIELD ĐA KÊNH 266

Lê Nhật Huy, Lê Minh Hưng

35. TỐI ƯU THAM SỐ TÍNH MỜ TRONG MÔ HÌNH DỰ BÁO CHUỖI THỜI GIAN NGÔN NGỮ BẬC CAO SỬ DỤNG TỐI ƯU BẦY ĐÀN 274

Phạm Đình Phong, Nguyễn Duy Hiếu, Hoàng Văn Thông, Mai Văn Linh

36. A STUDY ON DIGITAL TRANSFORMATION IN MEDICAL EXAMINATION AND TREATMENT 282

Pham Vu Thu Nguyet, Ngo Chung Luc, Nguyen Luong Bang, Nguyen Quang Chung, Nguyen Van To Thanh, Ho Thanh Phong, Nguyen Quang Vu

37. DỰ ĐOÁN NHỊP TIM BẰNG PHƯƠNG PHÁP HỌC SÂU 291

Đỗ Thanh Nghị, Võ Trí Thức

38. ỨNG DỤNG MÔ HÌNH REPVGG VÀO BÀI TOÁN PHÂN LOẠI TÌNH TRẠNG GIAO THÔNG 298

Vũ Lê Quỳnh Phương, Trần Nguyễn Minh Thư, Phạm Nguyên Khang

39. ĐỀ XUẤT CÁC KỸ THUẬT CẢI TIẾN VÀO QUY TRÌNH HOÀN TRẢ CHI PHÍ DI CHUYỂN 306

Trần Lương Phán, Nguyễn Đình Thuân

40. GIẢI PHÁP XÂY DỰNG HỆ THỐNG TRỢ LÝ ẢO TRONG NÔNG NGHIỆP THÔNG MINH 314

Nguyễn Thái Nghe, Trần Lý Văn, Nguyễn Hữu Hòa

41. RÚT GỌN THUỘC TÍNH DỰA TRÊN MÔ HÌNH TẬP THÔ MỜ TRỰC CẢM SỬ DỤNG ĐỘ ĐO KHOẢNG CÁCH MỞ RỘNG VÀ LÁT CẮT $\boldsymbol{\alpha}$ 320

Phạm Việt Anh, Nguyễn Long Giang, Nguyễn Ngọc Thủy, Cao Chính Nghĩa, Vũ Đức Thi

42. CỐ VẤN HỌC TẬP ẢO HỖ TRỢ SINH VIÊN ĐẠI HỌC 332

Nguyễn Duy Phương, Trần Việt Châu, Trần Nguyễn Minh Thư

43. HỆ THỐNG GỢI Ý DỰA TRÊN KHOẢNG CÁCH NĂNG LƯỢNG 339
Trần Thị Cẩm Tú, Phan Phương Lan, Huỳnh Xuân Hiệp

44. TÌM KIẾM ẢNH DỰA TRÊN MẠNG HỌC SÂU YOLO VÀ CẤU TRÚC KD-TREE RANDOM FOREST 347
Nguyễn Thị Định, Văn Thế Thành

45. GIẢI PHÁP HỆ GỢI Ý CÓ ĐẢM BẢO TÍNH RIÊNG TƯ HIỆU QUẢ VÀ THỰC TIỄN 357
Vũ Thị Vân, Lương Thế Dũng, Hoàng Văn Quân, Trần Thị Lượng

46. MỘT HÀM THUỘC MỜ HIỆU QUẢ TRONG GIẢI THUẬT FSVM-CIL CHO BÀI TOÁN KHUYẾN NGHỊ ĐỒNG TÁC GIẢ 366
Võ Đức Quang, Nguyễn Hải Yến, Trần Đình Khang

47. THUẬT TOÁN CHE GIẤU THÔNG TIN NHẠY CẢM TRONG KHAI PHÁ TẬP MỤC HỮU ÍCH CAO DỰA TRÊN KỸ THUẬT HEURISTIC 374
Huỳnh Triệu Vỹ, Lê Quốc Hải, Trương Ngọc Châu, Lê Quốc Hiếu

48. KHAI THÁC TẬP LỢI ÍCH CAO CÓ TRỌNG SỐ ÂM TRONG CƠ SỞ DỮ LIỆU PHÂN TÁN DỌC BẢO TOÀN TÍNH RIÊNG TƯ 384
Cao Tùng Anh, Ngô Quốc Huy , Lê Thị Quỳnh Chi

49. NGHIÊN CỨU ĐỀ XUẤT HỆ THỐNG NHẬN DẠNG VÀ BÓC TÁCH THÔNG TIN TỰ ĐỘNG HỖ TRỢ PHÂN LOẠI VĂN BẢN HÀNH CHÍNH 392
Phùng Thế Huân, Đỗ Hồng Quân, Lê Minh Tuấn, Nguyễn Thị Lan Anh, Lương Văn Nghĩa, Hoàng Thị Cành, Nguyễn Quang Trung, Lê Hoàng Sơn, Đinh Thu Khánh, Lương Hồng Lan

50. MỘT MÔ HÌNH TRUY VẤN ẢNH KẾT HỢP ĐỒ THỊ LÁNG GIỀNG VÀ ĐỒ THỊ NGỮ NGHĨA 400
Lê Thị Vĩnh Thanh, Văn Thế Thành

51. PHƯƠNG PHÁP WMD-CGAN BIẾN ĐỔI ẢNH NHUỘM MÔ HE THÀNH ẢNH IHC NHẰM HỖ TRỢ XÁC ĐỊNH PHÁC ĐỒ ĐIỀU TRỊ UNG THƯ VÚ 413
Trần Đình Toàn, Nguyễn Đức Toàn, Lê Minh Hưng, Trần Văn Lăng

52. PHƯƠNG PHÁP LẬP CHỈ MỤC VÀ TÌM KIẾM VIDEO THEO NỘI DUNG 423
Trang Thanh Trí, Phạm Thế Phi, Đỗ Thanh Nghị

53. MỘT PHƯƠNG PHÁP CHÚ THÍCH ẢNH TỰ ĐỘNG DỰA TRÊN ĐỒ THỊ NGỮ CẢNH VÀ MẠNG LTSM 431
Nguyễn Văn Thịnh, Trần Văn Lăng, Văn Thế Thành

54. EFFECT OF ADDITIVE ANGULAR MARGIN LOSS FUNCTION WITH IMBALANCED DATA IN SKIN LESION RECOGNITION 440
Phung Dao Vinh Chung, Le Minh Hung

55. PHÂN TÍCH CẢM XÚC CHO TIẾNG VIỆT SỬ DỤNG MÔ HÌNH PHOBERT 447
Huỳnh Thanh Tú, Võ Bách Khôi, Hồ Anh Dũng, Vũ Đức Lung

56. HYBRID MODEL OF CNN-XGBOOST FOR HOUSEHOLD GARBAGE IMAGE CLASSIFICATION 455
Luong Cao Dong, Tran Quy Nam

57. ỨNG DỤNG MẠNG GAN CÓ ĐIỀU KIỆN PHÁT HIỆN VÙNG BẤT THƯỜNG TRÊN ẢNH MRI NÃO 462
Trần Nguyễn Minh Thư, Bùi Thanh Liêm, Lê Minh Lợi, Phù Trí Nghĩa, Phạm Nguyên Khang

58. TRUY VẤN ẢNH SỬ DỤNG ĐỒ THỊ VÀ SOM ĐỆ QUY 470
Nguyễn Minh Hải, Nguyễn Phương Nam, Văn Thế Thành, Trần Văn Lăng

59. KHUNG LÀM VIỆC CHO TRA CỨU ẢNH VỚI MẠNG NƠ RON ĐỒ THỊ BÁN GIÁM SÁT 477
Nguyễn Hữu Quỳnh, Đào Thị Thúy Quỳnh, Cù Việt Dũng, An Hồng Sơn

60. NÂNG CAO HIỆU NĂNG CỦA ĐÁNH HẠNG ĐA TẠP EMR TRONG TRUY VẤN HÌNH ẢNH SỬ DỤNG PHƯƠNG PHÁP ĐÁNH HẠNG KẾT HỢP ĐA ĐẶC TRƯNG ẢNH 486
Trần Văn Huy, Đào Văn Tuyết, Hoàng Văn Quý, Nguyễn Văn Đoàn, Hoàng Xuân Trung, Nguyễn Văn Quyền, Vũ Thị Khánh Toàn, Lê Đình Nghiệp

61. PHÁT HIỆN VÀ KHOANH VÙNG TỔN THƯƠNG PHỔI DO COVID-19 TRÊN ẢNH X-QUANG BẰNG PHƯƠNG PHÁP DEEP LEARNING 493
Phan Thượng Cang, Phan Anh Cang, Trần Hồ Đạt

62. TỔNG HỢP HÌNH ẢNH Y HỌC DỰA TRÊN GIẢI THUẬT TỐI ƯU MPA 501
Đinh Phú Hùng, Nguyễn Huy Đức, Nguyễn Long Giang

63. MỘT CÁCH TIẾP CẬN ỨNG DỤNG QUY HOẠCH TUYẾN TÍNH TRONG BÀI TOÁN PHÁT HIỆN VA CHẠM CỦA CÁC MÔ HÌNH 3D 510
Nghiêm Văn Hưng, Đặng Văn Đức, Nguyễn Văn Căn, Hoàng Việt Long, Trịnh Hiền Anh

64. MỘT PHƯƠNG PHÁP PHÂN LOẠI ĐA LỚP HIỆU QUẢ TRONG PHÂN TÍCH QUAN ĐIỂM 517
Nguyễn Thị Ngọc Tú, Nguyễn Thị Thu Hà, Nguyễn Long Giang, Nguyễn Việt Anh, Nguyễn Trần Quốc Vinh

65. XÂY DỰNG TỪ ĐIỂN CẢM XÚC THEO LĨNH VỰC VÀ ỨNG DỤNG VÀO HỆ THỐNG GỢI Ý SẢN PHẨM 527
Bùi Thị Diễm Trinh, Huỳnh Thị Ngọc Yến, Trương Quốc Định

66. KIỂM CHỨNG THÔNG TIN TIẾNG VIỆT DỰA TRÊN ĐỒ THỊ TRI THỨC, HỌC SÂU VÀ LUẬT SUY DIỄN 534
Dương Tố Hương, Hồ Hải Văn, Đỗ Phúc

67. MỘT SỐ TÍNH CHẤT CỦA VỀ TRÁI CỰC TIỂU VÀ KHÓA VỚI PHÉP DỊCH CHUYỂN LƯỢC ĐỒ KHỐI 542
Trịnh Đình Thắng, Đỗ Thị Lan Anh, Trần Minh Tuyến, Nguyễn Văn Cường

68. MỘT HƯỚNG TIẾP CẬN GIÁM SÁT THI TRỰC TUYẾN TRÊN NỀN TẢNG IOT ỨNG DỤNG CÔNG NGHỆ NHÚNG 550
Nguyễn Xuân Huy, Lê Phạm Việt Mẫn, Nguyễn Minh Sơn

69. THUẬT TOÁN KẾT HỢP GIỮA THUẬT TOÁN TIẾN HÓA VÀ THUẬT TOÁN METAHEURISTIC CHO TÌM KIẾM ƯU TIÊN NGẪU NHIÊN GIẢI BÀI TOÁN TÌM ĐƯỜNG ĐI LIÊN MIỀN VỚI RÀNG BUỘC MIỀN DUY NHẤT TRÊN NÚT MẠNG 557
Phạm Đình Thành

70. USING DATA MINING, SEASONAL TIME SERIES AND ARTIFICIAL NTELLIGENCE ALGORITHM FOR BITCOIN PRICE PREDICTION 566
Hoang Tung, Ngo Hien Dat, Nguyen Dinh Thuan

DOI: 10.15625/vap.2022.0261

TỔNG HỢP HÌNH ẢNH Y HỌC DỰA TRÊN GIẢI THUẬT TỐI ƯU MPA

Đinh Phú Hùng[1], Nguyễn Huy Đức[2], Nguyễn Long Giang[3]

[1]Bộ môn Mạng và An toàn thông tin, Đại học Thuỷ lợi
[2]Bộ môn Tin học và Kĩ thuật tính toán, Đại học Thuỷ lợi
[3]Viện Công nghệ thông tin, Viện Hàn lâm Khoa học và Công nghệ Việt Nam

hungdp@tlu.edu.vn, ducnghuy@tlu.edu.vn, giangnl@ioit.ac.vn

TÓM TẮT: *Tổng hợp hình ảnh Y học đóng vai trò quan trọng trong việc hỗ trợ các bác sĩ chẩn đoán lâm sàng tốt hơn. Cho đến nay, có rất nhiều các cách tiếp cận để giải quyết bài toán này đã được đề xuất. Tuy nhiên, hình ảnh tổng hợp vẫn gặp một số vấn đề về mặt chất lượng như bị giảm cường độ sáng, độ tương phản và thậm chí bị mất các chi tiết. Bài báo này đề xuất một phương pháp mới để cải thiện những hạn chế đề cập ở trên. Đầu tiên các hình ảnh đầu vào sẽ được phân rã thành hai thành phần (thành phần cơ sở và thành phần chi tiết) bằng cách sử dụng bộ lọc Rolling guidance filter (RGF). Sau đó, các thành phần cơ sở được tổng hợp với nhau bằng cách sử dụng giải thuật tối ưu hoá MPA (Marine predators algorithm). Các thành phần chi tiết được tổng hợp lại với nhau sử dụng toán tử la bàn Prewitt kết hợp với hàm năng lượng cục bộ. Các thực nghiệm cho thấy rằng phương pháp mà chúng tôi đề xuất có cải thiện đáng kể chất lượng hình ảnh được tổng hợp cũng như bảo toàn tốt các chi tiết trong ảnh.*

Từ khóa: *Tổng hợp hình ảnh y học, giải thuật tối ưu MPA, bộ lọc Rolling guidance filter (RGF).*

I. GIỚI THIỆU

Với sự đa dạng của các thiết bị thu nhận hình ảnh. Chúng ta có thể thu nhận được một số loại hình ảnh y học khác nhau như hình ảnh cộng hưởng từ (MRI), hình ảnh chụp cắt lớp vi tính (CT), hình ảnh chụp cắt lớp phát xạ đơn photon (PET). Mỗi một loại hình ảnh đều mang những thông tin mà những hình ảnh còn lại không có. Ví dụ, hình ảnh MRI cung cấp các thông tin về cấu trúc xương. Hình ảnh PET cung cấp thông tin đến quá trình trao đổi chất. Trong quá trình chẩn đoán bệnh, các bác sĩ cần quan sát thông tin từ nhiều loại hình ảnh khác nhau để đưa ra những chẩn đoán bênh một cách chính xác. Do đó, việc tổng hợp hình ảnh y học là quá trình kết hợp các thông tin bổ sung từ các hình ảnh riêng lẻ theo các phương thức khác nhau để tạo thành một hình ảnh duy nhất.

Nhìn chung, chúng ta có thể chia các cách tiếp cận để giải quyết bài toán tổng hợp hình ảnh ra làm hai loại chính. Các cách tiếp cận dựa trên miền không gian và các cách tiếp cận dựa trên miền biến đổi. Có ba bước chính cần thực hiện trong các cách tiếp cận dựa trên miền biến đổi. Đầu tiên, một thuật toán biến đổi ảnh được áp dụng để phân tách hình ảnh đầu vào thành các thành phần tần số thấp và các thành phần tần số cao. Tiếp theo, các thành phần tần số thấp được tổng hợp lại với nhau và các thành phần tần số cao tổng hợp lại với nhau theo các quy tắc tổng hợp được định nghĩa trước. Cuối cùng, các thành phần đã được tổng hợp được biến đổi ngược về miền không gian để thu được hình ảnh tổng hợp. Hiện nay, có rất nhiều các phương pháp biến đổi ảnh khác nhau đã được áp dụng để giải quyết cho bài toán tổng hợp hình ảnh. Biến đổi SWT (Stationary wavelet transform) được Dinh [1] sử dụng để phân rã hình ảnh đầu vào trong nghiên cứu tổng hợp hình ảnh. Biến đổi NSCT (Non-subsampled contourlet transform) được sử dụng để phân rã hình ảnh trong nghiên cứu của Wang và các đồng nghiệp [2]. Biến đổi NSST (Non-subsampled shearlet transform) được sử dụng trong nghiên cứu của Jose và các đồng nghiệp [3]. Một số các cách biến đổi khác cũng được sử dụng trong bài toán tổng hợp hình ảnh y học như LP (Laplacian pyramid) [4], TVD (Total-variational decomposition) [5] và SIDWT (Shift-invariant discrete wavelet transform) [6]. Cách tổng hợp cho các thành phần tần số thấp có thể kể đến như quy tắc Max [7], quy tắc trung bình [8] và quy tắc thích nghi [9], [10], [11], [12]. Các quy tắc tổng hợp cho các thành phần tần số cao cũng rất đa dạng. Một số quy tắc phổ biến có thể đề cập như quy tắc dựa trên cực đại hàm năng lượng cục bộ MLE [13], quy tắc cực đại hàm năng lượng cục bộ sử dụng toán tử la bàn [9].

Bên cạnh các phương pháp được đề cập ở trên, biểu diễn thưa (SR - Sparse representation) và các mạng học sâu cũng được ứng dụng trong bài toán tổng hợp hình ảnh. Yousif và các đồng nghiệp [14] đã đề xuất kết hợp biểu diễn thưa với mạng SCNN (Siamese convolutional neural network). Shibu và các động nghiệp [15] đã giới thiệu một phương pháp tổng hợp hình ảnh dựa trên SR và mạng tích chập (CNN). Li và các đồng nghiệp [16] đã kết hợp SR với bộ lọc SGF (segment graph filter) để tổng hợp hình ảnh. Trong thời gian gần đây, một số cách tiếp cận dựa trên tối ưu hoá đã cho thấy sự hiệu quả đối với bài toán tổng hợp hình ảnh y học. Ví dụ, Dinh [9] đã đề xuất một phương pháp tổng hợp hình ảnh hiệu quả dựa trên giải thuật tối ưu bầy châu chấu. Gao và các đồng nghiệp [17] đã sử dụng giải thuật tối ưu PSO (Particle swarm optimization) trong việc đề phương pháp tổng hợp hình ảnh. Duan và các đồng nghiệp [18] đã đề xuất sử dụng giải thuật di truyền GA (Genetic algorithm) cho việc tổng hợp hình ảnh. Một số giải thuật tối ưu khác cũng đã được sử dụng để tổng hợp hình ảnh y học như EOA (Equilibrium Optimization Algorithm) [1], [11] và AISA (Adolescent identity search algorithm) [3].

Theo quan sát của chúng tôi, hình ảnh tổng hợp thường bị suy giảm về mặt chất lượng ở các khía cạnh như cường độ sáng, độ tương phản và thậm chí mất các chi tiết từ hình ảnh gốc. Ví dụ, một số giải thuật tổng hợp [19], [20] sử dụng quy tắc trung bình dẫn đến hình ảnh tổng hợp bị giảm cường độ sáng và độ tương phản. Trong nghiên cứu này,

chúng tôi tập trung giải quyết vấn đề về sự suy giảm cường độ sáng của hình ảnh tổng hợp bằng cách tạo ra một quy tắc tổng hợp thích nghi cho thành phần tần số thấp. Một số đóng góp chính của nghiên cứu có thể liệt kê như sau:

- Đề xuất một phương pháp phân rã hình ảnh hai thành phần dựa trên bộ lọc RGF.
- Đề xuất một quy tắc tổng hợp thích nghi cho các thành phần cơ sở dựa trên giải thuật tối ưu MPA.

Các phần còn lại của bài báo được bố trí như sau: Phần II giới thiệu một số kiến thức nền tảng, bao gồm bộ lọc hướng dẫn quay vòng (RGF) và giải thuật tôi ưu hoá MPA. Phần III trình bày về phương pháp đề xuất, bao gồm phương pháp phân rã ảnh hai thành phần dựa trên bộ lọc RGF và phương pháp tổng hợp hình ảnh dựa trên giải thuật tối ưu MPA kết hợp với hàm năng lượng cục bộ sử dụng toán tử la bàn Prewitt (FR_PCO) do Dinh [11] đề xuất. Thiết kế thực nghiệm và các kết quả thực nghiệm được trình này trong Phần IV. Kết luận và các công việc tương lai được trình bày trong Phần V.

II. KIẾN THỨC NỀN TẢNG

A. Bộ lọc hướng dẫn quay vòng

Bộ lọc hướng dẫn quay vòng (RGF - Rolling guidance filter) được giới thiệu bởi Zhang và các đồng nghiệp [21] vào năm 2014. Cho đến nay, bộ lọc này đã được ứng dụng trong rất nhiều các bài toán xử lý ảnh như tổng hợp hình ảnh y học [22], tổng hợp hình ảnh hồng ngoại và hình ảnh khả kiến [23] và phân cụm dữ liệu [24]. Bộ lọc RGF hoạt động dựa trên hai bước chính: xoá bỏ các thành phần cấu trúc nhỏ và phục hồi đường biên.

Bước 1: Xoá bỏ các thành phần cấu trúc nhỏ

Kí hiệu I và I_G lần lượt là hình ảnh đầu vào và hình ảnh thu được sau khi lọc Gaussian. Khi đó, I_G được tính toán theo phương trình (1).

$$I_G(p) = \frac{1}{K_p} \sum_{q \in N(p)} exp\left(-\frac{||p-q||^2}{2\sigma_s^2}\right) I(q) \tag{1}$$

trong đó:

p và q là các vị trí;

σ_s là độ lệch chuẩn của bộ lọc Gaussian;

$N(p)$ là tập các hàng xóm mà có tâm là p;

K_p được sử dụng cho mục đích chuẩn hoá và nó được xác định theo phương trình (2).

$$K_p = \sum_{q \in N(p)} exp\left(-\frac{||p-q||^2}{2\sigma_s^2}\right) \tag{2}$$

Bước 2: Phục hồi đường biên bởi bộ lọc hướng dẫn

Kí hiệu J^1 là đầu ra của bộ lọc Gausian thu được từ bước 1. Kí hiệu J^{t+1} là kết quả thu được từ vòng lặp thứ t. J^{t+1} được xác định theo phương trình (3).

$$J^{t+1}(p) = \frac{1}{K_p} \sum_{q \in N(p)} exp\left(-\frac{||p-q||^2}{2\sigma_s^2} - \frac{||J^t(p) - J^t(q)||^2}{2\sigma_r^2}\right) I(q) \tag{3}$$

trong đó:

K_p được sử dụng cho mục đích chuẩn hoá và nó được xác định theo phương trình (4).

$$K_p = \sum_{q \in N(p)} exp\left(-\frac{||p-q||^2}{2\sigma_s^2} - \frac{||J^t(p) - J^t(q)||^2}{2\sigma_r^2}\right) I(q) \tag{4}$$

σ_r là độ lệch chuẩn của bộ lọc hướng dẫn.

Hình 1 minh hoạ một hình ảnh đầu vào và một số hình ảnh đầu ra thông qua một số vòng lặp của bộ lọc RGF.

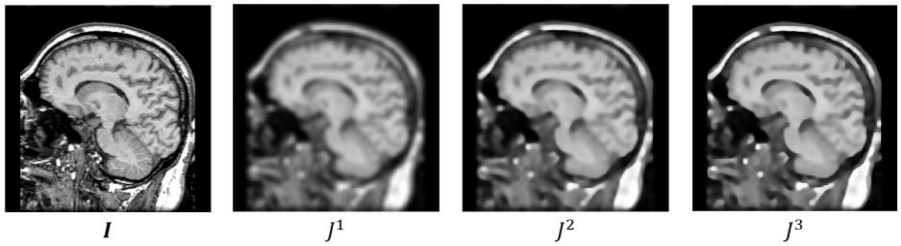

Hình 1. Minh hoạ kết quả thu được bởi bộ lọc RGF.

B. Giải thuật tối ưu MPA

Giải thuật tối ưu MPA được đề xuất bởi Faramarzi và các đồng nghiệp [25] vào năm 2020. Giải thuật này đã cho thấy có hiệu quả trong rất nhiều các ứng dụng như tổng hợp hình ảnh y học [26] và nâng cao chất lượng ảnh [27].

Ba giai đoạn chính của thuật toán có thể được mô tả như sau:

Giai đoạn 1: Trong một phần ba đầu tiên của vòng lặp, kích thước bước di chuyển của con mồi ($\overrightarrow{SS_i}(x,y)$) và vị trí của nó ($\overrightarrow{Pr_i}(x,y)$) được xác định bởi các phương trình (5) và (6) tương ứng.

$$\overrightarrow{SS_i}(x,y) = \overrightarrow{R_B}(x,y)\otimes\left(\overrightarrow{E_i}(x,y) - \overrightarrow{R_B}(x,y)\otimes\overrightarrow{Pr_i}(x,y)\right) \quad (5)$$

$$\overrightarrow{Pr_i}(x,y) = \overrightarrow{Pr_i}(x,y) + K.\vec{R}\otimes\overrightarrow{SS_i}(x,y) \quad (6)$$

trong đó:

$\overrightarrow{SS_i}(x,y)$ là một véctơ chứa kích thước bước di chuyển của con mồi;

$E(x,y)$ là một ma trận được xây dựng trên các giải pháp phù hợp nhất;

$\vec{R}$ là một véctơ chứa các giá trị ngẫu nhiên tuân theo một phân phối đồng nhất;

K là hằng số có giá trị 0,5;

$\otimes$ là toán tử nhân entry-wise;

$\overrightarrow{R_B}$ là một véctơ các số ngẫu nhiên.

Giai đoạn 2: Trong một phần ba của vòng lặp tiếp theo, kích thước bước di chuyển của con mồi và vị trí của nó được xác định bởi các phương trình (7), (8), (9) và (10).

Đối với một phần hai của dân số đầu:

$$\overrightarrow{SS_i}(x,y) = \overrightarrow{R_L}(x,y)\otimes\left(\overrightarrow{E_i}(x,y) - \overrightarrow{R_L}(x,y)\otimes\overrightarrow{Pr_i}(x,y)\right) \quad (7)$$

$$\overrightarrow{Pr_i}(x,y) = \overrightarrow{Pr_i}(x,y) + K.\vec{R}\otimes\overrightarrow{SS_i}(x,y) \quad (8)$$

Đối với một phần hai của dân số còn lại:

$$\overrightarrow{SS_i}(x,y) = \overrightarrow{R_B}(x,y)\otimes\left(\overrightarrow{R_B}(x,y)\otimes\overrightarrow{E_i}(x,y) - \overrightarrow{Pr_i}(x,y)\right) \quad (9)$$

$$\overrightarrow{Pr_i}(x,y) = \overrightarrow{E_i}(x,y) + K.CF\otimes\overrightarrow{SS_i}(x,y) \quad (10)$$

trong đó:

$CF = \left(1 - \frac{l}{l_{max}}\right)^{\frac{2*l}{l_{max}}}$ là một tham số thích nghi để kiểm soát kích thước bước cho sự di chuyển của động vật ăn thịt.

Giai đoạn 3: Trong một phần ba cuối cùng của vòng lặp, kích thước bước di chuyển của con mồi và vị trí của nó được xác định bởi các phương trình (11) và (12).

$$\overrightarrow{SS_i}(x,y) = \overrightarrow{R_L}(x,y)\otimes\left(\overrightarrow{R_L}(x,y)\otimes\overrightarrow{E_i}(x,y) - \overrightarrow{Pr_i}(x,y)\right) \quad (11)$$

$$\overrightarrow{Pr_i}(x,y) = \overrightarrow{E_i}(x,y) + K.CF\otimes\overrightarrow{SS_i}(x,y) \quad (12)$$

trong đó:

$\overrightarrow{R_L}$ là một véctơ được sinh ra bởi phân phối Lévy.

Với sự hình thành của các dòng xoáy trên biển và sự ảnh hưởng của các thiết bị thu hút cá (FDAs - Fish Aggregating Devices), vị trí của các con mồi được cập nhật lại như phương trình (13):

$$\begin{aligned} \overrightarrow{Pr_i}(x,y) &= \overrightarrow{Pr_i}(x,y) + CF\left[\vec{X}_{min} + R\otimes\left(\vec{X}_{max} - \vec{X}_{min}\right)\right]\otimes\vec{U} && \text{Nếu } r \le FDAs \\ \overrightarrow{Pr_i}(x,y) &= \overrightarrow{Pr_i}(x,y) + [FDAs(1-r) + r]\left(\overrightarrow{Pr_{r1}} - \overrightarrow{Pr_{r2}}\right) && \text{Nếu } r > FDAs \end{aligned} \quad (13)$$

trong đó:

FDAs = 0,2 là xác xuất của FDA ảnh hưởng tới quá trình tối ưu;

$\vec{U}$ là một véctơ nhị phân;

r là một tham số ngẫu nhiên thuộc khoảng (0,1);

$\vec{X}_{max}$ và $\vec{X}_{min}$ là các véctơ chứa cận trên và cận dưới;

Các chỉ số con r_1 và r_2 biểu thị các chỉ số ngẫu nhiên của ma trận con mồi.

III. PHƯƠNG PHÁP ĐỀ XUẤT

A. Phân rã ảnh hai thành phần

Trong phần này, chúng tôi giới thiệu phương pháp phân rã ảnh ảnh hai thành phần dựa trên bộ lọc RGF. Cho I là một hình ảnh đầu vào. Gọi C_1 và C_2 là các thành phần cơ sở và thành phần chi tiết thu được khi phân rã ảnh I. Hình 2 minh họa các thành phần C_1 và C_2 thu được từ một hình ảnh đầu vào I. Các bước để phân rã hình ảnh hai thành phần như sau:

Bước 1: Sử dụng bộ lọc RGF đối với ảnh đầu vào I, thu được thành phần C_1.

Bước 2: Thành phần C_2 được xác định như sau: $C_2 = I - C_1$

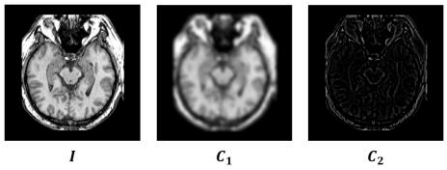

Hình 2. Minh hoạ hình ảnh đầu vào I và hai thành phần C_1 và C_2 thu được sau phân rã ảnh

B. Mô hình đề xuất

Trong phần này, chúng tôi giới thiệu mô hình tổng hợp hình ảnh.
Đầu vào: Hình ảnh xám I_{MRI}, hình ảnh màu I_{PET}.
Đầu ra: Hình ảnh tổng hợp màu (I^F_{Color})

Sơ đồ các bước của giải thuật tổng hợp hình ảnh y học của chúng tôi được minh hoạ trong Hình 3.

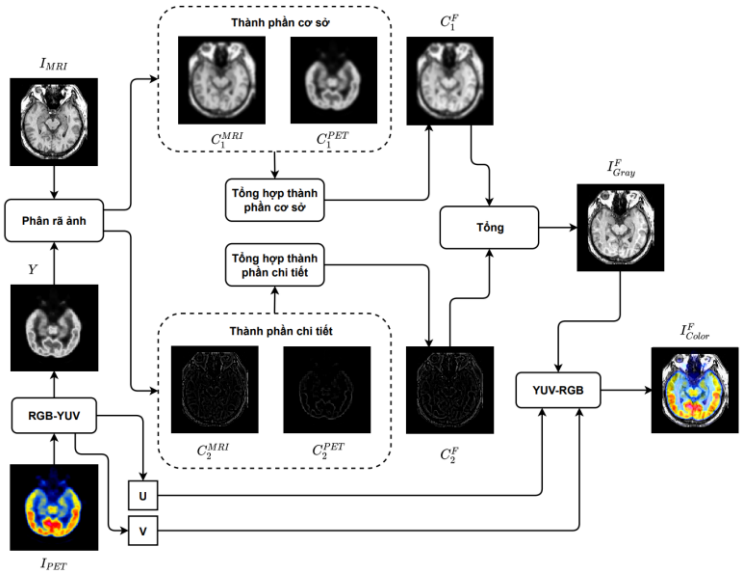

Hình 3. Sơ đồ tổng hợp hình ảnh

Bước 1: Hình ảnh màu I_{PET} được chuyển sang không gian màu YUV, thu được 3 kênh Y, U và V.

Bước 2: Áp dụng phương pháp phân rã ảnh hai thành phần đối với hai hình ảnh xám I_{MRI} và Y, thu được các thành phần cơ sở C_1^{MRI}, C_1^{PET} và các thành phần chi tiết C_2^{MRI}, C_2^{PET} tương ứng.

Bước 3: Tổng hợp các thành phần cơ sở theo phương trình (14).

$$C_1^F = \beta_1 . C_1^{MRI} + \beta_2 . C_1^{PET} \tag{14}$$

trong đó: $\beta_1 \in (0{,}5;\ 0{,}999)$ và $\beta_2 \in (0{,}01;\ 0{,}5)$ là hai tham số tối ưu tìm được bằng cách sử dụng giải thuật MPA để tối ưu hàm mục tiêu F theo phương trình (15).

$$F = \frac{K_1}{K_2}(E_2 - E_1) \tag{15}$$

trong đó:

K_1 và K_2 là phương sai và trung bình cường độ sáng của hình ảnh I_{MRI};

E_1 và E_2 là entropy của hình ảnh tổng hợp tạm thời I_T trong mỗi vòng lặp của giải thuật MPA và I_{MRI}.

Bước 4: Tổng hợp các thành phần chi tiết theo quy tắc FR_PCO được đề xuất bởi Dinh [11] như phương trình (16).

$$C_2^F = FR\_PCO(C_2^{MRI}, C_2^{PET}) \quad (16)$$

Bước 5: Hình ảnh tổng hợp xám được xác định theo phương trình (17).

$$I_{Gray}^F = C_1^F + C_2^F \quad (17)$$

Bước 6: Sử dụng 3 kênh I_{Gray}^F, U, V để chuyển về không gian màu RGB, thu được hình ảnh tổng hợp màu I_{Color}^F.

C. Thiết lập thực nghiệm và đánh giá

1. Dữ liệu thực nghiệm

Chúng tôi sử dụng 120 hình ảnh y học để tiến hành thực nghiệm. Những hình ảnh này được lấy từ nguồn: http://www.med.harvard.edu/AANLIB/. Chúng tôi chia 120 hình ảnh này thành các tập dữ liệu nhỏ dựa trên lát cắt theo các trục S, C và T.

Tập dữ liệu $D1$ gồm 20 cặp hình ảnh MRI và PET được lấy từ lát cắt 61 đến 82 theo trục T.
Tập dữ liệu $D2$ gồm 20 cặp hình ảnh MRI và PET được lấy từ lát cắt 61 đến 82 theo trục S.
Tập dữ liệu $D3$ gồm 20 cặp hình ảnh MRI và PET được lấy từ lát cắt 61 đến 82 theo trục C.
Tập dữ liệu $D4$ gồm 3 cặp hình ảnh MRI và PET tại vị trí cắt #068T, #068S và #068C.

Một số cặp hình ảnh MRI và PET được minh họa trong Hình 4.

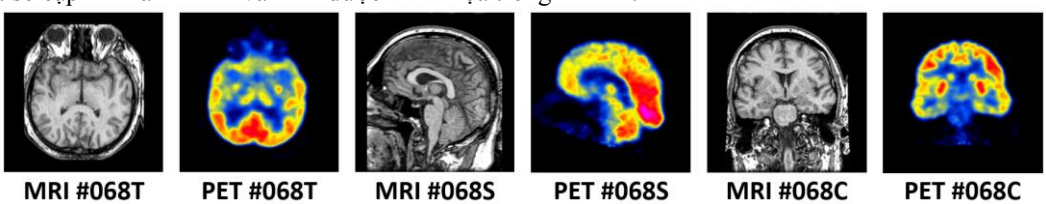

Hình 4. Minh họa một số cặp hình ảnh MRI và PET trong tập dữ liệu thực nghiệm

2. Thiết lập thực nghiệm

Chúng tôi thiết lập hai thực nghiệm như sau:

Thực nghiệm 1: Để kiểm tra hiệu quả của giải thuật MPA, chúng tôi lựa chọn 4 giải thuật tối ưu khác để so sánh. Những giải thuật tối ưu này là: DA (Dragonfly algorithm) [28], MVO (Multi-Verse Optimizer) [29], GWO (Grey Wolf Optimizer) [30], SCA (Sine Cosine Algorithm) [31]. Mỗi giải thuật tối ưu được thực hiện 30 lần khác nhau trên tập dữ liệu $D4$. Hai chỉ số đánh giá được sử dụng là trung bình và độ lệch chuẩn.

Thực nghiệm 2: Để kiểm tra sự hiệu quả của mô hình tổng hợp hình ảnh của chúng tôi. Một số giải thuật tổng hợp hình ảnh gần đây được lựa chọn để so sánh dựa trên tiêu chí có quy tắc tổng hợp trung bình như CSR (Convolutional Sparse Representation) [32], CSMCA (Convolutional Sparsity Based Morphological Component Analysis) [19] và mới được đề xuất gần đây như CSE (Contrast and Structure Extraction) [33]. Bốn chỉ số đánh giá được sử dụng là: Trung bình cường độ sáng (MLI - Meaning light intensity), độ tương phản (CI - Contrast index), lượng thông tin (E - Entropy) và độ sắc nét (AG - Average gradient).

Các tham số cần thiết được thiết lập như sau:

- Số vòng lặp của giải thuật MPA: 50.
- Số cá thể trong đàn: 50.
- Tham số K = 0,5, FDAs = 0,2, r là số ngẫu nhiên thuộc khoảng (0,1).

Các thực nghiệm đươc tiến hành trên máy Laptop: Intel Core i9 11900K, 2.5GHz processor với 32G Ram. Phần mềm thực hiện là Matlab 2020b.

3. Đánh giá

Kết quả của thực nghiệm 1: Bảng 1 minh hoạ kết quả của 30 lần chạy khác nhau ứng với mỗi giải thuật tối ưu. Nhận thấy rằng chỉ số trung bình của giá trị hàm mục tiêu thu được từ giải thuật MPA là cao nhất. Hơn nữa, giá trị độ lệch chuẩn thu được là thấp nhất trong các giải thuật. Điều này giải thích tại sao chúng tôi lựa chọn giải thuật MPA.

Bảng 1. Đánh giá các giải thuật tối ưu

Dữ liệu	Giải thuật	Trung bình	Độ lệch chuẩn
#068T	DA	0,433636782839501	0,000004888251470
	MVO	0,433136725452688	0,001133554592505
	GWO	0,433591810141287	0,000034863811703
	SCA	0,433510434889032	0,000074852304021
	MPA	**0,433642307567949**	**0,000000680545469**

#068S	DA	0,379947631345572	0,000006450111434
	MVO	0,379483877270243	0,001107439439358
	GWO	0,379888571418946	0,000044418568464
	SCA	0,379668034265813	0,000220148086905
	MPA	**0,379953426866101**	**0,000000591667461**
#068C	DA	0,421684429086385	0,000008135482162
	MVO	0,420366962998119	0,003838198434025
	GWO	0,421647587248824	0,000022284171740
	SCA	0,421602884338091	0,000042975103021
	MPA	**0,421698227058338**	**0,000003290488120**

Kết quả của thực nghiệm 2: Bảng 2 minh hoạ 4 chỉ số đánh giá của các giải thuật tổng hợp hình ảnh khác nhau. Dễ dàng nhận thấy rằng cả 4 chỉ số đánh giá thu được từ giải thuật tổng hợp của chúng tôi là cao nhất. Điều này cho thấy rằng giải thuật của chúng tôi tạo ra hình ảnh có cường độ sáng, độ tương phản, lương thông tin và độ sắc nét hơn các hình ảnh được tạo ra từ các phương pháp tổng hợp hình ảnh còn lại. Bằng trực quan, chúng ta có thể quan sát kết quả tổng hợp trên các Hình 5, 6 và 7.

Bảng 2. Chỉ số đánh giá của các giải thuật tổng hợp hình ảnh

Tập dữ liệu	Giải thuật	MLI	CI	E	AG
$D1$	CSR	0,2391	0,2860	5,0076	0,0578
	CSMCA	0,2526	0,3037	5,0212	0,0623
	CSE	0,2729	0,3089	5,2688	0,0648
	Ours	**0,3156**	**0,3528**	**5,3925**	**0,0684**
$D2$	CSR	0,2548	0,2701	5,8969	0,0655
	CSMCA	0,2711	0,2889	5,8106	0,0700
	CSE	0,3102	0,2965	6,2673	0,0751
	Ours	**0,3464**	**0,3293**	**6,3618**	**0,0789**
$D3$	CSR	0,2224	0,2682	5,2186	0,0814
	CSMCA	0,2363	0,2874	5,1642	0,0863
	CSE	0,2841	0,3089	5,6113	0,0950
	Ours	**0,3110**	**0,3375**	**5,7529**	**0,0986**

Hai tham số tối ưu trung bình β_1 và β_2 thu được từ ba tập dữ liệu $D1$, $D2$ và $D3$ được trình bày trong Bảng 3. Nhận thấy rằng tham số β_1 khá lớn (lớn hơn 0,96), trong khi β_2 nhỏ hơn đáng kể (nhỏ hơn 0,2). Điều này cho thấy thành phần cơ sở của hình ảnh MRI đóng góp một lượng lớn thông tin đến hình ảnh tổng. Trong khi thành phần cơ sở của hình ảnh PET đóng góp một lượng nhỏ thông tin đến hình ảnh tổng.

Bảng 3. Tham số tối ưu thu được

Tập dữ liệu	β_1	β_2
$D1$	0,9714	0,1999
$D2$	0,9669	0,1999
$D3$	0,9679	0,1999

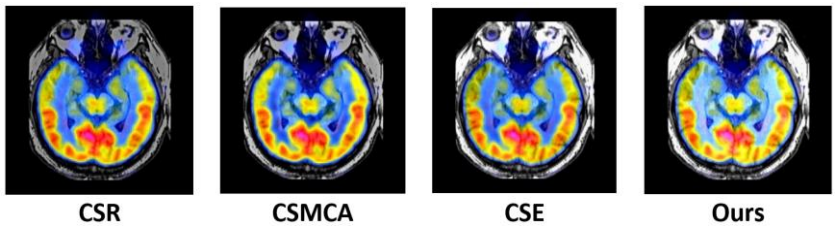

Hình 5. Minh hoạ hình ảnh tổng hợp thu được từ các giải thuật tổng hợp trên tập dữ liệu D1

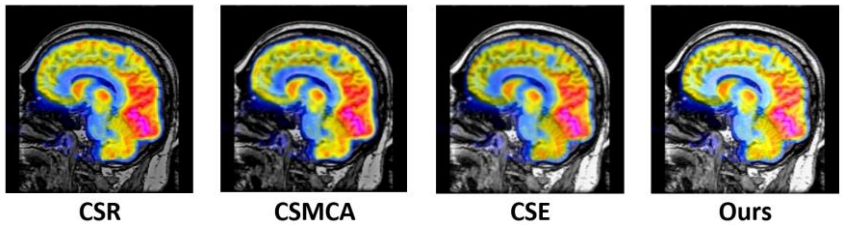

Hình 6. Minh hoạ hình ảnh tổng hợp thu được từ các giải thuật tổng hợp trên tập dữ liệu D2

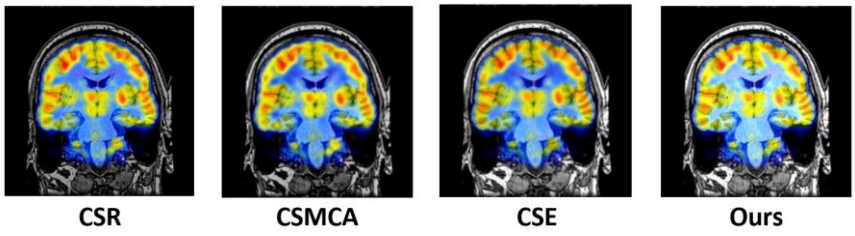

Hình 7. Minh hoạ hình ảnh tổng hợp thu được từ các giải thuật tổng hợp trên tập dữ liệu D3

Thời gian chạy trung bình của các giải thuật được trình bày trong Bảng 4. Phương pháp của chúng tôi cho thời gian chạy thấp nhất khoảng 1,73 giây với 50 vòng lặp và 50 cá thể trong đàn của giải thuật MPA, trong khi các phương pháp còn lại có thời gian chạy trung bình lớn hơn đáng kể. Tuy nhiên, nếu chọn số vòng lặp và số cá thể con đàn tăng lên thì thời gian chạy cũng sẽ tăng lên.

Bảng 4. Thời gian chạy trung bình của các giải thuật tổng hợp ảnh

Giải thuật	Thời gian chạy trung bình (giây)
CSR	14,2426
$CSMCA$	38,4796
CSE	14,2642
Ours	**1,7325**

D. Kết luận và công việc tương lai

Trong bài báo này, chúng tôi đề xuất một phương pháp tổng hợp hình ảnh hiệu quả dựa trên giải thuật MPA. Hình ảnh đầu vào được phân rã hai thành phần để thu được các thành phần cơ sở và thành phần chi tiết. Các thành phần cơ sở được tổng hợp lại với nhau dựa trên các tham số thích nghi. Những tham số này được tìm được bằng giải thuật tối ưu MPA. Những thành phần chi tiết được tổng hợp với nhau dựa trên toán tử la bàn Prewitt kết hợp với hàm năng lượng cục bộ. Phương pháp tổng hợp này đã cho thấy hiệu quả trong đề xuất của Dinh [11]. Những thành phần tổng hợp cơ sở và chi tiết được lấy tổng lại với nhau để tạo ra hình ảnh tổng hợp. 120 hình ảnh chụp não MRI và PET đã được sử dụng trong phần thực nghiệm. Các kết quả thực nghiệm cho thấy rằng phương pháp tổng hợp hình ảnh của chúng tôi đảm bảo cho hình ảnh tổng hợp đầu ra có chất lượng tốt về cách kía cạnh cường độ sáng, độ tương phản, lượng thông tin và độ sắc nét.

Trong tương lai, một số giải pháp khả thi có thể được sử dụng để cải thiện hiệu quả của việc tổng hợp hình ảnh y học. Giải pháp thứ nhất là cải thiện chất lượng của hình ảnh đầu vào. Ví dụ, nghiên cứu của Dinh và đồng nghiệp [27] đã cho thấy rằng việc nâng chất lượng của hình ảnh đầu vào cho phép cải thiện đáng kể hiệu năng của việc tổng hợp hình ảnh. Giải pháp thứ hai là áp dụng các phương pháp mới để tổng hợp cho các thành phần cơ sở và chi tiết. Ví dụ, quy tắc tổng hợp dựa trên cấu trúc Tensor đã được đề xuất để tổng hợp các thành phần chi tiết theo nghiên cứu của Dinh [26]. Giải pháp thứ ba là áp dụng các giải thuật tối ưu mới được đề xuất gần đây. Giải pháp này có thể cho phép cải thiện sự hiệu quả trong việc tìm kiếm các tham số tối ưu.

LỜI CẢM ƠN

Tác giả Đinh Phú Hùng được tài trợ bởi Tập đoàn Vingroup - Công ty CP và hỗ trợ bởi Chương trình học bổng thạc sĩ, tiến sĩ trong nước của Quỹ Đổi mới sáng tạo Vingroup (VINIF), Viện Nghiên cứu Dữ liệu lớn, mã số VINIF.2021.TS.133.

TÀI LIỆU THAM KHẢO

[1] P. H. Dinh, "Combining Gabor energy with equilibrium optimizer algorithm for multi-modality medical image fusion", *Biomed Signal Process Control*, Vol. 68, p. 102696, Jul. 2021, doi: 10.1016/j.bspc.2021.102696.

[2] Z. Wang, X. Li, H. Duan, Y. Su, X. Zhang, and X. Guan, "Medical image fusion based on convolutional neural networks and non-subsampled contourlet transform", *Expert Syst Appl*, Vol. 171, 2021, doi: 10.1016/j.eswa.2021.114574.

[3] J. Jose *et al.*, "An image quality enhancement scheme employing adolescent identity search algorithm in the NSST domain for multimodal medical image fusion", *Biomed Signal Process Control*, Vol. 66, 2021, doi: 10.1016/j.bspc.2021.102480.

[4] Z. Wang, Z. Cui, and Y. Zhu, "Multi-modal medical image fusion by Laplacian pyramid and adaptive sparse representation", *Comput Biol Med*, 2020, doi: 10.1016/j.compbiomed.2020.103823.

[5] Y. Liu *et al.*, "Robust spiking cortical model and total-variational decomposition for multimodal medical image fusion", *Biomed Signal Process Control*, Vol. 61, 2020, doi: 10.1016/j.bspc.2020.101996.

[6] J. Reena Benjamin and T. Jayasree, "Improved medical image fusion based on cascaded PCA and shift invariant wavelet transforms", *Int J Comput Assist Radiol Surg*, Vol. 13, No. 2, 2018, doi: 10.1007/s11548-017-1692-4.

[7] X. Li, F. Zhou, H. Tan, W. Zhang, and C. Zhao, "Multimodal medical image fusion based on joint bilateral filter and local gradient energy", *Inf Sci (N Y)*, Vol. 569, 2021, doi: 10.1016/j.ins.2021.04.052.

[8] Y. Liu, X. Chen, R. K. Ward, and Z. J. Wang, "Medical image fusion via convolutional sparsity based morphological component analysis", *IEEE Signal Process Lett*, Vol. 26, No. 3, pp. 485-489, 2019, doi: 10.1109/LSP.2019.2895749.

[9] P. H. Dinh, "A novel approach based on Grasshopper optimization algorithm for medical image fusion", *Expert Syst Appl*, Vol. 171, Jun. 2021, doi: 10.1016/j.eswa.2021.114576.

[10] P. H. Dinh, "An improved medical image synthesis approach based on marine predators algorithm and maximum Gabor energy", *Neural Comput Appl*, Vol. 34, No. 6, 2022, doi: 10.1007/s00521-021-06577-4.

[11] P. H. Dinh, "Multi-modal medical image fusion based on equilibrium optimizer algorithm and local energy functions", *Applied Intelligence*, 2021, doi: https://doi.org/10.1007/s10489-021-02282-w.

[12] P. H. Dinh, "A novel approach based on Three-scale image decomposition and Marine predators algorithm for multi-modal medical image fusion", *Biomed Signal Process Control*, No. January, p. 102536, 2021, doi: 10.1016/j.bspc.2021.102536.

[13] S. Polinati and R. Dhuli, "Multimodal medical image fusion using empirical wavelet decomposition and local energy maxima", *Optik (Stuttg)*, Vol. 205, p. 163947, Mar. 2020, doi: 10.1016/j.ijleo.2019.163947.

[14] A. Sabeeh Yousif, Z. Omar, and U. Ullah Sheikh, "An improved approach for medical image fusion using sparse representation and Siamese convolutional neural network", *Biomed Signal Process Control*, Vol. 72, 2022, doi: 10.1016/j.bspc.2021.103357.

[15] D. S. Shibu and S. S. Priyadharsini, "Multi scale decomposition based medical image fusion using convolutional neural network and sparse representation", *Biomed Signal Process Control*, Vol. 69, 2021, doi: 10.1016/j.bspc.2021.102789.

[16] Q. Li, W. Wang, G. Chen, and D. Zhao, "Medical image fusion using segment graph filter and sparse representation", *Comput Biol Med*, Vol. 131, 2021, doi: 10.1016/j.compbiomed.2021.104239.

[17] Y. Gao, S. Ma, J. Liu, Y. Liu, and X. Zhang, "Fusion of medical images based on salient features extraction by PSO optimized fuzzy logic in NSST domain", *Biomed Signal Process Control*, Vol. 69, 2021, doi: 10.1016/j.bspc.2021.102852.

[18] J. Duan, S. Mao, J. Jin, Z. Zhou, L. Chen, and C. L. P. Chen, "A Novel GA-Based Optimized Approach for Regional Multimodal Medical Image Fusion with Superpixel Segmentation", *IEEE Access*, Vol. 9, 2021, doi: 10.1109/ACCESS.2021.3094972.

[19] Y. Liu, X. Chen, R. K. Ward, and Z. J. Wang, "Medical image fusion via convolutional sparsity based morphological component analysis", *IEEE Signal Process Lett*, Vol. 26, No. 3, pp. 485-489, Mar. 2019, doi: 10.1109/LSP.2019.2895749.

[20] Y. Liu, X. Chen, R. K. Ward, and J. Wang, "Image Fusion with Convolutional Sparse Representation", *IEEE Signal Process Lett*, Vol. 23, No. 12, pp. 1882-1886, 2016, doi: 10.1109/LSP.2016.2618776.

[21] Q. Zhang, X. Shen, L. Xu, and J. Jia, "Rolling guidance filter", in *Lecture Notes in Computer Science (including subseries Lecture Notes in Artificial Intelligence and Lecture Notes in Bioinformatics)*, 2014, Vol. 8691 LNCS, No. PART 3. doi: 10.1007/978-3-319-10578-9_53.

[22] J. Fu, W. Li, A. Ouyang, and B. He, "Multimodal biomedical image fusion method via rolling guidance filter and deep convolutional neural networks", *Optik (Stuttg)*, Vol. 237, 2021, doi: 10.1016/j.ijleo.2021.166726.

[23] F. Liu, L. Chen, L. Lu, G. Jeon, and X. Yang, "Infrared and visible image fusion via rolling guidance filter and convolutional sparse representation", *Journal of Intelligent and Fuzzy Systems*, Vol. 40, No. 6, 2021, doi: 10.3233/JIFS-201494.

[24] T. Hattori, K. Inoue, and K. Hara, "Rolling guidance filter as a clustering algorithm", *IEICE Trans Inf Syst*, Vol. E104D, No. 10, 2021, doi: 10.1587/transinf.2021PCL0001.

[25] A. Faramarzi, M. Heidarinejad, S. Mirjalili, and A. H. Gandomi, "Marine Predators Algorithm: A nature-inspired metaheuristic", *Expert Syst Appl*, Vol. 152, 2020, doi: 10.1016/j.eswa.2020.113377.

[26] P.-H. Dinh, "A novel approach using structure tensor for medical image fusion", *Multidimens Syst Signal Process*, pp. 1-21, 2022.

[27] P.-H. Dinh, "A new medical image enhancement algorithm using adaptive parameters", *Int J Imaging Syst Technol*, 2022, doi: https://doi.org/10.1002/ima.22778.

[28] S. Mirjalili, "Dragonfly algorithm: a new meta-heuristic optimization technique for solving single-objective, discrete, and multi-objective problems", *Neural Comput Appl*, Vol. 27, No. 4, 2016, doi: 10.1007/s00521-015-1920-1.

[29] S. Mirjalili, S. M. Mirjalili, and A. Hatamlou, "Multi-Verse Optimizer: a nature-inspired algorithm for global optimization", *Neural Comput Appl*, Vol. 27, No. 2, pp. 495-513, 2016, doi: 10.1007/s00521-015-1870-7.

[30] S. Mirjalili, S. M. Mirjalili, and A. Lewis, "Grey Wolf Optimizer", *Advances in Engineering Software*, Vol. 69, 2014, doi: 10.1016/j.advengsoft.2013.12.007.

[31] S. Mirjalili, "SCA: A Sine Cosine Algorithm for solving optimization problems", *Knowl Based Syst*, Vol. 96, pp. 120-133, Mar. 2016, doi: 10.1016/j.knosys.2015.12.022.

[32] Y. Liu, X. Chen, R. K. Ward, and J. Wang, "Image Fusion with Convolutional Sparse Representation", *IEEE Signal Process Lett*, Vol. 23, No. 12, pp. 1882-1886, Dec. 2016, doi: 10.1109/LSP.2016.2618776.

[33] A. Sufyan, M. Imran, S. A. Shah, H. Shahwani, and A. A. Wadood, "A novel multimodality anatomical image fusion method based on contrast and structure extraction", *Int J Imaging Syst Technol*, Vol. 32, No. 1, 2022, doi: 10.1002/ima.22649.

MEDICAL IMAGE FUSION BASED ON MPA OPTIMIZATION ALGORITHM

Dinh Phu Hung, Nguyen Huy Duc, Nguyen Long Giang

ABSTRACT: *Medical image fusion plays an important role in supporting clinicians make better clinical diagnoses. Up to now, many approaches to solve this problem have been proposed. However, the composite image still has some quality problems, such as reduced brightness, contrast, and even loss of details. This paper proposes a new method to overcome the limitations mentioned above. The input images will first be decomposed into two components (base component and detail component) using the Rolling guidance filter (RGF). Then, the base components are fused together using the MPA (Marine predators algorithm) optimization algorithm. The detailed components are fused using the Prewitt compass operator combined with the local energy function. Experiments show that our proposed method significantly improves the fused images' quality and preserves the images' details.*

NHÀ XUẤT BẢN KHOA HỌC TỰ NHIÊN VÀ CÔNG NGHỆ
Nhà A16 - Số 18 Hoàng Quốc Việt, Cầu Giấy, Hà Nội
Điện thoại: Phòng Phát hành: **024.22149040**;
Phòng Biên tập: **024.37917148**;
Phòng Quản lý Tổng hợp: **024.22149041**;
Fax: **024.37910147**; Email: **nxb@vap.ac.vn**; Website: **www.vap.ac.vn**

FAIR

KỶ YẾU HỘI NGHỊ KHOA HỌC CÔNG NGHỆ QUỐC GIA LẦN THỨ XV

Nghiên cứu cơ bản và Ứng dụng công nghệ thông tin

Proceedings of the 15th National Conference on Fundamental and Applied Information Technology Research (FAIR'2022)

Học viện Kỹ thuật Mật mã, Hà Nội, ngày 03-04/11/2022

Chịu trách nhiệm xuất bản
Giám đốc, Tổng biên tập
PHẠM THỊ HIẾU

Biên tập:	**Nguyễn Văn Vĩnh, Nguyễn Thị Chiên**
	Hà Thị Thu Trang
Trình bày kỹ thuật:	**Đỗ Hồng Ngân**
Trình bày bìa:	**Đỗ Hồng Ngân**

Liên kết xuất bản:
Liên hiệp các Hội Khoa học và Kỹ thuật Việt Nam
Địa chỉ: Số 53 Nguyễn Du, phường Nguyễn Du, quận Hai Bà Trưng, Hà Nội

ISBN: 978-604-357-119-6

In 150 cuốn, khổ 20x29,5 cm, tại Công ty Cổ phần Khoa học và Công nghệ Hoàng Quốc Việt. Địa chỉ: Số 18 Hoàng Quốc Việt, Cầu Giấy, Hà Nội.
Số xác nhận đăng ký xuất bản: 4581-2022/CXBIPH/02-64/KHTNVCN.
Số quyết định xuất bản: 87/QĐ-KHTNCN, cấp ngày 26 tháng 12 năm 2022.
In xong và nộp lưu chiểu quý IV năm 2022.